

An integrated approach to the study of biosignatures in mineralizing biofilms and microbial mats

Dissertation

Zur Erlangung des akademischen Grades

Doctor rerum naturalium

(Dr. rer. nat.)



Geowissenschaftliches Zentrum der Georg-August-Universität Göttingen
Abteilung Geobiologie



Vorgelegt von:

Diplom-Geologin

Christine Nora Heim

Göttingen 2010

D7

Gutachter:

1. Prof. Dr. Volker Thiel
2. Prof. Dr. Joachim Reitner

Tag der mündlichen Prüfung: 09.07.2010

Acknowledgements

It's nearly five years ago since I started this thesis, and with just a rough idea of what was expected of me - but all in all it was a great experience and I am indebted to all my colleagues, friends and family who helped me through this phase.

First of all, of course, great thanks to Volker Thiel and Joachim Reitner for giving me the opportunity to join this project, and for the critical but very constructive discussions. I am grateful to my working group, Andrea Hagemann, Cornelia Conrad, Juliane Germer, Tim Leefmann and Martin Blumenberg for nice tea-time chats, assistance in the lab and in the Äspö tunnel. Thank you Martin for the proofreading. Extra hours in the tunnel were brighter with Nadias Quéric's companionship.

I received analytical support from Klaus Simon, Jan Toporski, Erwin Schiffcyk, Bent Hansen, Nicole Nolte, Brigitte Dietrich, Andreas Kronz, Andreas Reimer, Dorothea Hause-Reitner, Birgit Röhring, Wolfgang Dröse, Volker Karius and Veit-Enno Hoffman. Thanks to Lothar Laake and his colleagues from the workshop for the help with all kinds of constructions for the tunnel equipment and further technical support from Alexander Satmatri and Michael Sosnitza.

The whole work in the Äspö tunnel wouldn't have been possible without the support from SKB, special thanks to Mats Ohlsson, Emmeli Johansson, Magnus Kronberg, Teresita Morales, Carljohan Hardenby, Linda Alakangas, Irene Hultberg and Ann-Sofie Karlson. Thank you Peter Sjövall and Jukka Lausmaa for the support during my three month stay in Borås, and thanks to Jakob Malm for the introduction to Swedish traditions (midsommar). I had a great and productive time with Barbara Zippel and Thomas Neu in Magdeburg.

Thomas Bode was always very helpful in all kinds of computer and software support and to remind me to have a little break now and then. Thanks also to Sharmishtha Dattagupta and Daniel Jackson for the recreational work distractions. Katja Milkereit, my best friend, was the special sponsor of my thesis – thank you for all the supportive phone calls, and high energy and motivation packages. For the everlasting support and encouragement I am especially indebted to Oliver Hach and my family. This thesis is dedicated to my parents, Renate and Kurt Heim.

This thesis was accomplished as part of the DFG Research Group FOR 571, subproject 1 "Microbial biomineralization, biogeochemistry and biodiversity of chemolithotrophic microorganisms in the tunnel of Äspö (Sweden).

Preface

This doctoral thesis comprises the following papers, book entries and manuscripts:

Heim C, Lausmaa J, Sjövall P, Toporski J, Dieing T, Simon K, Hansen B, Kronz A, Reitner J, Thiel V (2010) Ancient microbial activity recorded in fracture fillings from granitic rocks (Äspö Hard Rock Laboratory, Sweden). *Geobiology*, in revision.

Heim C, Simon K, Quéric N-V, Reitner J, Thiel V (2010) Trace and rare earth element accumulation and fractionation in microbial iron oxyhydroxides. *Geochimica et Cosmochimica Acta*, in revision

Heim C (2011) Terrestrial Deep Biosphere. *Encyclopedia of Geobiology*, Springer, in press.

Heim C (2011) Microbial Biomineralization. *Encyclopedia of Geobiology*, Springer, in press.

Rodríguez-Martines M, **Heim C**, Quéric N-V, Reitner J (2011) Frutexites. *Encyclopedia of Geobiology*, Springer, in press.

Toporski J, Dieing T, **Heim C** (2011) Raman microscopy (confocal). *Encyclopedia of Geobiology*, Springer, in press.

Heim C, Sjövall P, Lausmaa J, Leefmann T, Thiel V (2009) Spectral characterization of eight glycerolipids and their detection in natural samples using time-of-flight secondary ion mass spectrometry. *Rapid Communications in Mass Spectrometry*, **23**, 2741-2753.

Sjövall P, Thiel V, Siljeström S, **Heim C**, Hode T, Lausmaa J (2008) Organic geochemical microanalysis by time-of-flight secondary ion mass spectrometry (ToF-SIMS). *Geostandards and Geoanalytical Research*, **32**, 267-277.

Thiel V, **Heim C**, Arp G, Hahmann U, Sjövall P, Lausmaa J (2007) Biomarkers at the microscopic range: ToF-SIMS molecular imaging of Archaea-derived lipids in a microbial mat. *Geobiology*, **5**, 413-421.

Table of contents

Chapter 1

Introduction.....	1
1.1 Microbial life.....	1
1.2 Biosignatures.....	2
1.3 Study Site – Äspö Hard Rock Laboratory Sweden.....	10
1.4 Integrated analytical approach – high lateral resolution concept.....	12
1.5 Introduction to the following chapters.....	14
References	16

Chapter 2

Biomarkers at the microscopic range: ToF-SIMS molecular imaging of Archaea-derived lipids in a microbial mat	25
2.1 Abstract	25
2.2 Introduction	26
2.3 Materials and methods.....	27
2.4 Results and discussion.....	28
2.5 Conclusions.....	36
Acknowledgements.....	37
References.....	38

Chapter 3

Organic geochemical microanalysis by time-of-flight secondary ion mass spectrometry (ToF-SIMS).....	41
3.1 Abstract	41
3.2 Introduction	41
3.3 Capabilities and limitations of ToF-SIMS	42
3.4 Experimental.....	46
3.5 Results and discussion.....	47

3.6 Concluding remarks.....	54
Acknowledgements.....	54
References.....	55

Chapter 4

Spectral characterization of eight glycerolipids and their detection in natural sample using time-of-flight secondary ion mass spectrometry.....	57
4.1 Abstract	57
4.2 Introduction.....	57
4.3 Experimental.....	59
4.4 Results and discussion.....	61
4.5 Archaeol in a methanotrophic microbial mat.....	72
4.6 Diglyceride and phosphatidylglycerol in a Gallionella-dominated microbial mat.....	73
4.7 Conclusions.....	75
Acknowledgements.....	76
References.....	77

Chapter 5

Trace and rare earth element accumulation and fractionation in microbial iron oxyhydroxides.....	79
5.1 Abstract.....	79
5.2 Introduction.....	80
5.3 Materials and methods.....	82
5.4 Results.....	84
5.5 Discussion.....	91
5.6 Conclusions.....	95
Acknowledgements.....	95
References.....	96

Chapter 6

Ancient microbial activity recorded in fracture fillings from granitic rocks (Äspö Hard Rock Laboratory, Sweden).....	99
6.1 Abstract.....	99
6.2 Introduction.....	100
6.3 Geological setting of the Äspö site.....	101
6.4 Methods.....	102
6.5 Results.....	103
6.6 Discussion.....	115
6.7 Conclusions.....	118
Acknowledgements.....	119
References.....	119

Chapter 7

Summary and Conclusions.....	127
------------------------------	-----

Appendix:

A Terrestrial Deep Biosphere.....	129
B Microbial Mineralization.....	141
C Frutexites.....	151
D Raman Microscopy.....	161
CV.....	175

1

Introduction

1.1 Microbial life

Since the early Precambrian, microbial life significantly contributes to the global biomass and drives element cycles in the geo-, hydro-, and atmosphere (Banfield and Nealson, 1997; Ehrlich, 1998; Fenchel and Finlay, 1995; Schieber *et al.*, 2007). Apart from controversies on the metabolism of the first cellular forms, i.e. heterotrophy vs. autotrophy (Wächtershäuser, 1990; Bult, 1996; Stetter, 1996; Ehrlich, 2002), microbial communities formed by chemolithoautotrophic and chemoheterotrophic microorganisms may be the most ancient ecosystems on Earth (e.g. Wächtershäuser, 1988; Teske and Stahl, 2002). Early life on Earth probably developed in the subsurface, protected from radiation penetrating the forming atmosphere and meteoric impacts (Trevors, 2002; Russel, 2003; Bailey *et al.*, 2009).

Since the discovery of the first subsurface microorganisms in the 1930s, numerous reports followed, describing living chemolithoautotrophic and chemoheterotrophic microorganisms being well adapted to the nutrients and energy sources available at great depth (Lipman, 1931; Lieske, 1932; Bailey *et al.*, 1973; Belyaev *et al.*, 1983; Pedersen, 1993, 1997; Chapelle, 2000). Continuation of the deep biosphere research led to the detection of novel organisms, metabolic pathways and adaption mechanisms (e.g. Sahl *et al.*, 2008; Wanger *et al.*, 2008), and growing knowledge on the Earth's deep biosphere enabled to retrace fundamental element cycles and to deduce implications for the early evolution of life (for more details and references, see **appendix A, Heim, 2011, "Terrestrial Deep Biosphere"**).

In the deep biosphere, as in any other aquatic environment, microorganisms often occur as aggregated communities, forming biofilms and microbial mats (Teske and Stahl, 2002). Wherever water and nutrients are available, any surface is rapidly covered with organic substances, followed by the colonization with microorganisms (bacteria, archaea, and unicellular eukaryotes), thus forming the initial stage of a biofilm. With time and under favorable conditions, further microbial species will consort resulting in a complex and diverse ecosystem at a submillimetre scale. Biofilms growing in thickness without disturbance can turn into decimeter thick microbial mats (Characklis and Marshall 1990; Teske and Stahl, 2002; Konhauser, 2007). Examples for recent microbial mats are shown in figure 1.1. An important characteristic of biofilms and microbial mats is the excretion of extracellular polymeric substances (EPS; Wingender *et al.*, 1999). In most cases, EPS serve as protection against desiccation, extreme pH and temperature changes, enhance surface adhesion and stabilize biofilms and microbial mats (Wolfaardt *et al.*, 1999). EPS is generally composed of polysaccharides, proteins, nucleic acids, lipids and humic substances (Nielsen *et al.*, 1997). The amount of EPS can exceed by far the volume of the producing cell.

Knowledge about microbial life in subterranean environments is the key to understand how life evolved and survived crises such as meteorite impacts, increased volcanic activity, or global glaciations such as the Late Precambrian Snowball Earth. Any attempt to reconstruct ancient microbial systems requires, first of all, a comparison with recent analogs and the determination of potential biosignatures for the microorganisms and metabolic pathways involved. The aim of this thesis was the study of recent chemolithotrophic and chemoheterotrophic mineralizing microbial mats in subsurface environments, with a focus on the establishment of biosignatures that can be related to their source organisms and the application of these biosignatures to the fossil record.

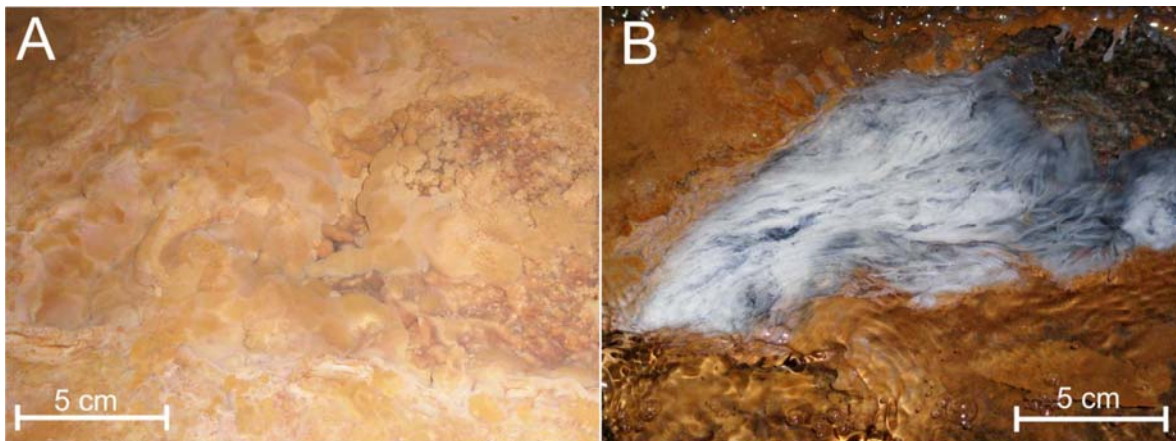


Fig. 1.1. Mineralizing microbial mats formed by (A) iron oxidizing and (B) sulfur oxidizing microorganisms, growing in subsurface aquifers in the Äspö Hard Rock Laboratory at ca. 150m depth.

1.2 Biosignatures

Biosignatures are traces of organisms which provide characteristic information about the organism itself and about the surrounding environmental conditions. These traces derive from the major characteristics of all living organisms, i.e. (i) their physical structure, (ii) their chemical composition (e.g., DNA, membrane lipids), and (iii) their metabolism and resulting interactions with the environment (Westall and Southam, 2006; Westall, 2008). Whereas these considerations hold true for all organisms, this thesis will place special emphasis on microbial biosignatures, due to their importance as drivers of manifold biogeochemical cycles.

Living (micro-) organisms shape their environment by their presence and metabolic activity. This results in changes of the adjacent physico-chemical environment, leaving traces like biomorphs, organic molecules, stable isotope and elemental fractionations, biomineral deposits and corrosion marks.

1.2.1 Morphological biosignatures

Morphological remnants comprise the preservation of the physical structure of microorganisms (as body fossil), the surrounding colony, biofilm or microbial mat. This may also include traces like

etching or corrosion marks and borings of organisms that have altered the surrounding minerals (e.g. Banerjee *et al.*, 2006; Staudigel *et al.*, 2008; Cockell *et al.*, 2009).

Soft organic matter without hard shells or supporting framework undergoes rapid degradation after death. However, the fossilization of organic material is favoured when penetrating fluids cause a permineralization, e.g. silicification. Especially reactive surfaces of microbial cells or EPS act as “mineralizing templates”, via cation sorption and mineral nucleation (Fig. 1.2; Konhauser, 2007; Westall, 2008). The degree of encrustation or permineralization depends on the abundance of exposed functional groups within the organic matter.

EPS, but also the thick peptidoglycan layer of Gram-positive bacteria seem to be more susceptible to cation and mineral sorption compared to Gram-negative bacteria with their thin peptidoglycan layers inserted between the outer lipopolysaccharide and inner phospholipid layer (Westall, 1997). The fossilization process itself can be described as passive mineralization (for details see **Heim, 2011; appendix B, “Microbial Biomineralization”**) and is often observed for not “actively” mineralizing cells, biofilms and microbial mats (e.g. Toporski *et al.*, 2002; Hofmann *et al.*, 2008; Westall, 2008). Morphological features like lamination (Fig. 1.3 A), dendrites (Fig. 1.3 B), and growth response to current and sediment flux allowed a relation of Precambrian stromatolites to recent analogues formed by filamentous calcifying cyanobacteria (e.g. Reid *et al.*, 2000; Kazmierczak and Kempe, 2006; Shiraishi *et al.*, 2008; Dupraz *et al.*, 2009).

Other biomorphs observed in the geological record indeed show characteristic shapes, but their relation to their precursor organisms or processes is yet unclear (for example the dendritic microfossil *Frutexites*; for details see **Rodriguez-Martinez *et al.*, 2011; appendix C, “Frutexites”**). Especially when reconstructing Precambrian life forms, the identification and interpretation of morphological biosignatures and their differentiation from pseudofossils or “look-alikes” is still a major issue (McCall, 2006; Sugitani *et al.*, 2007; Mc Loughlin *et al.*, 2008; Schopf *et al.*, 2010).

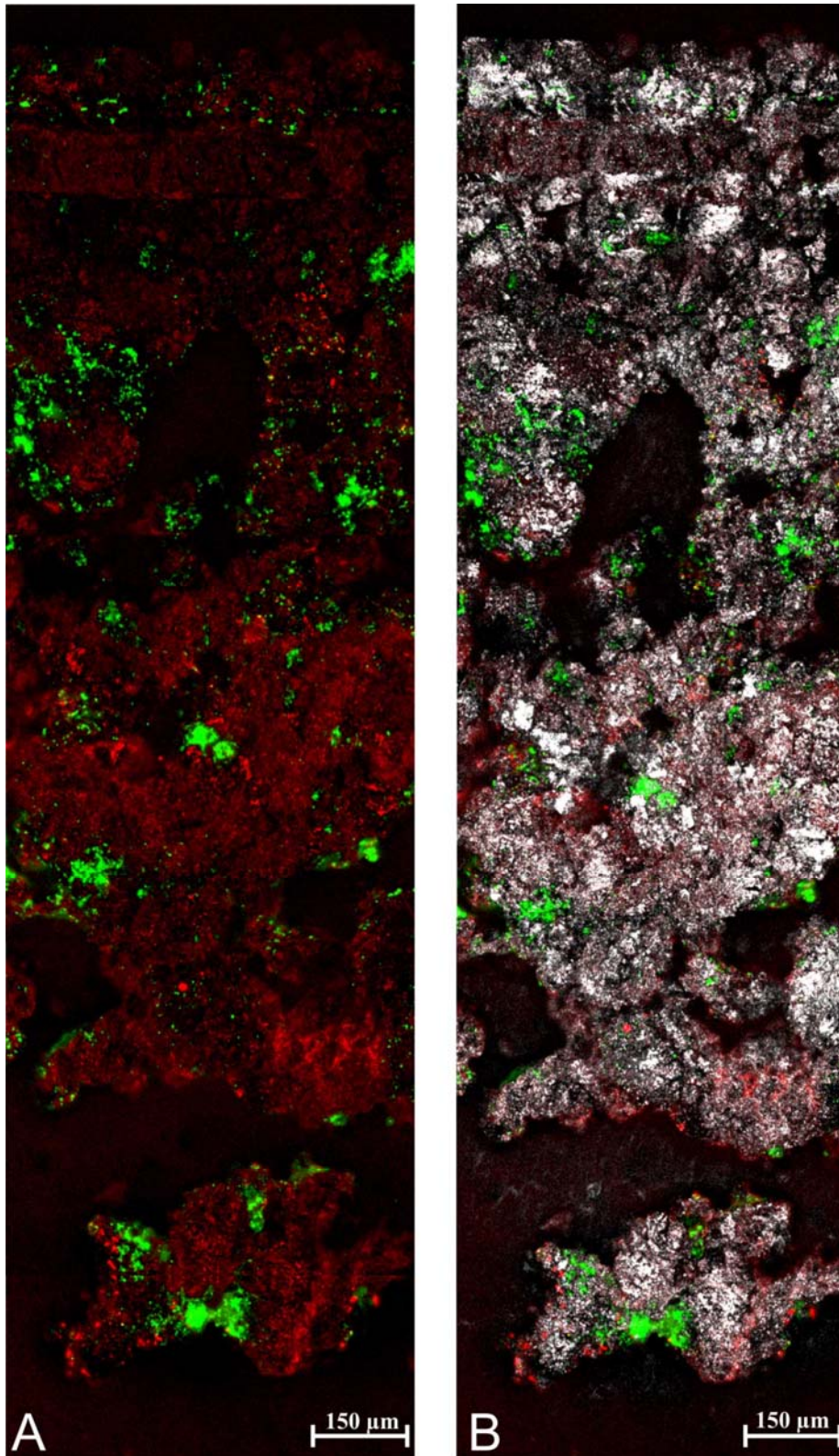


Fig. 1.2 Photomicrographs of a mineralizing microbial mat section, obtained by confocal Laser scanning microscopy. This microbial mat was formed by iron oxidizers in the Äspö Hard Rock Laboratory (HRL) at ca. 150m depth. (A) Color overlay of EPS (red, staining PSA_568), and microbial cells (green, staining sybr green). (B) The same area as in (A), with iron oxide precipitates made visible as white areas (reflectance). Note that, in this case, the mineral precipitates are predominantly associated with the EPS, rather than with the microbial cells.

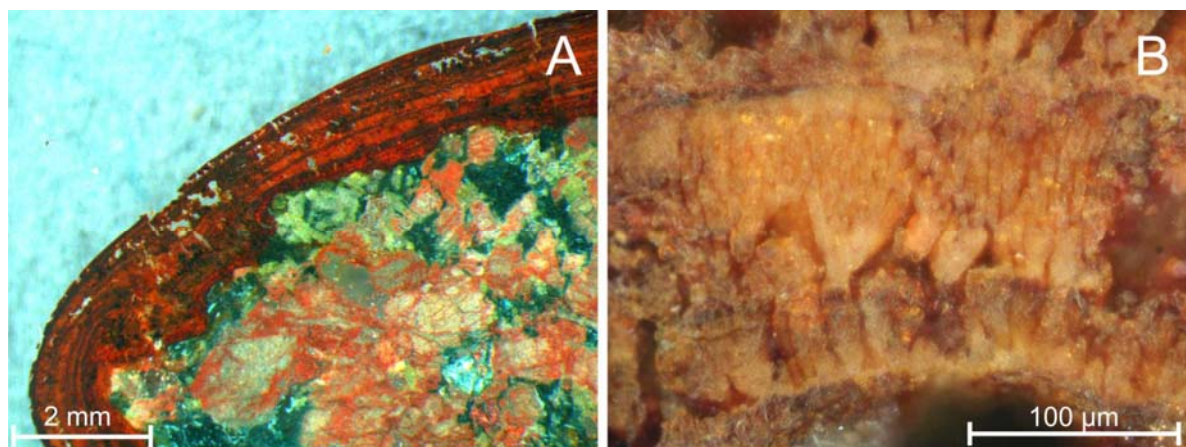


Fig. 1.3 Morphological biosignatures derived from recent iron-oxidizing microbial mats growing on a granodioritic rock surface in the Äspö HRL. (A) Laminated structures using reflected light microscopy and (B) *Frutexites*-like, dendritic structures are visible under dark-field reflected light microscopy.

1.2.2 Organic molecular markers / Biomarkers

The term “biomarker” is occasionally used as a synonym for biosignatures, but traditionally, biomarkers refer to organic molecular markers (especially lipids) and therefore, in order to avoid misunderstandings, the more specific synonym “molecular biosignatures” has been suggested (Summons *et al.*, 2008). In contrast to other biosignatures, organic molecules (biomarkers) provide evidence for a biosynthetic origin (Brocks and Pearson, 2005).

Nucleic acids, amino acids, proteins and carbohydrates are essential and characteristic constituents of living organisms and are used as biomarkers for recent or potential extraterrestrial life traces (Kminek, 2000; Botta *et al.*, 2002; Jia *et al.*, 2008; Summons *et al.*, 2008). However, lipids and pigments are more commonly used as biomarkers since they are more resistant to degradation. When suffering from diagenesis and catagenesis during burial, lipid biomarkers may be altered, e.g. by defunctionalization and isomerisation. However, the hydrocarbon skeletons can be stable over billions of years and still bear source specific information (e.g., Brocks and Summons, 2004; Peters *et al.*, 2004; Brocks and Pearson, 2005). The biomarker pattern extracted from ancient rocks may thus enable a relation between certain communities of microorganisms and their surrounding environment. This knowledge, together with an understanding of the potential degradation pathways helps to reconstruct ancient life forms and environmental conditions (Brocks and Pearson, 2005; Volkman, 2006; Summons *et al.*, 2008). Due to distinctive biosynthetic pathways for certain lipids in bacteria, archaea and eukaryotes, some intact lipids, as well as their derived biomarker molecules, can be attributed to distinctive groups of organisms. For example, for the achievement of membrane rigidity, eukaryotic organisms produce sterols, whereas bacteria use predominantly hopanoids (Fig. 1.4, e.g., Volkman, 1986; Ourisson and Albrecht, 1992; Ourisson and Rohmer, 1992; Brown, 1998; Kannenberg and Poralla, 1999; Härtner *et al.*, 2005; Summons *et al.*, 2006). Likewise, bacteria and eukaryotes both synthesize **ester-bound** phospholipids, but

archaea contain **ether-bound** phospho- and/or glycerol-lipids (Koga *et al.*, 1993; Wu *et al.*, 1997; Hanford and Peeples, 2002; Rütters *et al.*, 2002; Koga and Morii, 2007). Further, the detection of particular pigments like carotenoids indicates the presence of photosynthetic organisms (Fig. 1.4; Brocks *et al.*, 2005; Brocks and Pearson, 2005).

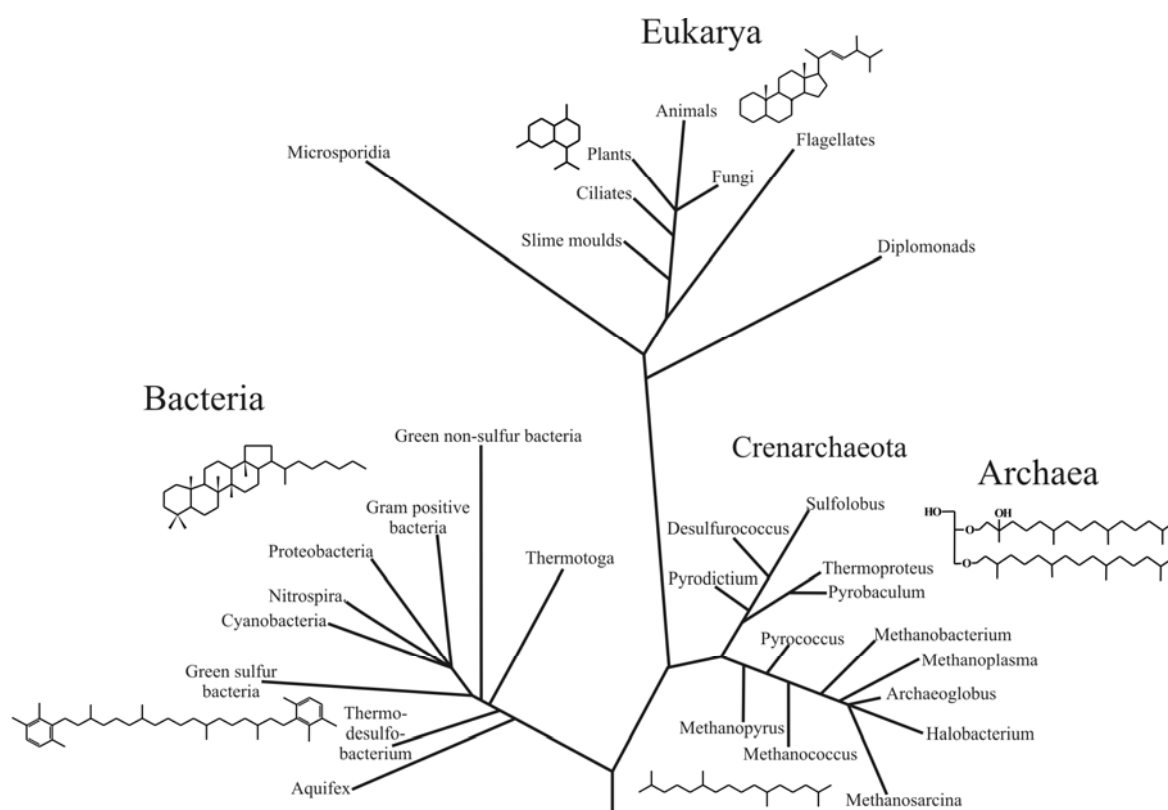


Fig. 1.4 Universal phylogenetic tree with lipid biomarkers specific for individual branches (modified after Brocks and Summons, 2004).

1.2.3 Stable isotope signatures

Specific stable isotope signatures, and the biosignatures described in the following, give only indirect evidence of the existence of organisms and consequently a critical and cautious interpretation is necessary.

Primary biosynthesis of organic molecules is accompanied by isotopic fractionation of ^{13}C over ^{12}C (expressed as $\delta^{13}\text{C}$ -values). ^{13}C -depletion of organic compounds can therefore be interpreted as a biosignature (for a review, see Hayes, 2001). Low $\delta^{13}\text{C}$ values in early Archaean rocks from Pilbara (Australia) and Isua (Greenland) are reported to harbor the oldest traces of life (e.g. Mojzsis *et al.*, 1996; Shidlowksi, 2001). However, under certain circumstances (i.e. hydrothermal conditions), this fractionation can also result from abiotic Fischer-Tropsch type reactions (McCollom *et al.*, 1999; van Zuilen *et al.*, 2002; Horita, 2005). Accordingly, evidence for ancient life cannot solely rely on carbon isotopic signatures.

Other isotopic systems have been utilized as indicators for early life, namely sulfur (S) isotopes as indicator for sulphate reduction by sulphate reducing prokaryotes (SRP, Shen and Buik, 2004; Canfield *et al.*, 2010), and nitrogen (N) isotope fractionation inferring microbial activity (Beaumont and Robert, 1999; Papineau *et al.*, 2005), and the practicability of iron (Fe) isotopes as biosignature is investigated (Beard *et al.*, 1999; Icopini *et al.*, 2004). Experiments demonstrated a biologically induced isotope fractionation for the transition metals molybdenum (Mo), zinc (Zn), chromium (Cr), nickel (Ni) and mercury (Hg) (Berquist and Blum, 2007; John *et al.*, 2008; Wasylenki *et al.*, 2007; Sikora *et al.*, 2008; Cameron *et al.*, 2009). Fe and Mo isotopes are also used as palaeoenvironmental proxies, for the reconstruction of anoxic, or euxinic conditions in water or respectively sediments (Anbar, 2004; Matthews *et al.*, 2004; Poulson *et al.*, 2006; Siebert *et al.*, 2006; Dauphas *et al.*, 2007; Fehr *et al.*, 2008).

Alkaline earth elements like Ca and Mg are also examined as potential biosignature to reconstruct environmental conditions, as for example palaeo sea-temperatures (Nägler *et al.*, 2000; Young and Galy, 2004)

1.2.4 Biominerals

Frequent products of microbial activity are biominerals, which are formed either under controlled crystallization conditions or, much more common, as a by-product of metabolic activity or organic matter-metal interaction (Lowenstamm and Weiner, 1989). Depending on the formation processes, the minerals show a broad diversity and may differ distinctly from the inorganically formed equivalents, in shape, size, crystallinity, isotopic and trace element composition (Fig. 1.5; Konhauser, 1997; Weiner and Dove, 2003; Bazylinski *et al.*, 2007; Haferburg and Kothe, 2007; Takahashi *et al.*, 2007). In the following, the focus lies on the two major groups of microbially induced biominerals. For a more detailed overview on biominerals and mineral-forming microorganisms, see **Heim (2011; appendix B, “Microbial Biomineralization”)**.

Photoautotrophic, chemolithoautotrophic and chemoheterotrophic microorganisms form organic carbon molecules using light energy (phototrophs), or gain energy through redox reactions with inorganic and organic substrates such as H₂, CO, CO₂ (HCO₃⁻), CH₄, NH₄⁺, H₂S, SO₄²⁻, Mn(II), Mn(IV), Fe(II), and Fe (III) (Staley, 2002; Konhauser, 2007). These processes may induce the formation of carbonates, iron minerals or other mineral precipitates. The most abundant biominerals, both in terms of the quantities produced and their widespread distribution among different taxa, are calcium carbonate minerals (Lowenstamm and Weiner, 1989; Weiner and Dove, 2003). Carbonate precipitation is commonly observed for photosynthetic microorganisms (cyanobacteria, algae) and results in the formation of a great variety of microbialites (Arp *et al.*, 2001; Reid *et al.*, 2000; Burns *et al.*, 2009; stromatolites, thrombolites). CaCO₃ deposits can also be found in aphotic environments, such as recent and ancient methane seeps. Methane-derived CaCO₃

precipitates form due to an increase in alkalinity which is caused by the anaerobic oxidation of methane (AOM) by consortia of methane oxidizing archaea and sulphate reducing bacteria (SRB) (Lein *et al.*, 2002; Nauhaus *et al.*, 2004; Peckmann and Thiel, 2004; Reitner *et al.*, 2005).

Iron biominerals are of particular geological significance, not only because they comprise approximately 40% of all minerals formed by organisms (Lowenstamm, 1986; Weiner and Dove, 2003), iron oxidizing microorganisms may have played a central role for the massive deposition of banded iron formations (BIF) in the Precambrian (Konhauser *et al.*, 2002). The mechanisms of BIF are widely discussed and scenarios involving abiotic and biotic processes have been proposed (e.g. Morris, 1983; Bau and Möller, 1993; Krapez *et al.*, 2003; Kappler *et al.*, 2005).

1.2.5 Trace and rare earth elements (TREE) biosignatures

Evidence of microbial activity can be obtained by distinct fractionations and or accumulations of elements such as iron (Fe), manganese (Mn), magnesium (Mg), cobalt (Co), nickel (Ni), copper (Cu), zinc (Zn), and molybdenum (Mo) (Silver, 1997; Lovley, 2000). These elements are known to have biochemical and physiological functions in metabolic pathways, for instance, Cu and Ni are included in proteins, and Mo is an important trace element necessary for nitrogen fixation (Zerkle, 2006). Negatively charged surfaces of cells, EPS offer extensive surfaces for the biosorption of metals, whereas elements with a higher positive charge are preferentially sorbed (Texier *et al.*, 1999; Haferburg and Kothe, 2007). Both, metabolic activity and biomineral precipitation of chemolithoautotrophic and chemoheterotrophic organisms play an important role in TREE co-precipitation and fractionation (Ferris *et al.*, 2000; Anderson and Pedersen, 2003; Yoshida *et al.*, 2004; Haferburg *et al.*, 2007; Takahashi *et al.*, 2007).

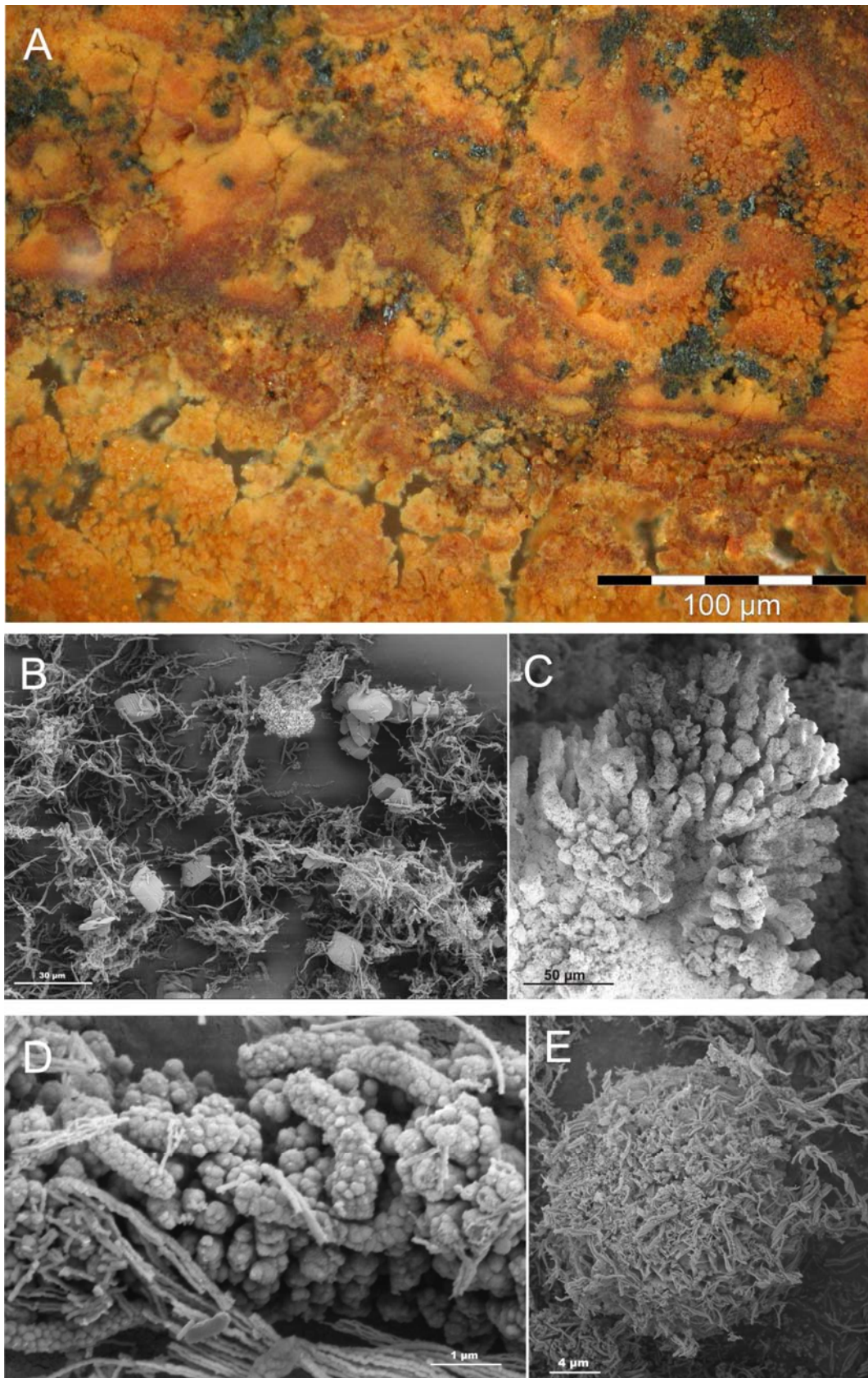


Fig. 1.5 Biomaterial formation within iron oxidizing microbial mats in the Äspö HRL. (A) Diverse iron oxide mineral phases using dark-field reflected-light microscopy; SEM images of (B) gypsum co-occurrence with *Gallionella* dominated microbial mats, (C) dendritic structures of iron oxides, (D) iron-oxide encrusted bacteria, (E) phosphate sphere formation.

1.3 Study site – Äspö Hard Rock Laboratory (Sweden)

The Äspö Hard Rock Laboratory (HRL), operated by the Swedish Nuclear Fuel and Waste Management Company (SKB), is a tunnel drilled beneath the island of Äspö in south-eastern Sweden, ca. 400km south of Stockholm (Fig. 1.6 A, B) and serves as a testing site for the long-term storage of nuclear waste. The host rock of the Äspö site belongs to the Precambrian Transscandinavian Igneous Belt and consists of ~1.8 Ga old granitic to quartz-monzodioritic rocks (Wahlgren *et al.*, 2006).

The Äspö HRL offers a unique window into the deep terrestrial biosphere, where the growth of different microbial consortia strongly depends on the flow, oxygen content and the chemical composition of the fluids available. Diverse chemolithoautotrophic and chemoheterotrophic microorganisms cover rock-water interfaces along the tunnel, dominated by iron oxidizing, sulphate reducing and/or sulphite oxidizing microbial mats (e.g. Pedersen, 1993, 1997). Occasionally, microbial mats of phototrophic microorganisms were observed below artificial light (tunnel illumination).

The recent subsurface biosphere in the Äspö HRL was used as a model system for the detection and characterization of microbial biosignatures and their relation to fluid composition and mineral fabrics within fractures. Vein minerals from 450m depth were sampled from drill cores (SKB core library) as potential archives for biosignatures, and were investigated to test the applicability of the results to the fossil record. Furthermore, a flow reactor experiment was designed to mimic conditions similar to fractures and cavities in the surrounding quartz-monzodioritic host rock. These reactors enabled the development of pristine microbial mats without contamination (Fig. 1.6 C to E). Only chemically inert materials such as polytetrafluoroethylene (PTFE, Teflon®), PTFE – fibre glass, fluorinated ethylene propylene (FEP) and special PTFE – foam were used as construction materials to avoid biological contamination from the surrounding environment and chemical contamination from glass and plastic ware. The flow reactor systems and connection tubings were thoroughly sterilized with ethanol (70%, overnight) before underground installation. A flow reactor set consists of 4 different flow reactors, enabling to provide basic requirements for different microorganisms: illuminated and aerated (1), illuminated and air-tight (2), dark and aerated (3) dark and air-tight (4). The flow reactor sets were connected to three chemically differing aquifers, and were monitored for physicochemical fluctuations and the development of microbial mats in regular intervals of 2-3 months (Fig. 1.6 F to H).

The microbial mats developing in the dark and air-tight flow reactors of two aquifers were dominated by *Gallionella ferruginea*, an auto- and mixotrophic, microaerophilic, iron-oxidizing bacterium that uses Fe(II) as an electron donor and CO₂ or carbohydrates as carbon source (Hallbeck and Pedersen, 1991; Hallbeck *et al.*, 1993). Because iron oxidizing bacteria have been hypothesized as crucial players in the processes that formed Archaean and Proterozoic banded iron

formations (BIF) (e.g. Konhauser, 2002; Kappler and Newmann, 2004), *G. ferruginea* dominated microbial mats were investigated for potential biosignatures, namely molecular biosignatures, iron oxide biomineralization phenomena, and TREE accumulation (Heim *et al.*, 2009, chapter 4; Heim *et al.*, in revision, chapter five).

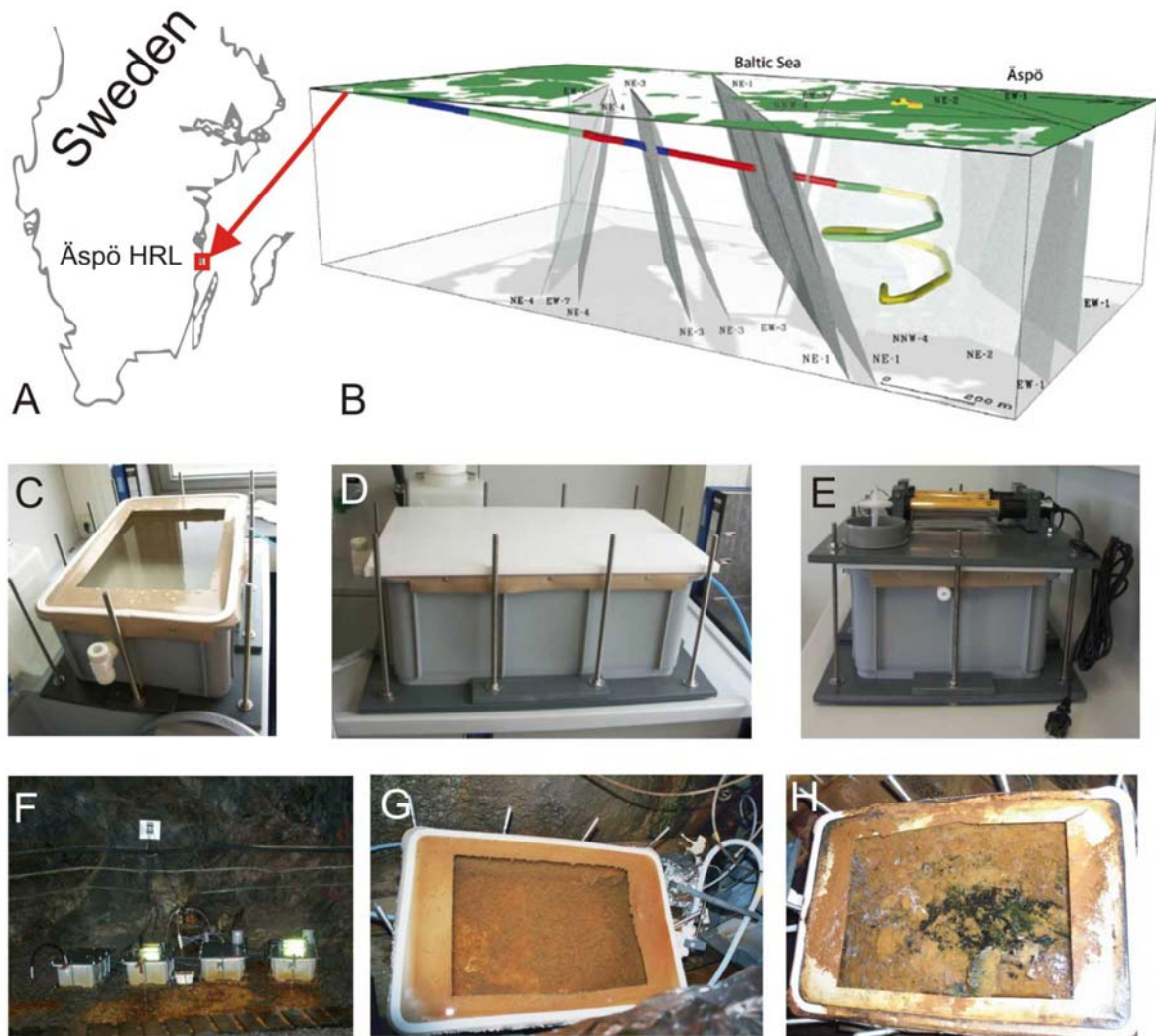


Fig. 1.6 (A) Location of the Äspö Hard Rock Laboratory, (B) 3-D-scheme of the tunnel and the major fracture zones modified after Laaksoharju and Wold (2005), colour changes of the tunnel sections indicate differences in the hydrochemistry of the aquifers (B). Assembly of the flow reactors (C - E), flow reactor set installed at tunnel site 2156B (F), opened flow reactors containing different microbial mats according to the conditions offered: dark and air-tight (G) and illuminated and air-tight (H).

1.4 Integrated analytical approach – high lateral resolution concept

Biosignatures tested in this study encompassed molecular biosignatures, biomineralization processes, and TREE accumulation and fractionation. However, the investigation of biomarkers in complex and inhomogenous environmental materials has to deal with the following difficulties:

- I. Recent microbial mats show an enormous biodiversity, and studies continuously report findings of new chemical and metabolic pathways, genotypic and phenotypic variations (Teske and Stahl, 2002).
- II. Knowledge on lipid compositions in microorganisms is limited (few species are available as pure cultures, and cultivation has as yet been impossible for most microorganisms).
- III. For source specific lipid biomarker analysis, conventional extraction-based techniques such as GC-MS and LC-MS (coupled gas chromatography-mass spectrometry, coupled liquid chromatography-mass spectrometry) are limited in their applicability, because these methods require relatively large sample quantities. Therefore samples are often homogenized, resulting in the loss of the spatial information within the sample.
- IV. Any attempt to combine biosignature analysis with complementary analytical techniques, e.g. microscopy, requires a non-destructive analytical procedure.

Unlike GC-MS and LC-MS, methods like microscopy and laser ablation inductively coupled mass spectrometry (LA-ICP-MS) can be conducted using relatively small sample amounts at high lateral or spatial resolution (μm -range) to investigate fine-scale biomineralization processes and TREE fractionations and accumulations.

However, for the approach presented here, a non-destructive methodological approach was sought that enabled a direct analysis of microbial biomarkers at a scale resolving the typical size range of microbial consortia. Such miniaturization of the biomarker approach would facilitate a linkage of molecular biosignature analysis and microscopic techniques which has not been achieved so far.

Particularly two analytical techniques fulfill these requirements, Time-of-Flight-Secondary Ion Mass Spectrometry (ToF-SIMS, Benninghoven, 1994; Pacholski and Winograd, 1999; Hagenhoff, 2000; Sodhi 2004) and Confocal Raman Microscopy (CRM, Nasdala *et al.*, 2004; Fries and Steele, 2009).

Although the high resolution analyses obtained by ToF-SIMS and CRM contain significantly less chemical information than provided by conventional biomarker analyses (GC-MS; LC-MS), they render unique constraints on the structure, chemistry and distribution of organics and associated minerals at the submicrometer-scale. So far, however, both techniques were predominantly used in material sciences (Vickerman and Briggs, 2001; Belu *et al.*, 2003; Ibach and Lüth, 2003; Nasdala *et al.*, 2004) rather than in biomarker studies (e.g. Arouri *et al.*, 2000; Steele *et al.*, 2001; Toproski and Steele, 2004; Edwards *et al.*, 2005).

1.4.1 Time-of-Flight secondary ion mass spectrometry (ToF-SIMS)

ToF-SIMS is a surface analysis technique that enables the simultaneous detection of organic and inorganic ionised molecules on a pre-defined area with μm -resolution (e.g., Vickerman and Briggs, 2001, Arlinghaus *et al.*, 2006). The principle of ToF-SIMS is as follows: A beam of positively charged ions scans the sample surface in a defined raster pattern. The impact of the primary ions on the uppermost molecule layers of the sample causes secondary ions that are measured by a time-of-flight mass spectrometer. Although SIMS was invented as non-imaging technique, the application and improvement of primary ion guns and secondary analyzers enabled the obtainment of ion images with high lateral and mass resolution (Hagenhoff, 2000). Recent developments improved the applicability of ToF-SIMS for the detection and imaging of organic molecules e.g. of lipids in organic tissue (Kollmer, 2004; Sjovall *et al.*, 2004; Touboul *et al.*, 2004, 2005). Figure 1.7 shows the ToF-SIMS used in this study and a sketch of the instrument design. A more detailed description of the ToF-SIMS technique is given in chapters two and three.

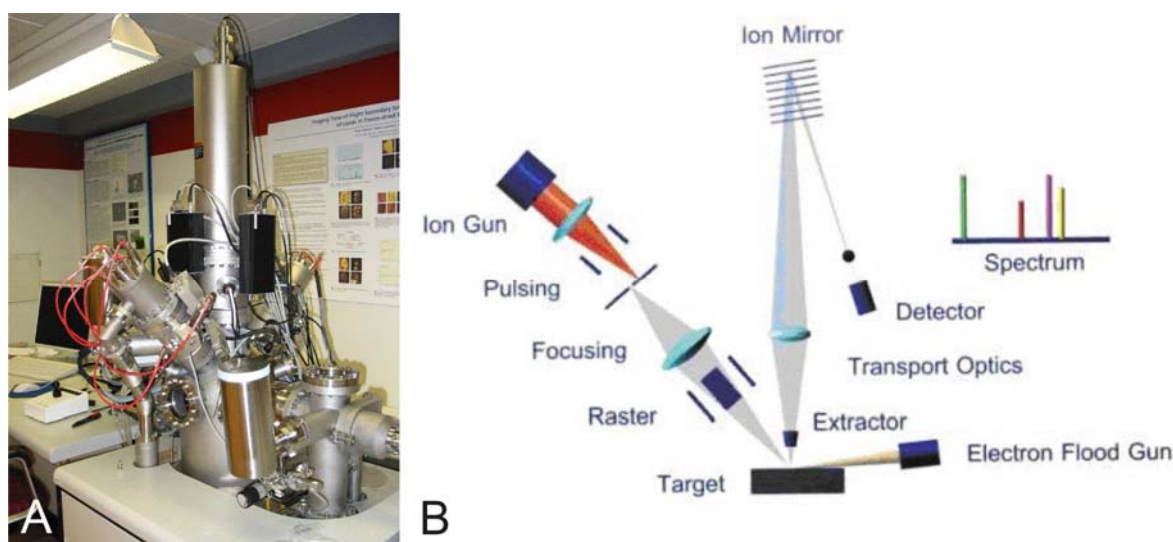


Fig. 1.7 (A) ToF-SIMS IV Instrument used in this study at the SP Technical Research Institute of Sweden, Borås, and (B) scheme of the ToF-SIMS principle, image courtesy of ION-TOF GmbH, Münster).

1.4.2 Confocal Raman Microscopy (CRM)

The theory of Raman spectroscopy is based on the interaction of light of a certain wavelength with a molecule. This interaction results in elastically (reflected) and, to a small proportion, in inelastically scattered light, i.e. the energy of the scattered photon is different to the incident photon. This shift in energy is characteristic for the type of molecule and its coordination to others and can consequently be used as fingerprint for the respective molecule. Confocal Raman Microscopy (CRM) merges Raman spectroscopy and confocal microscopy for the visualization of molecular information over a defined sample area, enabling the characterization of mineral phases

and organic compounds in the vicinity of the respective minerals in geological samples. For a detailed description of CRM, see **Toporski *et al.*, 2011, Appendix D, “Raman Microscopy”**.

1.5 Introduction to the following chapters

To test the utility of ToF-SIMS for the laterally resolved detection of lipid biomarkers in mineralizing microbial systems, pre-characterized calcifying microbial mats from the Black Sea were used as a model system. These mineralizing microbial mats form reef-like carbonate structures through AOM (Hinrichs *et al.*, 1999; Boetius *et al.*, 2000; Michaelis *et al.*, 2002) and are well characterized in terms of microbiology, structure, and lipid biomarker patterns (Thiel *et al.*, 2001; Lein *et al.*, 2002; Blumenberg *et al.*, 2004; Knittel *et al.*, 2005; Pape *et al.*, 2005; Reitner *et al.*, 2005; Treude *et al.*, 2005). Considerable efforts were undertaken to develop a contamination-free preparation protocol for microscopic sections to be analysed with ToF-SIMS. However, ToF-SIMS enabled a differentiation of biomarker patterns for individual microbial communities within the microscopic section, which so far has not been possible using conventional biomarker analysis. Further, the virtually non-destructive sample analysis of ToF-SIMS allowed a subsequent microscopical investigation of the same sample. The results are described in detail in **chapter two (Biomarkers at the microscopic range: ToF-SIMS molecular imaging of Archaea-derived lipids in a microbial mat)**.

A comprehensive overview of the use of ToF-SIMS the capabilities and limitations of this technique and the potential for geobiological samples, is given in **chapter three (Organic geochemical microanalysis by time-of-flight secondary ion mass spectrometry (ToF-SIMS))**.

Despite the promising results obtained in these pilot studies, the lack of reference data of fragmentation patterns and molecular ions has been hampering an accurate assignment of molecular structures. To enlarge the spectral data base for biomarker analyses, numerous lipid standards were analysed and their fragmentation patterns were interpreted. Using these fundamental data, individual lipids could be identified in microscopic sections from two mineralizing microbial mats. One of these samples was obtained from the methane seep associated Black Sea mats (see above) whereas the other was taken from *G. ferruginea*-dominated iron-oxidizing microbial mats from the Äspö HRL (**chapter four; spectral characterization of eight glycerolipids and their detection in natural samples using time-of-flight secondary ion mass spectrometry**).

Further biosignatures, namely biomineralization processes and corresponding TREE fractionations of the iron-oxidizing microbial mats and their implication for the formation of BIF are discussed in **chapter five (Trace and rare earth element accumulation and fractionation in microbial iron oxyhydroxides)**. This study showed that TREE are considerably accumulated within microbial iron oxyhydroxides. The observed REE+Y pattern differs significantly from those in inorganically

precipitated iron oxyhydroxides, indicating a great potential of TREE fractionations as biosignature for palaeoenvironmental studies.

Finally, an integrated geochemical approach to microbial biosignatures preserved in fracture fillings is described in **chapter six (Ancient microbial activity recorded in fracture fillings from granitic rocks (Äspö Hard Rock Laboratory, Sweden))**. This study aimed to examine the composition and spatial distribution of organic and inorganic molecules in the fracture fillings at the microscopic range. It was possible to identify different fracture mineral generations and a putative ancient biofilm that existed during a phase, when the fracture was reactivated and water conducting.

References:

- Anbar AD (2004) Iron stable isotopes: beyond biosignatures. *Earth and Planetary Science Letters*, **217**, 223-236.
- Anderson CR, Pedersen K. (2003) In situ growth of *Gallionella* biofilms and partitioning of lanthanides and actinides between biological material and ferric oxyhydroxides. *Gebiology*, **1**, 169-178.
- Arlinghaus HF, Kriegskotte C, Fartmann M, Wittig A, Sauerwein W, Lipinsky D (2006) Mass spectrometric characterization of elements and molecules in cell cultures and tissues. *Applied Surface Science*, **252**, 6941-6948.
- Arouri KR, Greenwood PF, Walter MR (2000) Biological affinities of neoproterozoic acritarchs from Australia: microscopic and chemical characterisation. *Organic Geochemistry*, **31**, 75-89.
- Arp G, Reimer A, Reitner J (2001) Photosynthesis-induced biofilm calcification and calcium concentrations in Phanerozoic Oceans. *Science*, **292**, 1701-1704.
- Banerjee NR, Furnes H, Muehlenbachs K, Staudigel H, de Wit M (2006) Preservation of ~3.4-3.5 Ga microbial biomarkers in pillow lavas and hyaloclastites from the Barberton Greenstone Belt, South Africa. *Earth and Planetary Science Letters*, **241**, 707-722.
- Bailey JV, Orphan VJ, Joye SB, Corsetti FA (2009) Chemotrophic microbial mats and their potential for preservation in the Rock Record. *Astrobiology*, **9**, 843-859.
- Bailey N J L, Jobson AM, Rogers MA (1973) Bacterial degradation of crude oil: Comparison of field and experimental data. *Chemical Geology*, **11**, 203-221.
- Banfield JF, Nealson KH (eds) (1997) *Interactions between microbes and minerals. Reviews in Mineralogy* 35, Mineralogical Society of America, Washington DC, 448p.
- Bau M, Möller P (1993) Rare earth element systematics of the chemically precipitated component in Early Precambrian iron-formations and the evolution of the terrestrial atmosphere-hydrosphere-lithosphere system. *Geochimica et Cosmochimica Acta*, **57**, 2239-2249.
- Bazylinski DA, Frankel RB, Konhauser KO (2007) Modes of biomineralization of magnetite by microbes. *Geomicrobiology Journal*, **24**, 465-475.
- Beard BL, Johnson CM, Cox L, Sun H, Nealson KH, Aguilar C (1999) Iron isotope biosignatures. *Science*, **285**, 1889-1892.
- Beaumont V, Robert F (1999) Nitrogen isotope ratios of kerogens in Precambrian cherts: a record of the evolution of atmospheric chemistry? *Precambrian Research*, **96**, 63-82.
- Belu AM, Graham DJ, Castner DG (2003) Time-of-flight secondary ion mass spectrometry: techniques and applications for the characterization of biomaterial surfaces. *Biomaterials*, **24**, 3635-3653.
- Belyaev SS, Wolkin R, Kenealy M, DeNiro MJ, Epstein S, Zeikus, JG (1983). Methanogenic bacteria from the bondyushskoe oil field: General characterization and analysis of stable-carbon isotopic fractionation. *Applied environmental microbiology*, **45**, 691-697.
- Benninghoven A (1994) Chemical Analysis of Inorganic and Organic Surfaces and Thin Films by Static Time-of-Flight Secondary Ion Mass Spectrometry (ToF-SIMS). *Angewandte Chemie International Edition in English*, **33**, 1023-1043.
- Bergquist BA, Blum JD (2007) Mass-Dependent and -Independent Fractionation of Hg Isotopes by Photoreduction in Aquatic Systems. *Science*, **318**, 417-420.

- Blumenberg M, Seifert R, Reitner J, Pape T, Michaelis W (2004) Membrane lipid patterns typify distinct anaerobic methanotrophic consortia. *Proceedings of the National Academy of Sciences of the United States of America*, **101**, 11111-11116.
- Boetius A, Ravensschlag K, Schubert CJ, Rickert D, Widdel F, Gieseke A, Amann R, Jørgensen BB, Witte U, Pfannkuche O (2000) A marine microbial consortium apparently mediating anaerobic oxidation of methane. *Nature*, **407**, 623-626.
- Botta O, Glavin DP, Kminek G, Bada JL (2002) Relative amino acid concentrations as a signature for parent body processes of carbonaceous chondrites. *Origins of Life and Evolution of the Biosphere*, **32**, 143-163.
- Brocks JJ, Love GD, Summons RE, Knoll AH, Logan GA, Bowden SA (2005) Biomarker evidence for green and purple sulphur bacteria in a stratified Palaeoproterozoic sea. *Nature*, **437**, 866-870.
- Brocks JJ, Pearson A (2005) Building the biomarker tree of life. In *Reviews in Mineralogy and Geochemistry*, Vol. 59, 233-258.
- Brocks JJ, Summons RE (2004) Sedimentary Hydrocarbons, Biomarkers for early life. In Schlesinger W.H: (ed), Holland H.D., Turekian K.K (chief eds), *Treatise on Geochemistry*, Vol 8, Elsevier, 63-115.
- Brown GD (1998) The biosynthesis of steroids and triterpenoids. *RCS Natural Product Reports*, 653- 696.
- Bult CJ, White O, Olsen GJ, Zhou L, Fleischmann RD, Sutton GG, Blake JA, FitzGerald LM, Clayton RA, Gocayne JD, Kerlavage AR, Dougherty BA, Tomb J-F, Adams MD, Reich CI, Overbeek R, Kirkness EF, Weinstock KG, Merrick JM, Glodek A, Scott JL, Geoghagen NSM, Weidman JF, Fuhrmann JL, Nguyen D, Utterback TR, Kelley JM, Peterson JD, Sadow PW, Hanna MC, Cotton MD, Roberts KM, Hurst MA, Kaine BP, Borodovsky M, Klenk H-P, Fraser CM, Smith HO, Woese CR, Venter JC (1996) Complete genome sequence of the methanogenic archaeon, *Methanococcus jannaschii*, *Science*, **273**, 1058-1073.
- Burns BP, Anitori R, Butterworth P, Henneberger R, Goh F, Allen MA, Ibañez-Peral R, Berquist PL, Walter MR, Neilan BA (2002) Modern analogues and the early history of microbial life. *Precambrian Research*, **173**, 10-18.
- Cameron V, Vance D, Archer C, House CH (2009) A biomarker based on the stable isotopes of nickel. *Proceedings of the National Academy of Sciences*, **106**, 10944-10948.
- Canfield D, Farquhar J, Zerkle AL (2010) High isotope fractionations during sulfate reduction in a low-sulfate euxinic ocean analog. *Geology*, **38**, 415-418.
- Chapelle FH (2000) *Ground-water Microbiology and Geochemistry*. Wiley-VCH, 496 pages.
- Charaklis WG, Marshall KC (eds) (1990) *Biofilms*. John Wiley and Sons, Inc, New York. 816 p.
- Cockell CS, Olsson-Francis K, Herrera A, Meunier A (2009) Alteration textures in terrestrial volcanic glass and the associated bacterial community. *Geobiology*, **7**, 50-65.
- Dauphas N, van Zuilen M, Busigny V, Lepland A, Wadhwa M, Janney PE (2007) Iron isotope, major and trace element characterization of early Archean supracrustal rocks from SW Greenland: Protolith identification and metamorphic overprint. *Geochimica et Cosmochimica Acta*, **71**, 4745-4770.
- Dupraz C, Reid RP, Braissant O, Decho AW, Norman RS, Visscher PT (2009) Processes of carbonate precipitation in modern microbial mats. *Earth Science Reviews*, **96**, 141-162.

- Edwards HGM, Moody CD, Villar SEJ, Wynn-Williams DD (2005) Raman spectroscopic detection of key biomarkers of cyanobacteria and lichen symbiosis in extreme Antarctic habitats: Evaluation for Mars Lander Missions. *Icarus*, **174**, 560-571.
- Ehrlich H.L. (2002) *Geomicrobiology* 4th edn. Marcel Dekker Inc, New York, 800p.
- Ehrlich H.L. (1998) Geomicrobiology: its significance for geology. *Earth Science Reviews*, **45**, 45-60.
- Fehr MA, Andersson PS, Halenius U, Morth C-M (2008) Iron isotope variations in Holocene sediments of the Gotland Deep, Baltic Sea. *Geochimica et Cosmochimica Acta*, **72**, 807-826.
- Fenchel T, Finlay BJ (1995) *Ecology and Evolution in anoxic worlds*. Oxford University Press, Oxford, 276p.
- Ferris FG, Hallberg RO, Lyvén B, Pedersen K (2000) Retention of strontium, cesium, lead and uranium by bacterial iron oxides from subterranean environment. *Applied Geochemistry*, **15**, 1035-1042.
- Fries M, Steele A (2009) Raman spectroscopy and confocal Raman imaging in mineralogy and petrography. In Dieing T, Hollricher O, Toporski J (eds) *Confocal Raman Microscopy*. Springer, Heidelberg, 320p.
- Haferburg G, Merten D, Büchel G, Kothe E (2007) Biosorption of metal and salt tolerant microbial isolates from a former uranium mining area. Their impact on changes in rare earth element patterns in acid mine drainage. *Journal of Basic Microbiology*, **47**, 474-484.
- Haferburg G, Kothe E (2007) Microbes and metals: interactions in the environment. *Journal of Basic Microbiology*, **47**, 453-467.
- Hagenhoff B (2000) High resolution surface analysis by TOF-SIMS. *Mikrochimica Acta*, **132**, 259-271.
- Hallbeck L, Ståhl F, Pedersen K (1993) Phylogeny and phenotypic characterization of the stalk-forming iron oxidizing bacterium *Gallionella ferruginea*. *Journal of General Microbiology*, **139**, 1531-1535.
- Hallbeck L, Pedersen K (1991) Autotrophic and mixotrophic growth of *Gallionella ferruginea*. *Journal of General Microbiology*, **137**, 2657-2661.
- Hanford MJ, Peoples TL (2002) Archaeal Tetraether Lipids. Unique structures and applications. *Applied Biochemistry and Biotechnology*, **97**, 45-62.
- Härtner T, Straub KL, Kannenberg E (2005) Occurrence of hopanoids lipids in anaerobic *Geobacter* species. *FEMS Microbiology Letters*, **243**, 59-64.
- Hayes JM (2001) Fractionation of the isotopes of carbon and hydrogen in biosynthetic processes. In J.W. Valley, DR. Cole (Eds.), *Stable isotope geochemistry. Reviews in Mineralogy and Geochemistry*, Vol. 43 Mineralogical Society of America, Washington D.C., 225-278.
- Hinrichs K-U, Hayes JM, Sylva SP, Brewer PG, DeLong EF (1999) Methane-consuming archaeobacteria in marine sediments *Nature* **398**, 802-805.
- Hofmann BA, Farmer JD, Von Blanckenburg F, Fallick AE (2008) Subsurface filamentous fabrics: An evaluation of origins based on morphological and geochemical criteria, with implications for exopaleontology. *Astrobiology*, **8**, 87- 117.
- Horita J (2005) Some perspective on isotope biosignatures for early life. *Chemical Geology*, **218**, 171-186.
- Ibach H, Lüth H (2003) *Solid State Physics. An Introduction to Principles of Materials Science*. Springer, Berlin, 402p.
- Icopini GA, Anbar AD, Ruebush SS, Tien M, Brantley SK (2004) Iron isotope fractionation during microbial reduction of iron, the importance of adsorption. *Geology*, **32**, 205-208.

- Jia G, Dungait JAJ, Bingham EM, Valiranta M, Korhola A, Evershed RP (2008) Neutral monosaccharides as biomarker proxies for bog-forming plants for application to palaeovegetation reconstruction in ombrotrophic peat deposits. *Organic Geochemistry*, **39**, 1790-1799.
- John S G, Rouxel OJ, Craddock PR, Engwall AM, Boyle EA (2008) Zinc stable isotopes in seafloor hydrothermal vent fluids and chimneys. *Earth and Planetary Science Letters*, **269**, 17-28.
- Kannenbergh EL, Poralla K (1999) Hopanoid biosynthesis and function in bacteria. *Naturwissenschaften*, **86**, 168-176.
- Kappler A, Straub B, Newman DK (2005) Fe(III) mineral formation and cell incrustation by the nitrate-dependent Fe(II)-oxidizer strain BoFeN1. *Geobiology*, **3**, 235-245.
- Kappler A, Newmann DK (2004) Formation of Fe(III)-minerals by Fe(II)-oxidizing photoautotrophic bacteria. *Geochimica et Cosmochimica Acta*, **68**, 1217-1226.
- Kazmierczak J, Kempe S (2006) Genuine modern analogues of Precambrian stromatolites from cladera lakes of Niuafu'ou Island, Tonga. *Naturwissenschaften*, **93**, 119-126.
- Kminek G, Bada JL, Botta O, Glavin DP, Grunthaner F (2000) MOD: an organic detector for the future robotic exploration of Mars. *Planetary and Space Science*, **48**, 1087-1091.
- Knittel K, Losekann T, Boetius A, Kort R, Amann R (2005) Diversity and Distribution of Methanotrophic Archaea at Cold Seeps. *Applied and Environmental Microbiology*, **71**, 467-479.
- Koga Y, Morii H (2007) Biosynthesis of ether-type polar lipids in archaea and evolutionary considerations. *Microbiology and Molecular Biology Reviews*, **71**, 97-120.
- Koga Y, Nishihara M, Morii H, Akagawa-Matsushita M (1993) Ether polar lipids of methanogenic bacteria: structures, comparative aspects and biosynthesis. *Microbiological Reviews*, **57**, 164-182.
- Kollmer F (2004) Cluster primary ion bombardment of organic materials. *Applied Surface Science*, **231**, 153-158.
- Konhauser K (2007) *Introduction to geomicrobiology*. Blackwell Publishing, Oxford, 425 p.
- Konhauser KO, Hamade T, Raiswell R, Morris RC, Ferris FG, Southam G, Canfield DE (2002) Could bacteria have formed the Precambrian banded iron formations? *Geology*, **20**, 1079-1082.
- Konhauser KO (1997) Bacterial iron biomineralization in nature. *FEMS Microbiology Reviews*, **20**, 315-326.
- Krapez B, Barley ME, Pickard AL (2003) Hydrothermal and resedimented origins of the precursor sediments to banded iron formation: sedimentological evidence from the Early Paleoproterozoic Brockman Supersequence of Western Australia. *Sedimentology*, **50**, 979-1011.
- Laaksoharju M, Wold S (2005) The colloid investigations conducted at the Äspö Hard Rock Laboratory during 2000-2004. Svensk Kärnbränslehanteriang AB, TR-05-20, 211p.
- Lein AY, Ivanov MV, Pimenov NV, Gulín MB (2002) Geochemical characteristics of the carbonate constructions formed during microbial oxidation of methane under anaerobic conditions. *Microbiology*, **71**, 78-90.
- Lieske R (1932) Über das Vorkommen von Bakterien in Kohlenflözen. *Biochemische Zeitschrift*, **250**, 339-351.
- Lipman CB (1931) Living microorganisms in ancient rocks. *Journal of Bacteriology*, **22**, 183-198.
- Lovley DR (2000) *Environmental microbe-metal interactions* (ed) ASM Press, Washington DC, 395p.
- Lowenstamm HA, Weiner S (1989) *On Biomineralization*. Oxford University Press, New York, 324p.

- Matthews A, Morhans-Bell HS, Emmanuel S, Jenkyns H, Erel Y, Halciz L (2004) Controls of iron-isotope fractionation in organic-rich sediments (Kimmeridge Clay, Upper Jurassic, southern England). *Geochimica et Cosmochimica Acta*, **68**, 3107-3123.
- McCall GJH (2006) The Vendian (Ediacaran) in the geological record: Enigmas in geology's prelude to the Cambrian explosion. *Earth Science Reviews*, **77**, 1-229.
- McCollom TM, Ritter G, Simoneit BRT (1999) Lipid synthesis under hydrothermal conditions by Fischer–Tropsch-type reactions. *Origins of Life and Evolution of the Biosphere*, **29**, 166–453.
- McLoughlin N, Wilson LA, Brasier MD (2008) Growth of synthetic stromatolites and wrinkle structures in the absence of microbes – implications for the early fossil record. *Geobiology*, **6**, 95-105.
- Michaelis W, Seifert R, Nauhaus K, Treude T, Thiel V, Blumenberg M, Knittel K, Gieseke A, Peterknecht K, Pape T, Boetius A, Amann R, Jørgensen BB, Widdel F, Peckmann J, Pimenov NV, Gulin MB (2002) Microbial reefs in the Black Sea fueled by anaerobic oxidation of methane. *Science*, **297**, 1013-1015.
- Mojzsis SJ, Arrhenius G, McKeegan KD, Harison TM, Nutman AP, Friend CRL (1996) Evidence for life on Earth before 3800 million years ago. *Nature*, **384**, 55–59.
- Morris RC, Horwitz RC (1983) The origin of the iron-formation-rich Hamersley Group of Western Australia – Deposition on a platform. *Precambrian Research*, **21**, 273-297.
- Nägler TF, Eisenhauer A, Müller A, Hemleben C, Kramers J (2000) The $\delta^{44}\text{Ca}$ -temperature calibration on fossil and cultured *Globigerinoides sacculifer*: New tool for reconstruction of past sea surface temperatures. *Geochemistry, Geophysics, Geosystems*, **1**, 1052.
- Nauhaus K, Treude T, Boetius A, Kruger M (2005) Environmental regulation of the anaerobic oxidation of methane: a comparison of ANME-I and ANME-II communities. *Environmental Microbiology*, **7**, 98-106.
- Nasdala L, Smith DC, Kaindl R, Ziemann MA (2004) Raman spectroscopy: Analytical perspectives in mineralogical research. In *Spectroscopic Methods in Mineralogy*. Beran A., Libowitzky E., (eds) *Emu Notes in Mineralogy*, Vol. 6, 281-343.
- Nielsen PH, Jahn A, Palmgren R (1997) Conceptual model for production and composition of exopolymers in biofilms. *Water Science and Technology*, **36**, 11-19.
- Ourisson G, Albrecht P (1992) Hopanoids. 1 Geohopanoids: The most abundant natural products on Earth? *Accounts of Chemical Research*, **25**, 398-402.
- Ourisson G, Rohmer M (1992) Hopanoids. 2 Biohopanoids: a novel class of bacterial lipids. *Accounts of Chemical Research*, **25**, 403-408.
- Pacholski ML, Winograd N (1999) Imaging with mass spectrometry. *Chemical Reviews*, **99**, 2977-3005.
- Pape T, Blumenberg M, Seifert R, Egorov VN, Gulin SB, Michaelis W (2005) Lipid geochemistry of methane-seep-related Black Sea carbonates. *Palaeogeography, Palaeoclimatology, Palaeoecology*, **227**, 31-47.
- Papineau D, Mojzsis SJ, Karhu JA, Marty B (2005) Nitrogen isotopic composition of ammoniated phyllosilicates: case studies from Precambrian metamorphosed sedimentary rocks. *Chemical Geology*, **216**, 37-58.
- Peckmann J, Thiel V (2004) Carbon cycling at ancient methane-seeps. *Chemical Geology*, **205**, 443-467.
- Pedersen K (1997) Microbial life in deep granitic rock. *FEMS Microbiology Reviews*, **20**, 399-414.

- Pedersen K (1993) The deep subterranean biosphere. *Earth-Science Reviews*, **34**, 243-260.
- Peters KE, Walters CC, Moldowan JM (2004) *The Biomarker Guide: Volume 1: Biomarkers and Isotopes in the Environments and Human History*. Cambridge University Press, Cambridge, 490 p.
- Poulson RL, McManus J, Siebert C, Berelson WM (2006) Authigenic molybdenum isotope signatures in marine sediments. *Geology*, **34**, 617-620.
- Reid RP, Visscher PT, Decho AW, Stolz JF, Bebout BM, Dupraz C, Macintyre IG, Paerl HW, Pinckney JL, Prufert-Bebout L, Stepe TF, Des Marais DJ (2000) The role of microbes in accretion, lamination and early lithification of modern marine stromatolites. *Nature*, **406**, 989-992.
- Reitner J, Peckmann J, Reimer A, Schumann G, Thiel V (2005) Methane-derived carbonate build-ups and associated microbial communities at cold seeps on the lower Crimean shelf (Black Sea). *Facies*, **51**, 66-79.
- Russel MJ (2003) The importance of being alkaline. *Science*, **302**, 580-581.
- Rütters H, Sass H, Cypionka H, Rulkötter J (2002) Phospholipid analysis as a tool to study complex microbial communities in marine sediments. *Journal of Microbiological Methods*, **48**, 149-160.
- Sahl JW, Schmidt R, Swanner ED, Mandernack KW, Templeton AS, Kieft TL, Smith RL, Sandford WE, Callaghan RL, Mitton JB, Spear JR (2008) Subsurface Microbial Diversity in Deep-Granitic Fracture Water in Colorado. *Applied and Environmental Microbiology*, **74**, 143-152.
- Schieber J, Bose P, Eriksson PG, Banerjee S, Sarkar S, Altermann W, Catuneanu O (2007) *Atlas of microbial mat features preserved within the siliciclastic rock record*. Elsevier, Amsterdam, 311p.
- Schopf JW, Kudryavtsev AB, Sugitani K, Water MR (2010) Precambrian microbe-like pseudofossils: A promising solution of the problem. *Precambrian Research*, **179**, 191-205.
- Shen Y, Buick R (2004) The antiquity of microbial sulfate reduction. *Earth Science Reviews*, **64**, 243-272.
- Shidlowski M (2001) Carbon isotopes as biogeochemical recorders of life over 3.8 Ga of Earth history: evolution of a concept. *Precambrian Research*, **106**, 117– 134.
- Shiraishi F, Bissett A, de Beer D, Reimer A, Arp G (2008) Photosynthesis, Respiration and Exopolymer Calcium-Binding in Biofilm Calcification (Westerhöfer and Deinschwanger Creek, Germany). *Geomicrobiology Journal*, **25**, 83-94.
- Siebert C, McManus J, Bice A, Poulson R, Berelson WM, (2006) Molybdenum isotope signatures in continental margin marine sediments. *Earth and Planetary Science Letters*, **241**, 723-733.
- Sikora E R, Johnson TM, Bullen TD (2008) Microbial mass-dependent fractionation of chromium isotopes. *Geochimica et Cosmochimica Acta*, **72**, 3631-3641.
- Silver S (1997) The bacterial view of the periodic table: specific functions for all elements. In Banfield JF, Nealson KH (eds) *Geomicrobiology: Interactions between microbes and minerals. Reviews in Mineralogy* Vol. 35. Mineralogical Society of America, Washington DC, 345-360.
- Sjovall P, Lausmaa J, Johansson B, (2004) Mass spectrometric imaging of lipids in brain tissue. *Analytical Chemistry*, **76**, 4271-4278.
- Sodhi RNS, (2004) Time-of-flight secondary ion mass spectrometry (ToF-SIMS): Versatility in chemical and imaging surface analysis. *The Analyst*, **129**, 483-487.
- Staley JT (2002) A microbiological perspective of biodiversity. In Staley JT, Reysenbach AL, *Biodiversity of Microbial Life*. Wiley-Liss, New York, 3-23.

- Staudigel H, Furnes H, McLoughlin N, Banerjee NR, Connel LB, Templeton A (2008) 3.5. billion years of glass bioalteration: Volcanic rocks as a basis for microbial life. *Earth-Science Reviews*, **89**, 156-176.
- Steele A, Toporski JKW, Avci R, Guidry S, McKay DS (2001) Time of flight secondary ion mass spectrometry (ToFSIMS) of a number of hopanoids. *Organic Geochemistry*, **32**, 905-911.
- Stetter KO (1996) Hyperthermophiles in the history of life. In Bock GR, Gode JA (eds) *Evolution of hydrothermal ecosystems on the Earth (and Mars)*. Wiley & Sons, Chichester, UK, 1-10.
- Sugitani K, Grey K, Allwood A, Nagaoka T, Mimura K, Minami M, Marshall CP, Van Kranendonk MJ, Walter MR (2007) Diverse microstructure from Archaean chert from the Mount Goldsworthy-Mount Grant area, Pilbara Craton, Western Australia: Microfossils, dubiofossils, or pseudofossils? *Precambrian Research*, **158**, 228-262.
- Summons RE, Albrecht P, McDonald G, Moldowan JM (2008) Molecular biosignatures. *Space Science Reviews*, **135**, 133-159.
- Summons RE, Bradley AS, Jahnke LL, Waldbauer JR (2006) Steroids, triterpenoids and molecular oxygen. *Philosophical Transactions of the royal society B*, **361**, 951-968.
- Takahashi Y, Hirata T, Shimizu H, Ozaki T, Fortin D, (2007) A rare earth element signature of bacteria in natural waters. *Chemical Geology*, **244**, 569-583.
- Teske A, Stahl DA, (2002) Microbial Mats and Biofilms: Evolution, structure, and function of fixed microbial communities. In Staley JT, Reysenbach A-L, *Biodiversity of Microbial Life*. Wiley-Liss, New York, 49-100.
- Texier A-L, Andrès Y, Le Cloirec P (1999) Selective biosorption of Lantanide (La, Eu, Yb) ions by *Pseudomonas aeruginosa*. *Environmental Science and Technology*, **33**, 489-495.
- Thiel V, Peckmann J, Richnow HH, Luth U, Reitner J, Michaelis W (2001) Molecular signals for anaerobic methane oxidation in Black Sea seep carbonates and a microbial mat. *Marine Chemistry*, **73**, 97-112.
- Touboul D, Halgand F, Brunelle A, Kersting R, Tallarek E, Hagenhoff B, Laprévotte O, (2004) Tissue molecular ion imaging by gold cluster ion bombardment. *Analytical Chemistry*, **76**, 1550-1559.
- Touboul D, Kollmer F, Niehuis E, Brunelle A, Laprevotte O, (2005) Improvement of biological time-of-flight-secondary ion mass spectrometry imaging with a bismuth cluster ion source. *Journal of the American Society for Mass Spectrometry*, **16**, 1608-1618.
- Toporski J, Steele A (2004) Characterization of purified biomarker compounds using time of flight-secondary ion mass spectrometry (ToF-SIMS). *Organic Geochemistry*, **35**, 793-811.
- Toporski JKW, Steele A, Westall F, Avci R, Martill DM, McKay DS (2002) Morphologic and spectral investigation of exceptionally well-preserved bacterial biofilms from the Oligocene Enspel formation, Germany. *Geochimica et Cosmochimica Acta*, **66**, 1773-1791.
- Treude T, Knittel K, Blumenberg M, Seifert R, Boetius A (2005) Subsurface Microbial Methanotrophic Mats in the Black Sea. *Applied and Environmental Microbiology*, **71**, 6375-6378.
- Trevors JT (2002) The subsurface origin of microbial life on Earth. *Research in Microbiology*, **153**, 487-491.
- Van Zuilen MA, Lepland A, Arrhenius G (2002) Reassessing the evidence for the earliest traces of life. *Nature*, **418**, 627-630.
- Vickerman JC, Briggs D (2001) *ToF-SIMS: Surface analysis by mass spectrometry*. IM Publications and SurfaceSpectra Limited (Charlton, Chichester, West Sussex, UK), 789pp.

- Volkman JK (1986) A review of sterol markers for marine and terrigenous organic matter. *Organic Geochemistry*, **9**, 83-99.
- Volkman JK (2006) Lipid markers for marine organic matter. In Hutziger O, *The Handbook of environmental chemistry*. Vol 2 part N. Reaction and processes, Springer, Berlin, 27-70.
- Wächtershäuser G (1990) Evolution of the first metabolic cycles. *Proceedings of the National Academy of Sciences*, **87**, 200-204.
- Wächtershäuser G (1988) Before Enzymes and Templates: Theory of surface metabolism. *Microbiological Reviews*, **52**, 452-484.
- Wahlgren C-H, Hermanson J, Forssberg O, Curtis P, Triumf C-A, Drake H, Tullborg E-L (2006) Geological description of rock domains and deformation zones in the Simpevarp and Laxemar subareas. Preliminary site description Laxemar subarea - version 1.2. Svensk Kärnbränslehanteriang AB, R-05-69, 265p.
- Wanger G, Onstott TC, Southam G (2008) Stars of the terrestrial deep subsurface: Anovel 'star-shaped' bacterial morphotype from a South African platinum mine. *Geobiology*, **6**, 325-330.
- Wasylenki LE, Anbar AD, Liermann LJ, Mathur R, Gordon GW, Brantley SL (2007) Isotope fractionation during microbial metal uptake measured by MC-ICP-MS. *Journal of Analytical Atomic Spectrometry*, **22**, 905-910.
- Weiner S, Dove PM (2003) An overview of biomineralization processes and the problem of the vital effect. In Dove PM, De Yoreo JJ, Weiner S (eds.), *Biomineralization. Reviews in Mineralogy and Geochemistry*. Washington DC, USA: Mineralogical Society of America and Geochemical Society, Vol. 54, pp. 1-29.
- Westall F (2008) Morphological Biosignatures in early terrestrial and extraterrestrial materials. *Space Science Reviews*, **135**, 95-114.
- Westall F, Southam G, (2006) Early life on Earth. In Benn K, Mareschal JC, Condie K (eds), *Archean Geodynamics and Environments. AGU Geophysical Monographs*, **163**, 283-304.
- Westall F (1997) The influence of cell wall composition on the fossilization of bacteria and the implications for the search of early life forms. In Cosmovici C, Bower S, Werthimer D (eds), *Astronomical and biochemical origins and the search for life in the Universe*. Bologna, Editori Compositrici, 491-504.
- Wingender J, Neu TR, Flemming H-C (1999) What are bacterial extracellular polymeric substances? In: Wingender J, Neu TR, Flemming H-C, (Eds) *Microbial extracellular polymeric substances: characterization, structure, and function*. Springer, Berlin, p.1-15.
- Wolfaardt GM, Lawrence JR, Korber DR (1999) Function of EPS. In Wingender J, Neu TR, Flemming HC (eds), *Microbial extracellular polymeric substances: characterization, structure, and function*. Springer-Berlag, Berlin, pp. 171-200.
- Wu Y, Wang J, Sui S-F (1997) Characterization of Phospholipids by electron impact, field desorption and liquid secondary ion mass spectrometry. *Journal of Mass Spectrometry*, **32**, 616-625.
- Young ED, Galy A (2004) The Isotope Geochemistry and Cosmochemistry of Magnesium. In C. M. Johnson, B. L. Beard, and F. Albarède (ed.), *Geochemistry of Non-Traditional Stable Isotopes*. Washington: Mineralogical Society of America and Geochemical Society, pp. 197-230.

- Yoshida T, Ozaki T, Ohnuki T, Francis A (2004) Adsorption rate of rare earth elements by γ -Al₂O₃ and *Pseudomonas fluorescens* cells in the presence of deferrioxamine B: implication of siderophores for the Ce anomaly. *Chemical Geology*, **212**, 239-246.
- Zerkle AL, House CH, Cox RP, Canfield DE (2006) Metal limitation of cyanobacterial N₂ fixation and implications for the Precambrian nitrogen cycle. *Geobiology*, **4**, 285–297.

2

Biomarkers at the microscopic range: ToF-SIMS molecular imaging of Archaea-derived lipids in a microbial mat

Volker Thiel, Christine Heim, Gernot Arp, Uwe Hahmann, Peter Sjövall, and Jukka Lausmaa

Geobiology (2007) 5, 413-421

2.1 Abstract

Time-of-Flight Secondary Ion Mass Spectrometry (ToF-SIMS) with a Bismuth cluster primary ion source was used for analysing microbial lipid biomarkers in 10 µm thick microscopic cryosections of methanotrophic microbial mats from the Black Sea. Without further sample preparation, archaeal isopranyl glycerol di- and tetraether core lipids, together with their intact diglycoside (gentiobiosyl-) derivatives were simultaneously identified by exact mass determination. Utilizing the imaging capability of ToF-SIMS, the spatial distributions of these biomarkers were mapped at a lateral resolution of < 5µm in 500 x 500µm² areas on the mat sections. Using Bi₃⁺ cluster projectiles in the burst alignment mode, it was possible to reach a lateral resolution of 1µm on an area of 233µm x 233µm, thus approaching the typical size of microbial cells. These mappings showed different 'provenances' within the sections that are distinguished by individual lipid fingerprints, namely (A) the diethers archaeol and hydroxyarchaeol co-occurring with glycerol dialkyl glycerol tetraethers (GDGT), (B) hydroxyarchaeol and dihydroxyarchaeol, and (C) GDGT and gentiobiosyl-GDGT. Because ToF-SIMS is a virtually non-destructive technique affecting only the outermost layers of the sample surface (typically 10 - 100nm), it was possible to further examine the studied areas using conventional microscopy, and associate the individual lipid patterns with specific morphological traits. This showed that provenance (B) was frequently associated with irregular, methane-derived CaCO₃ crystallites, whereas provenance (C) revealed a population of fluorescent, filamentous microorganisms showing the morphology of known methanotrophic ANME-1 archaea. The direct coupling of organic (and inorganic) biomarker analysis by imaging mass spectrometry with microscopic techniques reveals interesting perspectives for the *in-situ* study of environmental samples, and for the analysis of lipids in geobiology, microbial ecology, and organic geochemistry. After further developing protocols for handling different kinds of environmental samples, ToF-SIMS could be used as a tool to attack many universal problems in these fields, such as the attribution of biological source(s) to particular biomarkers in question, or the high-resolution tracking of biogeochemical processes in modern and ancient natural environments.

2.2 Introduction

Time-of-Flight Secondary Ion Mass Spectrometry (ToF-SIMS) is a powerful analysis technique that simultaneously detects inorganic and organic molecules on solid surfaces (Benninghoven, 1994; Chait and Standing, 1981; see Belu *et al.*, 2003, for a recent review). Positively charged primary ions are focussed to a beam that is scanned in a raster pattern over the sample surface. As a result of the impact of these primary ions, charged particles (secondary ions) from the upper few monolayers of the sample surface are ejected into vacuum. These secondary ions are separated by their mass in a Time-of-flight (ToF) mass spectrometer. A most advantageous property of ToF-SIMS is its ability to generate images displaying the intensities of any detected ion in a given area of interest on the sample surface. Thereby, ToF-SIMS can achieve spatial resolution on a very small scale (sub- μm , e.g. Hagenhoff, 2000), and at very small quantities (attomole level, e.g. Braun *et al.*, 1999; Kollmer, 2004), which is not possible with any of the extract-based techniques routinely used in biomarker studies, namely GC/MS and LC/MS (coupled gas chromatography/mass spectrometry, coupled liquid chromatography/mass spectrometry). Although the structural information that can be obtained by ToF-SIMS is limited due to the absence or as yet sparse definition of mass spectral fragmentation patterns, sound compound identification can be achieved through the precise mass determination of the molecular species, ideally in combination with GC/MS and/or LC/MS data. However, the effects of molecular structure of the target compounds, sample pre-treatment, surface conditions, and molecular environment on the information generated by ToF-SIMS are still not well understood, and are a matter of intense current research (e.g., Sostarecz *et al.*, 2004).

After the introduction of new polyatomic cluster ion sources (e.g. Au_n^+ , Bi_n^+ , C_{60}^+) the analytical window of ToF-SIMS has greatly been expanded towards the detection of biological molecules, and studies have demonstrated the capability to analyse the spatial distribution of lipids in mammalian tissue, and even in single eukaryotic cells (Fletcher *et al.*, 2007; Nygren *et al.*, 2005; Ostrowski *et al.*, 2004; Ostrowski *et al.*, 2005; Sjövall *et al.*, 2004; Touboul *et al.*, 2005). Yet, the potential of ToF-SIMS in geobiological and organic geochemical studies still remains to be explored, as only few attempts have been made to identify the spectral properties of common microbial and/or sedimentary biomarkers, namely from purified standards (Steele *et al.*, 2001; Toporski and Steele, 2004) and geological samples (Toporski *et al.*, 2002; Guidry and Chafetz, 2003; Guidry and Chafetz, 2003).

As an experiment aiming to analyse environmental lipid biosignatures with ToF-SIMS, we used methanotrophic microbial mats from methane seeps on the euxinic NW' Black Sea shelf (Michaelis *et al.*, 2002). These mats are associated with reef-like carbonates that precipitate as a result of the microbial anaerobic oxidation of methane by sulphate (AOM). Although the precise mechanisms of AOM are still unclear, phylogenetically distinct methanotrophic archaea of the ANME-1 (Hinrichs

et al., 1999; ANME = anaerobic methane oxidizers) and ANME-2 (Boetius *et al.*, 2000) clusters and sulphate-reducing bacteria of the *Desulfosarcina* / *Desulfococcus* group are commonly considered as the protagonists, according to the net reaction: $\text{CH}_4 + \text{SO}_4^{2-} \rightarrow \text{HCO}_3^- + \text{HS}^- + \text{H}_2\text{O}$. For further details on the different aspects of the Black Sea microbial reefs, namely their microbiology, structure and petrography, please refer to Knittel *et al.* (2005), Lein *et al.* (2002), Michaelis *et al.*, (2002), Peckmann *et al.* (2001), Pimenov and Ivanova (2005), Reitner *et al.* (2005), Seifert *et al.*, (2006), Tourova *et al.*(2002), Treude *et al.* (2005). Lipid biomarker patterns from the Black Sea materials have been previously studied using GC/MS (Blumenberg *et al.*, 2004; Pape *et al.*, 2005; Thiel *et al.*, 2001).

In a recent pilot study we reported the ToF-SIMS spectral characteristics of archaeol/hydroxyarchaeol and glycerol dialkyl glycerol tetraether lipids (GDGT, structures given in Fig. 2.1) from solvent extracts of microbial mats, and discussed the principles, possibilities and limitations of ToF-SIMS for the analysis of such systems (Thiel *et al.*, 2007). These data showed good agreement with previous GC/MS- and compound specific isotope studies on the Black Sea mats that characterized these lipids as molecular fingerprints of methanotrophic archaea (Blumenberg *et al.*, 2004; Pape *et al.*, 2005; Thiel *et al.*, 2001). With the extract data as a reference, the archaeal biosignature was identified by ToF-SIMS and its distribution imaged directly on the solid surface of methane-derived carbonate (Thiel *et al.*, 2007). To further explore the utility of ToF-SIMS for visualizing biomarkers in geobiological samples, we here present a study on the distribution of lipids in microscopic sections, i.e. at a μm -scale that resolves the typical size range of microbial colonies in biofilms and microbial mats.

2.3 Materials and methods

Samples were obtained in September 2004 from the NW' Black Sea shelf using the manned submersible 'Jago' from aboard the German R/V 'Poseidon' (see acknowledgement). Carbonate samples overgrown by microbial mats were taken in the 'GHOSTDABS' seep field (Michaelis *et al.*, 2002), from a tower-like carbonate structure at 230 m depth. Upon return of the submersible, the samples were frozen at -20°C until further preparation.

In the laboratory, the surface of the carbonate sample was allowed to thaw. Pin head sized mat samples showing intense, small scale intertwining of differently coloured mat types (grey, black, pink) were taken from the carbonate surface, and mounted with tissue glue (Tissue Tek[®]) on a cork disc acting as a sample holder. After snap freezing in methyl butane at -150°C for ~ 30 sec, the samples were quickly transferred to a Leica CM 3050 S cryo-microtome kept at -20°C . $10 \mu\text{m}$ thick serial sections were cut using a 25 cm Leica Profile D standard steel knife, which had been thoroughly washed with organic solvents. The sections were placed on solvent-rinsed microscope

slides, and stored in a closed glass tray at -20°C until ToF-SIMS analysis. Prior to analysis, the tray was allowed to warm up to room temperature before opening.

Without further treatment, the slides were inserted into a ToF-SIMS IV instrument (ION-TOF GmbH, Münster, Germany) equipped with a bismuth liquid metal primary cluster ion source. Spectra and images of positive and negative ions from the sample surfaces were recorded using 25 keV Bi_3^+ primary ions and low energy electron flooding for charge compensation. Mass spectra were recorded with the instrument optimised for maximum mass resolution (so-called 'bunched mode': $m/\Delta m \sim 3000\text{-}6000$), at a beam diameter of $\sim 5 \mu\text{m}$ and a repetition rate of 5 kHz. During acquisition, the primary ion beam (average pulsed current 0.1 pA) was scanned in a raster pattern (128x128 pixels) over an analysis area of $500 \times 500 \mu\text{m}^2$. High resolution images ($233 \times 233 \mu\text{m}^2$, 256×256 pixels) were obtained with the instrument in the so-called 'burst alignment mode', in which a smaller focus of the primary ion beam is obtained (200-300 nm), however, at the expense of significantly lower mass resolution ($m/\Delta m \sim 350$). The accumulated primary ion dose in all analyses was kept below the so-called static limit of $<10^{13}$ ions cm^{-2} , beyond which significant surface damage by the ion beam starts to occur. Spectra from the total analysis area or from selected regions of interest, and images for selected ions were extracted from the recorded raw data files using the instrument software.

Post-measurement microscopic investigations were performed using a Zeiss (Jena, Germany) Axioplan epifluorescence microscope equipped with a high-pressure mercury arc lamp (Zeiss HBO 50) and differential interference contrast optics (DIC, Nomarski optics). Images were obtained with a Peltier-cooled VISICAM-color CCD camera (PCO Computer Optics GmbH, Kehlheim, Germany) attached to the microscope.

2.4 Results and discussion

An overview of the total area spectrum in the m/z 600 to m/z 1800 range obtained in positive ion mode (i.e., positively charged secondary ions were recorded) from a mat section (BSX6-8) is shown in Fig. 2.1. From 1316.3 to 1325.3 Da, a prominent cluster of 10 peaks occurred with each peak separated from each other by 1 Da. Detailed inspection of the exact mass of the detected ions and comparison of the measured with the theoretical isotope distributions identified these peaks as sodium cationised ($[\text{M}+\text{Na}]^+$) acyclic GDGT (GDGT 0, caldarchaeol, $\text{C}_{86}\text{H}_{172}\text{O}_6$), and its mono- to tetracyclic derivatives (GDGT 1-4, Table 2.1, Fig. 2.1b, see also Thiel *et al.*, 2007).

The spectrum also contained a second peak cluster with a similar pattern at 1640.3 to 1649.4 Da (Fig. 2.1c), which is in good agreement with the $[\text{M}+\text{Na}]^+$ ions of gentiobiosyl-caldarchaeol ($\text{C}_{98}\text{H}_{192}\text{O}_{16}$) and its mono- to tetracyclic derivatives (referred to as gentiobiosyl-GDGT in the following). These compounds represent the intact GDGT-based lipids with a disaccharide headgroup consisting of gentobiose ($\beta\text{-D-Glucopyranosyl-(1-6)-D-glucose}$) (Koga *et al.*, 1993b);

Table 2.1, Fig. 2.1). Gentiobiosyl-caldarchaeol is known as the major membrane lipid in the methanogenic families *Methanobacteriaceae*, thermophilic *Methanococcaceae*, and *Methanomicrobiaceae*, but seems to be absent in *Methanosarcinales* and mesophilic *Methanococcus* species (Koga *et al.*, 1993b). Together with its cyclic derivatives, it was recently observed in extracts of marine, methane-rich sediments (Biddle *et al.*, 2006; Sturt *et al.*, 2004).

Another prominent peak group consists of the sodium cationized diether lipids archaeol and hydroxyarchaeol (Fig. 2.1, Table 2.1). Whereas the former is ubiquitously present in methanogens, the latter seem to typify the *Methanosarcinales* and mesophilic *Methanococcus* species (Koga *et al.*, 1993b). Both diethers commonly occur in the Black Sea mat extracts (mainly *sn*-2 hydroxyarchaeol, (Blumenberg *et al.*, 2004; Pape *et al.*, 2005), and were also detected in our previous ToF-SIMS study on Black Sea mat extracts and carbonate (Thiel *et al.*, 2007).

Remarkably, all of the above compounds exclusively occur as their sodium adducts. It therefore seems that glycerolipids in natural samples high in sodium from sea water or mineral matrix strongly prefer the formation of $[M+Na]^+$ over protonated $[M+H]^+$ and dehydroxylated $[M-OH]^+$ molecular ions. Although $[M+H]^+$ of diethers and GDGT were detected in our previous study on the mat extracts, the corresponding $[M+Na]^+$ species were almost equally abundant even in those sodium-poor samples (Thiel *et al.*, 2007).

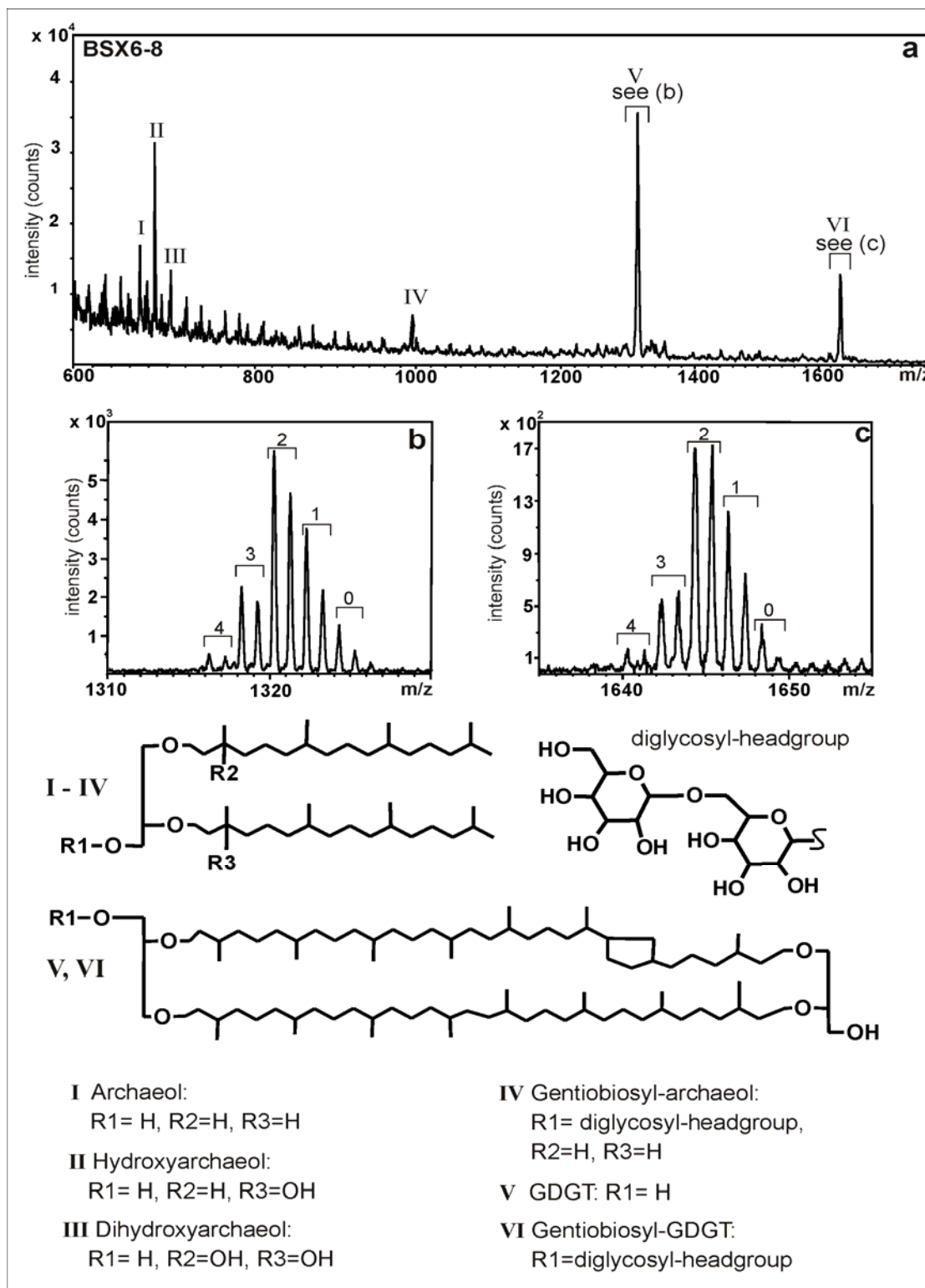


Fig. 2.1. a: Partial ToF-SIMS spectrum (m/z 600-1800), collected in positive mode from a $500 \times 500 \mu\text{m}^2$ area of a microbial mat section (BSX6-8). Roman numbers denote sodium adduct ions $[M+\text{Na}]^+$ of individual Archaea-derived lipids. b, c: Enlargements showing the spectral patterns of GDGT (b) and gentiobiosyl-GDGT (c) in detail. Numbered brackets denote peaks with predominant contribution from molecules with the respective number of cyclopentyl rings (0-4). Representatively, a GDGT 1 structure with one acyclic and one monocyclic C_{40} isopranyl moiety is displayed. Doublet peaks are due to ^{13}C -containing isotopomers.

Compound	Formula	Mass (M) calculated	[M+Na] ⁺ calculated	[M+Na] ⁺ measured
Archaeol	C ₄₃ H ₈₈ O ₃	652.673	675.663	675.67
Hydroxyarchaeol	C ₄₃ H ₈₈ O ₄	668.668	691.658	691.67
Dihydroxyarchaeol	C ₄₃ H ₈₈ O ₅	684.663	707.653	707.65
Gentiobiosyl-archaeol	C ₅₅ H ₁₀₈ O ₁₃	976.779	999.769	999.77
GDGT 0	C ₈₆ H ₁₇₂ O ₆	1301.315	1324.305	1324.29
GDGT 1	C ₈₆ H ₁₇₀ O ₆	1299.300	1322.290	1322.28
GDGT 2	C ₈₆ H ₁₆₈ O ₆	1297.284	1320.274	1320.27
GDGT 3	C ₈₆ H ₁₆₆ O ₆	1295.268	1318.258	1318.25
GDGT 4	C ₈₆ H ₁₆₄ O ₆	1293.253	1316.242	1316.24
Gentiobiosyl-GDGT 0	C ₉₈ H ₁₉₂ O ₁₆	1625.421	1648.411	1648.38
Gentiobiosyl-GDGT 1	C ₉₈ H ₁₉₀ O ₁₆	1623.405	1646.395	1646.35
Gentiobiosyl-GDGT 2	C ₉₈ H ₁₈₈ O ₁₆	1621.390	1644.380	1644.34
Gentiobiosyl-GDGT 3	C ₉₈ H ₁₈₆ O ₁₆	1619.374	1642.364	1642.31
Gentiobiosyl-GDGT 4	C ₉₈ H ₁₈₄ O ₁₆	1617.358	1640.348	1640.26

Table 2.1. List of archaeal ether lipid biomarkers analysed, and calculated vs. measured exact masses [Da] of relevant molecular ions. All masses given correspond to the first peak in the isotope cluster due to ¹³C. GDGT numbers denote the numbers of cyclopentyl rings in the C₄₀ isoprenoid moieties ether-linked to the glycerol backbones (see Fig. 2.1 for structures).

By means of the imaging capability of ToF-SIMS, we explored the distribution of Archaea-derived lipids on the sections at a lateral resolution of about 5 μm (bunched mode, 128 pixels per 500 μm). The relative abundances of (quasi-)molecular ions ([M+Na]⁺) showed several 'provenances' with individual biomarker fingerprints, as most evidently revealed by section BSX6-8 (Fig. 2.2). Obviously, these areas correlated with differently composed microbial colonies producing the respective lipids. Specifically, one provenance (A) showed the diethers archaeol and hydroxyarchaeol co-occurring with abundant GDGT, but virtually lacked gentiobiosyl-GDGT. Another region (B) revealed abundant diethers, particularly hydroxyarchaeol, but only a weak GDGT signal, and no gentiobiosyl-GDGT. By contrast, the third provenance (C) contained nearly exclusively GDGT and gentiobiosyl-GDGT, whereas archaeol and hydroxyarchaeol were missing.

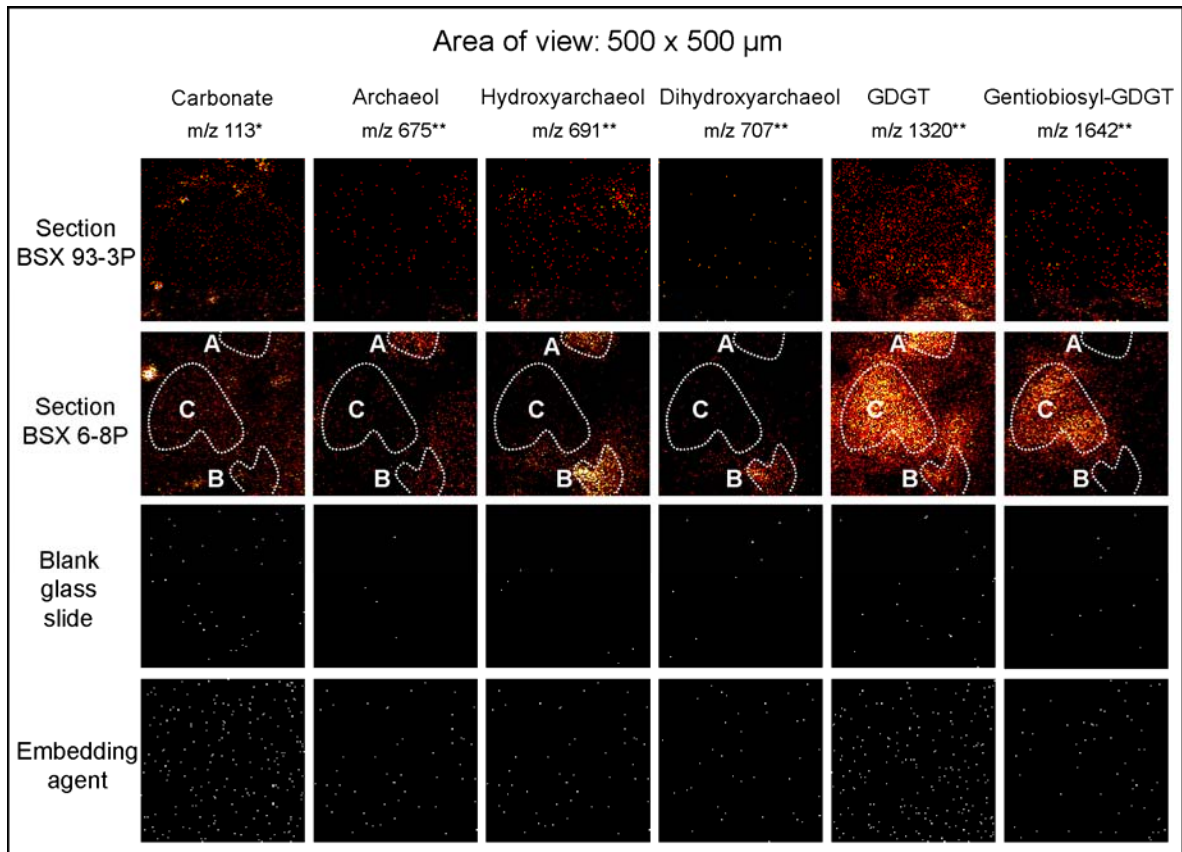


Fig. 2.2. Molecular ion images of the microbial mat sections (area of view: 500 x 500 μm^2). The images reveal cluster-like accumulations of archaeal biomarkers that relate to the distribution of individual microbial populations. Similar to thermo-images, colours indicate the relative signal yield for selected lipids from bright orange (= > 6 counts/pixel) to black (= no signal detected). * = $(\text{CaO})_2\text{H}^+$ ion at 112.96 Da; ** = sodium adduct ions ($[\text{M}+\text{Na}]^+$). Areas A, B, and C on section BSX6-8P outline the biomarker provenances discussed in the text. Control measurements of the blank glass slide surface next to section BSX6-8 and of the embedding agent show the background signal levels: white, 1 count per pixel; black, no signal detected.

Additional measurements were performed in the burst alignment mode to approach the limits of the lateral resolution feasible with ToF-SIMS. For the present samples this provided a lateral resolution of about 1 μm (256 pixels per 233 μm), i.e. in the typical size range of microbial cells, and confirmed the distinctiveness of lipid biomarker traits, even on a very small spatial scale (Fig. 2.3). For the microbial colony analysed, the data clearly confirmed that the prevailing, diether-producing archaea are no concomitant source of GDGT. High resolution measurements are, however, time consuming, and the considerable loss of mass resolution in the burst alignment mode requires thorough knowledge of the samples lipid inventory in order to avoid misidentifications. Using the ToF-SIMS instrument software, additional information can be obtained by defining regions of interest, from which individual mass spectra can be extracted from the raw data.

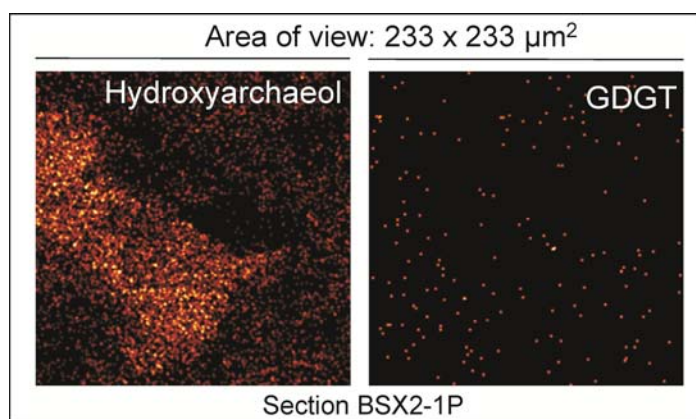


Fig. 2.3. High resolution ion images of a microbial colony obtained in the burst alignment mode at a lateral resolution of about 1 μm (256 x 256 pixel). The archaea in this colony appear to be selective for hydroxyarchaeol ($[\text{M}+\text{Na}]^+$, 691.7 Da), whereas virtually no signal was obtained for tetraether lipids ($[\text{M}+\text{Na}]^+$, summed GDGT range, 1316 to 1324 Da).

This feature is advantageous for identifying background (contaminant) peaks, but also for producing more representative mass spectra for selected areas or compounds that are spatially concentrated within a small area of the surface analysed. Specific occurrences of known and unknown compounds, which tend to be overlooked in the total mass spectrum, can be precisely tracked with this technique. In Fig. 2.4, such individual mass spectra for the three biomarker provenances A, B, and C are displayed. These spectra highlight two interesting additional traits. First, a prominent peak at 707.7 Da exclusively occurred in provenance B.

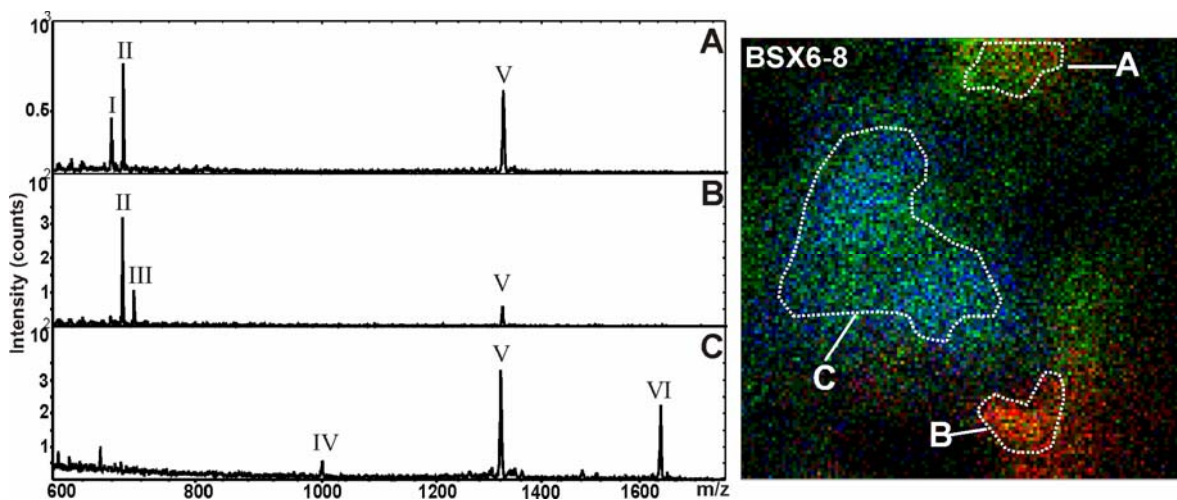


Fig. 2.4. Positive ToF-SIMS spectra (m/z 600-1800) in the biomarker provenances A, B, and C on section BSX6-8, revealing the individual lipid patterns of the respective regions. Roman numbers labeling the spectral peaks correspond to: I, archaeol; II, hydroxyarchaeol; III, dihydroxyarchaeol; IV, gentiobiosyl archaeol; V, GDGT; VI, Gentiobiosyl-GDGT (for structures, see Fig. 2.1). For orientation, exact locations of provenances are shown on an overlay of key compound distributions in the respective areas: red, hydroxyarchaeol; green, GDGT; blue, gentiobiosyl-GDGT.

Detailed inspection of masses and isotope patterns showed this ion to be in excellent agreement with the $[M+Na]^+$ ion of dihydroxyarchaeol (most likely *sn*-2,3-dihydroxyarchaeol, Table 2.1, Fig. 2.1), a rare archaeal diether that has tentatively been identified in methane-rich sediments of the Eel River Basin (Orphan *et al.*, 2002), and in the 'Lost City' hydrothermal field (Kelley *et al.*, 2005). Second, provenance C, high in GDGT and gentiobiosyl-GDGT, was accompanied by a significant signal at 999.8 Da which is in exact agreement with the $[M+Na]^+$ ion of gentiobiosyl-archaeol ($C_{55}H_{108}O_{13}$, Table 2.1, Fig. 2.1), an intact glycosyl-functionalised lipid that is widespread in methanogens (Koga *et al.*, 1993b) and was recently found in marine sediment extracts using LC/MS (Biddle *et al.*, 2006).

Because the ToF-SIMS analysis affected only the outermost molecular layers (10-20 nm) of the sample surface, the areas analysed could subsequently be examined using conventional and fluorescence light microscopy. On section BSX6-8, the area studied was identified based on the original ToF-SIMS video image (Fig. 2.5a), and a clearer microscopic image of the microbial colonies in the respective region was obtained (Fig. 2.5b). Even the morphology of the microorganisms present in provenance C could be elucidated (Fig. 2.5c) due to their strong autofluorescence. These organisms were filamentous forms obviously representing the known, chain-like assemblages of cylindrical ANME-1 cells (Knittel *et al.*, 2005; Michaelis *et al.*, 2002; Pimenov *et al.*, 1997; Reitner *et al.*, 2005). Hence the combined ToF-SIMS/fluorescence light microscopy data strongly corroborate previous suggestions of ANME-1 as major GDGT producers (Blumenberg *et al.*, 2004). In addition, the distinctive lipid pattern observed here from provenance C (Figs. 2.2, 2.4) clearly indicates that gentiobiosyl-GDGT 0 to 4 are the principal intact ANME-1 membrane lipids.

Examination with cross-polarized light furthermore showed the presence of $CaCO_3$ precipitates that could easily be identified due to their characteristic birefringence (Fig. 2.5d). Two types of these 'methane-carbonates' occurred; one spheroidal that had been previously described from the Black Sea towers (Reitner *et al.*, 2005), and one consisting of small irregularly shaped crystallites. An overlay with the molecular map in Fig. 2.2 revealed a close spatial association of provenance B with an irregular $CaCO_3$ aggregate, suggesting an involvement of the hydroxyarchaeol-producing archaea in the precipitation process. According to their close phylogenetic relationship to the *Methanosarcinales* (Koga *et al.*, 1993a), ANME-2 were proposed as an important source of *sn*-2-hydroxyarchaeol in the Black Sea mats (Blumenberg *et al.*, 2004), and represent the most plausible contributors of the diethers in the sections studied. The close spatial association with carbonate precipitates rather supports than disagrees with the finding that ANME-2 achieve significantly higher methane oxidation and thus, bicarbonate production rates than ANME-1 (Nauhaus *et al.*, 2005).

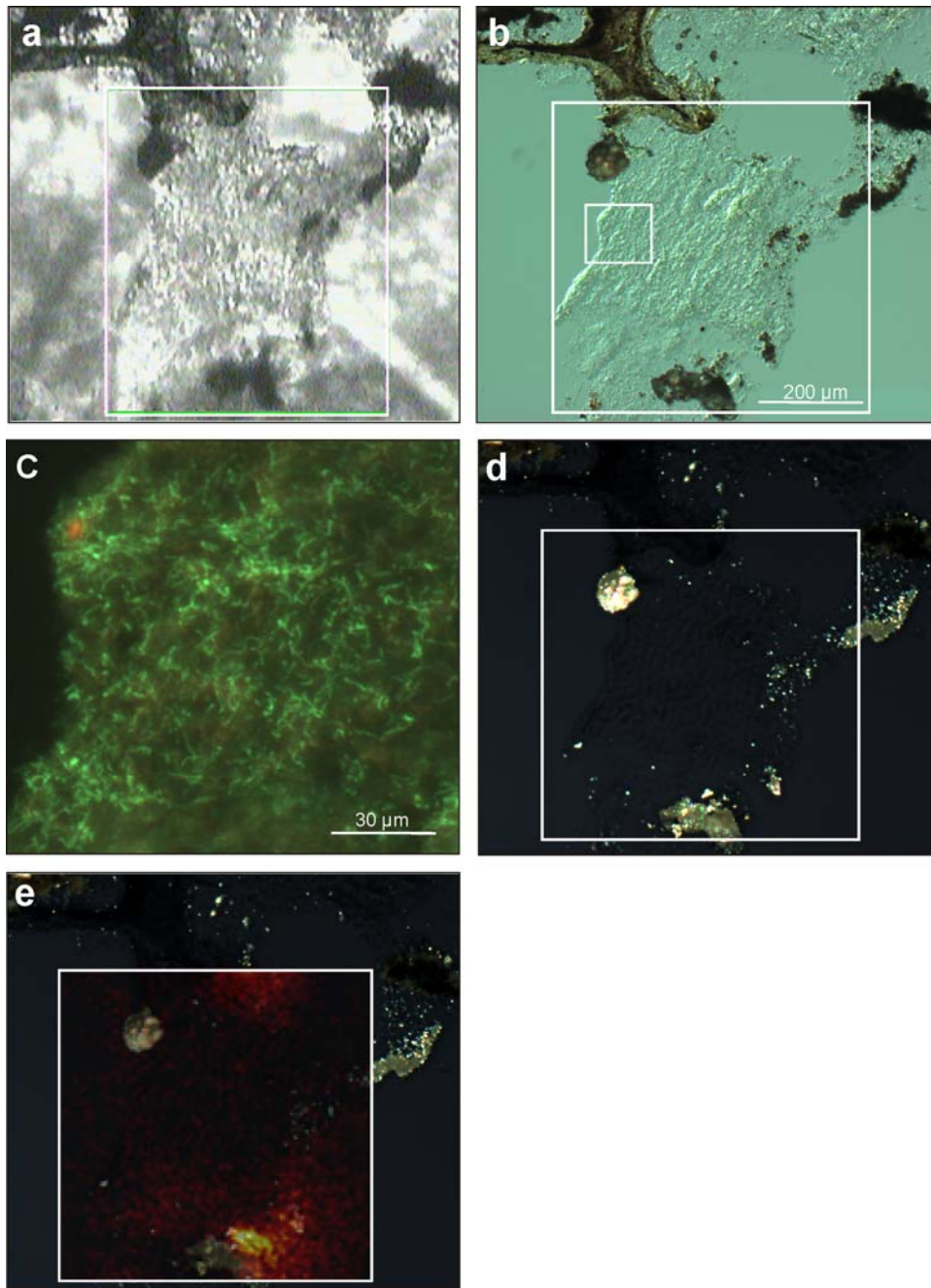


Fig. 2.5. a: Video image (reflected light) of the microbial mat cryosection BSX6-8, obtained by the built-in camera of the ToF-SIMS instrument. The frame indicates the $500 \times 500 \mu\text{m}^2$ area, from which mass spectra were collected. b: Differential interference contrast image of the microbial mat cryosection BSX6-8 taken after ToF-SIMS analysis. The large frame denotes the area analyzed with ToF-SIMS, see (a). The small frame indicates the area analysed by fluorescence microscopy, see (c). c: Detail of (b) showing densely arranged filamentous microorganisms, most likely ANME-1 cells, with autofluorescence properties of F430. Epifluorescence micrograph (ex 450-490 nm, em 515-565 nm). d: Crossed nicols view of image (b) showing a CaCO_3 spherulite (upper left) and irregular microcrystalline CaCO_3 aggregates. The frame denotes the area analyzed with ToF-SIMS, see (a). e: Overlay image of hydroxyarchaeol ($[\text{M}+\text{Na}]^+$, 691.7 Da) and (d). Hydroxyarchaeol is co-localized with the irregular CaCO_3 aggregates. The frame denotes the area analyzed with ToF-SIMS, see (a).

Additional sections analysed to further assess such a relationship showed other instances of co-localization of hydroxyarchaeol and irregular carbonate. However, this co-occurrence did not build a general rule (Fig. 2.6). It therefore seems that the mineralization potential of this microbial system varies with the metabolic state (age) of the colonies, and/or their immediate physicochemical environment. ToF-SIMS images thus represents a 'chemical snapshot' of the organic and inorganic traits that characterize the complex process of biomineralization in the natural mat system.

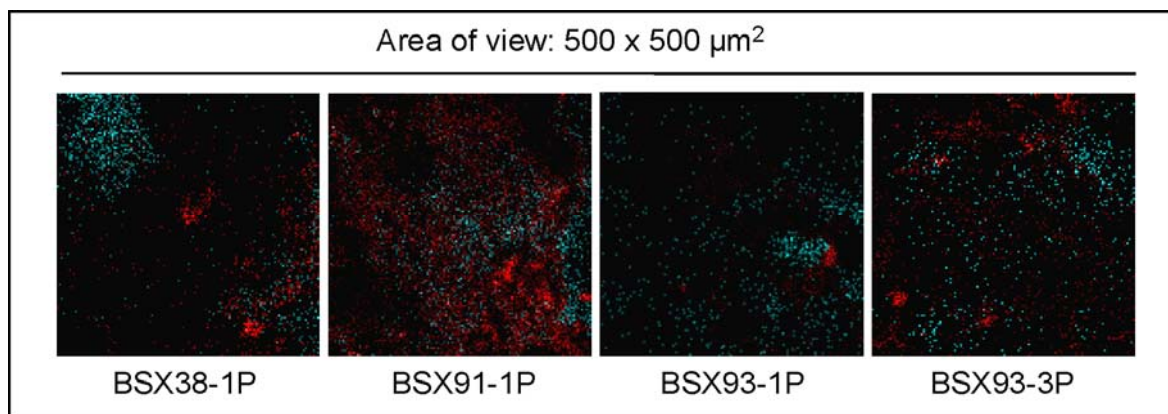


Fig. 2.6. Color overlay of the ion images for carbonate represented by the $(\text{CaO})_2\text{H}^+$ ion (112.96 Da, red) and hydroxyarchaeol ($[\text{M}+\text{Na}]^+$, 691.7 Da, blue) showing different levels of co-localization for this biomarker and the precipitate in four different mat sections/areas.

2.5 Conclusions

ToF-SIMS is capable of breaking the limits of conventional biomarker analysis by resolving the spatial distribution of lipids at the microscopic level. Using this technique, the highly complex and patchy distribution of lipids in a microbial mat could be visualized. The simultaneous analysis of major archaeal biomarker classes, including bare core ether lipids and their intact diglycoside derivatives, revealed the existence of different biomarker provenances on a μm -scale. These provenances are congruent with individual microbial colonies, and ultimately reflect the lipid composition of the microorganisms present. Evidence on the lipid composition of distinctive members of the microbial population, namely ANME-1 vs. ANME-2, could be obtained from the environmental sample with a high level of confidence, and without the need to isolate, culture, and extract these organisms in the laboratory. As a virtually non-destructive technique, ToF-SIMS allows subsequent microscopic examinations, thus permitting a synopsis of lipid biomarker results with morphological and inorganic properties of the samples in question.

These capabilities further highlight ToF-SIMS as a promising tool for a wide range of geological, ecological, biological, and medical applications, which all share the need to detect and precisely

localize organic compounds in natural systems. Potential geobiological applications include the elucidation of microbially assisted mineral precipitation, the analysis of organic compounds in unculturable microorganisms, and the clear-cut assignment of biomarkers to their biological source.

Acknowledgements

We are grateful to Richard Seifert and Walter Michaelis (IfBM, Institute for Biogeochemistry and Marine Chemistry, University of Hamburg), who initiated and coordinated the joint project BEBOP through which the microbial mats studied here were retrieved (**B**iogeochemistry and Microbiology of **B**ioherms **P**rospering in the Black Sea; R/V Poseidon cruise PO 317/2). We also wish to acknowledge two anonymous reviewers for their critical feedback on the original manuscript. We further thank Martin Blumenberg (IfBM) and Jan Toporski (WITec, Ulm) for thoughtful scientific comments, Christine Flies (University of Göttingen) for on-board sampling and logistic support, Jakob Malm (SP, Borås) for assistance in the lab and introduction into the ToF-SIMS software, Joachim Reitner (University of Göttingen) for sub-project coordination and helpful scientific discussions, Walter Schulz-Schaeffer (University Hospital of Göttingen) for helpful advise pertaining to sample preparation, and Oliver Stückrad (University of Göttingen) for assisting on-board sampling. Our study received financial support from the German Research Foundation (DFG) through grants Th 713/4 and FOR 571, the University of Hamburg (joint project BEBOP, see above), and the Swedish Governmental Agency for Innovation Systems (VINNOVA). This is publication No. 14 of the DFG Research Unit FOR 571 'Geobiology of Organo- and Biofilms'.

References

- Belu AM, Graham DJ, Castner DG (2003) Time-of-flight secondary ion mass spectrometry: techniques and applications for the characterization of biomaterial surfaces. *Biomaterials*, **24**, 3635-3653.
- Benninghoven A (1994) Chemical Analysis of Inorganic and Organic Surfaces and Thin Films by Static Time-of-Flight Secondary Ion Mass Spectrometry (ToF-SIMS). *Angewandte Chemie International Edition in English*, **33**, 1023-1043.
- Biddle JF, Lipp JS, Lever MA, Lloyd KG, Sorensen KB, Anderson R, Fredricks HF, Elvert M, Kelly TJ, Schrag DP, Sogin ML, Brenchley JE, Teske A, House CH, Hinrichs K-U (2006) Heterotrophic Archaea dominate sedimentary subsurface ecosystems off Peru. *Proceedings of the National Academy of Sciences of the United States of America*, **103**, 3846-3851.
- Blumenberg M, Seifert R, Reitner J, Pape T, Michaelis W (2004) Membrane lipid patterns typify distinct anaerobic methanotrophic consortia. *Proceedings of the National Academy of Sciences of the United States of America*, **101**, 11111-11116.
- Boetius A, Ravenschlag K, Schubert CJ, Rickert D, Widdel F, Gieseke A, Amann R, Jørgensen BB, Witte U, Pfannkuche O (2000) A marine microbial consortium apparently mediating anaerobic oxidation of methane. *Nature*, **407**, 623-626.
- Braun RM, Beyder A, Xu J, Wood MC, Ewing AG, Winograd N (1999) Spatially Resolved Detection of Attomole Quantities of Organic Molecules Localized in Picoliter Vials Using Time-of-Flight Secondary Ion Mass Spectrometry. *Analytical Chemistry*, **71**, 3318-3324.
- Chait BT, Standing KG (1981) A time-of-flight mass spectrometer for measurement of secondary ion mass spectra. *International Journal of Mass Spectrometry and Ion Physics*, **40**, 185-193.
- Fletcher JS, Lockyer NP, Vaidyanathan S, Vickerman JC (2007) ToF-SIMS 3D biomolecular imaging of *Xenopus laevis* oocytes using Buckminsterfullerene (C₆₀) primary ions. *Analytical Chemistry*, **79**, 2199-2206
- Guidry SA, Chafetz HS (2003) Depositional facies and diagenetic alteration in a relict siliceous hot-spring accumulation: examples from Yellowstone National Park, U.S.A. *Journal of Sedimentary Research*, **73**, 806-823.
- Hagenhoff B (2000) High resolution surface analysis by TOF-SIMS. *Mikrochimica Acta*, **132**, 259-271.
- Hinrichs K-U, Hayes JM, Sylva SP, Brewer PG, DeLong EF (1999) Methane-consuming archaeobacteria in marine sediments *Nature* **398**, 802-805.
- Kelley DS, Karson JA, Fruh-Green GL, Yoerger DR, Shank TM, Butterfield DA, Hayes JM, Schrenk MO, Olson EJ, Proskurowski G, Jakuba M, Bradley A, Larson B, Ludwig K, Glickson D, Buckman K, Bradley AS, Brazelton WJ, Roe K, Elend MJ, Delacour A, Bernasconi SM, Lilley MD, Baross JA, Summons RE, Sylva SP (2005) A Serpentinite-Hosted Ecosystem: The Lost City Hydrothermal Field. *Science*, **307**, 1428-1434.
- Knittel K, Losekann T, Boetius A, Kort R, Amann R (2005) Diversity and Distribution of Methanotrophic Archaea at Cold Seeps. *Applied and Environmental Microbiology*, **71**, 467-479.
- Koga Y, Akagawa-Matsushita M, Ohga M, Nishihara M (1993a) Taxonomic significance of the distribution of component parts of polar ether lipids in methanogens. *Systematic and Applied Microbiology*, **16**, 342-351.

- Koga Y, Nishihara M, Morii H, Akagawa-Matsushita M (1993b) Ether polar lipids of methanogenic bacteria: structures, comparative aspects, and biosyntheses. *Microbiological Reviews*, **57**, 164-182.
- Kollmer F (2004) Cluster primary ion bombardment of organic materials. *Applied Surface Science*, **231-232**, 153-158.
- Lein AY, Ivanov MV, Pimenov NV, Gulin MB (2002) Geochemical characteristics of the carbonate constructions formed during microbial oxidation of methane under anaerobic conditions. *Microbiology*, **71**, 78-90.
- Michaelis W, Seifert R, Nauhaus K, Treude T, Thiel V, Blumenberg M, Knittel K, Gieseke A, Peterknecht K, Pape T, Boetius A, Amann R, Jørgensen BB, Widdel F, Peckmann J, Pimenov NV, Gulin MB (2002) Microbial reefs in the Black Sea fueled by anaerobic oxidation of methane. *Science*, **297**, 1013-1015.
- Nauhaus K, Treude T, Boetius A, Kruger M (2005) Environmental regulation of the anaerobic oxidation of methane: a comparison of ANME-I and ANME-II communities. *Environmental Microbiology*, **7**, 98-106.
- Nygren H, Borner K, Hagenhoff B, Malmberg P, Mansson J-E (2005) Localization of cholesterol phosphocholine and galactosylceramide in rat cerebellar cortex with imaging TOF-SIMS equipped with a bismuth cluster ion source. *Biochimica et Biophysica Acta (BBA) - Molecular and Cell Biology of Lipids*, **1737**, 102-110.
- Orphan V, House CH, Hinrichs KU, McKeegan KD, DeLong EF (2002) Multiple archaeal groups mediate methane oxidation in anoxic cold seep sediments. *Proceedings of the National Academy of Sciences of the United States of America*, **99**, 7663-7668.
- Ostrowski SG, Bell CTV, Winograd N, Ewing AG (2004) Mass spectrometric imaging of highly curved membranes during *Tetrahymena* mating. *Science*, **305**, 71-73.
- Ostrowski SG, Szakal C, Kozole J, Roddy TP, Xu J, Ewing AG, Winograd N (2005) Secondary Ion MS Imaging of Lipids in Picoliter Vials with a Buckminsterfullerene Ion Source. *Analytical Chemistry*, **77**, 6190-6196.
- Pape T, Blumenberg M, Seifert R, Egorov VN, Gulin SB, Michaelis W (2005) Lipid geochemistry of methane-seep-related Black Sea carbonates. *Palaeogeography, Palaeoclimatology, Palaeoecology*, **227**, 31-47.
- Peckmann J, Reimer A, Luth U, Luth C, Hansen BT, Heinicke C, Hoefs J, Reitner J (2001) Methane-derived carbonates and authigenic pyrite from the northwestern Black Sea. *Marine Geology*, **177**, 129-150.
- Pimenov N, Ivanova AE (2005) Anaerobic methane oxidation and sulfate reduction in bacterial mats on coral-like carbonate structures in the Black Sea. *Microbiology (translated from Mikrobiologiya)*, **74**, 362-370.
- Pimenov NV, Rusanov II, Poglazova MN, Mityushina LL, Sorokin DY, Khmelenina VN, Trotsenko YA (1997) Bacterial mats on coral-like structures at methane seeps in the Black Sea. *Microbiology (Translated from Mikrobiologiya)*, **66**, 354-360.
- Reitner J, Peckmann J, Reimer A, Schumann G, Thiel V (2005) Methane-derived carbonate build-ups and associated microbial communities at cold seeps on the lower Crimean shelf (Black Sea). *Facies*, **51**, 66-79.

- Seifert R, Nauhaus K, Blumenberg M, Kruger M, Michaelis W (2006) Methane dynamics in a microbial community of the Black Sea traced by stable carbon isotopes in vitro. *Organic Geochemistry*, **37**, 1411-1419.
- Sjövall P, Lausmaa J, Johansson B (2004) High-resolution mass-spectrometric imaging of lipids in brain tissue. *Analytical Chemistry*, **76**, 4271-4278.
- Sostarecz AG, Cannon DM jr, McQuaw CM, Sun S, Ewing AG, Winograd N (2004) Influence of molecular environment on the analysis of phospholipids by time-of-flight secondary ion mass spectrometry. *Langmuir*, **20**, 4926-4932.
- Steele A, Toporski JKW, Avci R, Guidry S, McKay DS (2001) Time of flight secondary ion mass spectrometry (ToFSIMS) of a number of hopanoids. *Organic Geochemistry*, **32**, 905-911.
- Sturt HF, Summons RE, Smith K, Elvert M, Hinrichs K-U (2004) Intact polar membrane lipids in prokaryotes and sediments deciphered by high-performance liquid chromatography/ electrospray ionization multistage mass spectrometry—new biomarkers for biogeochemistry and microbial ecology. *Rapid Communications in Mass Spectrometry*, **18**, 617–628.
- Thiel V, Peckmann J, Richnow HH, Luth U, Reitner J, Michaelis W (2001) Molecular signals for anaerobic methane oxidation in Black Sea seep carbonates and a microbial mat. *Marine Chemistry*, **73**, 97-112.
- Thiel V, Toporski J, Schumann G, Sjövall P, Lausmaa J (2007) Analysis of archaeal core ether lipids using Time of Flight - Secondary Ion Mass Spectrometry (ToF-SIMS): Exploring a new prospect for the study of biomarkers in geobiology. *Geobiology*, **5**, 75-83.
- Toporski J, Steele A (2004) Characterization of purified biomarker compounds using time of flight-secondary ion mass spectrometry (ToF-SIMS). *Organic Geochemistry*, **35**, 793-811.
- Toporski J, Steele A, Westall F, Avci R, Martill M, McKay DS (2002) Morphological and spectral investigation of exceptionally well preserved bacterial biofilms from the Oligocene Enspel formation, Germany. *Geochimica et Cosmochimica Acta*, **66**, 1773-1791.
- Touboul D, Brunelle A, Halgand F, De La Porte S, Laprevote O (2005) Lipid imaging by gold cluster time-of-flight secondary ion mass spectrometry: application to Duchenne muscular dystrophy. *Journal of Lipid Research*, **46**, 1388-1395.
- Tourova TP, Kolganova TP, Kusnetsov KB, Pimenov N (2002) Phylogenetic diversity of the Archaeal component of bacterial mats on coral-like structures in zones of methane seeps in the Black Sea. *Microbiology (Translated from Mikrobiologiya)*, **71**, 196-201.
- Treude T, Knittel K, Blumenberg M, Seifert R, Boetius A (2005) Subsurface Microbial Methanotrophic Mats in the Black Sea. *Applied and Environmental Microbiology*, **71**, 6375-6378.

3

Organic geochemical microanalysis by time-of-flight secondary ion mass spectrometry (ToF-SIMS)

Peter Sjövall, Volker Thiel, Sandra Siljeström, Christine Heim, Tomas Hode, Jukka Lausmaa

Geostandards and Geoanalytical Research (2008) 32, 268-277

3.1 Abstract

Time-of-flight secondary ion mass spectrometry (ToF-SIMS) is a powerful method for chemical analysis of solid surfaces. In this paper, the capabilities and limitations of this technique and the potential for its use in geochemical research is outlined. Using ToF-SIMS, the chemical composition of sample structures down to 10 – 100 μm can be determined, without the need for preselection or labeling of the analysed substances. In addition, the lateral distribution of organic and inorganic compounds can be mapped in geochemical samples at a resolution in the micrometer range. The capabilities of the technique in geochemistry are illustrated by two examples. In the first example, it is shown that ToF-SIMS can be used to detect biomarkers in oil samples, making it a promising method for the analysis of biomarkers in fluid inclusions. In the second example, a number of specific lipid biomarkers were identified and mapped on the surface of a microbial mat cryosection surface. Post-measurement optical microscopy correlated the localisation of the lipids with the presence of methanotrophic archaea in the microbial mat.

3.2 Introduction

Information about organic molecules in geological samples is not easily accessed at a high chemical specificity and at a spatial resolution in the micrometer range, primarily because of limitations in the techniques used for organic analysis. Mass spectrometric methods like GC/MS and LC/MS provide excellent tools for identifying and quantifying organic substances in geological samples. However, as these methods require solvent extraction, the spatial origin of the different substances within the sample cannot be specified. Microscopy can be used to characterise and identify organic material in geological samples at high spatial resolution but, in this case, the chemical specificity is limited to optically active or labeled compounds. Time-of-flight secondary ion mass spectrometry (ToF-SIMS) offers a method that combines the two analytical approaches, namely mass spectrometric detection, providing chemical specificity, and high spatial resolution

(Benninghoven, 1994; Pacholski and Winograd, 1999; Sodhi, 2004). ToF-SIMS has been used for chemical surface analysis in a number of application areas during the last 10-20 years, including semiconductor and polymer characterisation (Belu *et al.*, 2003; Vickerman and Briggs, 2001). Recently, instrument developments have improved the method considerably for organic analysis, providing new opportunities for analysis of biological materials (Kollmer, 2004; Sjovalld *et al.*, 2004; Touboul *et al.*, 2004; Touboul *et al.*, 2005). Other methods for imaging mass spectrometry which are presently experiencing intense development include imaging matrix assisted laser desorption ionisation (MALDI) (Cornett *et al.*, 2007) and desorption electrospray ionisation (DESI) (Takats *et al.*, 2004).

The objective of the present paper is to provide a brief overview of the capabilities and limitations of ToF-SIMS as an analysis tool in organic geochemical research. After a general discussion of ToF-SIMS, the capabilities of the technique are illustrated by two examples from our laboratory, namely (i) analysis of biomarkers in oils and (ii) analysis of archaeal lipids in microbial mats. In the first example, the work is aimed at developing a technique for biomarker analysis of single fluid inclusions in rock samples, utilising the capability of ToF-SIMS to analyse microscopic sample amounts (Siljeström *et al.*, 2008). In the second example, the lateral distribution of source-specific archaeal lipids and inorganic components in microbial mats are mapped in order to examine simultaneously the spatial distribution of specific organisms, their organic inventory and biomineralisation mechanisms (Thiel *et al.*, 2007a, 2007b).

3.3 Capabilities and limitations of ToF-SIMS

3.3.1 ToF-SIMS technique

ToF-SIMS is based on the SIMS principle, in which a focused beam of high energy ions (primary ions) bombards the sample surface in a vacuum, causing atoms, molecular fragments and intact molecules to be ejected from the sample surface. Some of the ejected particles will be ionised (secondary ions) and these ions are extracted into a mass analyser, where they are separated with respect to their mass-to-charge ratio. Identification of the secondary ions provides detailed information about the chemical composition of the sample surface at the specific spot bombarded by the primary ion beam. By scanning the primary ion beam over a selected area on the sample surface, ionspecific images are obtained showing the lateral distribution of the different chemical components on the sample surface. Since only particles originating from the outermost molecular layers of the sample can be ejected during the SIMS process, the secondary ions provide chemical information exclusively about the surface region of the sample (1-10 nm). Furthermore, mixing between different chemical species within the interaction volume (approximately 5 nm diameter) of

the primary ion with the surface may occur, giving rise to secondary ions composed of atomic species from one or several chemical compounds originally located within the interaction volume.

In a ToF-SIMS instrument, the primary ions are applied in short duration pulses and the secondary ions are analysed in a time-of-flight detector. With this setup, all secondary ions produced from a specific spot bombarded by a primary ion pulse are detected in parallel and an entire mass spectrum from each pixel may be stored in the resulting data file. This allows the extraction of selected ion images and spectra from selected regions of interest or from the total analysis area. Another important advantage of this setup is that it allows for so called static SIMS conditions, which is a requirement for obtaining detailed molecular information on the surface chemical composition. Since the primary ions cause severe fragmentation of the molecules remaining at the collision site after the collision, the molecular information is gradually lost in the recorded mass spectrum as a significant fraction of the surface becomes damaged by the primary ions.

In static SIMS, the data acquisition is therefore terminated before the accumulated primary ion dose density has reached the so called static limit, 10^{12} – 10^{13} ions cm^{-2} , which is the dose density at which changes in the mass spectrum due to primary ion induced molecular damage typically start to be significant. The main advantage of static SIMS is thus its capability to provide detailed molecular information of organic substances up to 10,000 Da. In dynamic SIMS, primary ion dose densities well beyond the static limit are applied, usually with a continuous primary ion beam, which means that the analysis is done on a molecularly damaged and continuously eroding surface. Consequently, the information in dynamic SIMS is restricted to elements, isotopes and small fragments. However, since one is no longer limited by the static SIMS requirements, the sensitivity and image resolution can be considerably higher in dynamic SIMS as compared to static SIMS.

A number of important properties of ToF-SIMS and typical values of instrument specifications are listed in Table 3.1. The stated numbers are typical values for the type of instrument used in our laboratory (TOF-SIMS IV, manufactured by ION-TOF GmbH, Münster, Germany). The capabilities of the other types of instruments currently in use are very similar and the table therefore provides representative values of the present state-of-the-art capabilities of ToF-SIMS.

Property / feature	Capability / specification
Mass resolution (high mass resolution mode)	$m/\Delta m$ 5,000 – 10,000
Mass resolution (imaging mode)	$m/\Delta m$ 300
Lateral resolution (high mass resolution mode)	3 – 5 μm
Lateral resolution (imaging mode)	0.1 – 0.3 μm
Analysis area (primary ion beam deflection)	Max 500 x 500 μm^2
Analysis area (sample stage scan)	Max 7 x 7 cm^2
Analysis time (primary ion beam deflection)	Typically 100 s
Analysis time (sample stage scan)	Typically 90 min
Depth resolution	1-10 nm
Detection limit	Down to 10,000 molecules (depending on substance, primary ion and molecular environment)
Mass range	0 – ca. 10,000
Parallel detection	Entire mass spectrum
Sample requirements	Reasonably flat, vacuum compatible

Table 3.1. Key features of TOF-SIMS (TOF-SIMS IV, ION-TOF GmbH).

3.3.2 Mass resolution versus lateral resolution

Two of the most important specifications of the ToF-SIMS instrument are the mass resolution, which is important for the ability to identify and separate the secondary ions, and the lateral resolution, important for the ability to image small structures with specific chemical composition. Due to physical constraints on the primary ion pulses, the instrument is normally optimised either for maximum mass resolution (short pulses) or for maximum lateral resolution (highly focused beam). In the high mass resolution mode, the measured spectra allow for identification and separation of organic and inorganic secondary ions as well as organic ions with different C, H, O and N stoichiometries at the same nominal mass, while in the imaging mode (high lateral resolution) only nominal mass resolution is obtained. The beam diameter is, however, significantly narrower in the imaging mode, making the ion images significantly sharper than in the high mass resolution mode.

3.3.3 Secondary ion yield

The detection limit in a ToF-SIMS measurement is directly related to the so-called secondary ion yield, which is the number of detected secondary ions per incident primary ion. The secondary ion yield depends strongly on several factors, including: (i) the type of primary ion used in the analysis, (ii) the analysed substance and the specific secondary ion used for detecting it and (iii) the chemical environment of the analysed molecules on the sample surface (the so-called matrix effect).

During the last few years, the use of heavy cluster primary ions has been shown to result in dramatically higher secondary ion yields, thereby improving detection limits for characteristic

molecular ions of organic substances as compared to the previously used atomic primary ions. Among the cluster ion sources, Au_n^+ and Bi_n^+ are so-called liquid metal ion guns (LMIG), making it possible to obtain beams with a narrow focus (down to < 100 nm), while with the C60^+ (buckminsterfullerene) cluster sources the ion beam can not easily be focused to a beam diameter below $1 \mu\text{m}$ without severe sacrifice in the beam current. The Au_n^+ and Bi_n^+ sources thus provide superior imaging capabilities. A recently discovered advantageous property of using C60^+ as primary ions, however, is that some of the molecular information can be retained in the organic material also after extensive bombardment by C60^+ ions. This makes C60^+ a promising sputtering projectile for ion etching (depth profiling) of organic materials (Wucher *et al.*, 2007). Secondary ion yields vary over several orders of magnitude between different substances and specific secondary ions. In favourable cases, the detection limit of large, molecule-specific organic ions can be in the range of 10^4 molecules (Kollmer, 2004). This is approximately the number of molecules contained in a single molecular layer within a surface area of $100 \times 100 \text{ nm}^2$. However, for other substances, moleculespecific secondary ions may show a much lower secondary ion yield in the spectrum, making it necessary to use other, less specific secondary ions to probe the presence of a particular substance (or type of substance) on the sample surface.

Due to the limited number of molecules present in small areas of a sample surface, the lateral resolution that can be obtained in the ion images is closely related to the secondary ion yield. In order to obtain an image with a certain lateral resolution, e.g., 100 nm , the secondary ion yield must be sufficiently high to provide a significant signal within a surface area of the same length scale, e.g., $100 \times 100 \text{ nm}^2$. The ultimate lateral resolution that can be obtained can thus be limited either by the ion yield of the selected secondary ion or the focal width of the primary ion beam.

3.3.4 Sample preparation

Sample preparation is critical in ToF-SIMS analysis for several reasons. Firstly, the surface sensitivity of the technique has two important consequences; (i) the material to be analysed must be exposed on the sample surface and (ii) even very low amounts of contaminants present on the sample surface may affect the results significantly. Therefore, it is necessary that the sample is stored and handled under very clean conditions. Preferably, the sample surface should be prepared (e.g., by cutting or fracture) immediately prior to analysis. Secondly, the sample must be compatible with vacuum, which means that water-containing samples must be dried (or frozen) and that the analysis of volatile substances requires cooling. If the lateral distribution is to be investigated, it is also important to prevent migration of the chemical components during preparation of the sample. In case of biological materials, such as cells, primitive organisms or tissues, the vacuum compatibility is particularly critical since most biological structures are stable only in an aqueous environment. In addition, methods that may cause chemical rearrangements in

the sample, such as chemical fixation and the use of embedding media should be avoided or applied only with great caution. Strategies that have been used typically include plunge freezing for cryofixation and then either freeze drying at controlled temperatures (Kraft *et al.*, 2006; Prinz *et al.*, 2007) or freeze fracturing and analysis in the hydrated state (Cannon *et al.*, 2000).

The samples are mounted on specially designed sample holders and inserted into the ToF-SIMS vacuum chamber via a load lock, allowing the start of analysis within 5 min after initial evacuation of the load lock. Apart from the requirements of vacuum compatibility and minimising surface contamination, no additional sample preparation is typically needed. It is important, however, that the topography of the sample surface is minimised, as surface topography adds contrast to the ion images and also often deteriorates the mass resolution in the acquired spectra. Furthermore, charging of insulating sample materials resulting from the primary ion bombardment has to be compensated for. This is typically achieved by electron flooding of the sample using a low energy electron source.

3.4 Experimental

3.4.1 Preparation of biomarker reference and oil samples

The following samples were prepared for ToF-SIMS analysis:

1. Reference material of 5 β (H),14 α (H),17 α (H)- cholestane (20R) purchased from Chiron AS, Norway (further referred to as “cholestane”),
2. Crude oil (Miocene, California, USA),
3. Saturate hydrocarbon fraction separated from the above crude oil.

The cholestane reference sample was dissolved in isooctane at a concentration of 0.1 mg ml⁻¹. In a laminar air flow chamber, a small droplet (10 μ l) was deposited on a \sim 1 cm² piece of ozone-cleaned Si wafer and allowed to dry immediately before analysis. The saturate hydrocarbon fraction was separated from the crude oil by column chromatography over silica gel (Merck silica gel 60) using three column volumes of pre-distilled n-hexane. The resulting fraction was concentrated in a stream of nitrogen. Immediately before ToF-SIMS analysis, the saturate hydrocarbon fraction and unfractionated crude oil samples were deposited on separate Si substrates by dissolving them in heptane (0.3 mg μ l⁻¹) and, for each sample, allowing a 2 μ l droplet to dry on the Si substrate surface.

3.4.2 Preparation of microbial mat cryosections

Microbial mat samples were taken from tower-like carbonate structures forming at methane seeps on the NW Black Sea shelf (230 m water depth). In anoxic waters, these carbonates are precipitated

as a result of the microbial anaerobic oxidation of methane by sulfate, in a concerted mechanism involving methanotrophic archaea and sulfate-reducing bacteria (see Michaelis et al., 2002 and Reitner et al., 2005 for details). Pin-head-sized mat samples were cut out from the surface of the collected carbonate samples and mounted with tissue glue (Tissue Tek®, O.C.T. Compound, Sakura Finetek B.V., Zouterwoude, The Netherlands) on a cork disk substrate (Thiel *et al.*, 2007a). The sample was plunge frozen in methyl butane at -150 °C for ~ 30 s and immediately transferred to a cryomicrotome kept at -20 °C (Leica CM 3050 S, Leica Microsystems, Wetzlar, Germany). Serial thin sections (10 µm) were cut using a thoroughly solvent-cleaned 300 mm standard steel knife, placed on solvent-rinsed glass slides and stored in a closed glass tray at -20 °C until ToF-SIMS analysis. Prior to analysis, the tray was allowed to thaw to room temperature before opening. The glass slides were then mounted on the ToF-SIMS sample holder and analysed at room temperature.

3.4.3 Equipment and analysis procedures

ToF-SIMS analyses were carried out in a TOF-SIMS IV instrument (ION-TOF GmbH, Münster, Germany) equipped with a bismuth cluster primary ion source. Positive and negative ion spectra were recorded using 25 keV Bi₃⁺ primary ions and electron flooding for charge compensation. The instrument was optimised for high mass resolution (bunched mode, $M/\Delta M \sim 3000-6000$, where ΔM is the full width at half maximum of a peak at ion mass m , normally in the m/z 25-40 range) at a beam diameter of ~ 5 µm, a repetition rate of 5 kHz and a pulsed primary ion current of 0.1-0.2 pA. During analysis, the primary ion beam was scanned in a raster pattern and data were acquired in 128 x 128 pixels over an analysis area of 500 x 500 µm² for the microbial mat samples and 200 x 200 µm² for the oil samples. The analysis time was typically 2-5 min for each spectrum/image acquisition. The accumulated primary ion dose density was kept below the static limit of 10¹² ions cm⁻².

After ToF-SIMS, optical microscopy of the microbial mat cryosections was carried out using a Zeiss (Jena, Germany) Axioplan epifluorescence microscope equipped with a Peltier-cooled VISICAM-colour CCD camera (PCO Computer Optics GmbH, Kehlheim, Germany).

3.5 Results and discussion

3.5.1 Biomarkers in oil

The purpose of this study was to investigate whether biomarkers in natural oils could be detected using ToF-SIMS. This was initially done by recording ToF-SIMS spectra from a pure biomarker reference sample (cholestane), in order to identify mass fragments that are characteristic of the biomarker. Subsequently, the oil samples were investigated for the presence of cholestane using the

identified characteristic mass fragments. Cholestane was chosen as the target compound, because it is a major hydrocarbon degradation product of steroid alcohols being a constituent of lipid membranes in all eukaryotic cells. Cholestane isomers and pseudo homologues have been used both as tracers for the supply of eukaryotic biomass to geological samples reaching back to the Precambrian (Brocks *et al.*, 2003) and as organic matter thermal maturity indicators (Peters *et al.*, 2005). Typical values of the relative concentrations of single cholestanes in various crude oils have been reported to be in the range of 10-100 ppm (Peters *et al.*, 2005).

Figure 3.1 shows the molecular structure and a positive ion ToF-SIMS spectrum of the cholestane reference sample. In the low-mass range, below $m/z \sim 150$, the spectrum mainly contained small hydrocarbon fragment ions consisting of $C_xH_y^+$. Since these fragments are commonly produced from a large number of organic substances, they are of limited chemical specificity. However, these signals can still be used to distinguish, for example, between organic and inorganic compounds and between hydrocarbons and oxygen-, nitrogen- or sulfur-bearing organic compounds.

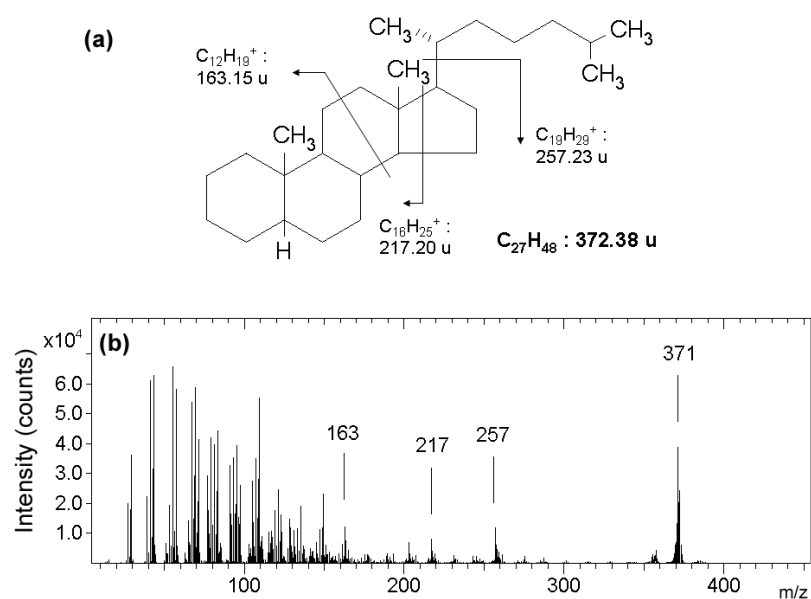


Fig. 3.1. a) Molecular structure of cholestane including possible fragment ions in TOF-SIMS and (b) TOF-SIMS spectrum of positive ions from a pure cholestane standard sample.

At higher masses, the spectrum displayed a number of pronounced mass fragments originating from the cholestane molecule (see Figure 3.1a for fragment identification). The strong signal at 371.36 u can be identified as the molecular ion minus one hydrogen ($C_{27}H_{47}^+$, $(M-H)^+$, theoretical value 371.368 u) and represents the most specific peak that can be obtained by ToF-SIMS for cholestane. The fragment ion pattern exhibiting prominent peaks at m/z 163, 217 and 257 strongly

resembles conventional electron impact mass spectra of cholestane (Peters *et al.*, 2005) and thus reveals further particular indications for identifying this biomarker in oils.

Figure 3.2 shows the ToF-SIMS spectra from the (a) biomarker reference sample, (b) the saturate hydrocarbon fraction of the crude oil and (c) the unfractionated crude oil in the mass region of the molecular peak of cholestane. Comparison of the three spectra shows that the molecular peak (minus hydrogen) of cholestane (371.38 u) is clearly detected in the non-polar component and observed as a small peak following a larger peak of an unknown compound at 371.28 u in the unfractionated oil sample. The observation of the peak at m/z 371.38 in the spectrum from the unfractionated oil sample is consistent with the presence of cholestane in the sample oil. However, in order to make a conclusive assignment of the peak to cholestane, it is necessary to eliminate the possibilities for alternative contributions to this peak. Its strong signal intensity in the hydrocarbon fraction indicates that the main contribution to the m/z 371.38 peak in the unfractionated sample originates from the hydrocarbon fraction, excluding polar oil components including aromatic compounds. Furthermore, the high mass resolution in ToF-SIMS makes it possible to rule out non-polar hydrocarbon compounds with different H/C stoichiometries.

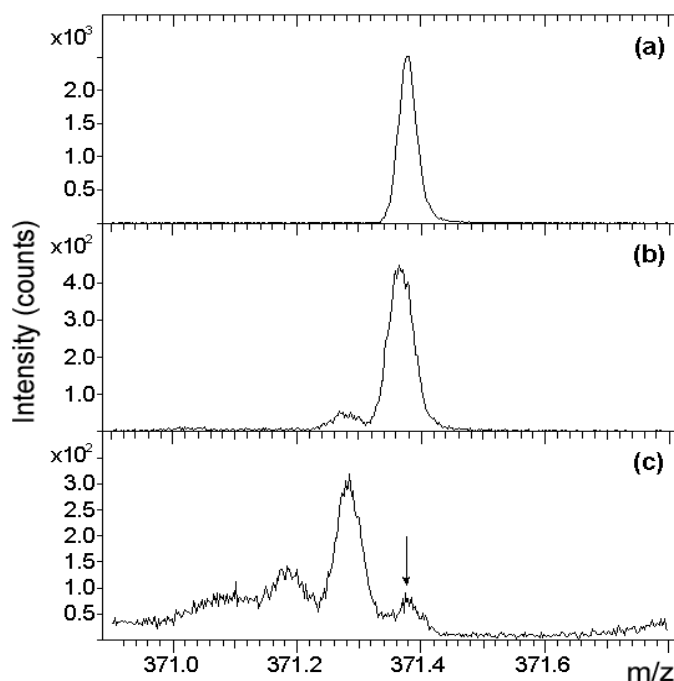


Fig. 3.2. Expanded view of the cholestane molecular peak $(M-H)^+$ region in positive ion TOF-SIMS spectra of (a) the pure cholestane standard, (b) the saturate hydrocarbon fraction of a California crude oil and (c) the unfractionated California crude oil. The arrow in fig (c) indicates the position of the molecular peak of cholestane.

By using similar strategies, combining ToF-SIMS with GC/MS analysis, the assignment of peaks to biomarkers, such as steranes and hopanes, can often be made with reasonable confidence in unfractionated oil samples and, with sufficient sample content and detection efficiency, it should be possible to detect biomarkers in single fluid inclusions (Siljeström *et al.*, 2007).

3.5.2 Archaeal lipids in microbial mats

The identification and exact localisation of organic molecules in microbially-controlled environmental systems has been a long-standing challenge in many scientific fields ranging from microbial ecology to biogeochemistry and medicine. In two recent pilot studies on Black Sea microbial mat and biomineralised carbonate samples, we tested the potential of ToF-SIMS for investigating the qualitative and spatial distribution of archaea-derived lipid biomarkers (Thiel *et al.*, 2007a, b). Figure 3.3 shows a partial ToF-SIMS spectrum of positive ions obtained from a 500 x 500 μm^2 area of a microbial mat cryosection. The spectrum shows three intense peak clusters that can be assigned to molecular ions of major cell membrane lipids in archaea, namely hydroxyarchaeol, glycerol dialkyl glycerol tetraethers (GDGT) and gentiobiosyl-GDGT (Thiel *et al.*, 2007a). In all cases, the observed peaks correspond to the glycerol ether lipids cationised by a sodium adduct, $(M+\text{Na})^+$, which is a type of complex commonly observed in ToF-SIMS analysis of organic materials (Hagenhoff, 2001). For hydroxyarchaeol (Figure 3.3b), the molecular ion shows two clear peaks corresponding to the expected isotope pattern due to the natural abundance of ^{13}C . For GDGT and gentiobiosyl-GDGT (Figure 3.3c and d), each group consists of 9-10 peaks corresponding to the isotopologues of the acyclic tetraether molecule and its cyclic derivatives with up to four cyclopentyl rings in the isoprenoid chains. Similar peak patterns of tetraether lipids have been observed by coupled liquid chromatography mass spectrometry (LC/MS) of archaeal cell material and environmental samples containing archaeal lipids (Hopmans *et al.*, 2000). The peak labels in Figure 3.3c and d indicate the number of cyclopentyl rings in the corresponding molecules and the drawn molecular structures show examples of a representative core and functionalised tetraether lipid containing one cyclopentyl ring.

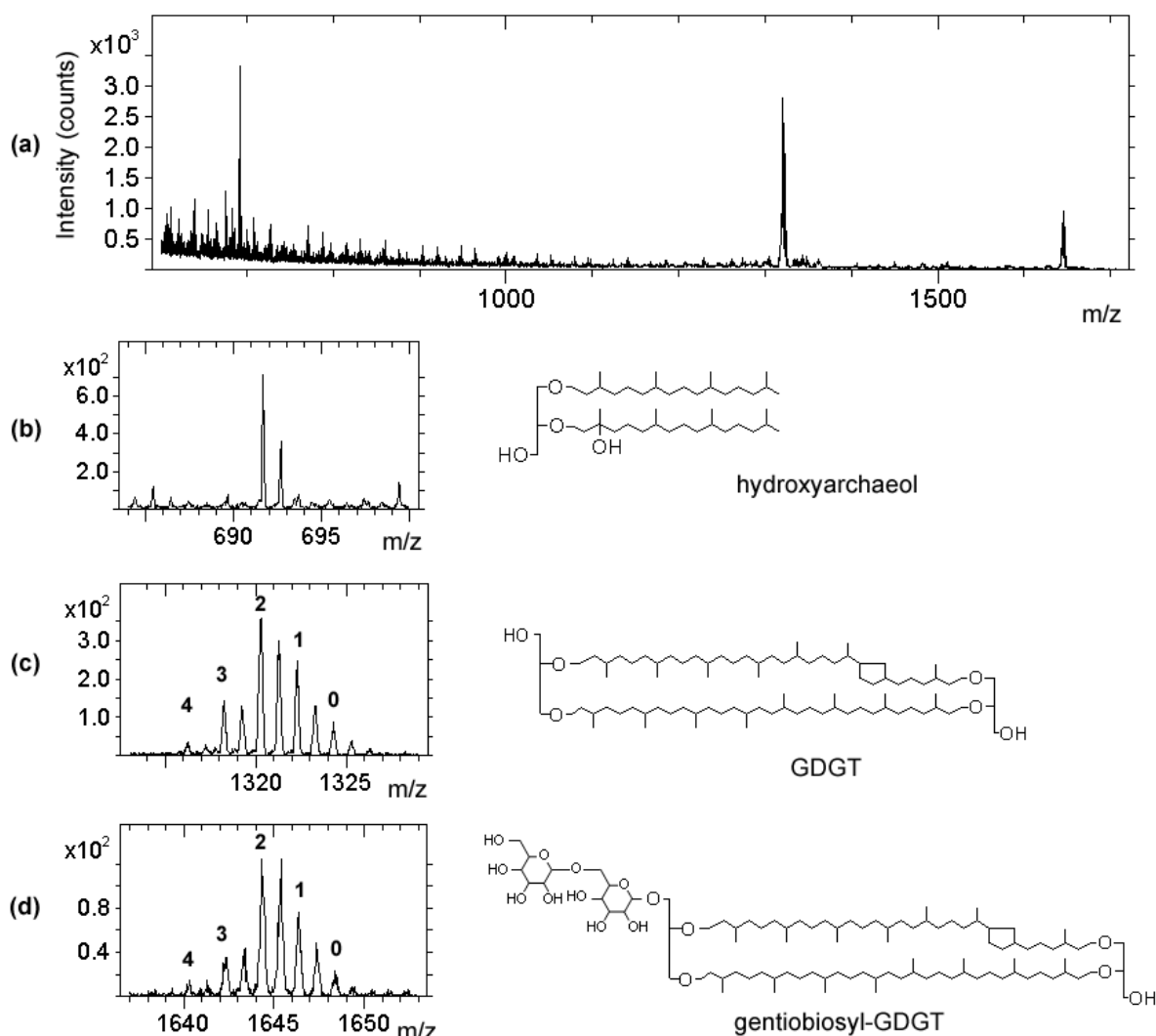


Fig. 3.3. (a) Overview partial TOF-SIMS spectrum of positive ions from a microbial mat cryosection (field of view $500 \times 500 \mu\text{m}^2$) and expanded views of the peaks indicated by the arrows as well as molecular structures of the assigned lipid molecules, (b) hydroxyarchaeol, (c) glycerol dialkyl glycerol tetraethers (GDGTs) and (d) gentiobiosyl-GDGTs. The labels in (c) and (d) indicate the number of cyclopentyl rings in the isoprenoid chains of the respective tetraether molecules (modified after (Thiel, *et al.*, 2007a)).

Furthermore, additional peaks with lower signal intensities could be assigned to archaeol, dihydroxyarchaeol and gentiobiosyl-archaeol. A summary of all observed peaks assigned to archaeal lipids and their theoretical values is presented in Table 3.2. The imaging capability of ToF-SIMS is demonstrated in Figures 3.4 and 3.5, which show ion images of specific lipids and inorganic components in two different microbial mat cryosections.

Compound	Formula	Mass (M) calculated	[M+Na] ⁺ calculated	[M+Na] ⁺ measured
Archaeol	C ₄₃ H ₈₈ O ₃	652.673	675.663	675.67
Hydroxyarchaeol	C ₄₃ H ₈₈ O ₄	668.668	691.658	691.67
Dihydroxyarchaeol	C ₄₃ H ₈₈ O ₅	684.663	707.653	707.65
Gentiobiosyl-archaeol	C ₅₅ H ₁₀₈ O ₁₃	976.779	999.769	999.77
GDGT 0	C ₈₆ H ₁₇₂ O ₆	1301.315	1324.305	1324.29
GDGT 1	C ₈₆ H ₁₇₀ O ₆	1299.300	1322.290	1322.28
GDGT 2	C ₈₆ H ₁₆₈ O ₆	1297.284	1320.274	1320.27
GDGT 3	C ₈₆ H ₁₆₆ O ₆	1295.268	1318.258	1318.25
GDGT 4	C ₈₆ H ₁₆₄ O ₆	1293.253	1316.242	1316.24
Gentiobiosyl-GDGT 0	C ₉₈ H ₁₉₂ O ₁₆	1625.421	1648.411	1648.38
Gentiobiosyl-GDGT 1	C ₉₈ H ₁₉₀ O ₁₆	1623.405	1646.395	1646.35
Gentiobiosyl-GDGT 2	C ₉₈ H ₁₈₈ O ₁₆	1621.390	1644.380	1644.34
Gentiobiosyl-GDGT 3	C ₉₈ H ₁₈₆ O ₁₆	1619.374	1642.364	1642.31
Gentiobiosyl-GDGT 4	C ₉₈ H ₁₈₄ O ₁₆	1617.358	1640.348	1640.26

Table 3.2. List of archaeal ether lipid biomarkers analysed, and calculated *vs.* measured exact masses [u] of relevant molecular ions (Thiel *et al.*, 2007a) All masses given correspond to the first peak in the isotope cluster due to ¹³C. GDGT numbers denote the numbers of cyclopentyl rings in the C₄₀ isoprenoid moieties ether-linked to the glycerol backbones (see Fig. 3.3 for structures).

Figures 3.4a-c show ion images of the specific ion signals from (a) hydroxyarchaeol, (b) all GDGTs and (c) all gentiobiosyl-GDGTs over an analysis area of 500 x 500 μm², demonstrating different lateral distributions for these lipids (Thiel *et al.*, 2007a). Figure 3.4d shows a video image of the analysis area, acquired by the built-in camera of the ToF-SIMS instrument during analysis. Figure 3.4e shows a micrograph, obtained after ToF-SIMS analysis of the same sample area using an optical microscope, onto which the specific lipid ion images recorded by ToF-SIMS have been superimposed. Thus, the combination of ToF-SIMS and optical microscopy makes it possible to relate specific structures or organisms with organic compounds at a microscopic length scale. In our present study, post-measurement fluorescence microscopy was used furthermore to assign the micro-organisms in the sample as chain-like assemblages of cylindrical cells of ANME-1 archaea, a phylogenetic cluster of anaerobic methanotrophic archaea known from previous investigations (Pimenov *et al.*, 1997; Michaelis *et al.*, 2002; Knittel *et al.*, 2005; Reitner *et al.*, 2005). This provided strong evidence that the GDGT and gentiobiosyl-GDGT lipids are produced by ANME-1 cells (Thiel *et al.*, 2007a).

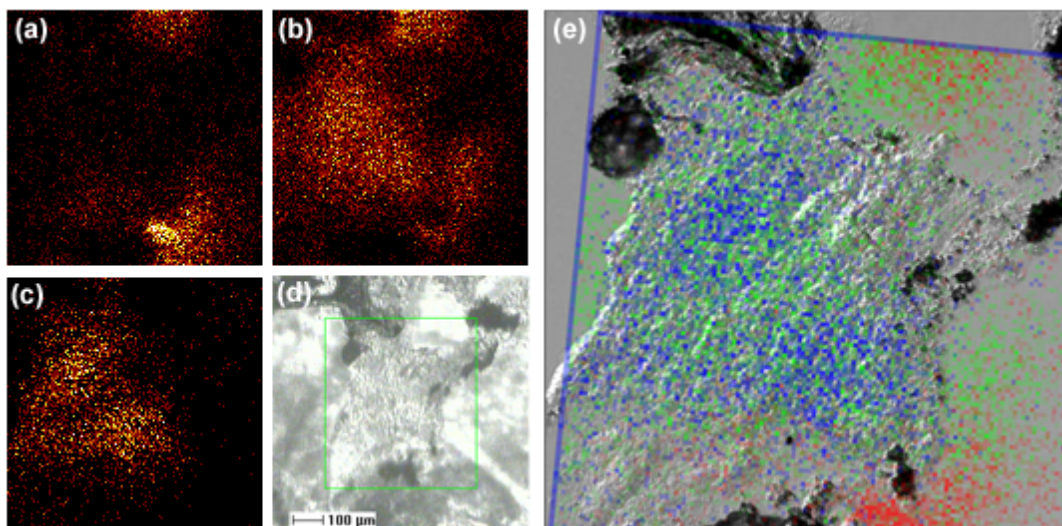


Fig. 3.4. TOF-SIMS images from a microbial mat cryosection showing the lateral distributions of (a) hydroxyarchaeol, $(M+Na)^+$, (b) GDGTs, $(M+H)^+$ and (c) gentiobiosyl-GDGTs, $(M+H)^+$. (d) Video image of the analysis area on the cryosection sample and (e) optical micrograph of the analysis area superimposed by the lipid ion images of hydroxyarchaeol (red), GDGTs (green) and gentiobiosyl-GDGTs (blue). (a) to (d) modified after (Thiel *et al.*, 2007a).

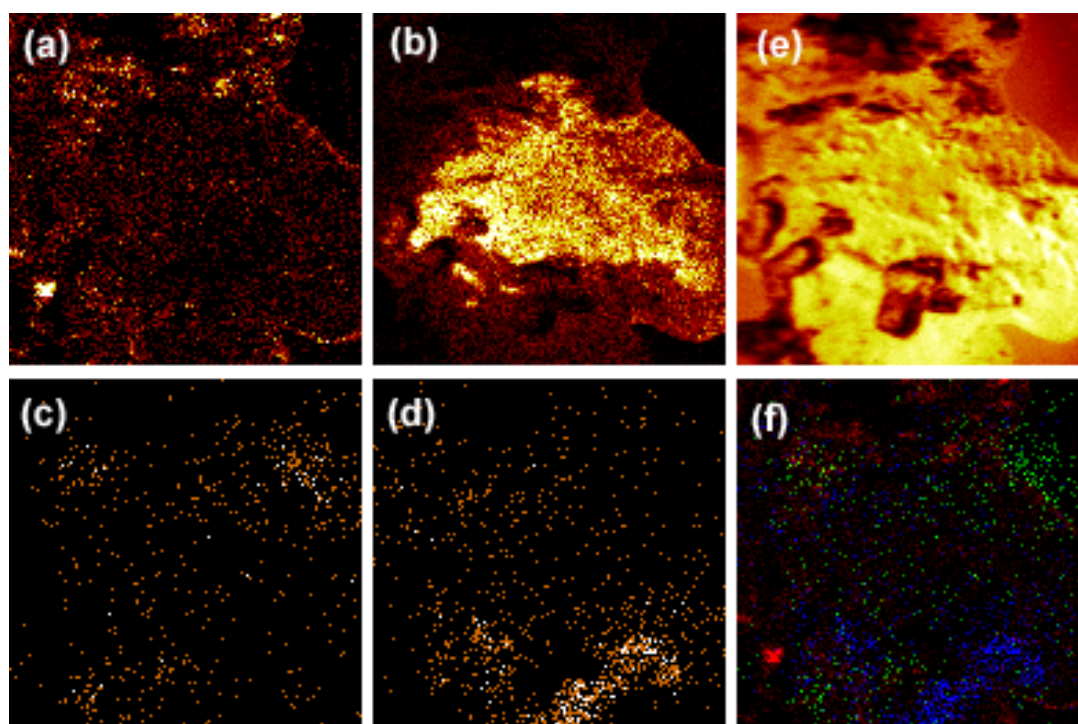


Fig. 3.5. TOF-SIMS images from a microbial mat cryosection showing the lateral distributions of (a) $Ca_2O_2H^+$, representing microbially induced calcium carbonate, (b) $Na_3Cl_2^+$, representing NaCl, (c) hydroxyarchaeol, $(M+Na)^+$, (d) GDGTs, $(M+H)^+$ and (e) the sum of all detected secondary ions. (f) Overlay image of $Ca_2O_2H^+$ (red), hydroxyarchaeol (green) and GDGTs (blue).

Figures 3.5a-d show the spatial distributions of (a) $\text{Ca}_2\text{O}_2\text{H}^+$, representative for the microbially-induced calcium carbonate precipitate, (b) Na_3Cl_2^+ , representative for NaCl, and the molecular ions of (c) hydroxyarchaeol and (d) all GDGTs. Figure 3.5e shows the lateral distribution of the sum of all secondary ions detected, providing an indication of the topography of the sample surface. The relative localisation of calcium carbonate with hydroxyarchaeol and GDGT is shown in the three-colour overlay image in Figure 3.5f. In this case, there seems to be no correlation in localisation between calcium carbonate and GDGT. For hydroxyarchaeol, three regions with somewhat elevated signal intensities (lower left, upper left and upper right, respectively) are located in the vicinity of regions with elevated calcium carbonate signal levels. However, analysis of additional samples is required in order to determine whether a spatial correlation between the two compounds exists.

3.6 Concluding remarks

The strong potential of ToF-SIMS in geochemistry is its ability to provide molecule-specific detection, identification and microscopic localisation (mapping) of inorganic and organic compounds without the need for pre-selection or labelling of the compounds of interest. In comparison with more established techniques such as GC/MS and LC/MS for substance identification, ToF-SIMS can be used to analyse smaller samples or microscopic areas within a particular macroscopic sample. Applications where these capabilities are advantageous, and which our team is presently pursuing, are identification of biomarkers in single oil-bearing fluid inclusions in ancient rocks, and the identification of specific biomarkers that might be assigned to particular organisms involved in biomineralisation. Important ingredients and challenges in this research are the development of appropriate sample preparation protocols, measurement of reference spectra from pure substances as an aid in spectrum interpretation, and validation of the ToF-SIMS results against established knowledge and methods.

Acknowledgements

This work received financial support from the Deutsche Forschungsgemeinschaft (DFG, grants Th 713/3, 4, and Research Unit FOR 571 “Geobiology of Organo- and Biofilms”), the University of Hamburg, the Swedish Research Council (VR, grant 60573901), the Swedish Space Agency (grant 140/06) and the Swedish Governmental Agency for Innovation Systems (VINNOVA). We are grateful to two anonymous reviewers for their constructive comments that helped to improve the original manuscript.

References

- Belu AM, Graham DJ, Castner DG (2003) Time-of-flight secondary ion mass spectrometry: techniques and applications for the characterization of biomaterial surfaces. *Biomaterials*, **24**, 3635-3653.
- Benninghoven A (1994) Chemical Analysis of Inorganic and Organic Surfaces and Thin Films by Static Time-of-Flight Secondary Ion Mass Spectrometry (ToF-SIMS). *Angewandte Chemie International Edition in English*, **33**, 1023-1043.
- Brocks JJ, Buick R, Logan GA, Summons RE (2003) Composition and syngeneity of molecular fossils from the 2.78 to 2.45 billion-year-old Mount Bruce Supergroup, Pilbara craton, Western Australia. *Geochimica et Cosmochimica Acta*, **67**, 4289-4319.
- Cannon DM, Pacholski ML, Winograd N, Ewing AG (2000) Molecule specific imaging of freeze-fractured, frozenhydrated model membrane systems using mass spectrometry. *Journal of the American Chemical Society*, **122**, 603-610.
- Cornett DS, Reyzer ML, Chaurand P, Caprioli RM (2007) Maldi imaging mass spectrometry: Molecular snapshots of biochemical systems. *Nature Methods*, **4**, 828-833.
- Hagenhoff B (2001) Optimisation methods: Cationisation. In: Vickerman JC and Briggs D (eds), *ToF-SIMS: Surface analysis by mass spectrometry*. IM Publications and SurfaceSpectra Limited (Charlton, Chichester, West Sussex, UK), 285-308.
- Hopmans EC, Schouten S, Pancost RD, van der Meer MTJ, Damste JSS (2000) Analysis of intact tetraether lipids in archaeal cell material and sediments by high performance liquid chromatography/atmospheric pressure chemical ionization mass spectrometry. *Rapid Communications in Mass Spectrometry*, **14**, 585-589.
- Knittel K, Losekann T, Boetius A, Kort R, Amann R (2005) Diversity and distribution of methanotrophic archaea at cold seeps. *Applied and Environmental Microbiology*, **71**, 467-479.
- Kollmer F (2004) Cluster primary ion bombardment of organic materials. *Applied Surface Science*, 231-2, 153-158.
- Kraft ML, Weber PK, Longo ML, Hutcheon ID, Boxer SG (2006) Phase separation of lipid membranes analyzed with high-resolution secondary ion mass spectrometry. *Science*, **313**, 1948-1951.
- Michaelis W, Seifert R, Nauhaus K, Treude T, Thiel V, Blumenberg M, Knittel K, Gieseke A, Peterknecht K, Pape T, Boetius A, Amann R, Jorgensen BB, Widdel F, Peckmann JR, Pimenov NV, Gulin MB (2002) Microbial reefs in the black sea fueled by anaerobic oxidation of methane. *Science*, **297**, 1013-1015.
- Pacholski ML, Winograd N (1999) Imaging with mass spectrometry. *Chemical Reviews*, **99**, 2977-3005.
- Peters K, Walters C, Moldowan M (2005) *The biomarker guide*. Cambridge University Press (Cambridge, UK), 1155pp.
- Pimenov NV, Rusanov II, Poglazova MN, Mityushina LL, Sorokin DY, Khmelenina VN, Trotsenko YA (1997) Bacterial mats on coral-like structures at methane seeps in the black sea. *Microbiology*, **66**, 354-360.
- Prinz C, Hook F, Malm J, Sjoval P (2007) Structural effects in the analysis of supported lipid bilayers by time-of-flight secondary ion mass spectrometry. *Langmuir*, **23**, 8035-8041.

- Reitner J, Reimer A, Schumann G, Thiel V, Peckmann J (2005) Methane-derived carbonate build-ups and associated microbial communities at cold seeps on the lower Crimean shelf (Black Sea). *Facies*, **51**, 71-84.
- Siljeström S, Hode T, Lausmaa J, Toporski J, Thiel V, Sjövall P (2007) Detection of biomarkers in oils using ToF-SIMS. *Geochimica et Cosmochimica Acta*, **71**, A937.
- Sjovall P, Lausmaa J, Johansson B (2004) Mass spectrometric imaging of lipids in brain tissue. *Analytical Chemistry*, **76**, 4271-4278.
- Sodhi RNS (2004) Time-of-flight secondary ion mass spectrometry (ToF-SIMS): Versatility in chemical and imaging surface analysis. *The Analyst*, **129**, 483-487.
- Takats Z, Wiseman JM, Gologan B, Cooks RG (2004) Mass spectrometry sampling under ambient conditions with desorption electrospray ionization. *Science*, **306**, 471-473.
- Thiel V, Heim C, Arp G, Hahmann U, Sjövall P, Lausmaa J (2007a) Biomarkers at the microscopic range: ToF-SIMS molecular imaging of archaea-derived lipids in a microbial mat. *Geobiology*, **5**, 413-421.
- Thiel V, Toporski J, Schumann G, Sjövall P, Lausmaa J (2007b) Analysis of archaeal core ether lipids using time of flight-secondary ion mass spectrometry (ToF-SIMS): Exploring a new prospect for the study of biomarkers in geobiology. *Geobiology*, **5**, 75-83.
- Touboul D, Halgand F, Brunelle A, Kersting R, Tallarek E, Hagenhoff B, Laprévotte O (2004) Tissue molecular ion imaging by gold cluster ion bombardment. *Analytical Chemistry*, **76**, 1550-1559.
- Touboul D, Kollmer F, Niehuis E, Brunelle A, Laprevotte O (2005) Improvement of biological time-of-flight-secondary ion mass spectrometry imaging with a bismuth cluster ion source. *Journal of the American Society for Mass Spectrometry*, **16**, 1608-1618.
- Vickerman JC, Briggs D (2001) ToF-SIMS: Surface analysis by mass spectrometry. IM Publications and SurfaceSpectra Limited (Charlton, Chichester, West Sussex, UK), 789pp.
- Wucher A, Cheng J, Winograd N (2007) Protocols for three-dimensional molecular imaging using mass spectrometry. *Analytical Chemistry*, **79**, 5529-5539.

4

Spectral characterisation of eight glycerolipids and their detection in natural samples using Time-of-Flight Secondary Ion Mass Spectrometry (ToF-SIMS)

Christine Heim, Peter Sjövall, Jukka Lausmaa, Tim Leefmann, Volker Thiel

Rapid Communications in Mass Spectrometry (2009) 23, 1-13

4.1 Abstract

In recent years, Time of Flight - Secondary Ion Mass Spectrometry (ToF-SIMS) with cluster ion sources has opened new perspectives for the analysis of lipid biomarkers in geobiology and organic geochemistry. However, published ToF-SIMS reference spectra of relevant compounds are still sparse, and the influence of the chemical environment (matrix) on the ionization of molecules and their fragmentation is still not well explored. This study presents ToF-SIMS spectra of eight glycerolipids as common target compounds in biomarker studies, namely ester- and ether-bound phosphatidylethanolamine, ester- and ether-bound phosphatidylcholine, ester-bound phosphatidylglycerol, ester- and ether-bound diglycerides and archaeol, obtained with a Bi_3^+ cluster ion source. For all of these compounds, the spectra obtained in positive and negative analytical modes showed characteristic fragments that could clearly be assigned to e.g. molecular ions, functional groups and alkyl chains. By comparison with the reference spectra, it was possible to track some of these lipids in a pre-characterised organic extract and in cryosections of microbial mats. The results highlight the potential of ToF-SIMS for the laterally resolved analysis of organic biomarkers in environmental materials. The identification of the target compounds, however, may be hampered by matrix effects (e.g. adduct formation) and often require careful consideration of all spectral features and taking advantage of the molecular imaging capability of ToF-SIMS.

4.2 Introduction

Time of Flight - Secondary Ion Mass Spectrometry (ToF-SIMS) is a surface analysis technique that allows simultaneous analysis of inorganic and organic molecules on solid surfaces (Benninghoven *et al.*, 1994; Pacholski and Winograd, 1999). During the last 10-20 years, ToF-SIMS has been used mainly in material sciences (Vickerman and Briggs, 2001; Belu *et al.*, 2003). The introduction

of polyatomic cluster ion sources (e.g. Au_n^+ , Bi_n^+ , C_{60}^+) has expanded the capabilities of this technique, opening new possibilities for the analysis of biological materials (Kollmer, 2004; Sjövall *et al.*, 2004; Touboul *et al.*, 2004, 2005; Ostrowski *et al.*, 2004) and consequently, the application of ToF-SIMS in geobiology and organic geochemistry (Thiel *et al.*, 2007; Sjövall *et al.*, 2008, Siljeström *et al.*, 2009). A most advantageous property of ToF-SIMS is its ability to record the intensities of any detected ion in a given area of interest at a microscopic scale (e.g. Hagenhoff, 2000). To date, this is not possible with any of the extract-based techniques routinely used in biomarker studies, namely GC/MS and LC/MS (coupled gas chromatography/mass spectrometry, coupled liquid chromatography/mass spectrometry). Whereas GC/MS and LC/MS are effective tools for the identification and quantification of organic compounds, it remains difficult to link the chemical information obtained to specific structures of interest in heterogeneous and structurally complex biological or geological materials. In ToF-SIMS, identification of organic compounds is achieved mainly through precise mass determination, sometimes corroborated by the analysis of the lateral distribution of the species of interest in selected areas on the sample surface. However, the absence or as yet sparse number of published ToF-SIMS spectral fragmentation patterns may hamper an accurate structural assignment. Likewise, the influence of the chemical environment (matrix) on the ionization of molecules and their fragmentation appears to be an important factor (Sostarecz *et al.*, 2004), but is still not well explored.

Studies performed previously on reference compounds of widespread hydrocarbon biomarkers (Steele *et al.*, 2001, Toporski and Steele, 2004, Toporski *et al.*, 2002) showed that ToF-SIMS spectra may, or may not, differ considerably from those obtained with conventional mass spectrometric techniques (see also Vickerman and Briggs, 2001). By comparison with pure reference compounds, it was recently proven possible to detect hydrocarbon biomarkers, namely hopanes and steranes, in crude oils by ToF-SIMS¹². Recent studies on animal tissues, eukaryotic cells or microbial consortia also revealed the potential of ToF-SIMS with cluster ion sources for investigating the distribution of intact lipids in natural samples (Börner *et al.*, 2007; Thiel *et al.*, 2007a; Sjövall *et al.*, 2004; Ostrowski *et al.*, 2004, 2005). Whereas these studies focused on materials with a more or less pre-characterized lipid content, the authors pointed out that the establishment of ToF-SIMS reference data is a major prerequisite for the investigation of organic molecules in barely studied or unknown environmental materials.

This study presents previously unpublished ToF-SIMS spectra of eight functionalized glycerolipids as important members of cell membrane constituents of eukaryotes, bacteria, and archaea. These lipids, or their derivatives, are commonly used as biomarkers in geo- and microbiology, organic geochemistry, and microbial ecology (Börner *et al.*, 2007; Thiel *et al.*, 2007a; Sjövall *et al.*, 2004; Ostrowski *et al.*, 2004, 2005). Our work aims to provide basic information about the ToF-SIMS fragmentation patterns of these compounds in both, positive and negative ion modes. In addition to

'conventional' ester-bound glycerolipids, we also included a number of ether-bound counterparts, as such compounds may reveal important information on the protagonists in some microbially driven ecosystems (Pancost *et al.*, 2001). Emphasis was placed not only on high (molecular) mass species, but also on characteristic fragments that may enable a robust identification of the respective molecule, or the compound class, in a natural sample. However, detectability of a pure reference substance does not necessarily imply that the compound can be easily identified by the same features when analyzed in a complex chemical matrix. To assess the possibility of detecting such lipids in natural samples and the influence of matrix effects, ToF-SIMS spectra of selected glycerolipids (archaeol, phosphoglycerol, diglyceride) were therefore compared with those recorded from the same, or related, compounds in an organic extract and in cryosections of microbial mats.

4.3 Experimental

Eight commercially available glycerolipids (Avanti Lipids, Sigma, Chiron) were selected for analysis, namely; (i) L- α -phosphatidylethanolamine (GPEtn), (ii) 1,2 di-O-hexadecyl-*sn*-glycero-3-phosphatidylethanolamine (Diether-GPEtn), (iii) L- α -phosphatidylcholine (GPCho), (iv) 1,2-di-O-dialkyl-*sn*-glycero-3-phosphatidylcholine (Diether-GPCho), (v) L- α -phosphatidylglycerol (GPGro), (vi) 1-Palmitoyl-2-oleoyl-*sn*-glycerol (DG), (vii) 1,2-di-O-hexadecyl-*rac*-glycerol (Diether-DG), and (viii) 1,2-di-O-phytanyl-*sn*-glycerol (archaeol), see Table 4.1.

All reference lipids were stored cold and dark in glass vials with Teflon septa before, and between, analyses. 1 mg of each reference lipid was dissolved in 1 ml pre-distilled solvents (dichloromethane, *n*-hexane). For ToF-SIMS analysis, the compounds were deposited on silicon wafers. The wafers were rinsed with de-ionised water and cleaned in a UV ozone apparatus prior to use in order to remove any organic contaminants from the surface. Using a glass pipette, a few μ L of each lipid solution (except for GPCho, see below) were placed on a silicon wafer and the organic solvent was allowed to evaporate. The deposition processes were carried out in a laminar air flow cabinet in order to avoid airborne particulate contamination. The GPCho sample was prepared as a supported lipid bilayer, according to Prinz *et al.* (2007). As controls, blank silicon wafers were exposed to the same conditions during sample preparation, and analysed in parallel. To assess the presence of contaminants, ToF-SIMS spectra were also obtained from the evaporation residues of the pure solvents. These spectra were used as internal controls for a clean sample processing and are not shown here. Typically, sets of six samples were mounted on a sample holder and introduced to the vacuum chamber of the ToF-SIMS instrument immediately after preparation. A sample of an iron oxidizing microbial mat dominated by *Gallionella ferruginea* (Pedersen *et al.*, 1997) was obtained from a subterranean fluid discharge at -150 m depth in the Äspö Tunnel, SE Sweden. The mats were stored at -20°C prior to analysis. A sample of a methanotrophic microbial

mat was retrieved from the GHOSTDABS methane seep field on the NW' Black Sea shelf from a water depth of 230 m (joint project BEBOP, see acknowledgements). These microbial mats have been studied in detail for their lipid biomarker patterns (Thiel *et al.*, 2007b; Blumenberg *et al.*, 2004; Pape *et al.*, 2005; Michaelis *et al.*, 2002). An organic extract of the Black Sea microbial mat was prepared as it would be typically done for LC/MS and GC/MS analyses. An aliquot of each mat (10 mg) was extracted with 15 mL of dichloromethane / methanol (3:1, 1:1, 1:3) in a teflon capped glass vial (ultrasonication, 20 min). After evaporation of the solvent mixture and re-dissolution in pure dichloromethane, the extracts were deposited on silicon wafers and were transferred to the ToF-SIMS instrument as described above.

For the preparation of the cryosections, the Black Sea and the *Gallionella* microbial mats were allowed to thaw at room temperature, and a small amount (approx. 10 mm³) of each mat sample was mounted on a cork sample holder using an embedding agent (Cryo-Gel®, Electron Microscopy Sciences, PA). The samples were frozen for 30 sec in cold methyl butane at -150 °C and immediately transferred into the cryochamber of a Leica CM 3050 S cryomicrotome (Leica Microsystems, Wetzlar, Germany) that had been pre-cooled to -20 °C. Using a standard steel knife (Leica Profile D), serial sections of ca. 8 µm thickness were cut, deposited on standard microscope slides (76 x 26 mm), and stored at -20 °C in closed glass containers until analysis. Prior to transfer into the ToF-SIMS instrument, the slides were allowed to approach room temperature with the glass container kept closed, in order to avoid condensation of water vapor on the sample. All glassware (microscope slides, pipettes, vials, beakers, glass containers) were heated to 400 °C for 2 h prior to use, and/or cleaned by thoroughly rinsing with deionised water and acetone. Solvent rinsing was also used to clean all steelware (spatula, tweezers, microtome knives) prior to use.

ToF-SIMS images and spectra of positive and negative ions were recorded using a ToF-SIMS IV instrument (ION-TOF GmbH, Münster, Germany) equipped with a liquid bismuth cluster ion source. Data were acquired in bunched mode with a mass resolution of ca. $M/\Delta M$ 5000, using 25 keV Bi₃⁺ primary ions at a pulsed current of 0.1 pA. Low energy electron flooding was used for charge compensation, when necessary. The analysed areas were 100 x 100 µm² or 200 x 200 µm² for references and extracts, and 500 x 500 µm² for the microbial mat cryosections. The areas were scanned in a raster pattern at 128 x 128 pixels for reference lipids and extracts, and 256 x 256 pixels for the cryosections. The acquisition times were typically between 50 s and 100 s for the pure lipid reference samples and the extracts, and 300 s to 500 s for the cryosections. All analyses were thus done under so-called static SIMS condition, i.e. with primary ion doses well below those where significant surface damage due to the ion bombardment starts to appear (Sjövall *et al.*, 2008).

4.4 Results and Discussion

Through comparison of the spectra from the different lipids, it was possible to determine characteristic peaks and fragmentation schemes for the respective lipid classes. In the low mass range, fragments specifying phospholipids in general were m/z 78.95 [PO_3^-], and 96.97 [H_2PO_4^-] as previously reported (e.g. Ostrowski *et al.*, 2005; Sjövall *et al.*, 2004). In addition, other distinctive headgroup fragments are present in the spectra of particular phospholipid classes. Such fragments were reproducibly detected in both ester- and ether-bound phospholipids and are listed in Table 4.2. Fragmentation of ester-bound lipids leads to prominent peaks of the corresponding fatty acid chains whereas the ether-bound lipids exhibited weak fragment ion peaks of the alcohol side chains (Tab. 4.2). In general, the fragmentation tendency of ether lipids is considerably lower compared to ester-bound lipids, probably due to the higher chemical stability of the ether link.

4.4.1 Phosphatidylethanolamine (GPEtn):

$\text{C}_{39}\text{H}_{74}\text{NO}_8\text{P}$; exact mass 715.52 Da (Dalton)

Source: eukaryotes (Ostrowski *et al.*, 2004, 2005), bacteria (Mazalla *et al.*, 2005)

Molecular ions are detected as at m/z 716.53 and m/z 740.55 in the positive spectrum. Whereas the former is in accordance with the $[\text{M}+\text{H}]^+$ ion of the actual GPEtn molecule containing one $\text{C}_{16:0}$ and one $\text{C}_{18:2}$ moiety ($\text{C}_{16:0}/\text{C}_{18:2}$), the latter seems to originate from GPEtn that carries two $\text{C}_{18:2}$ chains ($\text{C}_{18:2}/\text{C}_{18:2}$). The observed distribution is in good agreement with the product specification from the distributor ($\text{C}_{16:0} = 24\%$, $\text{C}_{18:2} = 60\%$). Both molecular ions produce sodium adducts $[\text{M}+\text{Na}]^+$ at m/z 738.53 and m/z 762.54, respectively. Characteristic fragments in positive mode are observed at m/z 575.49 $[\text{M}-\text{headgroup}]^+$, 306.29 and 282.28 (Table 4.1) and are interpreted to result from cleavage within the glycerol backbone (see fragmentation scheme, Fig. 4.1 and Table 4.2). Specific headgroup fragments are observed at m/z 142.03 and 182.06 corresponding to $[\text{C}_2\text{H}_9\text{NO}_4\text{P}]^+$ and $[\text{C}_5\text{H}_{13}\text{NO}_4\text{P}]^+$.

In negative mode, deprotonated molecular ions $[\text{M}-\text{H}]^-$ occur at m/z 714.55 ($\text{C}_{16:0}/\text{C}_{18:2}$) and at m/z 738.55 ($\text{C}_{18:2}/\text{C}_{18:2}$). Ions at m/z 697.51 and 671.48 are interpreted as $[\text{M}-\text{NH}_3]^-$ and $[\text{M}-\text{C}_2\text{H}_7\text{N}]^-$. Prominent peaks at m/z 96.97 [H_2PO_4^-] and 78.96 [PO_3^-] (not shown) and at m/z 140.02 clearly specify the phosphate bearing headgroup, as observed in previous studies (Börner *et al.*, 2007; Ostrowski *et al.*, 2005). Fragments at m/z 279.25 ($\text{C}_{18:2}$) and m/z 255.24 ($\text{C}_{16:0}$) can be assigned to fatty acid chains (according to Börner *et al.*, 2007), whereas fragments at m/z 476.29, 452.29 and 434.28 putatively derive from the PE molecule after loss of the fatty acid chains as indicated in Fig. 4.1.

Tab.1 Glycerolipids studied and ions observed in the molecular weight range.

Compound	Abbreviation	Formula	Exact mass	Observed [M+H] ⁺	Observed [M+Na] ⁺	Observed [M-H] ⁻	Others
L- α -Phosphatidylethanolamine	GPEtn (16:0/18:2)	C ₃₉ H ₇₄ NO ₈ P	715.52	716.53	738.53	714.52	697.51 [M-NH ₃] ⁻
L- α -Phosphatidylethanolamine	GPEtn (18:2/18:2)	C ₄₁ H ₇₄ NO ₈ P	739.52	740.55	762.54	738.52	— —
1,2 Di- <i>O</i> -Hexadecyl- <i>rac</i> -Phosphatidylethanolamine	Diether-GPEtn	C ₃₇ H ₇₈ NO ₆ P	663.56	664.65	—	662.49	624.67 [M+Na-C ₂ H ₈ NO] ⁻
L- α -Phosphatidylcholine	GPCho	C ₄₂ H ₈₂ NO ₈ P	759.58	760.61	782.61	—	744.54 [M-CH ₃] ⁻ 699.47 [M-C ₃ H ₉ N] ⁻
1,2- <i>O</i> -Dialkyl- <i>sn</i> -Glycero-3-Phosphatidylcholine	Diether-GPCho	C ₄₀ H ₈₅ NO ₆ P	705.60	706.75	—	704.57	690.54 [M-CH ₃] ⁻ 645.47 [M-C ₃ H ₉ N] ⁻
L- α -Phosphatidylglycerol (sodium salt)	GPGro	C ₃₈ H ₇₄ O ₁₀ PNa	744.49	—	767.51	721.58	721.58 [M-Na] ⁻
1-Palmitoyl-2-Oleoyl- <i>sn</i> -Glycerol	DG	C ₃₇ H ₇₀ O ₅	594.52	595.58	617.53	593.49	577.52 [M-H ₂ O] ⁺
1,2 Di- <i>O</i> -Hexadecyl- <i>rac</i> -Glycerol	Diether-DG	C ₃₅ H ₇₂ O ₃	540.55	541.63	563.58	539.54	522.59 [M-H ₂ O] ⁺
1,2-Di- <i>O</i> -Phytanyl- <i>sn</i> -Glycerol	Archaeol	C ₄₃ H ₈₈ O ₃	652.67	653.72	675.68	651.66	634.69 [M-H ₂ O] ⁺

Tab. 2 Characteristic fragments and headgroup ions.

Abbreviation	Formula	Characteristic fragment ions (+) observed*	Tentative formula	Characteristic fragment ions (-) observed*	Tentative formula	Headgroup ions (+) observed*	Formula	Headgroup ions (-) observed*	Formula
GPEtn (C _{16:0/18:2})	C ₃₉ H ₇₄ NO ₈ P	575.49 282.28	C ₃₇ H ₆₇ O ₄ ⁺ C ₁₈ H ₃₄ O ₂ ⁺	279.25 255.24	C ₁₈ H ₃₁ O ₂ ⁻ C ₁₆ H ₃₁ O ₂ ⁻	142.03 182.06	C ₂ H ₉ NO ₄ P ⁺ C ₅ H ₁₃ NO ₄ P ⁺	140.02 180.04	C ₂ H ₇ NO ₄ P ⁻ C ₅ H ₁₁ NO ₄ P ⁻
GPEtn (C _{18:2/18:2})	C ₄₁ H ₇₄ NO ₈ P	599.50 306.29	C ₃₉ H ₆₇ O ₄ ⁺ C ₂₀ H ₃₄ O ₂ ⁺	279.25	C ₁₈ H ₃₁ O ₂ ⁻	142.03 182.06	C ₂ H ₉ NO ₄ P ⁺ C ₅ H ₁₃ NO ₄ P ⁺	140.02 180.04	C ₂ H ₇ NO ₄ P ⁻ C ₅ H ₁₁ NO ₄ P ⁻
Diether-GPEtn	C ₃₇ H ₇₈ NO ₆ P	??	??	239.21	C ₁₆ H ₃₁ O ⁻	—	—	180.04 140.01	C ₂ H ₇ NO ₄ P ⁻ C ₅ H ₁₁ NO ₄ P ⁻
GPCho	C ₄₂ H ₈₂ NO ₈ P	504.38 478.37	C ₂₆ H ₅₁ NO ₆ P ⁺ C ₂₄ H ₄₉ NO ₆ P ⁺	281.24 255.23	C ₁₈ H ₃₃ O ₂ ⁻ C ₁₆ H ₃₁ O ₂ ⁻	184.10 166.08	C ₅ H ₁₅ NO ₄ P ⁺ C ₅ H ₁₃ NO ₃ P ⁺	—	—
Diether-GPCho	C ₄₀ H ₈₅ NO ₆ P	464.44 450.41	C ₂₄ H ₅₁ NO ₅ P ⁺ C ₂₃ H ₄₉ NO ₅ P ⁺	239.21	C ₁₆ H ₃₁ O ⁻	184.11	C ₅ H ₁₅ NO ₄ P ⁺	—	—
GPGro	C ₃₈ H ₇₄ O ₁₀ PNa	551.52 511.28	C ₃₅ H ₆₇ O ₄ ⁺ C ₂₂ H ₄₂ Na ₂ O ₈ P ⁺	255.24	C ₁₆ H ₃₁ O ₂ ⁻	198.99	C ₃ H ₆ Na ₂ O ₅ P ⁺	171.04 211.06 153.02	C ₃ H ₈ O ₆ P ⁻ C ₆ H ₁₂ O ₆ P ⁻ C ₃ H ₆ O ₅ P
DG	C ₃₇ H ₇₀ O ₅	339.31 313.28 265.26 239.24	C ₂₁ H ₃₉ O ₃ ⁺ C ₁₉ H ₃₇ O ₃ ⁺ C ₁₈ H ₃₃ O ⁺ C ₁₆ H ₃₁ O ⁺	281.24 255.23	C ₁₈ H ₃₃ O ₂ ⁻ C ₁₆ H ₃₁ O ₂ ⁻	—	—	91.04	C ₃ H ₇ O ₃ ⁻
Diether-DG	C ₃₅ H ₇₂ O ₃	297.32 299.33 253.27	C ₁₉ H ₃₇ O ₂ ⁺ C ₁₉ H ₃₉ O ₂ ⁺ C ₁₇ H ₃₃ O ⁺	241.23 239.19	C ₁₆ H ₃₃ O ⁻ C ₁₆ H ₃₁ O ⁻	—	—	91.02	C ₃ H ₇ O ₃ ⁻
Archaeol	C ₄₃ H ₈₈ O ₃	373.39 371.27	C ₂₃ H ₄₉ O ₃ ⁺ C ₂₃ H ₄₇ O ₃ ⁺	371.37 297.32 295.29	C ₂₃ H ₄₇ O ₃ ⁻ C ₂₀ H ₄₁ O ⁻ C ₂₀ H ₄₁ O ⁻	—	—	91.03	C ₃ H ₇ O ₃ ⁻

*: Ostrowski *et al.* (2005) described further, yet unknown negative ions at m/z 137, 153 and 181 as common phospholipid fragments. These findings were partly confirmed in our study. Both fragments at 137.01 and 153.02 were found in the ester bound phospholipids, whereas the ether-bound phospholipids yielded m/z 137.01. An ion at m/z 181 was not observed in our spectra. Further positive ions described by Ostrowski *et al.* (2005), at m/z 125, 143, and 165 were exclusively observed in the spectrum of GPGro (Na salt) and may represent Na containing fragments.

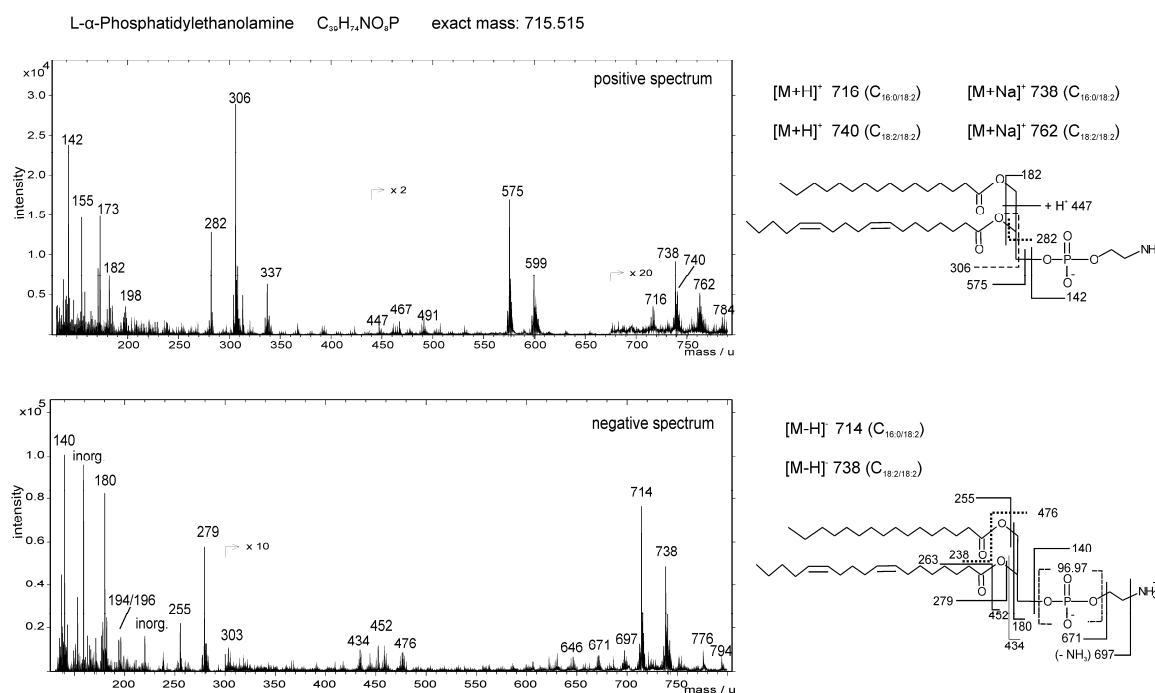


Fig. 4.1 Partial positive (top) and negative (bottom) ToF-SIMS spectra (m/z 140 - 800) of phosphatidylethanolamine (GPEtn). This reference standard mainly contains GPEtn carrying two $C_{18:2}$ or each one $C_{16:0}$ and $C_{18:2}$ fatty acid chains ($C_{16:0} = 24\%$; $C_{18:2} = 60\%$ of the total fatty acids). See text for a detailed discussion of the spectral patterns. The prominent phosphate peak at m/z 96.97 is out of the displayed range. Peaks labeled with “inorg” are inorganic ions and do not belong to the compound spectrum.

4.4.2 1,2 Di-O-hexadecyl-*sn*-glycero-3-phosphatidylethanolamine (Diether-GPEtn)

$C_{37}H_{78}NO_6P$; exact mass 663,56 Da

Source: bacteria (Rütters *et al.*, 2001)

The positive mass spectrum observed for Diether-GPEtn reveals a weak protonated molecular ion $[M+H]^+$ at m/z 664.65 (Fig. 4.2). A single, most prominent and possibly diagnostic peak occurs at m/z 624.67. It is tentatively interpreted as a fragment ion resulting from loss of the ethanolamine group and adduction of Na $[M-C_2H_7NO+Na]^+$ (Fig. 4.2). Another, less abundant sodium adduct of a fragment ion may occur at m/z 654.68 $[M-CH_6N+Na]^+$.

The negative spectrum shows a clear deprotonated molecular ion $[M-H]^-$ at m/z 662.49. In addition, minor fragments at m/z 645.47 and m/z 619.46 can be interpreted as $[M-NH_3]^-$ and $[M-C_2H_7N]^-$, respectively. It is interesting to see that in both positive and negative mode, peaks expected from lyso-fragments or aliphatic side chains (around m/z 224) are weak or even missing. Likewise, headgroup fragments of Diether-GPEtn are only observed in the negative spectrum (Fig. 4.2, Tab. 4.1). Generally, the fragmentation pattern of Diether-GPEtn is less prominent than that observed for ester-bound GPEtn (Fig. 4.1). This is interpreted as reflecting the greater stability of

the ether- compared to the ester linkage, which appears to hamper rearrangement reactions and cleavage of the side chains under primary ion bombardment.

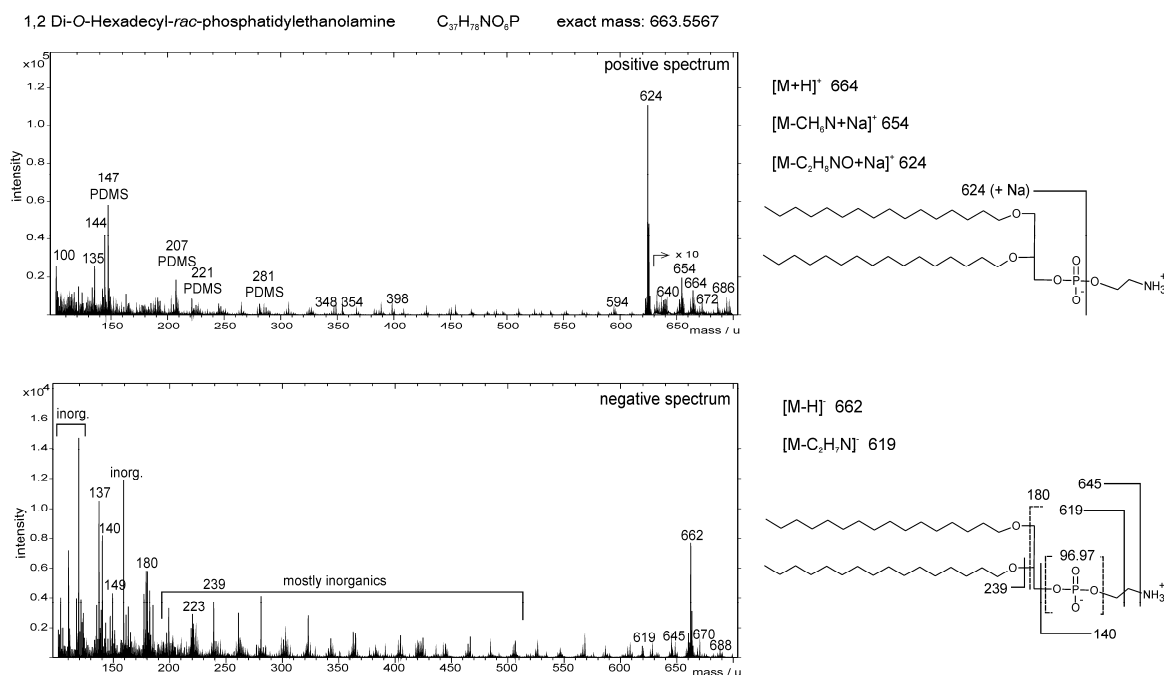


Fig. 4.2 Partial positive (top) and negative (bottom) ToF-SIMS spectra (m/z 100 - 700) of 1,2 Di-O-hexadecyl-*sn*-glycero-3-phosphatidylethanolamine (Diether-GPEtn). See text for a detailed discussion of the spectral patterns. Peaks labeled with inorganics are contaminant ions and do not belong to the compound spectrum.

4.4.3 L- α -Phosphatidylcholine (GPCho):

$C_{42}H_{82}NO_8P$; exact mass 759.58 Da

Source: eukaryotes (Ostrowski et al., 2004, 2005; Sjövall et al., 2004), bacteria (Zink *et al.*, 2003)

Weak molecular ions of GPCho are detected as $[M+H]^+$ and $[M+Na]^+$ at m/z 760.61 and 782.61 in the positive spectrum (Fig. 4.3). Similarly abundant peaks of Lyso-GPCho-fragments occur at m/z 478.37 and 504.38. The most prominent peaks in the positive GPCho spectrum are observed at m/z 166.08 and m/z 184.10 and correspond to the headgroup fragments $[C_5H_{13}NO_3P]^+$ and $[C_5H_{15}NO_4P]^+$.

The negative spectrum of GPCho does not show a deprotonated molecular ion. Instead, characteristic fragments at m/z 744.54 and m/z 699.47 can be assigned to $[M-CH_3]^-$ and $[M-C_3H_9N]^-$. Ions at m/z 255.23 and m/z 281.24 derive from $C_{16:0}$ and $C_{18:1}$ fatty acid moieties, respectively. The relatively low intensities of the molecular ions and characteristic higher mass fragments make it difficult to use these ions for analysing intact GPCho in environmental samples. Furthermore, it has been reported that the intensity of the molecular ion peak is highly sensitive to

the structural configuration of the lipid, showing higher intensity in bilayer structures as compared to disordered structures (Prinz *et al.*, 2007), making the lack of a molecular ion a somewhat uncertain indicator for the absence of GPCho. Although the detection of molecular GPCho ions have been reported in tissue samples (Sjövall *et al.*, 2004), the headgroup fragment (m/z 184.07) provides a strong and characteristic peak for phosphocholine-containing lipids and is therefore frequently used for mapping of these lipids in cell and tissue samples (Börner *et al.*, 2007, Nygren *et al.*, 2005). Comparison of the ToF-SIMS spectra of GPEtn and GPCho with published ToF-SIMS and Electrospray - Ionisation (ESI) (LC/MS) mass spectra of phosphatidylcholine (Mazalla *et al.*, 2005; Ostrowski *et al.*, 2005; Börner *et al.*, 2007) suggests similar principles for the fragmentation of complex ester-bound phospholipids. Beside the molecular ion, both methods yield fragment peaks, phospholipid headgroup ions in positive and negative spectra as well as the fatty acid chains in the negative spectra, which may be used to corroborate structural identification.

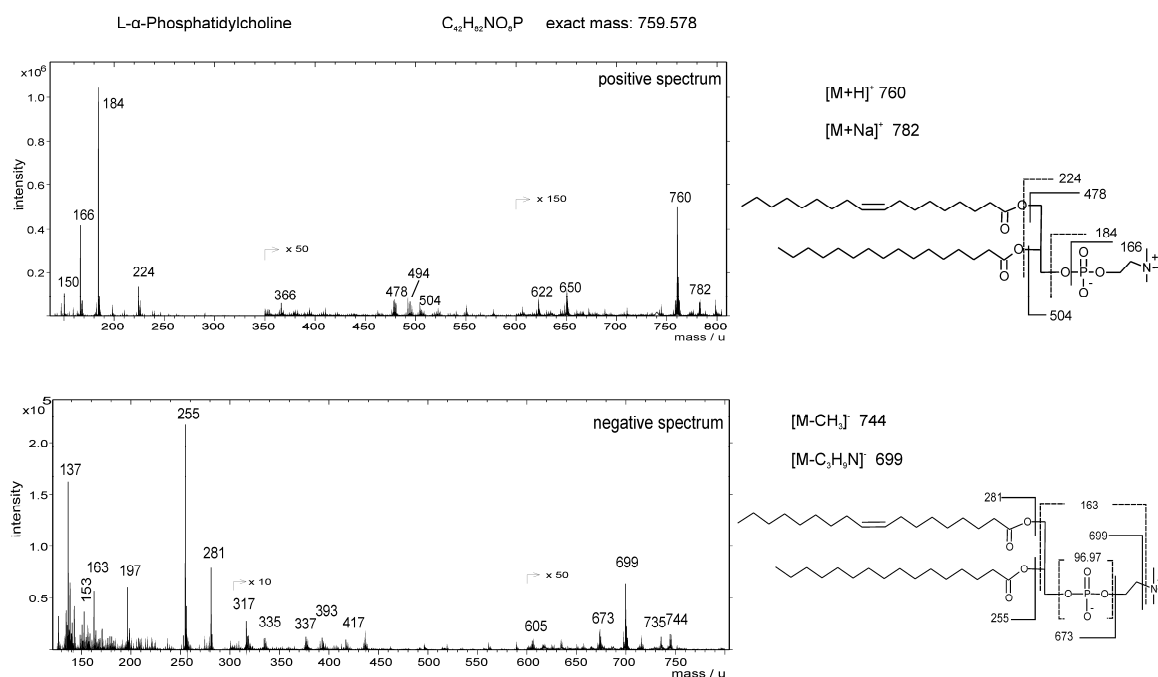


Fig. 4.3 Partial positive (top) and negative (bottom) ToF-SIMS spectra (m/z 130 - 800) of L- α -Phosphatidylcholine (GPCho). See text for a detailed discussion of the spectral patterns.

4.4.4 1,2-O-dialkyl-sn-glycerol-3-phosphatidylcholine (Diether-GPCho)

$C_{40}H_{85}NO_6P$; exact mass 705.60 Da

Source: bacteria (Rütters *et al.*, 2001)

Unlike ester bound GPCho, Diether-GPCho produces a prominent $[M+H]^+$ ion at m/z 706.75 (Fig. 4.4). Weak fragment ions occur in the positive spectrum at m/z 450.41, 464.44, 480.42, and 494.47, and may originate from the cleavage of one alkyl moiety at different positions close to the

respective ether bond (Fig. 4.4). A rather prominent doublet of fragment ions at m/z 224.15/226.13 can be plausibly explained by loss of both side chains.

In the positive spectrum of Diether-GPCho, the phosphocholine (PC) headgroup fragment is clearly identified at m/z 184.11 (Fig. 4.4). The observed formation of a strong PC fragment is in good agreement with the results obtained from the ester bound GPCho (Fig. 4.3) and other lipid studies that used the PC headgroup fragment at m/z 184.11 for GPCho identification in ToF-SIMS spectra of animal cells and tissues (Sjövall *et al.*, 2004; Börner *et al.*, 2007).

The negative spectrum of Diether-GPCho shows a very weak $[M-H]^-$ peak at m/z 704.57, whereas strong fragment ions occur at m/z 690.54, 645.47 and 619.47. These fragments most probably result from the molecule after loss of a methyl group from the trimethylamine moiety of the PC, $[M-CH_4]^-$, loss of the trimethylamine moiety, $[M-C_3H_9N]^-$, or loss of the entire PC headgroup, respectively. Notably, this pattern differs considerably from the counterpart lipid with an ethanolamine headgroup (Diether-GPEtn, see above) that shows $[M-H]^-$ as the most prominent peak in the molecular mass range. Fragment ions at 391.24, 403.24/405.25, and 448.29 may result from cleavage of the hexadecyl chain, with or without loss of C-1 of the glycerol, and the trimethylamine moiety of the PC headgroup.

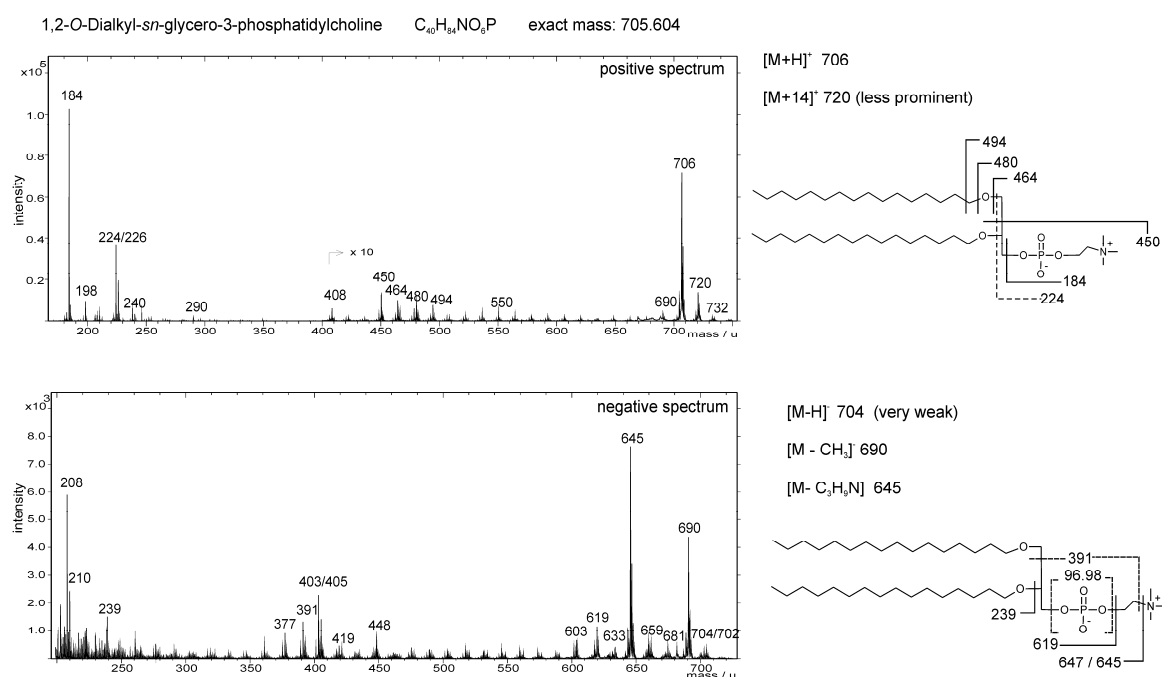


Fig. 4.4 Partial positive (top) and negative (bottom) ToF-SIMS spectra (m/z 170 - 750) of 1,2-O-dialkyl-*sn*-glycerol-3-phosphocholine (Diether-GPCho). See text for a detailed discussion of the spectral patterns.

4.4.5 L- α -Phosphatidylglycerol (GPGro) sodium salt

$C_{38}H_{74}O_{10}PNa$; exact mass 744.49 Da

Source: eukaryotes (Ostrowski *et al.*, 2005), bacteria (Zink *et al.*, 2003; Mazalla *et al.*, 2005)

GPGro sodium salt produces a prominent $[M+Na]^+$ ion at m/z 767.51 in the positive spectrum (Fig. 4.5). A protonated molecule $[M+H]^+$ was not observed. Due to the high abundance of sodium, the GPGro fragments including the headgroup are charged with an additional Na^+ ion, e.g. m/z 511.28 ($C_{22}H_{42}Na_2O_8P^+$) and 198.99 ($C_3H_6Na_2O_5P^+$). Prominent peaks at 124.94, 142.96 and 164.94 are putatively Na^+ -adducts.

Beside the weak deprotonated GPGro molecule $[M-H]^-$ at m/z 721.58, the ion at m/z 255.24 represents the $C_{16:0}$ fatty acid moiety. Peaks at m/z 153.02, m/z 171.04 and m/z 211.06 can be assigned as fragments involving the PG headgroup. The occurrence of a strong fragment at m/z 153.02 is in good agreement with observations reported for ESI/MS (Mazalla *et al.*, 2005). However, for this fragment Mazalla *et al.* (2005) proposed a precursor ion at m/z 227, which was not observed in the ToF-SIMS spectra. Ions at m/z 211.06, 171.04, and 153.02 suggest a preferred fragmentation within the glycerol backbone of the GPGro rather than a scission of the glycerol headgroup (Fig. 4.5), as observed for other ester-bound phospholipids (GPEtn, Fig. 4.1, and GPCho, Fig. 4.3).

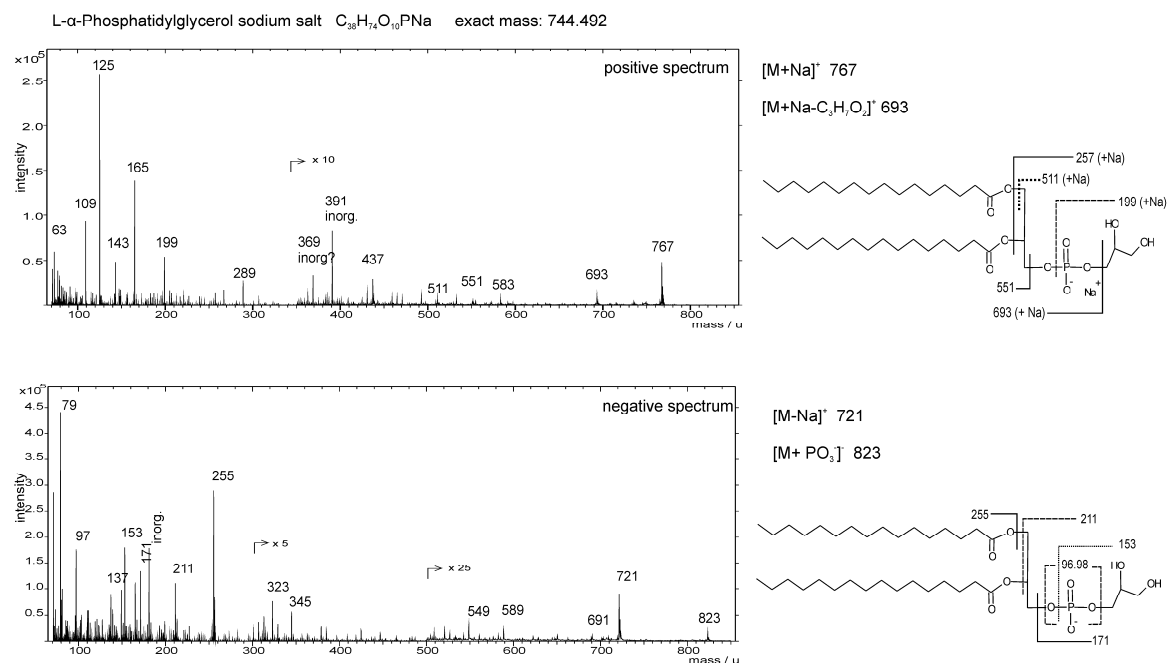


Fig. 4.5 Partial positive (top) and negative (bottom) ToF-SIMS spectra (m/z 50 - 850) of L- α -Phosphatidylglycerol sodium salt (GPGro). Peaks labeled 'inorg' are inorganic ions and do not belong to the compound spectrum. See text for a detailed discussion of the spectral patterns.

4.4.6 1-Palmitoyl-2-oleoyl-*sn*-glycerol (DG)

$C_{37}H_{70}O_5$; exact mass 594.52 Da

Source: eukaryotes (Malmberg *et al.*, 2007; Nygren and Malmberg, 2007), bacteria (Zink *et al.*, 2003)

DG produces very weak molecular ion peaks $[M+H]^+$ and $[M+Na]^+$ at m/z 595.58 and 617.53, but a prominent $[M-H_2O]^+$ at m/z 577.52 (Fig. 4.6). Distinct positive ions at m/z 339.31, and 313.28 represent lyso fragments of DG, whereas m/z 265.26, and 239.24 may originate from fatty acyl fragments.

In the negative spectrum of DG, a weak molecular ion $[M-H]^-$ is detected at m/z 593.49. Strong fatty acid fragments are observed at m/z 281.24 ($C_{18:1}$) and m/z 255.23 ($C_{16:0}$). It should be considered that triacylglycerides (TG) were reported to produce a prominent DG-fragment ($[M-H_2O]^+$) in the positive spectrum (Malmberg *et al.*, 2007, Nygren and Malmberg, 2007). Moreover, this fragment was clearly visible in the GPEtn spectrum (Fig. 4.1, Tab. 4.2) and was detectable, though in low abundance, in the spectra of other ester-bound lipids studied. Hence, when analysing natural samples, positive and negative spectra and ion images have to be checked carefully, whether the respective ions can be assigned confidently to DG, TG or phospholipids.

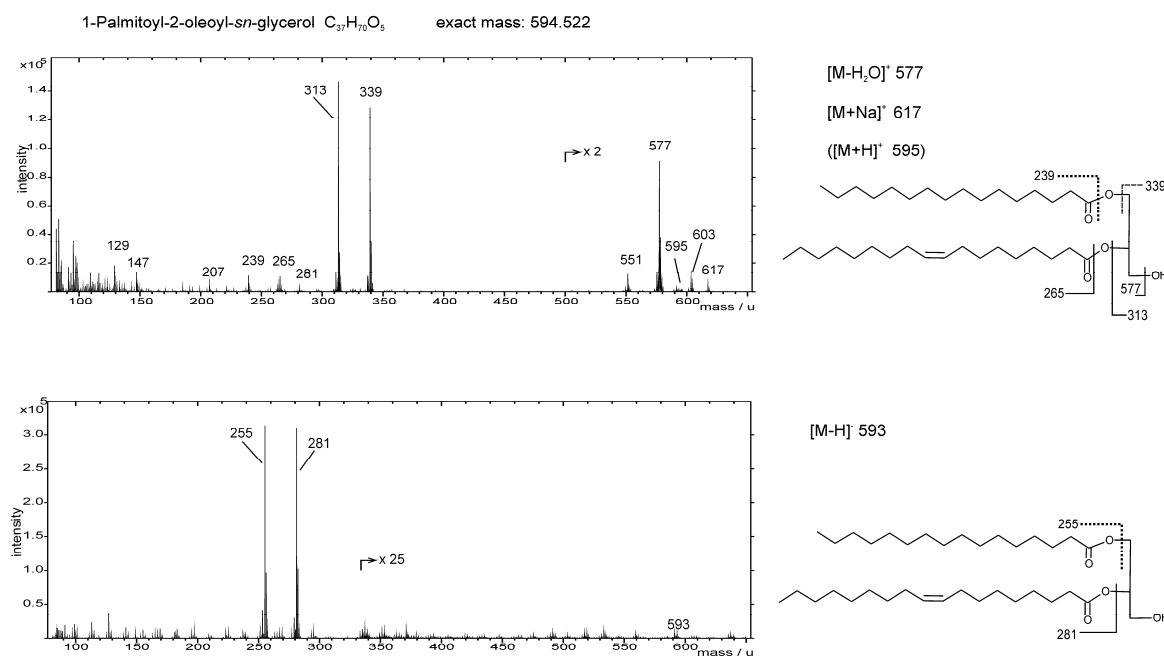


Fig. 4.6 Partial positive (top) and negative (bottom) ToF-SIMS spectra (m/z 80 - 650) of 1-palmitoyl-2-oleoyl-*sn*-glycerol (DG). See text for a detailed discussion of the spectral patterns.

4.4.7 1,2 Di-O-hexadecyl-*rac*-glycerol (Diether-DG)

$C_{37}H_{72}O_3$; exact mass 540.55 Da

Source: bacteria (Pancost *et al.*, 2001)

The partial positive spectrum of 1,2 di-O-hexadecyl-*rac*-glycerol (Diether-DG) shows the protonated molecular ion at m/z 541.63 as the base peak (Fig. 4.7). Loss of the functional group with, or without, the C-3 of glycerol produces additional, less intense peaks at m/z 522.59 and 508.57, respectively. Further ions at m/z 253.27, 267.29, 297.32 and 299.33 can be explained by fragmentations within the glycerol backbone whereas m/z 317.34 most likely results from loss of one of the hydrocarbon side chains $[M-C_{16}H_{31}]^+$ (Tab. 4.2).

In the negative spectrum, the deprotonated molecular ion at m/z 539.54 $[M-H]^-$ is very weak, as also observed for the isoprenoid glycerol diether archaeol (see below). The most abundant ion in the higher molecular weight range at m/z 239.18 most probably derives from the side chain $[C_{16}H_{31}O]^-$. This interpretation is supported by a corresponding, 56 Da heavier, fragment ion observed in the negative spectrum of archaeol at m/z 295.29 (see below), that obviously represents the functionalized C_{20} phytanyl side chain $[C_{20}H_{39}O]^-$.

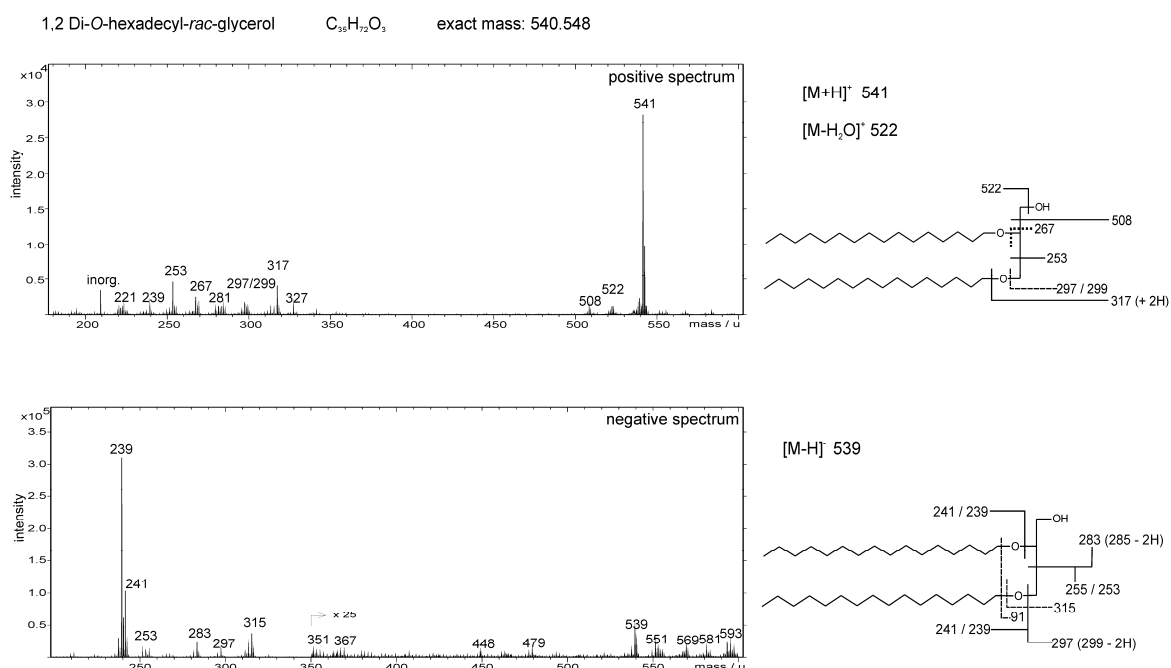


Fig. 4.7 Partial positive (top) and negative (bottom) ToF-SIMS spectra (m/z 180 - 600) of 1,2 Di-O-hexadecyl-*rac*-Glycerol (Diether-DG). See text for a detailed discussion of the spectral patterns. Peaks labeled 'inorg' are inorganic ions and do not belong to the compound spectrum.

Similar to the positive spectrum, minor ions at m/z 253.20, 255.20, 283.22 and 297.28 indicate fragmentations within the glycerol backbone of Diether-DG. Another significant ion at m/z 315.26

most likely results from loss of one of the hydrocarbon side chains $[M-C_{16}H_{33}]^-$, again corroborated by a 56 Da heavier corresponding fragment observed in the negative spectrum of archaeol (m/z 371.25). The presence of a glycerol moiety in the Diether-DG molecule is recognized by a prominent $C_3H_7O_3$ fragment ion peak at m/z 91.03 (not shown).

4.4.8 1,2-Di-O-phytanyl-*sn*-glycerol (archaeol)

$C_{43}H_{88}O_3$; exact mass 652.67 Da

Source: archaea (Pape *et al.*, 2005; Thiel *et al.*, 2007)

The positive spectrum of archaeol displays the protonated molecular ion $[M+H]^+$ at m/z 653.72 as the base peak (Fig. 4.8). The formation of a Na^+ adduct causes a further, yet minor, peak at m/z 675.68. Loss of the hydroxyl group (as H_2O) from the glycerol moiety is the most plausible explanation for a fragment peak at m/z 634.69 whereas cleavage of the adjacent methyl group results in a peak at m/z 620.65. The fragmentation scheme of archaeol producing ions at m/z 620.65, 373.39, 371.27, and 278.23 is similar to the peak formation in GC/MS (data not shown).

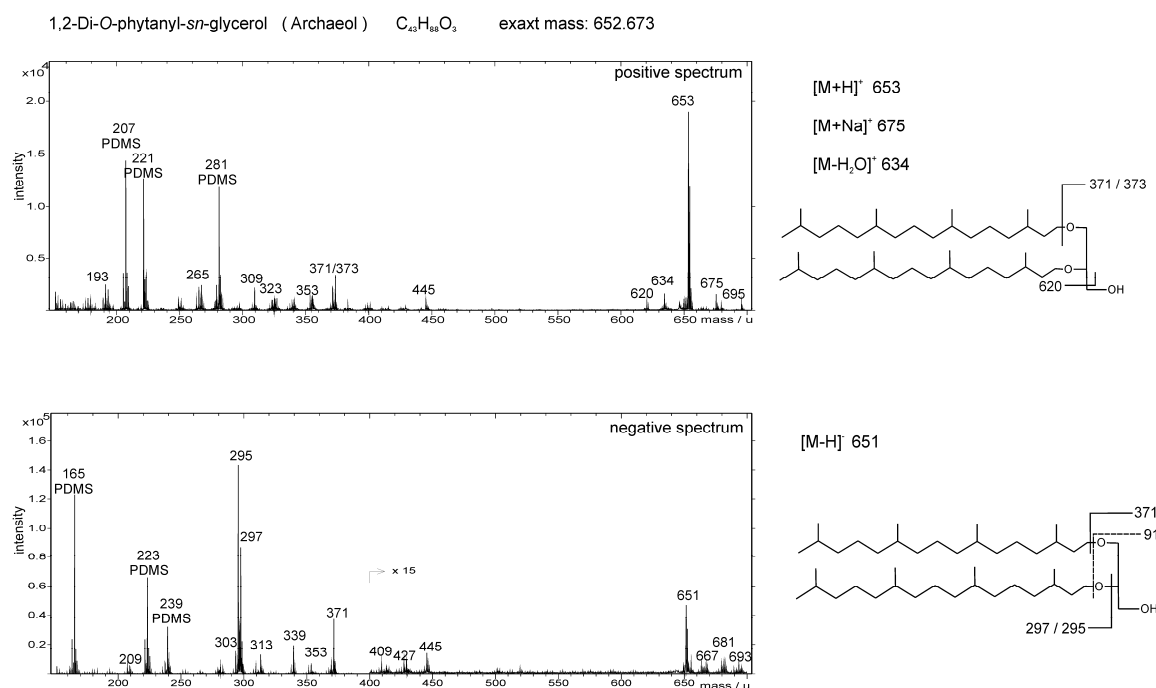


Fig. 4.8 Partial positive (top) and negative (bottom) ToF-SIMS spectra (m/z 140 - 700) of 1,2-Di-O-phytanyl-*sn*-glycerol (archaeol). See text for a detailed discussion of the spectral patterns. A peak at m/z 91.02 specifying the glycerol moiety is out of the displayed range of the negative spectrum. Peaks labeled with PDMS are polysiloxane-contaminants and do not belong to the compound spectrum.

In the negative ToF-SIMS spectrum, a deprotonated molecular ion $[M-H]^-$ at m/z 651.66 is clearly recognized, though much weaker than the $[M+H]^+$ observed in positive mode. Pronounced

fragment ions occur at m/z 371.37, 297.32, 295.29, 239.07, 223.02 and 165.04. Whereas m/z 371.37, 297.32 and 295.29 can be explained by cleavage of the ether bonds, the latter three are due to polydimethylsiloxane (PDMS) contamination. Additional characteristic fragments contributing to clear identification of archaeol as a glycerolipid are the glycerol fragments at m/z 91.02 $[C_3H_7O_3]^-$ and 57.04 $[C_3H_5O]^-$ in the negative spectrum (data not shown).

4.5 Archaeol in a methanotrophic microbial mat

Extracts of the Black Sea microbial mats typically contain archaeol among other lipids derived from methanotrophic archaea (Michaelis *et al.*, 2002, Blumenberg *et al.* 2004; Pape *et al.*, 2005). Based on these findings, our group recently used ToF-SIMS to study the distribution of archaeal lipids, including intact glycerol tetraethers, in microscopic cryosections of the microbial mats (Thiel *et al.*, 2007a,b). Figure 4.9a shows partial positive ToF-SIMS spectra of (i) the archaeol reference (as described above), (ii) a total organic extract of a microbial mat and (iii) a cryosection of the same mat. In fact, the molecular ion as $[M+Na]^+$ of archaeol (Fig. 4.9a) and some of its characteristic fragments such as m/z 371.27 and 373.37 were observed in the spectra of all samples (Fig. 4.9b). Unlike the reference lipid, the spectra of the extract and the cryosection show $[M+Na]^+$ at m/z 675.68, rather than $[M+H]^+$. Clearly, archaeol easily forms the $[M+Na]^+$ ion wherever sodium is present, either from biological material, sea water, or the mineral matrix of a natural sample. The same is evidently the case for the hydroxylated diether, hydroxyarchaeol (m/z 691.68), that co-occurs with archaeol in the Black Sea mats (Fig. 4.9a; see also e.g. Blumenberg *et al.*, 2004). The strong tendency of these isoprenyl diethers, to form sodium adduct ions, is in full agreement with previous data (Thiel *et al.*, 2007b), thus pointing at the reproducibility of the mass spectral patterns characterizing these important lipid biomarkers.

Although the $[M+H]^+$ and $[M-H]^-$ were not detected in the spectra of the organic extract and the microscopic section of the Black Sea microbial mat, characteristic archaeol fragments at m/z 371.27 and 373.39 in the positive spectra and at m/z 295.29 and 297.32 in the negative spectra (described in Fig. 4.8) were clearly present (Fig. 4.9b). Thus, the co-occurrence of the $[M+Na]^+$ ion in positive mode and these fragment peaks in negative mode corroborate the identification of archaeol in the environmental sample. Microscopic, video and total ion images of the microscopic section (Fig. 4.9c: I, II, III) allow the accurate assignment of the area analyzed. Figure 4.9c (IV, V, VI) shows positive ion images obtained from the microscopic section, proving the co-localization of the fragment ions at m/z 371.27, 373.39 with the $[M+Na]^+$ ion of archaeol.

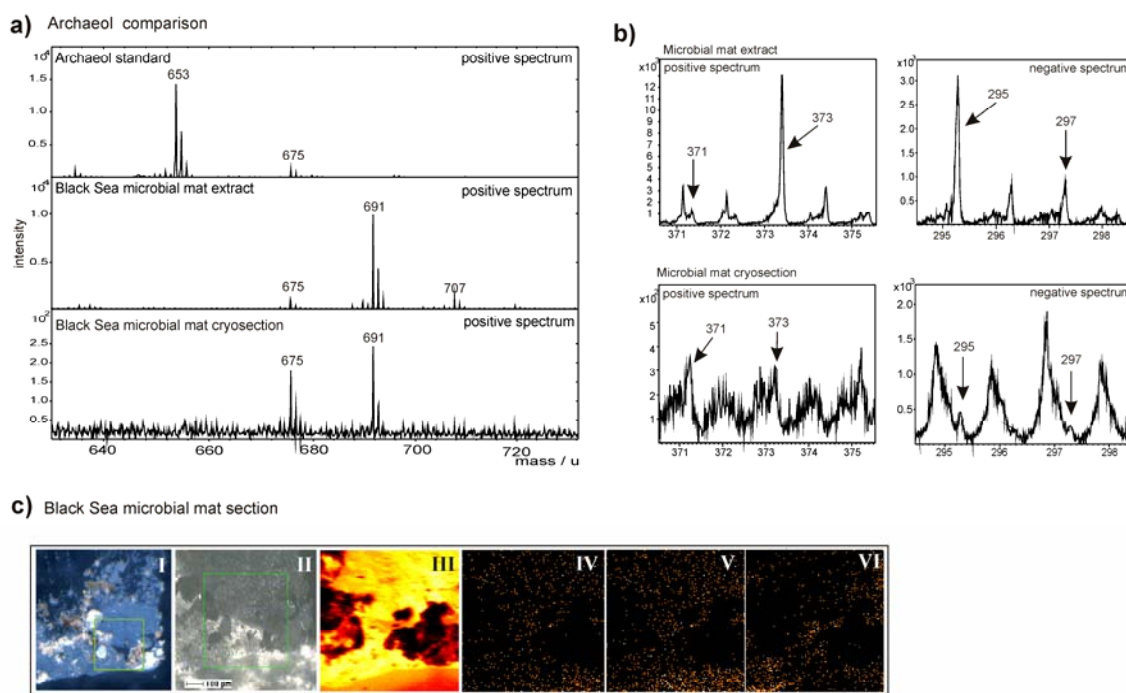


Fig. 4.9. a) Partial positive ToF-SIMS spectra (m/z 630 - 730) showing molecular ions ($[M+H]^+$ and $[M+Na]^+$) of archaeol from the standard, in a complex organic extract of the Black Sea microbial mat, and on a microscopic cryosection of the same microbial mat. The peaks at 691.67 and 707.65 Da in the environmental samples represent the $[M+Na]^+$ of hydroxyarchaeol and dihydroxyarchaeol, respectively. b) Characteristic archaeol fragments observed in the partial positive and negative spectra of the organic extract and the microbial mat cryosection. c) Microscopic and Ion images of the Black Sea microbial mat section: under reflected light (I), built in video camera in the ToF-SIMS (II), total ion image (III), distribution of m/z 371.27 and m/z 373.39 (IV), distribution of archaeol (V), and distribution of hydroxyarchaeol (VI).

4.6 Diglycerides and phosphatidylglycerol in a *Gallionella*-dominated microbial mat

Generally, analyses of environmental samples of iron-oxidizing *Gallionella* mats is hampered by obscuring effects caused by the iron oxide precipitates that commonly make up more than 90 wt% of the dry sample. It was nonetheless possible to reconstruct partially the lipid pattern of the microbial system using spectra and the imaging capability of ToF-SIMS (Fig. 4.10). In the positive spectrum ions at m/z 549.50, 577.54, 603.55, 639.47, and 643.49 are in agreement with the $[M-H_2O]^+$ ions of diglyceride lipids namely $C_{32:1}$, $C_{34:1}$, $C_{36:2}$, $C_{40:12}$ and $C_{40:10}$. This assignment was corroborated through the fragmentation scheme of the DG reference (Fig. 4.6) including occurrence of a glycerol derived fragment at m/z 91.02 $[C_3H_7O]^+$ and the corresponding fatty acyl moieties in the negative spectrum. Here, fragment ions at m/z 253.19 and 255.21 correspond to $C_{16:1}$ and $C_{16:0}$ moieties, whereas m/z 279.20 and 281.215 arise from $C_{18:2}$ and $C_{18:1}$ moieties respectively. Additional ions at m/z 299.18, 301.19, and 303.21, are in agreement with hexaenoic, pentaenoic and tetraenoic C_{20} fatty acids, respectively. These fatty acids were also

observed in GC/MS analyses of *Gallionella* dominated mat bulk extracts (data not shown). In the phospholipid molecular ion range in the negative spectrum, significant peaks at m/z 761.55, 763.56 and 789.57 were detected. A distinct ion at m/z 171.08 (negative spectrum) corresponding to the GPGro headgroup is also present. The high mass peaks may therefore be related to the phosphatidylglycerols (GPGro), namely $C_{35:1}$, $C_{35:0}$ and $C_{37:1}$, thus implying the presence of odd numbered fatty acyl moieties (Fig. 4.10b).

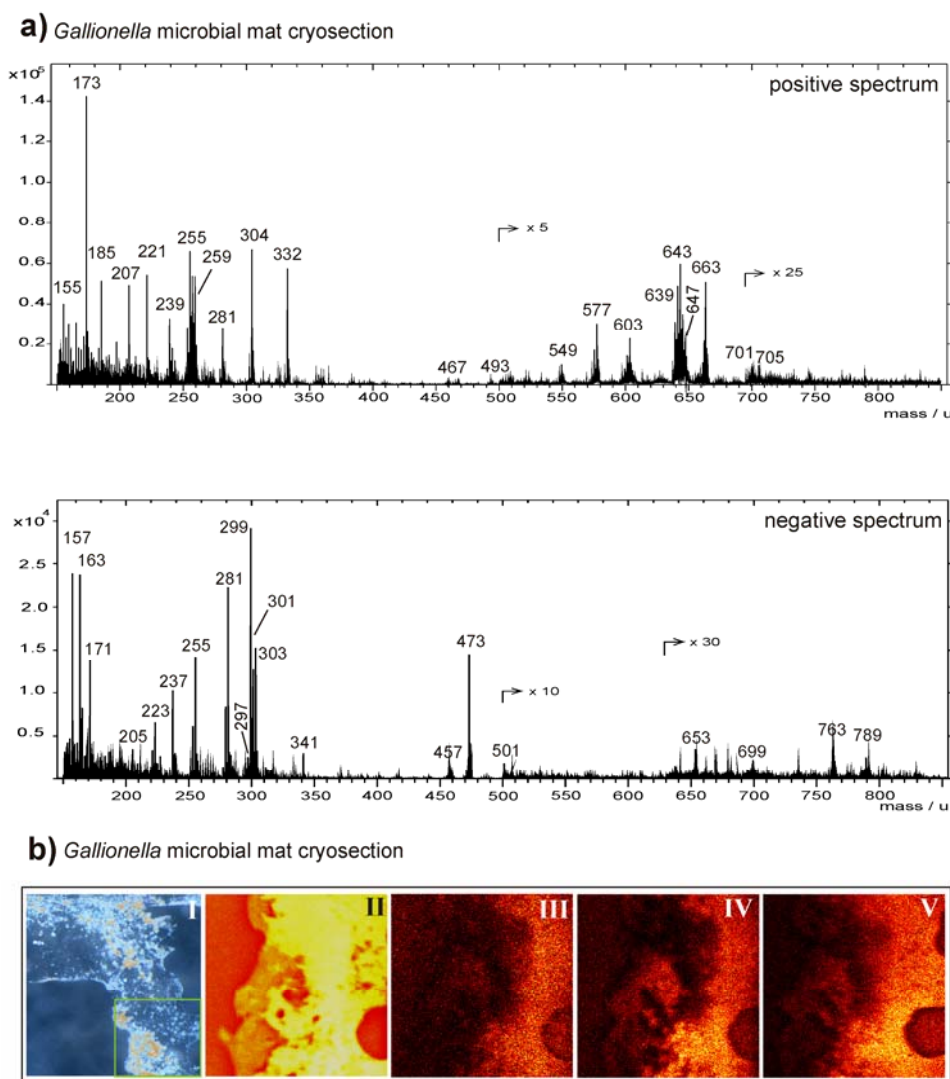


Fig. 4.10. a) Partial positive and negative ToF-SIMS spectra (m/z 150 - 850) of a microscopic section obtained from a *Gallionella*-rich microbial mat from the tunnel of Äspö. Peaks at m/z 207.04, 221.12 and 281.08 in the positive spectrum belong to PDMS contaminants, and peaks at m/z 647.47 and 663.47 in the positive spectrum and at m/z 473.28 in the negative spectrum most likely derive from contamination by the polymer additive Irgafos 168. The peaks at m/z 341.09 and 163.05 originate from carbohydrate fragments of the embedding agent. See text for a detailed discussion of the spectral patterns. b) Microscopic and Ion images of the *Gallionella* microbial mat section: under reflected light (I), total ion image (II), the distribution of the PG headgroup (III), fatty acids (IV), and diglycerides (V).

Although the GPGro headgroup was co-localized with C₁₇ and C₁₉ fatty acids, this relation remains uncertain, as the latter were observed only in minor abundance on the cryosections. Additional prominent organic ions such as m/z 332.33, 304.29 and 173.08 in the positive spectrum and m/z 237.06, 157.11 in the negative spectrum still remain to be identified.

4.7 Conclusions

Our study showed that ToF-SIMS with a Bi cluster ion source is capable of revealing characteristic mass spectral features of each of the eight glycerolipids investigated. However, a robust assignment of the target compounds in the total ToF-SIMS spectrum of environmental samples should not only rely on the presence of molecular ions (including adducts), but also on specific headgroup fragments and other structural moieties, such as functional groups and alkyl chains. The establishment of characteristic mass spectral features for a range of glycerolipids further expands the range of complex lipids that can be analyzed using ToF-SIMS and provides the crucial basis for the identification of these and related biomarkers in environmental materials. Nevertheless, the question whether the patterns reported here represent general rules for the interpretation of ToF-SIMS spectra of environmental samples still has to be corroborated by further studies.

A major advantage of ToF-SIMS is its capacity to provide simultaneous detection, identification and microscopic localisation (mapping) of inorganic and organic compounds without the need for bulk sample extraction or labelling. Unlike the more traditional techniques for lipid analysis such as GC/MS and LC/MS, ToF-SIMS can be used to study compound distributions within microscopic areas of interest on a sample surface. The imaging capacity of ToF-SIMS can also be used to support the identification of organic compounds and their association with inorganic species through the co-localisation of key ions on the area of interest. As the analytical procedure is virtually non-destructive, subsequent examinations, e.g. microscopy, may allow a further characterization of the sample in question.

The capability of visualizing lipid distributions on a micrometer scale makes ToF-SIMS a promising tool for a wide range of geological, ecological, biological, and medical applications. However, published ToF-SIMS spectra of lipid biomarkers as yet exist for a still limited number of relevant compounds, and little research has been conducted on the effects of substrates and compound concentrations on the quality of ToF-SIMS spectra. Furthermore, structural assignments using the current single-stage TOF analyzers are still not satisfactory, and isomers can not be easily differentiated. Moreover, SIMS is very susceptible to surface contamination. Further efforts are therefore essential to minimise, or overcome these limitations and further increase the utility of ToF-SIMS for molecular imaging in bio- and geosciences. Such efforts may

include the implementation of tandem mass spectrometry, the improvement of preparation techniques particularly for environmental samples, the establishment of further reference data from pure substances, and the validation of the ToF-SIMS results against established knowledge and methods.

Acknowledgements:

We are grateful to Michael Wiedenbeck and Jan Toporski for their constructive reviews that greatly helped to improve the original manuscript. The authors acknowledge Jakob Malm (SP Borås) for constructive discussions and help in the lab. We are also grateful to Walter Michaelis, Richard Seifert (University of Hamburg) and Joachim Reitner (University of Göttingen), who initiated and coordinated the joint projects through which the microbial mats studied here were retrieved. Our study received financial support from the German Research Foundation (DFG) through grants Th 713/4 and FOR 571, the University of Hamburg (joint project BEBOP, R/V Poseidon cruise PO 317/2), and the Swedish Governmental Agency for Innovation Systems (VINNOVA). This is publication no. 46 of the DFG Research Unit FOR 571 'Geobiology of Organo- and Biofilms'.

References

- Belu AM, Graham DJ, Castner DG (2003) Time-of-flight secondary ion mass spectrometry: techniques and applications for the characterization of biomaterial surfaces. *Biomaterials*, **24**, 3635-3653.
- Benninghoven A (1994) Chemical Analysis of Inorganic and Organic Surfaces and Thin Films by Static Time-of-Flight Secondary Ion Mass Spectrometry (ToF-SIMS). *Angewandte Chemie International Edition in English*, **33**, 1023-1043.
- Blumenberg M, Seifert R, Reitner J, Pape T, Michaelis W (2004) Membrane lipid patterns typify distinct anaerobic methanotrophic consortia. *Proceedings of the National Academy of Sciences of the United States of America*, **101**, 11111-11116.
- Börner K, Malmber P, Månsson J-E, Nygren H (2007) Molecular imaging of lipids in cells and tissues. *Mass Spectrometry*, **260**, 128 – 136.
- Hagenhoff B (2000) High resolution surface analysis by TOF-SIMS. *Mikrochimica Acta*, **132**, 259-271.
- Kollmer F (2004) Cluster primary ion bombardment of organic materials. *Applied Surface Science*, 231-2, 153-158.
- Malmberg P, Nygren H, Richter K, Chen Y, Dangardt F, Friberg P, Magnusson Y (2007) Imaging of lipids in human adipose tissue by cluster ion ToF-SIMS. *Microscopy Research and Technique*, **70**, 828-835.
- Mazalla N, Molinet J, Syakti AD, Dodi A, Bertrand J-C, Doumenq P (2005). Use of electrospray ionization mass spectrometry for profiling of crude oil effects on the phospholipid molecular species of two marine bacteria. *Rapid Communications in Mass Spectrometry*, **19**, 3579-3558.
- Michaelis W, Seifert R, Nauhaus K, Treude T, Thiel V, Blumenberg M, Knittel K, Gieseke A, Peterknecht K, Pape T, Boetius A, Amann R, Jørgensen BB, Widdel F, Peckmann J, Pimenov NV, Gulin MB (2002) Microbial reefs in the Black Sea fueled by anaerobic oxidation of methane. *Science*, **297**, 1013-1015.
- Nygren H, Borner K, Hagenhoff B, Malmberg P, Mansson J-E (2005) Localization of cholesterol phosphocholine and galactosylceramide in rat cerebellar cortex with imaging TOF-SIMS equipped with a bismuth cluster ion source. *Biochimica et Biophysica Acta (BBA) - Molecular and Cell Biology of Lipids*, **1737**, 102-110.
- Nygren H, Malmberg P (2007). High resolution imaging by organic secondary ion mass spectrometry. *Trends in Biotechnology*, **25**, 499-504.
- Ostrowski SG, Bell CTV, Winograd N, Ewing AG (2004) Mass spectrometric imaging of highly curved membranes during Tetrahymena mating. *Science*, **305**, 71-73.
- Ostrowski SG, Szakal C, Kozole J, Roddy TP, Xu J, Ewing AG, Winograd N (2005) Secondary Ion MS Imaging of Lipids in Picoliter Vials with a Buckminsterfullerene Ion Source. *Analytical Chemistry*, **77**, 6190-6196.
- Pacholski ML, Winograd N (1999) Imaging with mass spectrometry. *Chemical Reviews*, **99**, 2977-3005.
- Pape T, Blumenberg M, Seifert R, Egorov VN, Gulin SB, Michaelis W (2005) Lipid geochemistry of methane-seep-related Black Sea carbonates. *Palaeogeography, Palaeoclimatology, Palaeoecology*, **227**, 31-47.
- Pancost RD, Bouloubassi I, Aloisi G, Sinninghe Damsté JS, the Medinaut Shipboard Scientific Party (2001). Three series of non-isoprenoidal dialkyl glycerol diethers in cold-seep carbonate crusts. *Organic Geochemistry*. **32**, 695-707.

- Pedersen K (1997) Microbial life in deep granitic rock. *FEMS Microbiology Reviews*, **20**, 399–414.
- Prinz C, Hook F, Malm J, Sjövall P (2007) Structural effects in the analysis of supported lipid bilayers by time-of-flight secondary ion mass spectrometry. *Langmuir*, **23**, 8035-8041.
- Rütters H, Sass H, Cypionka H, Rullkötter (2001) Monoalkylether phospholipids in the sulfate reducing bacteria *Desulfosarcina variabilis* and *Desulforhabdus* sp. nov. *Archives of Microbiology*, **176**, 435-442.
- Siljeström S, Hode T, Lausmaa J, Sjövall P, Toporski J, Thiel V (2009) Detection of organic biomarkers in crude oils using ToF-SIMS. *Organic Geochemistry*, **40**, 1, 135-143.
- Sjövall P, Lausmaa J, Johansson B (2004) Mass spectrometric imaging of lipids in brain tissue. *Analytical Chemistry*, **76**, 4271-4278.
- Sjövall P, Thiel V, Siljeström S, Heim C, Hode T, Lausmaa J, (2008) Organic geochemical microanalysis by time-of-flight secondary ion mass spectrometry (ToF-SIMS). *Geostandards and Geoanalytical Research*, **32**, 267-277.
- Sostarecz AG, Cannon DM jr, McQuaw CM, Sun S, Ewing AG, Winograd N (2004) Influence of molecular environment on the analysis of phospholipids by time-of-flight secondary ion mass spectrometry. *Langmuir*, **20**, 4926-4932.
- Steele A, Toporski JKW, Avci R, Guidry S, McKay DS (2001) Time of flight secondary ion mass spectrometry (ToF-SIMS) of a number of hopanoids. *Organic Geochemistry*, **32**, 905-911.
- Thiel V, Heim C, Arp G, Hahmann U, Sjövall P, Lausmaa J (2007a) Biomarkers at the microscopic range: ToF-SIMS molecular imaging of archaea-derived lipids in a microbial mat. *Geobiology*, **5**, 413-421.
- Thiel V, Toporski J, Schumann G, Sjövall P, Lausmaa J (2007b) Analysis of archaeal core ether lipids using time of flight-secondary ion mass spectrometry (ToF-SIMS): Exploring a new prospect for the study of biomarkers in geobiology. *Geobiology*, **5**, 75-83.
- Toporski J, Steele A (2004) Characterization of purified biomarker compounds using time of flight-secondary ion mass spectrometry (ToF-SIMS). *Organic Geochemistry*, **35**, 793-811.
- Toporski J, Steele A, Westall F, Avci R, Martill M, McKay DS (2002) Morphological and spectral investigation of exceptionally well preserved bacterial biofilms from the Oligocene Enspel formation, Germany. *Geochimica et Cosmochimica Acta*, **66**, 1773-1791.
- Touboul D, Halgand F, Brunelle A, Kersting R, Tallarek E, Hagenhoff B, Laprévotte O (2004) Tissue molecular ion imaging by gold cluster ion bombardment. *Analytical Chemistry*, **76**, 1550-1559.
- Touboul D, Kollmer F, Niehuis E, Brunelle A, Laprévotte O (2005) Improvement of biological time-of-flight-secondary ion mass spectrometry imaging with a bismuth cluster ion source. *Journal of the American Society for Mass Spectrometry*, **16**, 1608-1618.
- Vickerman JC, Briggs D (2001) ToF-SIMS: Surface analysis by mass spectrometry. IM Publications and SurfaceSpectra Limited (Charlton, Chichester, West Sussex, UK), 789pp.
- Zink K-G, Wilkes H, Disko U, Elvert M, Horsfield B (2003) Intact phospholipids – microbial “life markers” in marine deep subsurface sediments. *Organic Geochemistry*, **34**, 755-769.

5

Trace and rare earth element accumulation and fractionation in microbial iron oxyhydroxides

Christine Heim, Klaus Simon, Nadia-Valérie Quéric, Joachim Reitner, Volker Thiel

Geochimica et Cosmochimica Acta, in revision

5.1 Abstract

Microbial iron oxyhydroxides are common deposits in natural waters, recent sediments and mine drainage systems. Along with these minerals, trace and rare earth elements (TREE) are being accumulated within the mineralizing microbial mats. TREE patterns are widely used to characterize minerals and rocks, and to elucidate their evolution and origin. However, whether and which characteristic TREE signatures allow to distinguish between a biological and an inorganic origin of these iron minerals is still not well understood. Here we report on long-term flow reactor studies performed in the Tunnel of Äspö (Äspö Hard Rock Laboratory, Sweden) to investigate the development of microbial mats dominated by the iron-oxidizing bacterium *Gallionella ferruginea*. The feeder fluids of the flow reactors were tapped at 183m and 290m below sea-level from two brackish, but chemically differing aquifers within the surrounding, ~ 1.8 Ga old, granodioritic rocks. The experiments allowed to investigate the accumulation and fractionation of TREE under controlled conditions of the deep continental biosphere, and enabled us to assess potential biosignatures evolving within the microbial iron oxyhydroxides. After two, respectively nine months, the REE+Y content in the microbial iron oxyhydroxides was found to be 10^4 and 10^6 fold enriched compared to the feeder fluids. Concentrations of Be, Y, Zn, Zr, Hf, W, Th, Pb, and U were 10^3 - to 10^5 -fold higher than in the feeder fluids. These enormous enrichments of TREE highlight the efficiency of *G. ferruginea* mats in removing metals from the supplying water, and point to the potential utility of these microbial systems for the recycling of precious trace metals and radionuclides. Except for a hydrothermally induced Eu anomaly, the normalized REE+Y patterns of the microbial iron oxyhydroxides were found to be very similar to published REE+Y distribution patterns of Archaean Banded Iron Formations (BIF). Furthermore, these patterns differ significantly from those of chemically precipitated iron oxyhydroxides. These findings further corroborate the hypothesis that iron-oxidizing microorganisms such as *G. ferruginea* were involved in the formation of BIF, and highlight the utility of TREE patterns and distinctive element fractionations as 'inorganic biosignatures' for palaeoenvironmental studies.

5.2 Introduction

Structure, properties and formation of iron oxyhydroxides have attracted the attention of many researchers during the last decades, due to their ubiquitous occurrence in natural settings and anthropogenic biotopes, as well as their properties as an efficient sorbent for (heavy) metals, with a resulting potential for technical applications (Stumm and Morgan, 1996; Ferris *et al.*, 2000; Cornell and Schwertmann, 2004; Michel *et al.*, 2007).

In natural environments, iron oxyhydroxide precipitates typically originate from the chemically or biologically controlled oxidation of Fe^{2+} to Fe^{3+} , whereas the oxidation rate strongly depends on the redox conditions and the pH of the aqueous solution (Stumm and Morgan, 1996; Fortin *et al.*, 1997).

Microbial precipitation of iron oxyhydroxides, as well as microbial mineral formation in general, can commonly be specified as 'biologically induced mineralization' (Frankel and Bazylinsky, 2003). Three modes of biologically induced mineralization occur. (i) Mineral nucleation and growth are extracellular processes triggered by the metabolic activity of the microorganisms. Thereby, local oversaturation is induced by the formation of reactive ions or ligands, as it is also the case in the microbial iron oxidation. (ii) Indirect mineral precipitation can take place due to gradual changes in the chemical equilibrium of the surrounding solution which may also be supported by the release of metabolic products from the microbial community (Thompson and Ferris, 1990; Fortin and Beveridge, 1997; Fortin *et al.*, 1997; Southam, 2000). (iii) Passive mineralization can be induced by non-living organic matter such as cell debris or extracellular polymeric substances (EPS). Thereby, exposed negatively charged surfaces act as adsorption and nucleation sites for metal cations (Urrutia and Beveridge, 1993; Anderson and Pedersen, 2003; Ercole *et al.*, 2007; Chan *et al.*, 2009).

Whereas these biologically induced mineralization pathways can be well specified in theory, they are often difficult to recognize and distinguish in natural samples. Nevertheless, such biogenic processes may produce minerals different from their inorganically formed varieties in shape, size, crystallinity, isotopic and trace element composition (Konhauser, 1997; Ferris *et al.*, 1999, 2000; Weiner and Dove, 2003; Bazylinski *et al.*, 2007; Haferburg and Kothe, 2007; Takahashi *et al.*, 2007). In studies of contemporary mineral deposits, such biosignatures may be specified and utilized for the identification of related biological processes in geological samples throughout the Earth history. Massive deposition of banded iron formations (BIF), for instance, occurred at 2.7-2.4 Ga, after molecular oxygen started to become available, due to the increasing photosynthetic activity of cyanobacteria (Anbar *et al.*, 2007). The mechanisms of BIF formation are widely discussed and scenarios involving abiotic and biotic processes have been proposed (e.g. Morris, 1983; Bau and Möller, 1993; Kraepel *et al.*, 2003; Kappler *et al.*, 2005). In 'biological' models iron

oxidizing microorganisms play a central role (Konhauser *et al.*, 2002). Therefore, the study of microbial iron oxyhydroxides and the bacteria involved in iron oxidation may help to better understand the deposition of BIF (Konhauser *et al.*, 2002; Kappler *et al.*, 2005).

Here we report on a flow reactor experiment investigating the development of iron-oxidizing microbial mats, in the Äspö HRL. We particularly aimed to explore TREE accumulation and fractionation patterns in these systems for their potential as biosignatures. The Tunnel of Äspö (Äspö Hard Rock Laboratory, Fig. 5.1a, b) offers a unique window into the deep continental biosphere, where the growth of different microbial consortia strongly depends on the flow, oxygen content and the chemical composition of the feeder fluids employed.

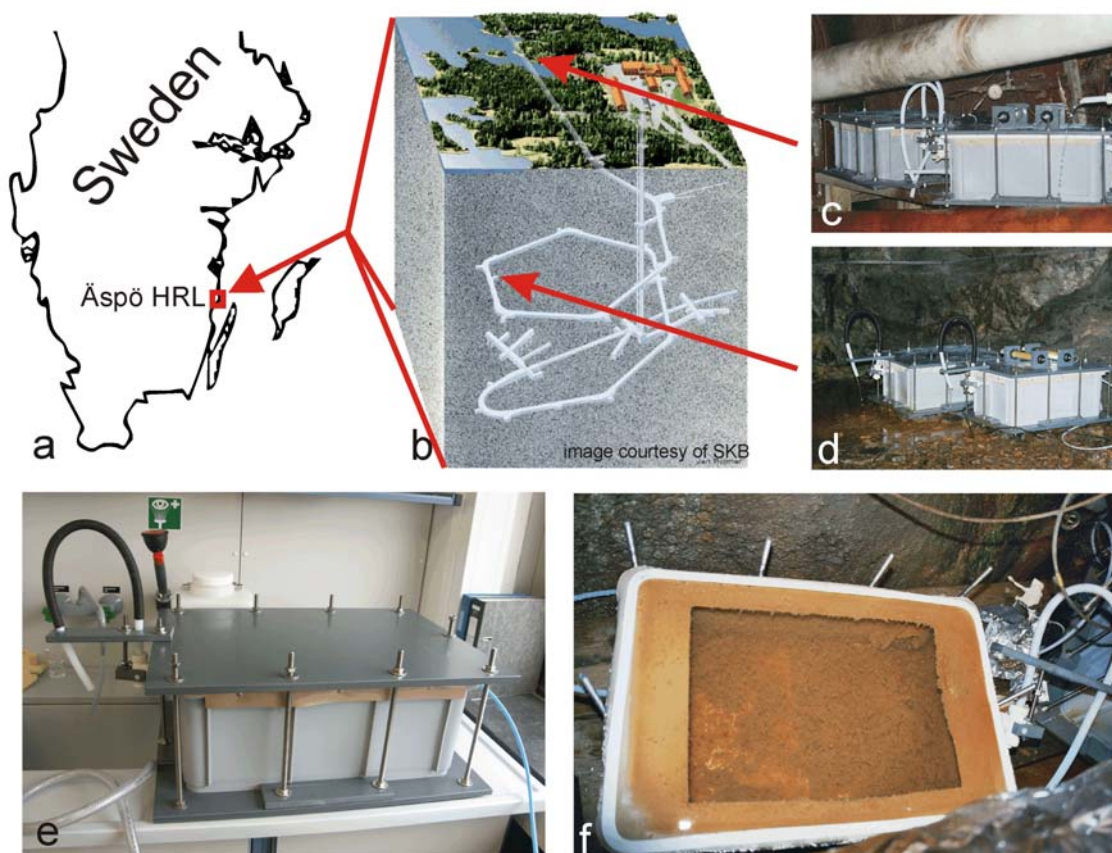


Fig. 5.1 (a) Location of the Äspö Hard Rock Laboratory (HRL); (b) 3D sketch of the HRL tunnel system beneath the island of Äspö; arrows indicate the location of the flow reactor experiments at (c) site 1327B and (d) site 2156B; (e) flow reactor, as used in this study, prior to installation; (f) flow reactor after opening, showing mineralized microbial mat development after two months.

Under appropriate conditions, the resulting microbial mats are dominated by *Gallionella ferruginea*, an auto- and mixotrophic, microaerophilic, iron-oxidizing bacterium that uses Fe(II) as an electron donor and CO₂ or carbohydrates as carbon source (Hallbeck and Pedersen, 1991; Hallbeck *et al.*, 1993). *G. ferruginea* was first described by Ehrenberg (1836) who characterized its

twisted extracellular stalk as a unique morphological trait. According to Hallbeck *et al.*, (1993), *G. ferruginea* lives at circum neutral pH and at temperatures between 5-25°C. The production of the stalks, which consists of as yet unknown extracellular polymeric substances (EPS), seems to be limited to pH values above 6 (Hallbeck *et al.*, 1993). Directing the iron oxidation to the stalks, at distance from the cells, probably protects *G. ferruginea* against oxygen radicals formed during the iron metabolism (Hallbeck and Pedersen, 1995; Hallberg and Ferris, 2004). The stalk length seems positively correlated with the amount of iron oxyhydroxides precipitated and the co-precipitation of lanthanides, Th and U (Anderson and Pedersen, 2003). Here, we demonstrate that the growth of *G. ferruginea* is accompanied by a massive enrichment of TREE in the iron oxidizing microbial systems, together with the establishment of distinctive fractionation patterns. The patterns observed were compared with those reported for ancient Banded Iron Formations (BIF) deposits indicate that iron oxidizing microorganisms may have contributed to the formation of BIF.

5.3 Materials and Methods

5.3.1 Flow reactors

A flow reactor experiment was designed to investigate microbial iron biomineralization and TREE accumulation under controlled conditions that should as far as possible mimic biomineral formation within any local natural biofilm. Dark, air-tight flow reactors (non-pressurized) were employed to simulate the environmental conditions similar to cavities within the surrounding granodioritic host rock (Figs. 5.1 b-f). Only chemically inert materials such as polytetrafluoroethylene (PTFE, Teflon®), PTFE – fibre glass, fluorinated ethylene propylene (FEP) and special PTFE – foam were used as construction materials to avoid biological contamination from the surrounding environment and chemical contamination from glass and plastic ware. The flow reactor systems and connection tubings were thoroughly sterilized with ethanol (70%, overnight) before underground installation.

Reference geochemical sampling of feeder fluids available at the different tunnel levels was performed prior to installation of the flow reactors to select suitable installation sites. According to the results, and considering published data (Ferris *et al.*, 1999; Laaksoharju *et al.*, 1999; SICADA database), the flow reactor sets were connected to two chemically different aquifers at 183m bsl (site 1327B) and 290m below sea level (site 2156B) (Fig. 5.1 b-d). The shallower aquifer shows a major Baltic Sea water influence, whereas the deeper aquifer contains a mixture of recent and ancient Baltic Sea water, and glacial melt water. Both aquifers contained the iron oxidizing bacterium *G. ferruginea*.

During the experiment the reactors were kept strictly unaffected, except for sampling of reactor water and microbial mats after two months, and nine months, respectively. The closed reactors were regularly controlled for maintenance/tightness, and in- and outflowing waters were routinely sampled and analyzed for physicochemical fluctuations.

5.3.2 Chemical Analysis

Oxygen was measured using the Winkler method (Hansen 1999). Anion concentrations, measured by titration and ion chromatography, conductivity, pH and spectrophotometrical $Fe_{total}/Fe(II)$ data were analysed immediately after sampling by the certified chemistry lab of the Swedish Nuclear Fuel and Waste Management Co (SKB) at the Äspö HRL. TREE were analysed using Inductive Coupled Plasma Mass Spectrometry (ICP-MS; Perkin Elmer SCIEX Elan DRCII) and Optical Emission Spectroscopy (ICP-OES; PerkinElmer Optima 3300 DV). For sample conservation and TREE measurements, concentrated, distilled HNO_3 was added to 50ml water samples (final concentration 2% HNO_3). After sampling, the microbial mats were frozen, transported in dry ice, and stored at $-20^{\circ}C$ until analysis. In order to quantify the amounts of REE in the mineral precipitates, 4ml of H_2O_2 and 2ml of concentrated, distilled HNO_3 were added to 500mg of lyophilized sample. The resulting solutions containing the dissolved mineral precipitates were diluted in 50ml of deionised water (final concentration 4% HNO_3). These solutions, a reference sample (blank) containing all chemicals used and the water samples were spiked with internal Ge, Rh, In and Re standards and analysed by ICP-MS and ICP-OES. As a reference, Fe_{total} was also measured by ICP-OES and was in good agreement with the spectrophotometrical data (1% deviation). Carbon (C_{tot}) and nitrogen analyses were performed with a CNS Elemental Analyzer (HEKAtech Euro EA) and C_{tot} and organic carbon (C_{org}) with a Leco RC 412 multiphase carbon analyzer.

5.3.3 Scanning Electron Microscopy and Energy dispersive X-ray Analysis (SEM-EDX)

For SEM-EDX analysis, samples were fixed in 2% glutardialdehyde immediately after sampling and stored at $4^{\circ}C$ until analysis. Prior to measurement, the samples were dehydrated in rising ethanol concentration (15% to 99%), mounted on SEM sample holders and sputtered with Au-Pd (7.3nm for 120sec). Samples were analysed using a field

emission SEM (LEO 1530 Gemini) combined with an INCA X-act EDX (Oxford Instruments).

5.4 Results

5.4.1 Feeder fluid chemistry

Basic water chemistry data for the feeder fluids are given in Table 1. Replicate analyses (data not shown) revealed that their chemical properties remained virtually stable over the duration of the experiments (STD below 10%). Both feeder fluids contained brackish waters with salinities of 5.8‰ at site 1327B (183m bsl), and 7‰ at site 2156B (290m bsl). Oxygen measurements revealed stable O₂-concentrations between 0.28 and 0.38mg/l in the feeder fluids and thus, suboxic conditions. The shallower aquifer, being influenced by recent Baltic Sea water, contained higher amounts of sulphate and showed a higher alkalinity. At both sites, Fe in the feeder fluids is exclusively present as ferrous iron (Fe (II), Tab. 5.1). Fe concentrations were considerably higher at site 1327B than at site 2156B.

	pH	Cond. mS/m	HCO ₃ ⁻ [mg/l]	Cl ⁻ [mg/l]	Br ⁻ [mg/l]	F ⁻ [mg/l]	SO ₄ ²⁻ [mg/l]	Sulfide [mg/l]	Fe _{total} [mg/l]	Fe ²⁺ [mg/l]	O ₂ [mg/l]
1327B feeder fluid	7.33	978	209	3059	14.3	1.54	425	0.07	1.68	1.68	0.28
2156B feeder fluid	7.41	1188	139	3926	19.4	1.51	313	0.03	0.60	0.59	0.38

Table 5.1 Basic chemical parameters characterizing the feeder fluids. Mean values (<10% STD) obtained from replicate sampling over the duration of the experiment.

5.4.2 Microbial mat development

Both flow reactors showed a rapid development of microbial mats after two months. Macroscopically, the mats consisted of ochre, fluffy material (Fig. 5.1f). SEM studies showed a massive abundance of twisted filamentous EPS stalks characteristic for *G. ferruginea* (Fig. 5.2a). These stalks still showed a delicate filamentous structure with only few mineral precipitates (Fig. 5.2b).

After nine months, the flow reactor at both sites still exhibited macroscopically similar microbial mats, but the stalks were extensively incrustated with mineral precipitates (Fig. 5.2c). These minerals predominantly consisted of 2-line ferrihydrite, as revealed by XRD measurements (data not shown). Although microbially formed ferrihydrites are

relatively stable mineral phases (Kennedy *et al.*, 2004), their water content may vary (Schwertmann *et al.*, 1999), and we therefore use the comprehensive term iron oxyhydroxides in this paper. Next to the iron oxyhydroxides, the aged mats also showed the presence of authigenic minerals which were identified as gypsum using SEM-EDX (Fig. 5.2d).

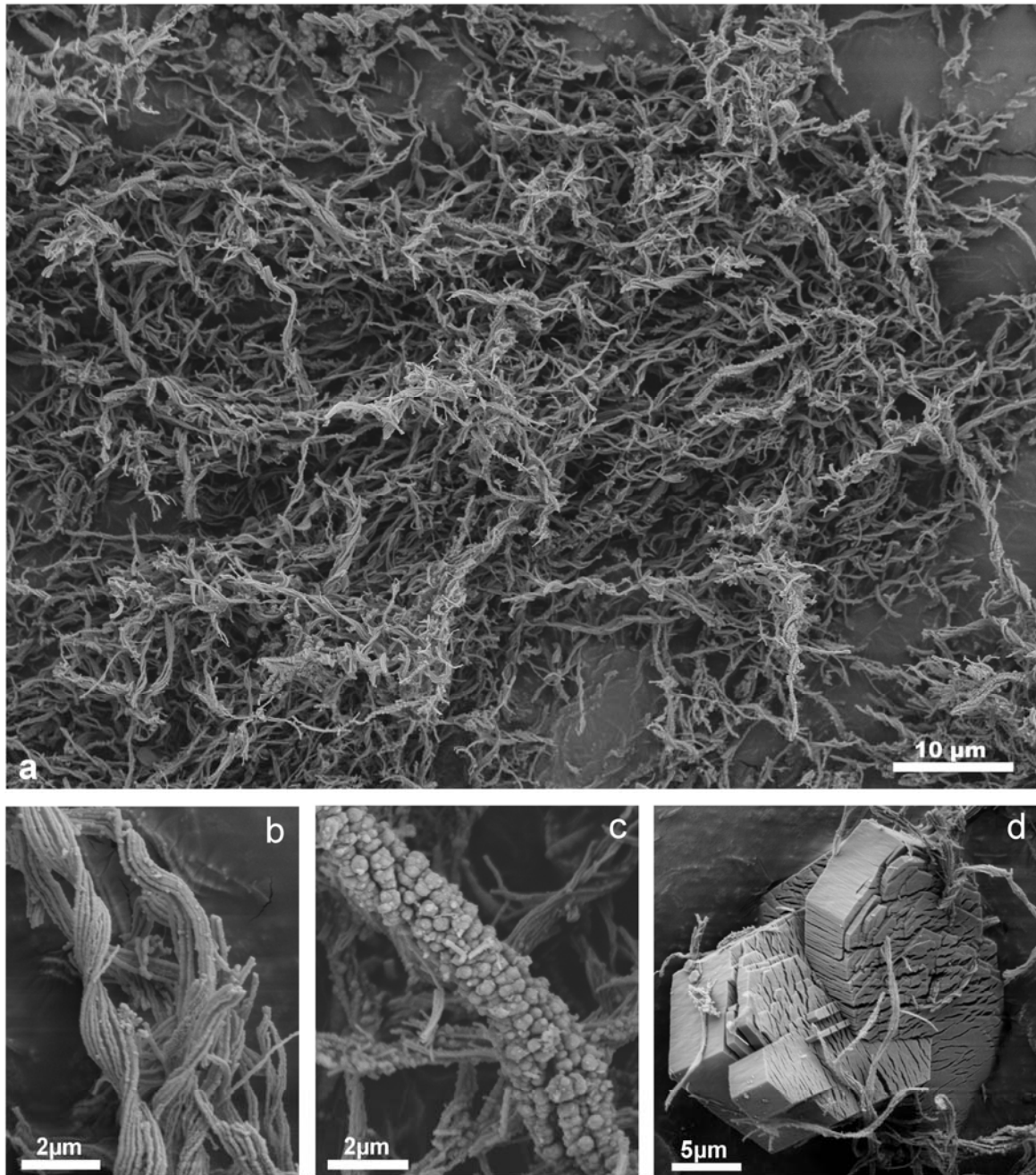


Fig. 5.2 (a) SEM micrograph of the two months old microbial mat from the flow reactor at site 1327B, showing the twisted EPS-stalks of *G. ferruginea*; (b) EPS-stalks sampled after two months, still showing a pristine filamentous structure; (c) EPS-stalks sampled after nine months, in part showing heavy iron oxyhydroxide impregnation; (d) authigenic gypsum crystals in a nine months old microbial mat.

The organic carbon (Tab. 5.2) concentrations of the microbial mats remained fairly constant during the experiment and did not exceed 3.7% at site 2156B and 7% at site 1327B. At both sites, the content of nitrogen remained stable at 0.3%.

%	1327B 2 months	1327B 9 months	2156B 2 months	2156B 9 months
C _{org}	7.0	5.7	3.6	3.7
C _{inorg}	1.3	0.4	0.1	0.2
N _{tot}	0.3	0.3	0.3	0.3

Table 5.2 Concentrations (%_{dry weight}) of organic carbon (C_{org}), inorganic carbon (C_{inorg}), and total nitrogen (N_{tot}) in the mineralized microbial mats after two and nine months.

5.4.3 TREE accumulation and fractionation

The concentrations of all cations analysed in the feeder fluids and in the microbial mats are given in table 5.3. In both flow reactors, the main element patterns of the microbial mats were always dominated by iron (Fig. 5.3). Other main elements, such as Al, Si, Na, Ca and Mg showed considerably different relative abundances at both sites after the initial two months period (Fig. 5.3a, c). After nine months, however, Si, Na, Ca and Mg approached similar distributions (Fig. 5.3b, d). The bivariate plots provided in figure 5.4 illustrate the element accumulation in the microbial mats. Compared to the feeder fluids, the microbial mats showed remarkable accumulations of most TREE. In both flow reactors, the REE and the trace elements Be, Y, Zr, Nb, Hf, Pb, Th and W were 10^3 - 10^4 fold enriched after two months. After nine months, these elements showed up to 10^6 fold enrichments. In contrast, Ca, Na, Mg, and K did not accumulate during the first two months in the mats though these elements were available at high concentrations in the feeder fluids. Even after nine months, only minor enrichments of these elements occurred (Fig. 5.4).

	Site 1327B						Site 2156B					
	Feeder fluids mean [mg/l]		Microbial mat after 2 months [mg/kg]		Microbial mat after 9 months [mg/kg]		Feeder fluids mean [mg/l]		Microbial mat after 2 months [mg/kg]		Microbial mat after 9 months [mg/kg]	
Li	0.050	± 0.0068	0.0082	± 0.0011	1.25	± 0.169	0.264	± 0.0356	0.130	± 0.018	14.2	± 1.91
Be	0.00009	± 0.00001	0.081	± 0.008	10.4	± 0.971	0.00004	± 0.000003	0.174	± 0.0163	13.1	± 1.23
Sc	0.002	± 0.0002	1.031	± 0.133	3.98	± 0.514	0.0019	± 0.00025	1.38	± 0.1776	7.74	± 1.00
V	0.011	± 0.0006	0.322	± 0.018	24.6	± 1.40	0.0159	± 0.00090	0.183	± 0.0104	9.31	± 0.530
Co	0.00037	± 0.00003	0.011	± 0.0008	0.21	± 0.015	0.0010	± 0.00007	0.025	± 0.0018	1.09	± 0.080
Ni	0.0056	± 0.0002	0.075	± 0.0025	1.55	± 0.052	0.0158	± 0.00053	0.097	± 0.0033	0.801	± 0.0270
Cu	0.00133	± 0.00007	0.049	± 0.0027	11.0	± 0.606	0.0016	± 0.00009	0.117	± 0.0065	0.905	± 0.0500
Zn	0.00158	± 0.00012	0.223	± 0.017	75.0	± 5.60	0.00056	± 0.000041	0.216	± 0.0161	9.95	± 0.742
Y	0.00017	± 0.00001	0.636	± 0.025	65.9	± 2.56	0.00046	± 0.000018	5.65	± 0.2197	313.0	± 12.2
Zr	0.00010	± 0.00001	0.141	± 0.018	14.4	± 1.82	0.000012	± 0.000002	0.157	± 0.0198	8.79	± 1.11
Nb	0.000008	± 0.0000001	0.0033	± 0.00006	0.357	± 0.006	0.000011	± 0.0000002	0.015	± 0.0003	0.963	± 0.0166
Mo	0.00094	± 0.00015	0.022	± 0.003	2.11	± 0.33	0.0061	± 0.00096	0.221	± 0.0348	11.0	± 1.73
Cd	0.000019	± 0.000003	0.00011	± 0.00002	0.042	± 0.0060	0.00012	± 0.000018	0.00076	± 0.00011	0.0128	± 0.00182
Sb	0.0000078	± 0.0000010	0.00048	± 0.00006	0.046	± 0.0056	0.000016	± 0.000002	0.00099	± 0.00012	0.0269	± 0.00327
Rb	0.025	± 0.002	0.0089	± 0.0008	1.10	± 0.103	0.0202	± 0.00189	0.016	± 0.0015	1.45	± 0.136
Sr	1.83	± 0.056	10.0	± 0.31	807	± 24.8	5.95	± 0.183	22.8	± 0.702	1197	± 36.9
Cs	0.0028	± 0.0003	0.0013	± 0.0001	0.162	± 0.015	0.0016	± 0.00015	0.0017	± 0.0002	0.12	± 0.01
Ba	0.076	± 0.0008	6.25	± 0.063	580	± 5.81	0.0328	± 0.00033	2.85	± 0.029	145	± 1.45
La	0.000029	± 0.000002	0.168	± 0.012	20.5	± 1.43	0.000074	± 0.000005	1.30	± 0.090	80.5	± 5.61
Ce	0.000049	± 0.000004	0.246	± 0.019	31.9	± 2.51	0.00010	± 0.000008	1.96	± 0.154	126	± 9.91
Pr	0.0000074	± 0.0000004	0.034	± 0.002	5.42	± 0.31	0.000013	± 0.000001	0.250	± 0.014	20.1	± 1.14
Nd	0.000041	± 0.000005	0.158	± 0.018	24.9	± 2.81	0.000061	± 0.000007	1.10	± 0.12	88.4	± 9.99
Sm	0.000011	± 0.000001	0.039	± 0.0022	6.20	± 0.346	0.000013	± 0.000001	0.26	± 0.015	21.3	± 1.19
Eu	0.000005	± 0.0000004	0.009	± 0.0006	1.15	± 0.082	0.0000033	± 0.0000002	0.037	± 0.0027	2.99	± 0.213
Gd	0.000016	± 0.000002	0.066	± 0.0101	9.75	± 1.496	0.000030	± 0.000005	0.483	± 0.074	35.9	± 5.50
Tb	0.0000017	± 0.0000003	0.008	± 0.0013	1.26	± 0.213	0.0000031	± 0.000001	0.070	± 0.012	5.62	± 0.952
Dy	0.000013	± 0.000002	0.053	± 0.0064	7.67	± 0.913	0.000027	± 0.000003	0.522	± 0.062	38.2	± 4.54
Ho	0.000003	± 0.000001	0.013	± 0.0026	1.89	± 0.367	0.000007	± 0.000001	0.129	± 0.025	9.28	± 1.80

Er	0.000010 ± 0.000002	0.040 ± 0.0091	5.73 ± 1.30	0.000023 ± 0.000005	0.392 ± 0.089	27.8 ± 6.31
Tm	0.0000010 ± 0.0000001	0.0050 ± 0.0004	0.70 ± 0.054	0.0000024 ± 0.0000002	0.048 ± 0.004	3.33 ± 0.258
Yb	0.000014 ± 0.000001	0.032 ± 0.0028	4.28 ± 0.376	0.000019 ± 0.000002	0.275 ± 0.024	18.9 ± 1.66
Lu	0.0000021 ± 0.00000002	0.0056 ± 0.0001	0.767 ± 0.009	0.0000032 ± 0.00000004	0.042 ± 0.0005	2.87 ± 0.032
Hf	0.0000014 ± 0.0000002	0.0009 ± 0.0001	0.095 ± 0.011	0.00000018 ± 0.00000002	0.001 ± 0.0001	0.082 ± 0.010
W	0.000248 ± 0.000043	0.115 ± 0.020	14.5 ± 2.50	0.00030 ± 0.000051	0.306 ± 0.0529	16.7 ± 2.88
Tl	0.0000056 ± 0.000001	0.000002 ± 0.000001	0.002 ± 0.00039	0.00000052 ± 0.0000001	0.000019 ± 0.000005	0.0018 ± 0.00042
Pb	0.0000082 ± 0.00000017	0.0016 ± 0.00003	0.787 ± 0.0166	0.000019 ± 0.0000004	0.0058 ± 0.00012	0.058 ± 0.001
Bi	0.0000006 ± 0.00000001	0.000035 ± 0.000001	0.005 ± 0.00011	0.00000040 ± 0.00000001	0.000098 ± 0.000002	0.001 ± 0.000
Th	0.0000004 ± 0.00000001	0.0011 ± 0.00003	0.229 ± 0.00701	0.0000016 ± 0.0000001	0.0043 ± 0.00013	0.612 ± 0.019
U	0.000351 ± 0.000013	0.0067 ± 0.0002	0.756 ± 0.0273	0.00033 ± 0.000012	0.014 ± 0.0005	0.638 ± 0.023
Al	0.164 ± 0.0090	8.5 ± 0.47	114 ± 6.28	0.260 ± 0.0143	2139 ± 118	7646 ± 421
Si	2.682 ± 0.147	61.6 ± 3.39	35478 ± 1951	1.23 ± 0.07	200.1 ± 11.0	40627 ± 2234
Fe	1.69 ± 0.093	2510 ± 138.0	498425 ± 27413	0.596 ± 0.033	11455 ± 630	375296 ± 20641
Mn	0.784 ± 0.049	7.81 ± 0.492	660 ± 41.6	0.608 ± 0.038	11.2 ± 0.70	385 ± 24.2
Ca	286 ± 17.2	1.4 ± 0.08	39083 ± 2345	764 ± 45.9	1.16 ± 0.07	56101 ± 3366
Mg	155 ± 8.5	0.305 ± 0.017	4585 ± 252	96.0 ± 5.3	0.422 ± 0.023	3558 ± 196
Na	1630 ± 89.7	0.128 ± 0.007	26763 ± 1472	1595 ± 87.7	0.312 ± 0.017	54181 ± 2980
K	25.2 ± 1.39	0.149 ± 0.008	706 ± 38.8	11.64 ± 0.64	0.250 ± 0.014	194 ± 10.6

Table 5.3 TREE concentrations of the feeder fluids and in the iron oxidizing microbial mats after two and nine months, respectively.

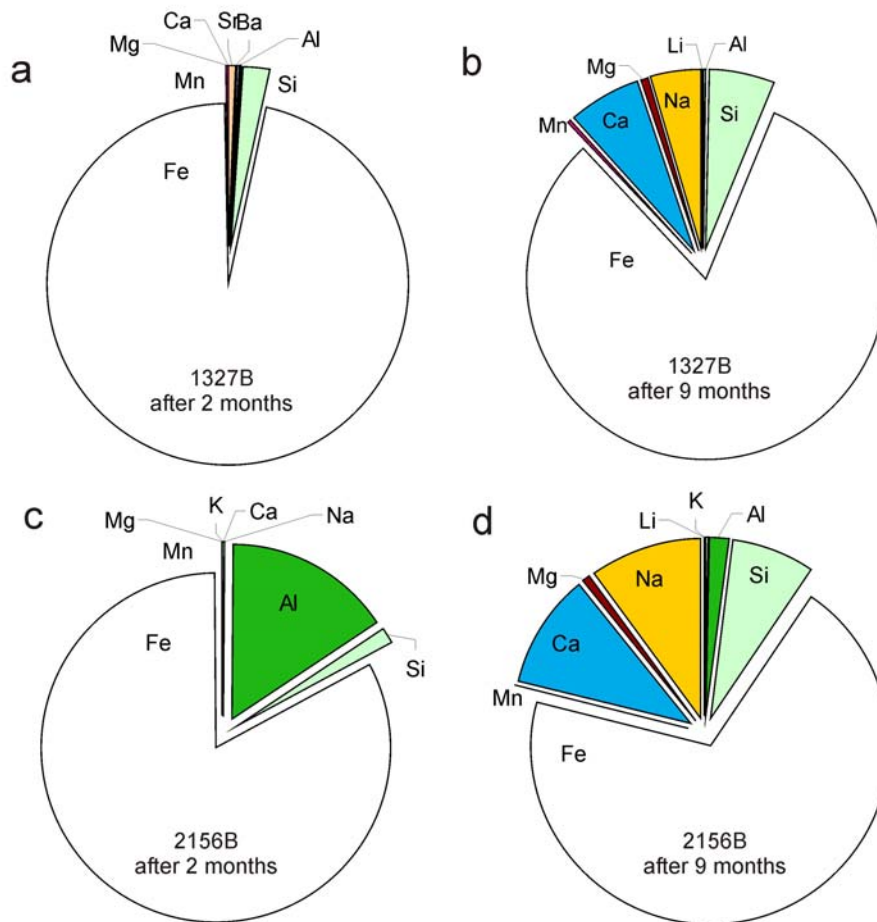


Fig. 5.3 Distribution of the major cations within the mineralized microbial mats after two months (a, c) and 9 months (b, d), respectively. Note the convergence of the major element patterns over time, although the mats were fed by chemically differing aquifers.

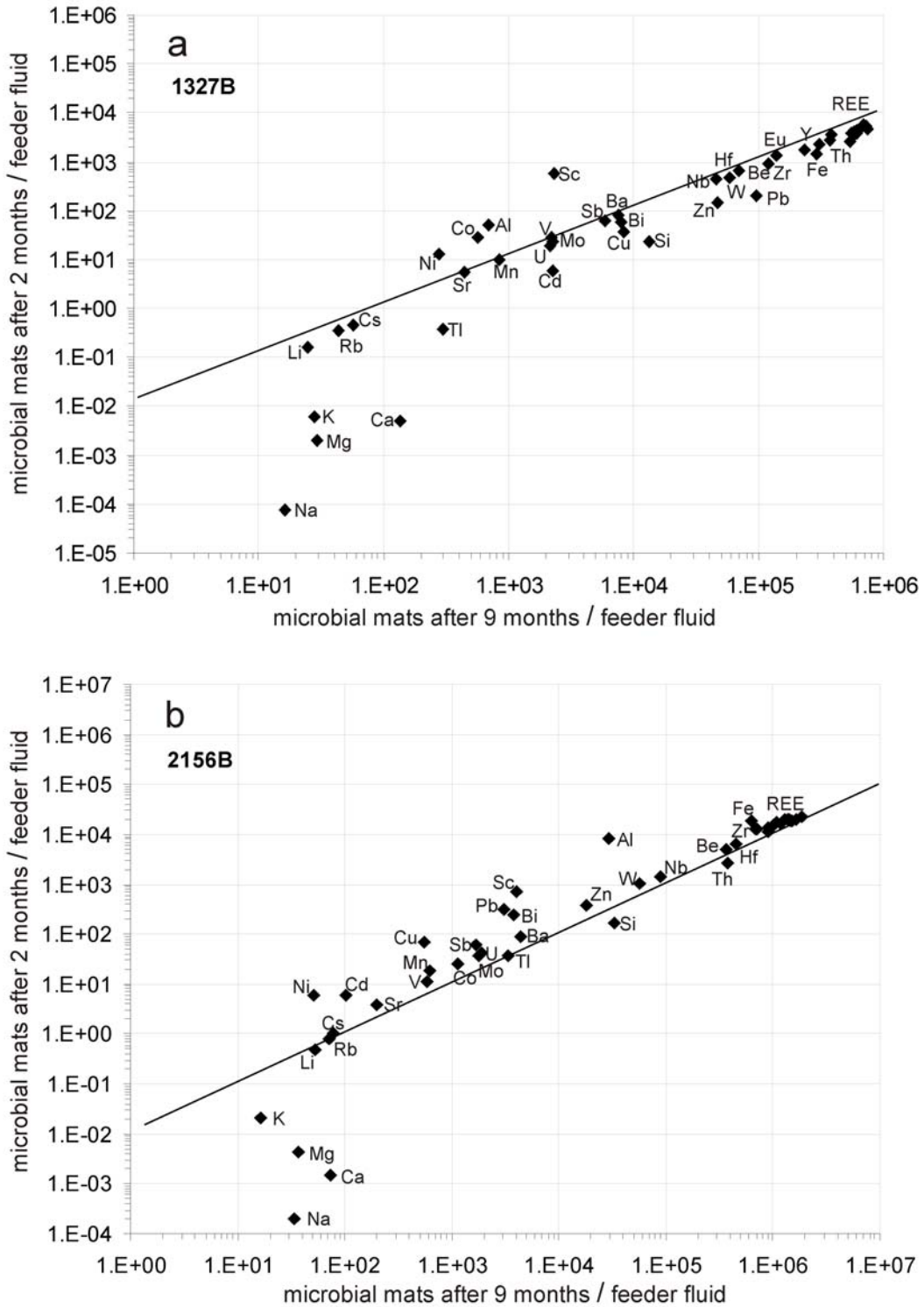


Fig. 5.4 Bivariate plots of TREE accumulation of the mineralized microbial mats after two and nine months with respect to the inflowing water, (a) at site 1327B, and (b) at site 2156B. At both sampling intervals and at both sites, highest accumulation rates are observed for REE, Be, Y, Zr, Nb, Hf, Pb, Th, and W, whereas Ca, Na, Mg, and K are accumulated in only low amounts, and only in the nine months old microbial mats.

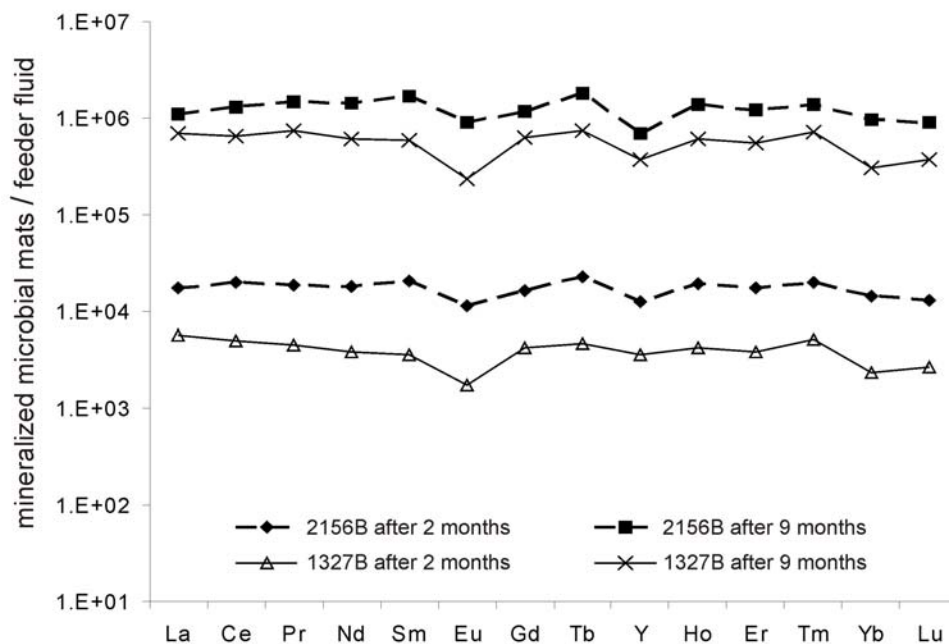


Fig. 5.5 Plot illustrating the REE +Y fractionation in the microbial iron oxyhydroxides from the respective feeder fluids. Nearly uniform REE+Y accumulations are observed, except for minor negative Eu and Y anomalies, indicating a largely radius-independent fractionation of REE+Y from the feeder fluids.

5.5 Discussion

The microbial mineral precipitates formed during the experiment showed distinct changes over time in their morphological structure as well as in their elemental composition (Figs. 5.2b, c, 5.3a-d, 5.4a, b). Inasmuch as the feeder fluid chemistry did not change considerably during the microbial mat development, we attribute these chemical changes to processes occurring within the microbial mat.

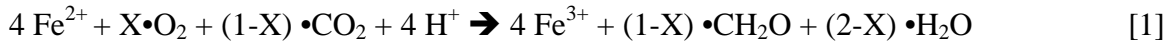
The *G. ferruginea* EPS-stalks, after two months, still showed a delicate structure of twisted filaments and only few iron oxyhydroxide precipitates, but the microbial mats already exhibited a 10^4 fold accumulation of Fe and TREE. It has been proposed that during the iron oxidation process in the young *G. ferruginea* stalks, initial mineralization of hematite (Fe_2O_3) takes place *within* the filaments, whereas aging stalks increasingly precipitate iron oxyhydroxides *outside* the filaments (Hallberg and Ferris, 2004). The presence of hematite was not observed in our experiments. But the still pristine filament surfaces (Fig. 5.2b) suggest that the iron oxidation process, accompanied by iron oxyhydroxide and TREE precipitation, is predominantly occurring within the filaments at an early stage of mineralization.

Within the ‘young’ microbial mats, the *G. ferruginea* EPS-stalks play a crucial role in mineral precipitation because they offer large reactive surfaces for the biosorption of metals. This process does not depend on the absolute amount of metals present (Haferburg *et al.*, 2007). Rather, metals with a higher positive charge tend to show enhanced biosorption. Such enhanced biosorption to the EPS-stalks may partially explain the higher enrichments observed for the 3- and 4-valent elements Al and Si, REE, Y, Zr, Hf, Pb, Th, and W compared to lower valent elements like Ca, K, Mg, Na, Cs, Rb and Li.

However, REE, Be, Y, Zr, Nb, Hf, Pb, Th and W show accumulation rates as high as those of Fe (Fig. 5.4a, b). Therefore, we consider scavenging within, and co-precipitation with the iron oxyhydroxides as another important process. This assumption is in good agreement with the property of iron oxyhydroxides as efficient metal sorbents, which is widely used in technical application and remediation activities (de Carlo *et al.*, 1998; Bau, 1999; Cornell and Schwertmann, 2004; Michel *et al.*, 2007). Laboratory studies investigating the properties of *inorganic* iron oxyhydroxides as metal sorbents have demonstrated their strong accumulation capacities for REE+Y (Carlo *et al.*, 1998; Bau, 1999). These studies also showed that the sorption of REE+Y onto iron oxyhydroxides increases strongly, up to a 10^4 fold, with increasing pH. With pH values increasing toward neutral conditions, however the REE+Y graphs develop (i) a strong negative Y anomaly and (ii) a more and more sigmoidal shape reflecting preferential accumulation of the middle and heavy REE (Sm-Lu), and a retard of the light REE (La-Nd) (Bau, 1999). The microbial iron oxyhydroxides formed in our experiments revealed extremely high accumulation rates of REE+Y, but their distribution pattern (Fig. 5.5) showed no sigmoidal shape and only a minor Y-anomaly. Rather, the REE+Y consistently accumulated in the microbial mats. This observation implies that the microbially assisted fractionation of REE+Y from the feeder fluids and their incorporation into the iron oxyhydroxides is a radius-independent process. We suggest this REE+Y pattern as a biosignature for the distinction between microbially mediated vs. inorganically formed iron oxyhydroxides.

The ongoing incrustation of the *G. ferruginea* stalks (Fig. 5.2c) most likely caused a gradual depletion of the biosorption capacities controlled by the organic surfaces of the EPS (i.e. passive mineralization). At a later stage of the experiment, indirect mineral precipitation becomes more and more apparent and is likely to account for significantly higher accumulations of Si and the lower valent cations Ca, Mg, Na (Fig. 5.3 b, d), Cs, Sr, Se, Li (Fig. 5.4) in the microbial mats. Gypsum precipitation, evidently due to the changing chemical equilibrium in the solution can likewise be attributed to indirect biomineralization,

and may be an inevitable result of the iron oxidation by *G. ferruginea*. Although the exact pathway is as yet unknown, the following equation has been plausibly proposed for the iron oxidation process performed by *G. ferruginea* (Hallberg and Ferris, 2004):



The removal of dissolved CO_2 during the iron oxidation process leads to a shift of the chemical equilibrium through a drop in alkalinity. The depletion of carbonates causes Ca to bind preferably to sulphate (SO_4^{2-}), which is present in high concentrations in the feeder fluid (Table 1), thus leading to the precipitation of gypsum (Fig. 5.2d). Elements similar to Ca in charge and/or size, like Mg, K, Na, Cs, and Sr, are easily incorporated in the gypsum lattice, a process which may contribute to the enhanced accumulation of these elements within the aged microbial mat (Fig. 5.4).

When normalized on PAAS (Post-Archaean average Australian sedimentary rock; McLennan, 1989), the REE+Y plots of the feeder fluids and the microbial iron oxyhydroxides show a slight enrichment of the heavy REE (Gd-Lu+Y) over the light REE (La-Eu) (Fig. 5.6). This pattern is often referred to as 'hydrogenous' (Takahashi *et al.*, 2002) and has been explained by different chemical complex formation of the REE+Y in aqueous solutions, rather than a merely charge- and radius-controlled behaviour (CHARAC; Takahashi *et al.*, 2002, Bau, 1996).

When normalized on the feeder fluids, the REE+Y patterns of the microbial iron oxyhydroxides quite exactly mirror the source, thus displaying a consistent radius-independent fractionation (Fig. 5.5). It is interesting to see that these patterns (Fig. 5.6) have a high similarity to published REE patterns of Archaean BIF (Bau and Dulski, 1996; Frei *et al.*, 2008). The only exception is a positive Eu anomaly in BIF, that is most likely derived from hydrothermal influence (Michard and Albrède, 1986; Frei *et al.*, 2008) and is lacking in the feeder fluids and in the iron oxyhydroxides from Äspö. The common REE+Y patterns in the microbial iron oxyhydroxides and BIF differ significantly from those observed in pure chemical iron oxyhydroxide precipitates. We therefore suggest the REE+Y pattern as a biosignature for microbial iron oxidation, supporting the idea that this process was a key factor in the formation of BIF (Konhauser *et al.*, 2002; Kappler and Newmann, 2004).

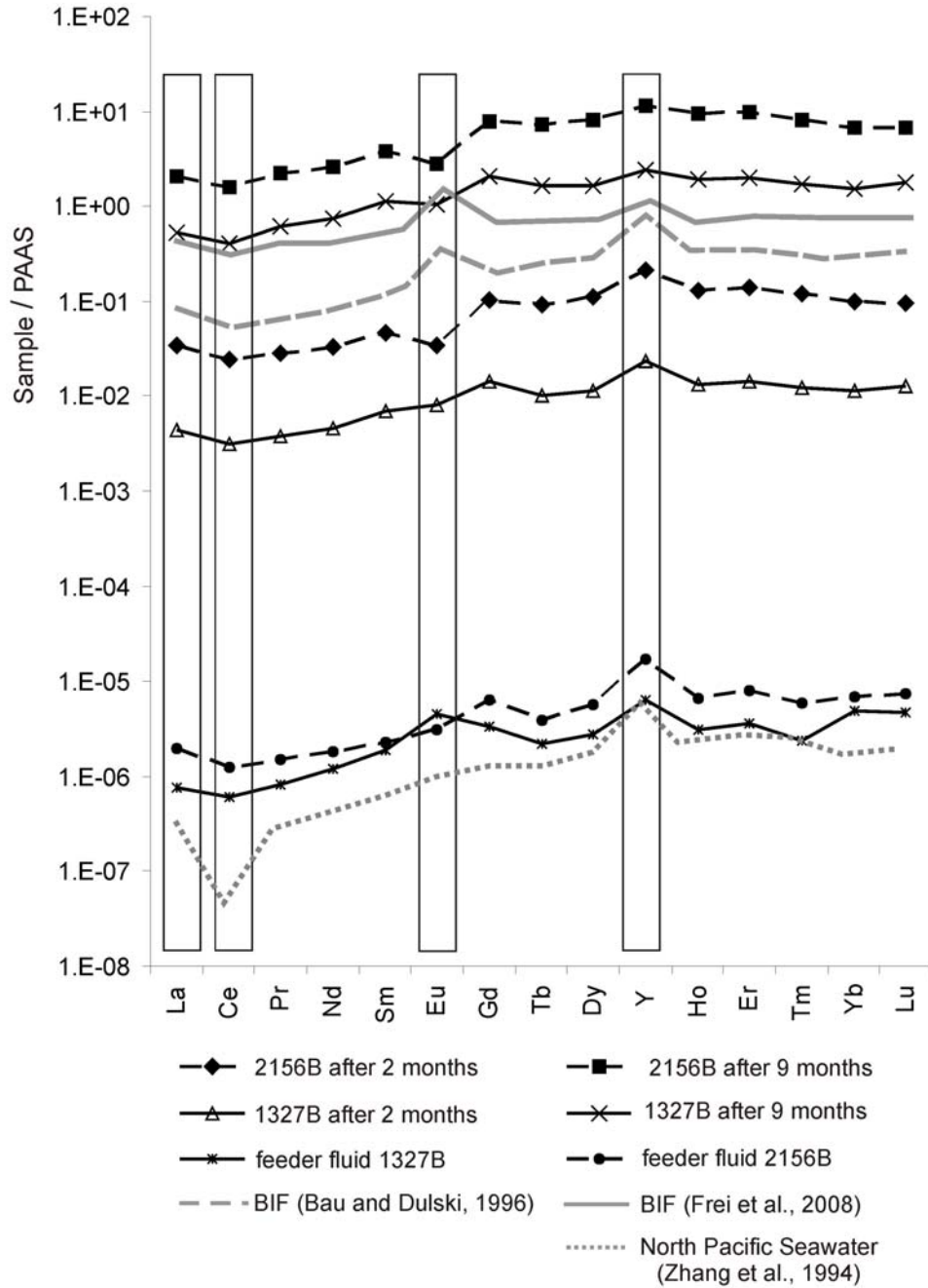


Fig. 5.6 Plot illustrating the PAAS-normalized REE +Y patterns of the feeder fluids and the microbial iron oxyhydroxides, in comparison to published data for modern seawater and BIF. Note the similarity between the REE +Y patterns of microbial iron oxyhydroxides and BIF.

5.6 Conclusions

In a suboxic aquifer system hosted by granodioritic rocks and influenced by Baltic Sea water, the development of iron oxidizing microbial mats was studied employing a closed flow-reactor system. Over the nine months of the experiment, the microbial mats were dominated by the iron-oxidizing bacterium *Gallionella ferruginea* which precipitated microbial iron oxyhydroxides along its EPS-stalks. The deposition of these iron minerals is initially controlled by the metabolic activity of *G. ferruginea* and passive mineralisation processes caused by the high biosorption capacity of the young EPS-stalks. Upon aging, ongoing iron oxyhydroxide impregnation causes a gradual depletion of the biosorption capacities of the EPS-stalks. As a result, indirect mineral precipitation becomes increasingly important over time.

The iron-oxidizing microbial mats proved to be extremely efficient in the accumulation of trace and rare earth elements (TREE), leading to massive (up to 10^6 fold) enrichments of individual metals in the microbial iron oxyhydroxides. The REE+Y pattern of the microbial iron oxyhydroxides is distinctly different from chemically precipitated iron oxyhydroxides, but shows a strong resemblance to REE+Y patterns of Banded Iron Formations (BIF). These findings lend further support to the hypothesis that iron-oxidizing microorganisms such as *G. ferruginea* may have been involved in the formation of BIF.

Acknowledgments:

Andreas Pack is acknowledged for his constructive comments that helped to improve the manuscript. We are grateful to Emmeli Johansson, Magnus Kronberg, Teresita Morales and the SKB Chemistry Lab staff from SKB for technical, logistic and analytical support at the Äspö HRL. Volker Karius and Veit-Enno Hoffmann, Erwin Schiffzyk, and Dorothea Hause-Reitner are acknowledged for their assistance with the XRD, ICP-OES, and SEM-EDX measurements, respectively. Our study received financial support from the German Research Foundation (DFG). This is publication no. XX of the DFG Research Unit FOR 571 'Geobiology of Organo- and Biofilms'.

References:

- Anbar AD, Duan Y, Lyons TW, Arnold GL, Kendall B, Creaser RA, Kaufman AJ, Gordon GW, Scott C, Garvin J, Buick R (2007) A whiff of oxygen before the Great Oxidation Event? *Science*, **317**, 1903-1906.
- Anderson C R, Pedersen K (2003) In situ growth of *Gallionella* biofilms and partitioning of lanthanides and actinides between biological material and ferric oxyhydroxides. *Gebiology*, **1**, 169-178.
- Bau M (1999) Scavenging of dissolved yttrium and rare earths by precipitating iron oxyhydroxide: Experimental evidence for Ce oxidation, Y-Ho fractionation, and lanthanide tetrad effect. *Geochimica et Cosmochimica Acta*, **63**, 67-77.
- Bau M (1996) Controls on the fractionation of isoivalent trace elements in magmatic and aqueous systems: evidence from Y/Ho, Zr/Hf, and lanthanide tetrad effect. *Contributions to Mineral Petrology*, **123**, 323-333.
- Bau M, Dulski P (1996) Distribution of yttrium and rare-earth elements in the Penge and Kuruman iron-formations, Transvaal Supergroup, South Africa. *Precambrian Research*, **79**, 37-55.
- Bau M, Möller P (1993) Rare earth element systematics of the chemically precipitated component in Early Precambrian iron-formations and the evolution of the terrestrial atmosphere-hydrosphere-lithosphere system. *Geochimica et Cosmochimica Acta*, **57**, 2239-2249.
- Bazylinski DA, Frankel RB, Konhauser KO (2007) Modes of biomineralization of magnetite by microbes. *Geomicrobiology Journal*, **24**, 465-475.
- Chan CS, Fakra SC, Edwards DC, Emerson D, Banfield JF (2009) Iron oxyhydroxide mineralization of microbial extracellular polysaccharides. *Geochimica et Cosmochimica Acta*, **73**, 3807-3818.
- Cornell M, Schwertmann U (2004) *The Iron Oxides*. Wiley-VCH, 664 p.
- De Carlo EH, Wen X-Y, Irving M (1998) The influence of redox reactions on the uptake of dissolved Ce by suspended Fe and Mn oxide particles. *Aquatic Geochemistry*, **3**, 257-289.
- Ehrenberg CG (1836) Vorläufige Mitteilungen über das wirkliche Vorkommen fossiler Infusorien und ihre große Verbreitung. *Poggendorf's Annalen der Physik und Chemie*, **38**, 213-227.
- Ercolo C, Cacchio P, Botta AL, Centi V, Lepidi A (2007) Bacterially induced mineralization of calcium carbonate: The role of exopolysaccharides and capsular polysaccharides. *Microscopy and Microanalysis*, **13**, 42-50.
- Ferris FG, Hallberg RO, Lyvén B, Pedersen K (2000) Retention of strontium, cesium, lead and uranium by bacterial iron oxides from subterranean environment. *Applied Geochemistry*, **15**, 1035-1042.
- Ferris FG, Konhauser KO, Lyvén B, Pedersen K (1999) Accumulation of metals by bacteriogenic iron oxides in a subterranean environment. *Geomicrobiology Journal*, **16**, 181-192.
- Fortin D, Beveridge TJ (1997) Role of the bacterium *Thiobacillus* in the formation of silicates in acidic mine tailings. *Chemical Geology*, **141**, 235-250.
- Fortin D, Ferris FG, Beveridge TJ (1997) Surface-mediated mineral development by bacteria. In *Geomicrobiology: Interactions between microbes and minerals*. *Reviews in Mineralogy* Vol. 35, Ribbe PH (series ed), Mineralogical Society of America. 161-180.
- Frankel RB, Bazylinski DA (2003) Biologically induced mineralization by bacteria. In Dove PM, De Yoreo JJ, Weiner S (eds), *Biomineralization*. *Reviews in Mineralogy and Geochemistry* Vol. 54, series editor Rosso JJ, Mineralogical Society of America & Geochemical Society, 95-114.

- Frei R, Dahl PS, Duke EF, Frei KM, Hansen TR, Fransson MM, Jensen LA (2008). Trace element and isotopic characterisation of Neoproterozoic and Paleoproterozoic formations in the Black Hills (South Dakota, USA): Assessment of chemical change during 2.9-1.9 Ga deposition bracketing the 2.4-2.2 Ga first rise of atmospheric oxygen. *Precambrian Research*, **162**, 441-474.
- Haferburg G, Merten D, Büchel G, Kothe E (2007) Biosorption of metal and salt tolerant microbial isolates from a former uranium mining area. Their impact on changes in rare earth element patterns in acid mine drainage. *Journal of Basic Microbiology*, **47**, 474-484.
- Haferburg G, Kothe E (2007) Microbes and metals: interactions in the environment. *Journal of Basic Microbiology*, **47**, 453-467.
- Hallbeck L, Pedersen K (1995) Benefits associated with the stalk of *Gallionella ferruginea*, evaluated by comparison of a stalk-forming and non-stalk-forming strain and biofilm studies in situ. *Microbial Ecology*, **30**, 257-268.
- Hallbeck L, Ståhl F, Pedersen K (1993) Phylogeny and phenotypic characterization of the stalk-forming iron oxidizing bacterium *Gallionella ferruginea*. *Journal of General Microbiology*, **139**, 1531-1535.
- Hallbeck L, Pedersen K (1991) Autotrophic and mixotrophic growth of *Gallionella ferruginea*. *Journal of General Microbiology*, **137**, 2657-2661.
- Hallberg R, Ferris FG (2004) Biomineralization by *Gallionella*. *Geomicrobiology Journal*, **21**, 325-330.
- Hansen HP (1999) Determination of oxygen. In Grasshoff K, Kremling K, Ehrhardt M (eds.) *Methods of seawater analysis*. Wiley-VCH, 75-89.
- Kappler A, Straub B, Newman DK (2005) Fe(III) mineral formation and cell encrustation by the nitrate-dependent Fe(II)-oxidizer strain BoFeN1. *Geobiology*, **3**, 235-245.
- Kappler A, Newmann DK (2004) Formation of Fe(III)-minerals by Fe(II)-oxidizing photoautotrophic bacteria. *Geochimica et Cosmochimica Acta*, **68**, 1217-1226.
- Kennedy DB, Scott SD, Ferris FG (2004) Hydrothermal phase stabilization of 2-line ferrihydrite by bacteria. *Chemical Geology*, **212**, 269-277.
- Konhauser KO, Hamade T, Raiswell R, Morris RC, Ferris FG, Southam G, Canfield DE (2002) Could bacteria have formed the Precambrian banded iron formations? *Geology*, **20**, 1079-1082.
- Konhauser KO (1997) Bacterial iron biomineralization in nature. *FEMS Microbiology Reviews*, **20**, 315-326.
- Krapez B, Barley ME, Pickard AL (2003) Hydrothermal and resedimented origins of the precursor sediments to banded iron formation: sedimentological evidence from the Early Paleoproterozoic Brockman Supersequence of Western Australia. *Sedimentology*, **50**, 979-1011.
- Laaksoharju M, Tullborg E-L, Wikberg P, Wallin B, Smellie J (1999) Hydrogeochemical conditions and evolution at the Äspö HRL, Sweden. *Applied Geochemistry*, **14**, 835-859.
- McLennan SM (1989) Rare earth elements in sedimentary rocks: influence of provenance and sedimentary processes. In Lipin BR, McKay GA (eds), *Geochemistry and mineralogy of rare earth elements*. *Reviews in Mineralogy*, **21**, 169-200.
- Michard A, Albarède F (1986) The REE content of some hydrothermal fluids. *Chemical Geology*, **55**, 51-60.
- Michel MF, Ehm L, Antao SM, Lee PL, Chupas PJ, Liu G, Strongin DR, Schoonen MAA, Phillips BL, Parise JB (2007) The structure of ferrihydrite, a nanocrystalline material. *Science*, **316**, 1726-1729.
- Morris RC, Horwitz RC (1983) The origin of the iron-formation-rich Hamersley Group of Western Australia – Deposition on a platform. *Precambrian Research*, **21**, 273-297.

- Schwertmann U, Friedl J, Stanjek H (1999) From Fe(III) ions to ferrihydrite and then to hematite. *Journal of Colloid and Interface Science*, **209**, 215-223.
- SICADA. Database of the Swedish organisation for nuclear fuel and waste management (SKB), owner of the Äspö HRL. See also www.skb.se
- Southam G (2000) Bacterial surface-mediated mineral formation. In Lovley DR (ed), *Environmental microbe-mineral interactions*. ASM Press, Washington DC, 257-276.
- Stumm W, Morgan JJ (1996) *Aquatic Chemistry: Chemical equilibria and rates in natural waters*. John Wiley and Sons, 1040 p.
- Takahashi Y, Hirata T, Shimizu H, Ozaki T, Fortin D (2007) A rare earth element signature of bacteria in natural waters. *Chemical Geology*, **244**, 569-583.
- Takahashi Y, Yoshida H, Sato N, Hama K, Yusa Y, Shimizu H (2002) W- and M-type tetrad effects in REE patterns for water-rock systems in the Tono uranium deposit, central Japan. *Chemical Geology*, **184**, 311-335.
- Thompson JB, Ferris FG (1990) Cyanobacterial precipitation of gypsum, calcite, and magnesite from natural alkaline lake water. *Geology*, **18**, 995-998.
- Urrutia MM, Beveridge TJ (1993) Mechanism of silicate binding to the bacteria cell wall in *Bacillus subtilis*. *Journal of Bacteriology*, **175**, 1936-1945.
- Weiner S, Dove PM (2003) An overview of biomineralization processes and the problem of the vital effect. In Dove PM, De Yoreo JJ, Weiner S (eds), *Biomineralization. Reviews in Mineralogy and Geochemistry* Vol. 54, series editor Rosso JJ, Mineralogical Society of America & Geochemical Society, 1-29.
- Zhang J, Amakawa H, Nozaki Y (1994) The comparative behaviours of yttrium and lanthanides in the seawater of the North Pacific. *Geophysical Research Letters*, **21**, 2677-2680.

6

Ancient microbial activity recorded in fracture fillings from granitic rocks (Äspö Hard Rock Laboratory, Sweden)

Christine Heim, Jukka Lausmaa, Peter Sjövall, Jan Toporski, Thomas Dieing, Klaus Simon,
Bent Hansen, Andreas Kronz, Joachim Reitner, Volker Thiel

Geobiology, in revision

6.1 Abstract

Fracture minerals within the ca 1.8 Ga old Äspö Diorite (Sweden) were investigated for fossil biosignatures of subterranean microbial activity. Core samples were obtained at 450 m depth in the Äspö Hard Rock Laboratory. To track organic or inorganic remnants of an ancient deep biosphere in situ, an analytical approach combining complementary techniques of high lateral resolution was adopted. This approach included polarization microscopy, time-of-flight secondary ion mass spectrometry (ToF-SIMS), confocal Raman microscopy, electron microprobe, and laser ablation inductively coupled mass spectrometry (LA-ICP-MS).

The analyses of a fracture mineral succession consisting of fluorite and low-temperature calcite demonstrated the presence of a thin (20-100 μ m), dark amorphous layer lining the boundary between the two phases. Exactly following the distribution of the amorphous layer, significant accumulations of Si, Al, Mg, Fe, and the light rare earth elements were observed. In the same area, ToF-SIMS imaging revealed numerous, partly functionalized organic ions, e.g. $C_2H_6N^+$, $C_4H_7^+$, $C_3H_5O^+$, and $C_6H_{11}^+$. The presence of such functionalized organic compounds within the amorphous layer was corroborated by Raman imaging showing bands characteristic for C-C, C-N, and C-O bonds. According to its organic nature and the abundance of relatively unstable N- and O-heterocompounds, the organic-rich amorphous layer was interpreted to represent the remains of a biofilm that established much later than the initial cooling of the Precambrian host rock. Indeed, $\delta^{13}C$, $\delta^{18}O$ and $^{87}Sr/^{86}Sr$ isotope analyses of the fracture minerals and the host rock pointed to an association of the fossil biofilm with a fracture reactivation event in the most recent geological past. This event probably occurred at the end of the last glaciation (Weichselian), and was induced by pressure relief due to melting of the Baltic ice masses. Along the reactivated fractures, glacial melt waters, meteoric and marine waters were injected deeply into the underlying igneous rocks. The fracture system thus provided surfaces and a steady fluid and nutrient supply that fueled intermittent microbial activity. Thriving of the deep biosphere organisms was cut off by secondary

calcite precipitates that now provide a unique archive of the microbial and hydrologic processes that once occurred at depth.

6.2 Introduction

Microbial life exists in, and seems to be adapted to, all kinds of ecological niches on earth. Numerous reports exist about diverse, well adapted, active microorganisms recovered from sedimentary and igneous rocks, being most likely indigenous, and occurring as deep as several kilometers. Such occurrences raise the questions of (a) how the organisms got down there, (b) how they are able to maintain life and growth, (c) what the limiting factors for life in the deep biosphere are. Fluids, minerals, and H₂ and CH₄ from degassing volcanic or plutonic rocks are considered as widespread nutrient and energy sources fueling chemotrophic ecosystems at depth (Pedersen, 2000; Amend and Teske, 2005; Dobretsov *et al.*, 2006). Learning more about recent and ancient life in deep subterranean environments may help to understand how life evolved and survived crises such as meteorite impacts, increased volcanic activity, or global glaciations such as the Late Precambrian Snowball Earth. Models about the habitability of the Hadean Earth indicate that even the late heavy meteorite bombardment around 3.9 Ga would not have been able to extinguish the primeval biosphere, considering the existence of near- and subsurface biota within the Earth's crust (Abramov and Mojzsis, 2009).

There is now ample evidence for the existence of living microorganisms and microbial mats in groundwater aquifers within terrestrial igneous rocks (Szewzyk *et al.*, 1994; Kotelnikova and Pedersen, 1998; Pedersen, 2000; Kotelnikova, 2002; Reitner *et al.*, 2005; Horsfield *et al.*, 2006; Kyle *et al.*, 2008; Sahl *et al.*, 2008; Eydal *et al.*, 2009). Likewise, numerous reports exist about fossilized remnants of microbial mats and microorganisms, but especially in sediments it is often difficult to distinguish whether such biosignatures derive from buried surface (or near-surface-) biota or from an indigenous subsurface biosphere (Ventura *et al.*, 2007). Many studies on fossil deep biosphere systems therefore focused on fracture fillings and mineral-filled cavities within different, mostly igneous, rocks that have never been exposed to the surface (Pedersen *et al.*, 1997; Banerjee *et al.*, 2006; Hofmann *et al.*, 2008; Ivarsson *et al.*, 2008; Staudigel *et al.*, 2008; Bons *et al.*, 2009). Within igneous rocks, fractures can provide a steady fluid and nutrient supply and surfaces suitable of hosting different kinds of chemoheterotrophic and chemolithotrophic microorganisms. These structures, after being sealed by fracture mineral precipitation, may archive geochemical traces of the microbial and hydrologic processes that once occurred at depth. Permineralized fractures can therefore be considered as promising targets in the search for ancient biosignatures in continental igneous rocks.

Apart from (electron) microscopy, geochemical tracers such as lipid biomarkers and stable isotopes (e.g. $\delta^{13}\text{C}$, $\delta^{34}\text{S}$, $\delta^{56}\text{Fe}$) are successfully used in paleoenvironmental studies to reconstruct

biocommunities, biogeochemical pathways, microbial phylogeny, biodegradation, and thermal maturation (e.g., Canfield, 2001, Joachimski *et al.*, 2001; Anbar, 2004; Peckmann and Thiel, 2004; Peters *et al.*, 2004; Brocks and Pearson, 2005; Blumenberg *et al.*, 2007). For *in situ* fracture mineral studies, lipid biomarker techniques are limited in their applicability, as they require relatively large sample quantities, and always cause destruction of the sample. Hence, isotope analyses, trace and rare earth element fractionations, and morphological studies of crystals and biomorphs are more frequently used for biogeochemical investigations of fracture fillings and mineral filled cavities (e.g. Westall and Folk, 2003; Banerjee *et al.*, 2006; Hofmann *et al.*, 2008; Staudigel *et al.*, 2008; Sandström and Tullborg, 2009; Dideriksen *et al.*, 2010). Here we present a comprehensive approach to the geochemical information preserved in fracture fillings, combining polarization microscopy, time-of-flight secondary ion mass spectrometry (ToF-SIMS), confocal Raman microscopy, electron microprobe (EMP), laser ablation inductively coupled plasma mass spectrometry (LA-ICP-MS) and isotope analyses ($\delta^{13}\text{C}$, $\delta^{18}\text{O}$ and $^{87}\text{Sr}/^{86}\text{Sr}$). This approach allowed to study the composition, structure, and spatial distribution of the molecules and chemical structures present in the fracture fillings at the microscopic range. Most analyses were performed on the same sample section, and with full control on the area of investigation, while preserving the structural integrity of the sample.

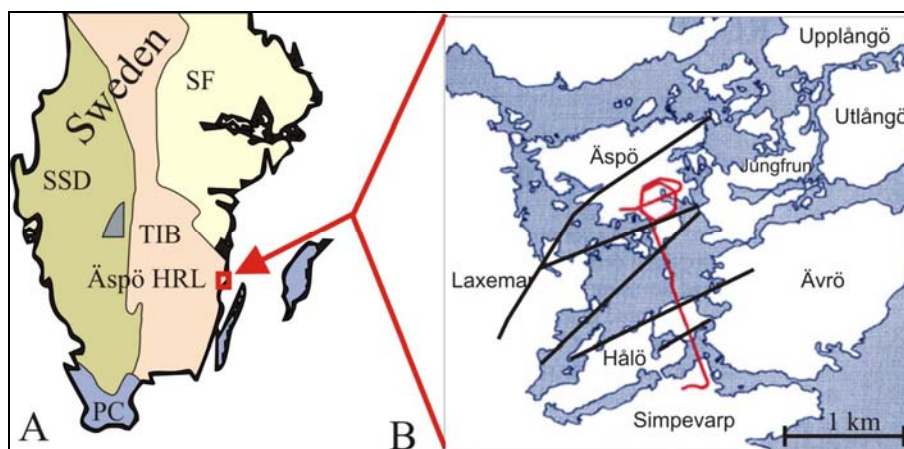


Fig. 6.1 Study area. (A) Major geological units of Sweden: SSD = Southwest Scandinavian Domain; TIB = Transcandinavian Igneous Belt; SF = Svecofennian Domain; PC = Phanerozoic cover; Äspö HRL = location of the Äspö Hard Rock Laboratory. (B) Sketch of the Äspö Hard Rock Laboratory tunnel system beneath the island of Äspö; black lines indicate major fracture zones.

6.3 Geological setting of the Äspö site

Samples were taken from a 50 mm drill core (KJ 0052F01, 11.6 m) obtained at 450 m depth in the Äspö Hard Rock Laboratory, a tunnel drilled beneath the island of Äspö in south eastern Sweden, ca. 400 km south of Stockholm (Fig. 6.1). The Äspö Hard Rock Laboratory is operated by the Swedish Nuclear Fuel and Waste Management Company (SKB) as a testing site for the long-term

deposition of nuclear waste. The host rock of the Äspö site belongs to the Precambrian Transscandinavian Igneous Belt and consists of ~ 1.8 Ga old granitic to quartz-monzodioritic rocks (Wahlgren *et al.*, 2006). Intrusions of the Götemar/Uthamar granites, concomitant hydrothermal fluids at 1.45 Ga (Kornfältt *et al.*, 1997; Åhäll 2001), and the Caledonian orogeny (e.g. Roberts, 2003) led to several fracture formation, -mineralization and –reactivation events. In the major Äspö area, six different fracture mineralization events can be distinguished (Tullborg *et al.*, 2008), whereof four were linked to Precambrian hydrothermal fluids (generations 1 to 4), one to warm Palaeozoic brine fluids (generation 5a and b) and one to low-temperature fluids of Quaternary age (generation 6, Drake *et al.*, 2007; Tullborg *et al.*, 2008; Drake and Tullborg, 2009). Fracture reactivation in the Quaternary has been attributed to glacially induced faulting (Lund, 2006). Fracture minerals and present ground waters are influenced by glacial and meteoric waters, as well as marine waters from earlier stages of the Baltic Sea (Yoldia Sea and Littorina Sea; Laaksoharju *et al.*, 2004; Wallin *et al.*, 2007).

6.4 Methods

Considerable efforts have been made to develop a protocol for the contamination-free sectioning of the drill core. Prior to and in between sectioning, the saw and the saw blade were thoroughly cleaned with pre-distilled acetone and de-ionised water. For complementary analysis, three parallel sections of 4 mm thickness were cut. One of these sections was prepared for polarization microscopy. The second section was glued on a glass slide, polished and sputtered with carbon for EMP analysis. The third section was rinsed, ultrasonicated with de-ionised water, and kept in sterile aluminum foil until ToF-SIMS analysis. This section was also used for LA-ICP-MS and Raman microscopy. A Leica DMRC was used for polarization microscopy.

LA-ICP-MS analyses were performed using a Perkin Elmer SCIEX Elan DRCII instrument coupled with a Lambda Physik 193 nm ArF-laser (3 J/cm², 30 kV, 10 Hz, laser beam diameter ca. 60 µm). Three LA-ICP-MS profiles were obtained, transecting the diorite, fluorite and calcite phases. Element concentrations were determined using the NBS 610 reference standard (Jochum *et al.*, 2005). Rare earth elements (REE) values were normalized to the upper continental crust (UCC, Taylor and Mc Lennan, 1981). Trace element and REE values reported in this paper are mean values of 15 data points.

ToF-SIMS molecular mappings were carried out with a ToF-SIMS IV instrument (ION-TOF GmbH, Münster, Germany) equipped with a liquid bismuth cluster ion source. Data were acquired with a mass resolution of $M/\Delta M$ 5000, using 25 keV Bi₃⁺ primary ions at a pulsed current of 0.1 pA and a lateral resolution of 3-4 µm. Low energy electron flooding was used for charge compensation. The analysed areas were 500 x 500 µm² and were scanned in a raster pattern at 256

x 256 pixels. Positive and negative mass spectra were internally calibrated using CH_3^+ , C_2H_3^+ , C_3H_5^+ , and CH^- , C_2H^- , C_3H^- , C_4H^- peaks, respectively. The acquisition times were between 340 s and 900 s. Molecular mappings were performed on three different areas along the fracture, including a mapping series from the fracture rim to the centre of the diorite. All analyses were done under static SIMS condition, i.e. with primary ion doses well below those where significant surface damage due to the ion bombardment starts to appear.

A Witec alpha 300 series instrument was used for Raman microscopy. The sample was examined with a 532 nm laser and a 50x air objective (NA 0.55). The scan range was 3000 μm in X and 1000 μm in Y with 600 x 200 points resolution. Each spectrum was integrated for 0.4 s. The advantage of confocal Raman microscopy is the retrievable spatial information of the sample, due to the possibility to shift the focal plane from the surface slightly into the sample. Thus it can be determined whether an observed peak derives from the sample or may be due to surface contamination.

EMP element mappings and chemical profiles were carried out with a JEOL JXA-8900RL.

Backscatter, cathode luminescence, Mn, Ca, Al and Si were mapped on an area of 3.5 mm length and 1.5 mm width at a resolution of 750 x 300 points. The acceleration voltage was set to 15 kV, the beam current to 50 nA.

For isotope measurements, sample material from the different mineral phases was obtained using a hand-held microdrill. A ThermoFinnigan Triton TI was used for the $^{87}\text{Sr}/^{86}\text{Sr}$ isotope analyses and a Thermo KIEL VI coupled to a Finnigan Delta⁺ gas mass spectrometer for $\delta^{13}\text{C}$ and $\delta^{18}\text{O}$ measurements.

6.5 Results

6.5.1 Microscopy

Investigation of microscopic thin sections using polarization microscopy revealed that the fracture fillings in the Äspö Diorite often consist of a fluorite phase, which initially precipitated onto the diorite, and calcite (Fig. 6.2). The calcite exhibits two crystal varieties, one with idiomorphic crystals (calcite phase 1) and one with poorly crystalline, granular calcite (calcite phase 2). Calcite phase 2 surrounds calcite phase 1, indicating a lower age of formation for the former (see also EMP results). Further, calcite phase 1 crystals seem altered, and smooth transitions between minerals of both calcite phases indicate partial dissolution of calcite phase 1 crystals and re-crystallisation with calcite phase 2. Along the boundary between the fluorite and the calcite phases, the fluorite crystals are corroded, showing some pocket-like niches (Fig. 6.2 C, D). A conspicuous layer of dark amorphous matter covers the immediate phase boundary, with some local enrichments in the pockets within the fluorite (Fig. 6.2). The thickness of this layer varies between 20 μm and 100 μm .

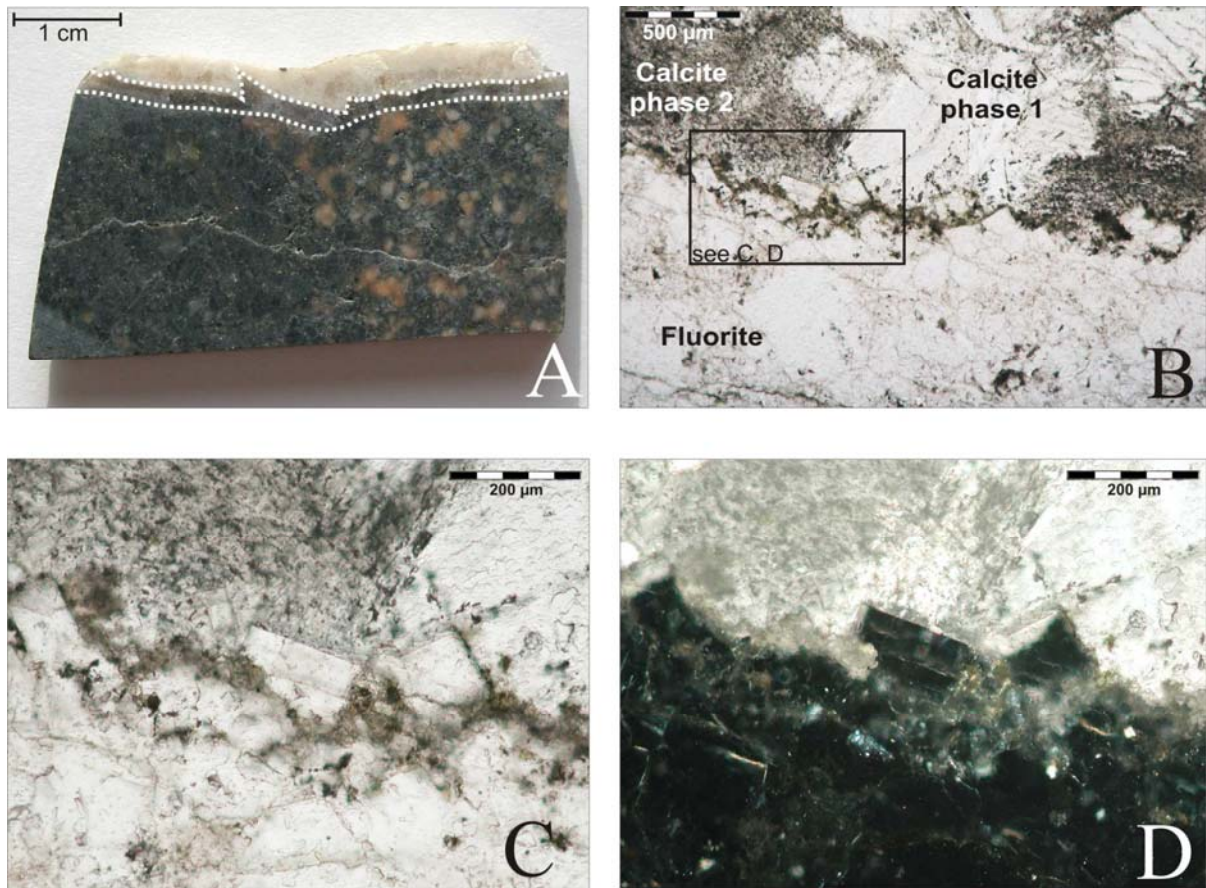


Fig. 6.2 Sections of the Äspö Diorite and the fracture minerals studied. (A) Thick section exhibiting a mineralized fracture on top of the diorite host rock. The dashed white lines indicate phase boundaries between the diorite and the fluorite, and between the fluorite and the calcites, respectively. (B) Thin section of the fracture minerals under transmitted light. Two calcite phases are distinguishable, one with idiomorphic transparent crystals (calcite phase 1) and one with granular and dull to opaque crystals (calcite phase 2), partly surrounding the former. The fluorite is altered and somehow corroded at the boundary to the calcite and small dark particles are distributed along this calcite-fluorite phase boundary. This amorphous matter is especially accumulated in small niches within of the fluorite. (C, D) Close-ups of the fluorite-calcite phase boundary, exhibiting the organic-rich amorphous layer under transmitted light (C) and corrosion marks on the fluorite surface along the contact area visible under cross-polarized light (D).

6.5.2 LA-ICP-MS

Trace element and REE concentrations of the fracture filling minerals are given in table 6.1. The results show that Fe and especially Mn are noticeably higher in calcite phase 1, whereas calcite phase 2 contains slightly higher amounts of Si and light REE (LREE, La-Sm). The amorphous layer at the boundary between the fluorite and the calcite phases exhibits particularly high amounts of Mg, Al, Si, Fe and REE.

UCC-normalized REE values (Fig. 6.3) show a considerable enrichment of heavy REE (HREE, Gd-Lu) within the calcite. A similar pattern is seen within the fluorite phase but with a preferential

enrichment of Gd to Er/Tm and less pronounced Yb and Lu. Both fluorite and calcite phases differ from the host rock, which shows a lower total REE content and a slight enrichment of LREE over HREE. In contrast to the calcite and fluorite phases, the dark amorphous layer between the calcite and fluorite phases exhibited a selective enrichment of the LREE, and a weak negative Eu anomaly (Fig. 6.3).

	Calcite Phase 1	Calcite Phase 1	Calcite Phase2	Calcite Phase 2	organic phase	organic phase	Fluorite	Fluorite
Ca	309850	395615	351174	430382	446169	414548	383600	368742
Mg	313	445	314	148	6595	9759	1130	1783
Al	126	224	152	175	7517	14613	1692	2450
Si	304	175	686	670	21796	41642	4054	5413
P	27	32	37	42	98	103	107	58
S	na	na	na	na	na	8	41	na
Mn	16434	25677	3847	6582	589	1184	112	127
Fe	1062	1703	565	345	10571	15937	2043	2552
Sr	90	78	99	106	87,6	99	60	67
Ba	8	5	21	43	50	128	359	195
La	21,80	24,06	45,8	55,62	149,2	239,9	23,67	31,25
Ce	42,35	45,45	53,2	72,93	263,0	354,1	40,49	50,79
Pr	4,65	4,95	4,7	6,49	25,53	43,98	5,19	6,06
Nd	17,60	18,80	17,3	24,87	124,8	242,7	24,72	28,70
Sm	4,16	4,64	3,7	5,39	18,33	28,58	6,54	6,51
Eu	1,14	1,22	0,9	1,28	8,32	4,20	1,51	1,43
Gd	4,84	4,70	4,3	4,62	20,51	21,27	8,86	8,19
Tb	1,10	1,06	0,8	1,04	2,78	2,85	1,73	1,42
Dy	7,50	7,70	5,7	6,84	18,17	15,27	11,26	9,07
Ho	1,74	1,77	1,3	1,70	3,38	3,27	2,21	1,93
Er	5,65	5,76	4,6	5,20	9,22	8,79	6,30	5,49
Tm	1,13	0,83	0,7	0,46	1,19	1,12	0,72	0,70
Yb	9,09	6,76	5,9	4,31	6,61	6,36	4,07	4,14
Lu	1,42	1,06	0,9	0,83	0,74	0,64	0,50	0,48
Th	0,01	na	0,0	0,11	1,32	1,35	0,19	0,14
U	0,01	0,01	0,0	0,14	0,91	0,98	0,07	0,11

Table 6.1 LA-ICP-MS and ICP-MS measurements of the fracture minerals. All values are given in ppm.

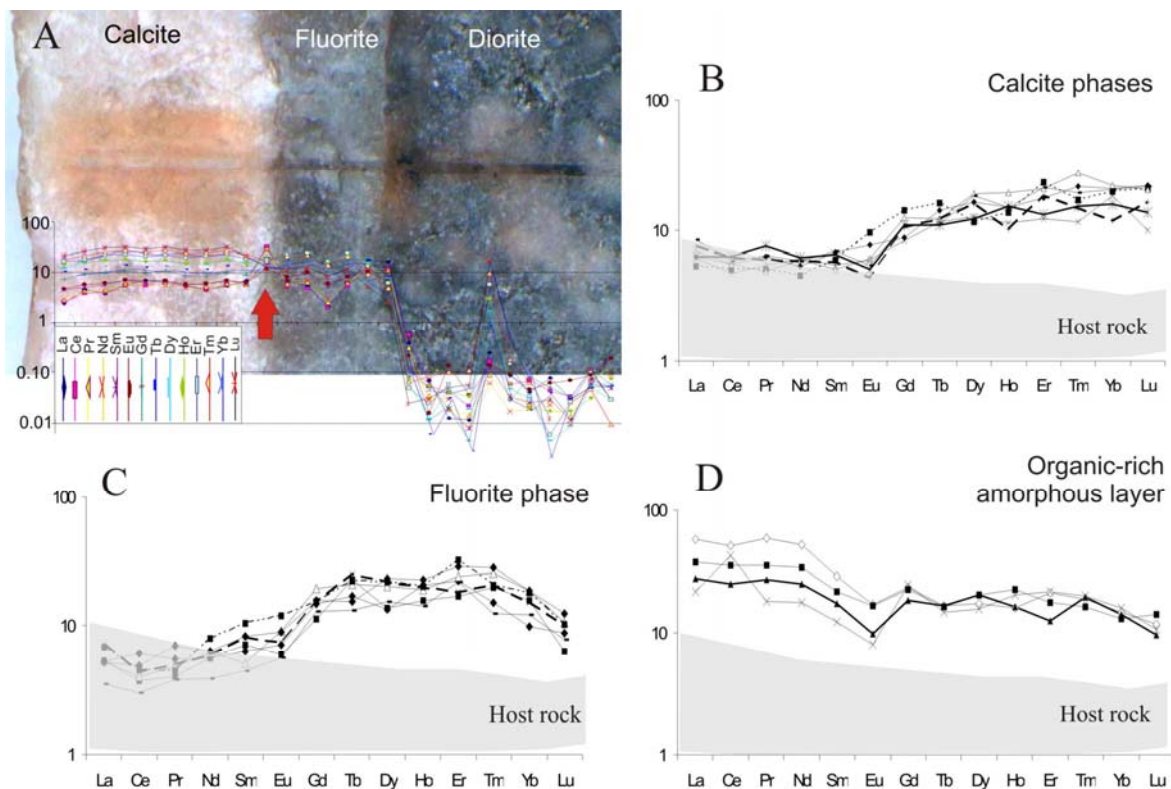


Fig. 6.3 REE data. (A) LA-ICP-MS line transecting the fracture fillings and the host rock. Note the distinct enrichment of REE at the calcite-fluorite phase boundary (red arrow). REE variations within the diorite are due to different minerals. (B, C, D) UCC-normalized REE patterns of the calcite phases (B), the fluorite phase (C), and the organic-rich amorphous layer (D). The gray shaded area in these diagrams denotes the range of host rock REE concentrations.

6.5.3 ToF-SIMS

Positive and negative ToF-SIMS spectra of the fracture minerals are shown in Fig. 6.4. Beside diagnostic ions produced by fluorite and calcite, e.g. F^- (19.00 Da) and $CaOH^+$ (56.97 Da), the presence of numerous organic fragments was observed (Table 2A, B). Due to the high mass resolution of the measurement ($M/\Delta M \sim 5000$), detailed assignments and separation of peaks at the same nominal mass, such as $CaOH^+$ (56.97 Da), $C_3H_5O^+$ (57.03 Da) and $C_4H_9^+$ (57.07 Da), were made possible. Organic fragments occur predominantly in the lower mass range, whereas no high-mass organic ions (> 400 Da) such as intact lipids were detected. Some of the organic ions contain nitrogen and oxygen, others are pure hydrocarbon fragments (Tables 6.2A, B).

Using the molecular imaging capacity of ToF-SIMS, the diagnostic mineral peaks F^- (19.00 Da) and $CaOH^+$ (56.97 Da) were used to map the fluorite and calcite phases, and the boundary between them (Fig. 6.5C, D). Most individual organic fragments show enhanced concentrations along the calcite-fluorite phase boundary, i.e. in the area of the dark amorphous layer (Fig. 6.5F,G). Sum images of the major positive and negative organic ions clearly illustrate that the organic fragments

are exactly co-localized with that layer (Fig. 6.5I, J). Organic molecules showing a low, but even distribution over the sample surface, such as the ion at 366.32 Da (Fig. 6.5K), were regarded as contaminants. Further interpretations are given in the discussion chapter.

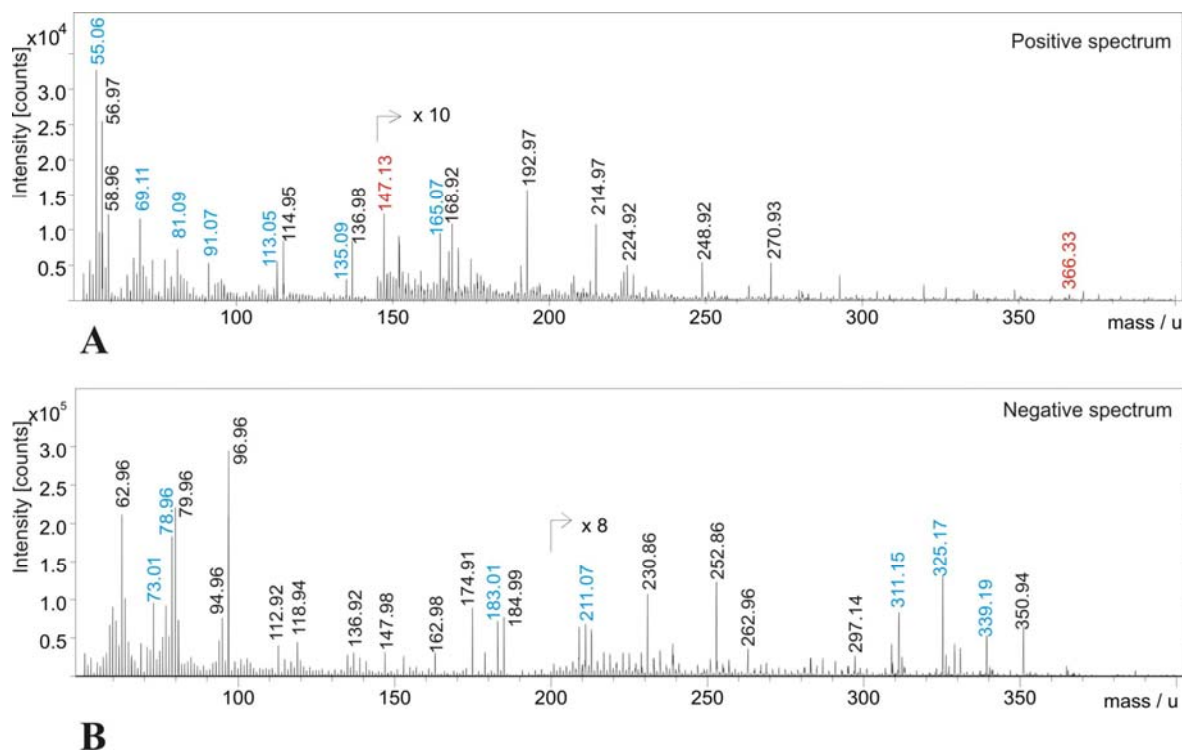


Fig. 6.4 Partial ToF-SIMS spectra from a 500 x 500 μm^2 area of the fracture minerals. (A) Positive spectrum. (B) Negative spectrum. Numbers denote observed m/z values of the respective peaks; black = inorganic ions; blue = organic ions, mainly derived from the organic-rich amorphous layer; red = contaminants (polydimethylsiloxane and unknowns).

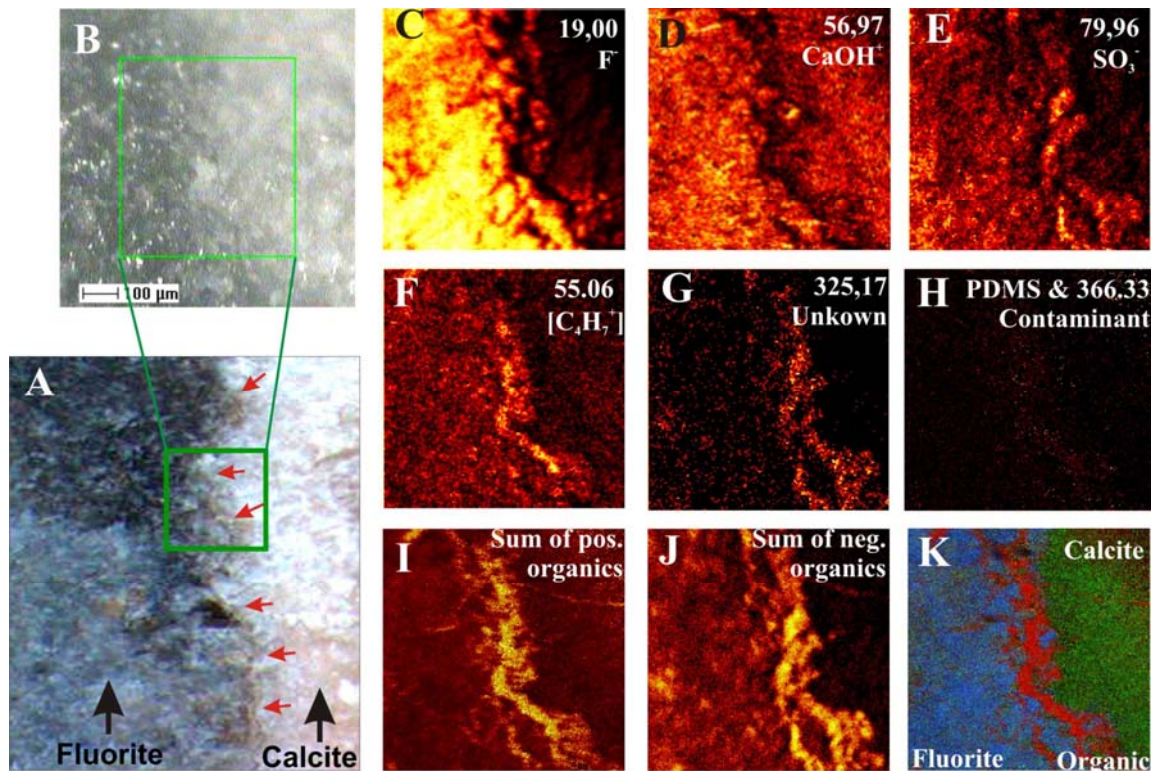


Fig. 6.5 ToF-SIMS ion images calculated from the spectra in Fig. 6.4. (A) Thick section under reflected light showing the phase boundary between fluorite and calcite, and the organic-rich amorphous layer (red arrows). The area mapped with ToF-SIMS is indicated by a green frame. (B) Close-up of the analysed area, as seen by the built-in video camera of the ToF-SIMS instrument. (C – K) Ion images obtained of F^- , fluor (C); $CaOH^+$, calcium-hydroxide (D); SO_3^- , derived from sulphate (E); $C_4H_7^+$, a small hydrocarbon fragment (F); an unknown organic ion of high molecular weight (G); summed ions derived from contaminants (H); sum of the most prominent positive organic ions (I); sum of the most prominent negative organic ions (J); colour overlay of three ion images for fluorite (F^- , blue), calcite (CaH^+ , green) and the organic-rich amorphous layer (summed ions, red), respectively (K).

Mass observed	Assignment	Theoretical mass
29.04	C ₂ H ₅	29.0391
30.03	CH ₄ N	30.0343
31.02	CH ₃ O	31.0184
41.04	C ₃ H ₅	41.0391
43.06	C ₃ H ₇	43.0548
44.05	C ₂ H ₆ N	44.0500
45.04	C ₂ H ₅ O	45.0340
53.04	C ₄ H ₅	53.0391
54.03	C ₃ H ₄ N	54.0344
55.02	C ₃ H ₃ O	55.0184
55.06	C ₄ H ₇	55.0548
56.06	C ₃ H ₆ N	56.0501
56.97	CaOH	56.9653
58.96	CaF	58.9610
57.04	C ₃ H ₅ O	57.0340
57.07	C ₄ H ₉	57.0704
59.05	C ₃ H ₇ O	59.0497
67.06	C ₅ H ₇	67.0548
69.04	C ₄ H ₅ O	69.0340
69.07	C ₅ H ₉	69.0704
71.06	C ₃ H ₇ N ₂	71.0609
73.06	C ₄ H ₉ O/C ₃ H ₇ NO	73.0653/ 73.0528
81.07	C ₆ H ₉	81.0704
83.06	C ₅ H ₇ O	83.0497
83.09	C ₆ H ₁₁	83.0861
84.05	C ₅ H ₈ O/ C ₄ H ₆ NO	84.0575/ 84.0449
84.09	C ₅ H ₁₀ N/ C ₆ H ₁₂	84.0813/ 84.0939
86.07	C ₅ H ₁₀ O / C ₄ H ₈ NO	86.0732/ 86.0606
91.06	C ₇ H ₇	91.0548
95.09	C ₇ H ₁₁	95.0861
102.05	C ₅ H ₁₀ S	102.0503
103.06	C ₅ H ₁₁ S/ C ₈ H ₇	103.0584/ 103.0548
107.09	C ₈ H ₁₁	107.0861
109.10	C ₈ H ₁₃	109.1017
115.05	C ₉ H ₇	115.0548
119.05	C ₅ H ₁₁ SO	119.0531
123.13	C ₉ H ₁₅	123.1174
128.06	C ₁₀ H ₈	128.0626
131.05	C ₉ H ₇ O	131.0497
135.09	C ₅ H ₁₃ NO ₃ / C ₈ H ₁₁ N ₂	135.0895/ 135.0922
138.14	C ₁₀ H ₁₈	138.1408
165.07	C ₆ H ₁₃ O ₅	165.0763
196.10	C ₁₄ H ₁₂ O	196.0888
213.10	C ₁₄ H ₁₃ O ₂	213.0916
366.33	Contam.	??

Table 6.2 A Overview of positive mass fragments observed with ToF-SIMS and their tentative assignments. Not all peaks related to the organic matter are presented here.

Mass observed	Assignment	Theoretical mass
41.00	C ₂ HO	41.0027
42.00	CNO	41.9980
43.02	C ₂ H ₃ O	43.0184
58.01	C ₂ H ₂ O ₂	58.0054
68.01	C ₃ H ₂ NO	68.01364
79.96	SO ₃	79.9568
93.04	C ₆ H ₅ O	93.0340
96.96	SO ₄ H	96.9596
117.03	C ₈ H ₅ O / C ₅ H ₉ O ₃	117.0340 /
133.06	C ₉ H ₉ O / C ₅ H ₉ O ₄	133.0653 / 133.0501
155.99	C ₆ H ₄ SO ₃ ??	155.9881
170.00	C ₇ H ₆ SO ₃ ??	170.0038
183.01	C ₈ H ₇ SO ₃ ??	183.0116
195.04	C ₁₃ H ₇ O ₂	195.0446
197.02	C ₉ H ₉ SO ₃ ?	197.0272
209.02	C ₉ H ₇ NSO ₃	209.0147
211.06	C ₁₃ H ₉ NO ₂	211.0633
221.02	unknown	
223.04	unknown	
225.06	unknown	
227.11	unknown	
235.05	unknown	
237.06	unknown	
239.07	unknown	
253.08	unknown	
255.08	unknown	
265.13	unknown	
267.10	unknown	
281.12	unknown	
293.17	unknown	
295.13	unknown	
297.14	unknown	
298.14	unknown	
309.15	unknown	
311.15	unknown	
323.16	unknown	
325.17	unknown	
337.18	unknown	
339.19	unknown	
353.20	unknown	

Table 6.2 B Overview of negative mass fragments observed with ToF-SIMS and their tentative assignments. Not all peaks related to the organic matter are presented here.

6.5.4 Raman Microscopy

To gain additional and complementary information about the organic molecules, their chemical bonding types and distribution within the fracture minerals, Raman microscopy was performed on the same drill core section as the ToF-SIMS analyses. Fig. 6.6A shows a combination of the ToF-SIMS image (Fig. 6.5K) and the Raman image. The Raman spectra obtained from the fracture mineral phases and the organic-rich amorphous layer in between are displayed in Fig. 6.6B. The spectra show characteristic fundamental vibrations at 1085, 711 and 285 cm^{-1} for calcite, and at 322 cm^{-1} for fluorite. Major Raman bands in the organic-rich amorphous layer range from 3050 to 3083 cm^{-1} and from 2850 to 2955 cm^{-1} , and can be attributed to C-H vibrations. Between 645 to 1625 cm^{-1} , less intense, but numerous bands of diverse vibrational modes of organic compounds were observed. The interpretations of these Raman bands are given in table 6.3. A minor part of the area analyzed showed a high autofluorescence without any specific peaks (Fig. 6.6B, yellow). The nature of this matter could not be further elucidated.

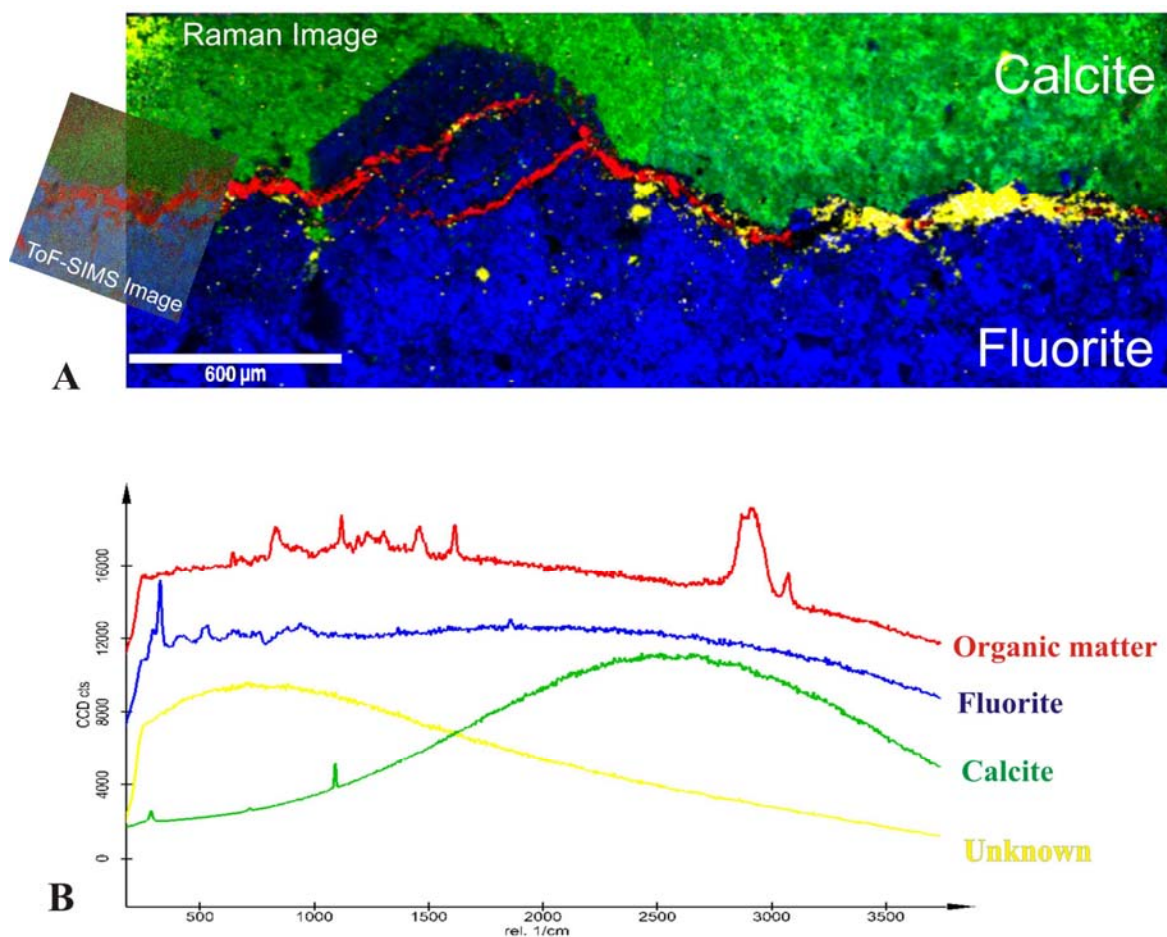


Fig. 6.6 Raman microscopy. (A) Colour-coded Raman image of the phase boundary between fluorite and calcite, extending the area mapped by ToF-SIMS (small image on the left, see Fig. 6.5 K). The colours relate to the corresponding Raman spectra that are characteristic for each mineral phase, see (B). (B) Raman spectra. Green = calcite; blue = fluorite; red = organic-rich amorphous layer; yellow = unidentified phase with high autofluorescence.

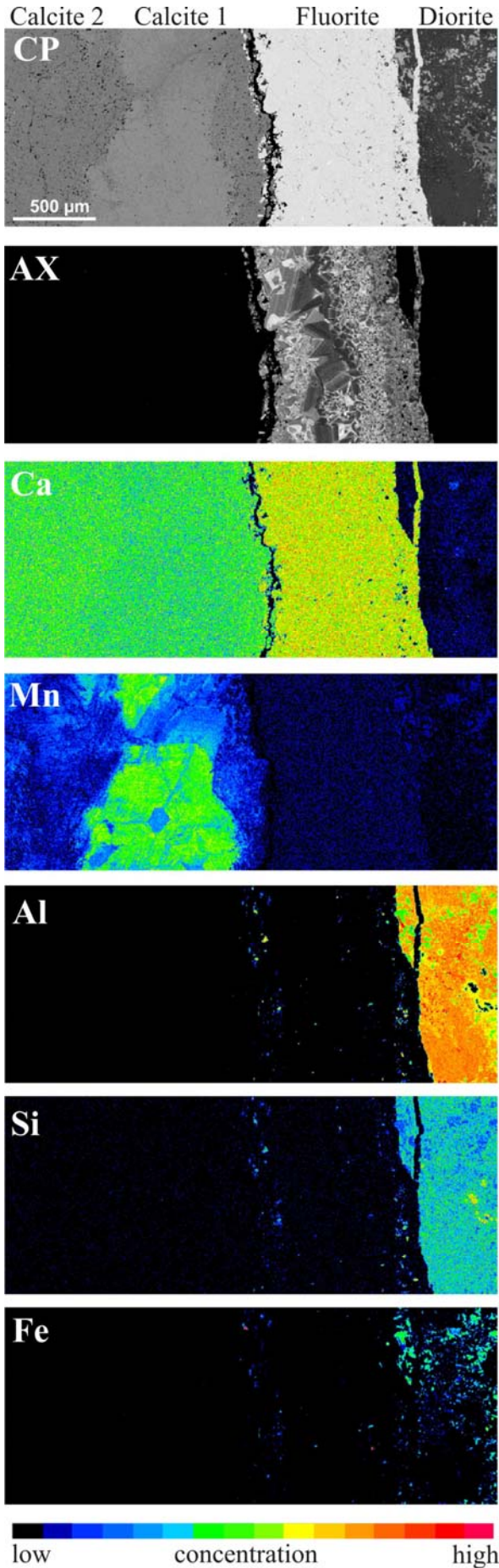
Peak range (Exact peak) cm^{-1}	Tentative assignments and references
3050 – 3083	$\nu(\text{CH})$ aromatic ⁹ , $\nu(\text{CH})$ olefinic ⁴ , $\nu(\text{CH})$, polycyclic aromatic ⁸
2900-2955	$\nu(\text{CH}_2)$ $\nu(\text{CH}_3)$ ⁸ , $\nu(\text{CH}_3)$ symm ⁴
2858 – 2970 (2870)	$\nu(\text{CH}_3)$ symm. ^{1, 8, 13} , $\nu(\text{CH}_3)$ asymm. ¹⁸ , $\nu(\text{CH}_2)$ symm. ⁴
2846	$\nu(\text{CH}_2)$ symm. ^{4, 18} , $\nu(\text{CH}_2)$ $\nu(\text{CH}_3)$ ⁸
1600 – 1625	$\nu(\text{C}=\text{C})$ arom. ring str. ⁷ , $\nu(\text{C}=\text{C})$ or $\nu(\text{C}=\text{O})$ ^{4, 6} , $\nu(\text{C}=\text{C})$ ³ , $\nu(\text{CO})$ ⁸ , Tyrosin, Trp ⁷ $\delta(\text{NH})$, $\nu(\text{C}-\text{N})$, amide II ^{16, 11, 5}
1615	Tyrosine, phenylalanine ¹² Tyrosine, tryptophan ¹⁹ , $\nu(\text{C}=\text{C})$ ^{4, 18} , $\nu(-\text{C}=\text{C}-)$ polycyclic ring system ⁸
1588	$\nu(\text{COO}^-)$ ²
(1568)	$(\text{C}=\text{C})$ ¹⁷ , Guanine, Adenine ^{5, 10}
1547	
(1520)	
1481	$\delta(\text{CH}_2)$ $\delta(\text{CH}_3)$ ⁸
1445-1465	(CH_2) deform. ^{12, 14} , $\delta(\text{CH}_2)$ ^{4, 16, 17, 18} , $\nu(\text{CH}_2)$, $\delta(\text{CH}_2)$ ¹⁹ , $\nu(\text{CO})$ or $\delta(\text{CH}_2)$ $\delta(\text{CH}_3)$ ⁸
1437	$\delta(\text{CH}_2)$ $\delta(\text{CH}_3)$ ⁸
1384-1397	$\nu(\text{C}=\text{C})$ in plane vibration, polycyclic ring system ⁸
1358-1370	$\delta \text{C}-\text{H}^2$
1341	$\delta(\text{CH}_2)$ ⁴
1323	$\delta(\text{OH})$, $\delta(\text{CH}_2)$ ¹⁸ , Protein (amide III), $\delta(\text{CH})$ ^{16, 17} , Guanine, adenine ^{5, 10}
1303	$\delta(\text{CH}_2)$ ⁴ , N-H (pyrole ring ⁸ , Adenine ¹² Amide III
1295	$\delta(\text{CH}_2)$ (1291, ⁴ $\delta(\text{CH}_2)$ twisting ⁸ , amide III ¹⁸
1276	$\delta(\text{CCH})$ ⁸
1262	$\delta(\text{CCH})$ $\delta(\text{CH}_2)$, twisting ⁸
1226-1246	Amide III, N-H, C-N ^{17, 7} $\delta(\text{CCH})$ (1226 ⁸ , $\nu(\text{C}-\text{O})$ ² Guanine, adenine ¹⁹ , Cytosin, thymine ¹² Amide III
1192	$\nu(\text{C}-\text{C})$ ⁴
1156	$\nu(\text{CC})$ ring breathing ⁸ , $\nu(\text{CC})$ ^{13, 14} , $\nu(\text{CC})$, $\delta(\text{COH})$ ¹⁸
(1110-1130) 1119	$=\text{C}-\text{C}=\text{unsatur. FA}$ ^{17, 28}
1094	$\nu(\text{CC})$ ring ⁸ , DNA ¹⁹
1076	$\nu(\text{CO})$ ⁸
1051	asym C-O-C glycosidic ²
(1038)	$\nu(\text{CO})$ ⁸
(1024)	$\rho(\text{CH}_2)$ ¹¹
(968)	$\rho(\text{CH}_3)$ ⁸
(956)	$\rho(\text{CH}_3)$ terminal ¹⁸ , $\nu(\text{CO})$ ⁸
936-937	$\rho(\text{CH}_3)$ terminal ¹⁸ , Protein: α -helix ¹²
922	$\rho(\text{CH}_2)$ ⁸
(908)	$\rho(\text{CH}_2)$ ⁸
881	$\rho(\text{CH}_2)$ ¹⁸
814-845 (840)	$\delta(\text{C}-\text{C})$, $\delta(\text{C}-\text{O})$, $\delta(\text{C}-\text{CH})$, $\delta(\text{C}-\text{C}-\text{O})$ ^{15, 18} , Ring breath Tyr ⁷ , $\delta(\text{C}-\text{CH})$ aromatic ⁴ , DNA, Tyrosine ¹⁹
(827)	$\nu(\text{CS})$ substituted thiophene ⁸ , $\delta(\text{CCH})$ ⁴ , Tyrosine ¹⁷
761-780	$\nu(\text{CC})$ ring or (COO) deform ⁸ $\delta(\text{C}_3\text{O}_2)$, $\rho(\text{CH}_2)$ ¹¹ , $\nu(\text{CC})$ ⁴ , Nucleic acids ¹⁶
734-747	Ring breathing ² $\nu(\text{CC})$ ^{4, 8}
645	Tyrosine ^{12, 19} $\nu(\text{CC})$, $\delta(\text{C}_3\text{O}_2)$ ¹¹ , $\delta(\text{NCO})$ ¹⁸ , ring deformation ²

Table 6.3 Raman bands observed within the fracture. ν stretching, δ bending, ρ rocking, π , ω wagging, τ twisting.

References Raman assignments:

- [1] Arouri K, Greenwood PF, Walter MR (2000) Biological affinities of Neoproterozoic acritarchs from Australia: microscopic and chemical characterisation. *Organic Geochemistry*, **31**, 75-89.

- [2] Campos-Vallette MM, Chandía NP, Clavijo E, Leal D, Matsuhira B, Osorio-Román IO, Torres S (2009) Characterization of sodium alginates and its block fractions by surface-enhanced Raman spectroscopy. *Journal of Raman Spectroscopy*, 2517-2523.
- [3] Czaja AD, Kudryavtsev AB, Cody GD, Schopf JW (2009) Characterization of permineralized kerogen from an Eocene fossil fern. *Organic Geochemistry*, **40**, 353-364.
- [4] Edwards HGM, Farwell DW, Quye A (1997) 'Dragon's Blood' I – Characterization of an Ancient Resin Using Fourier Transform Raman Spectroscopy. *Journal of Raman Spectroscopy*, **28**, 243-249.
- [5] Gaus K, Rösch P, Petry R, Peschke K-D, Ronneberger O, Burkhardt H, Baumann K, Popp J (2006) Classification of Lactic Acid Bacteria with UV-Resonance Raman Spectroscopy. *Biopolymers*, **82**, 286-290.
- [6] Himmelsbach DS, Akin DE (1998) Near-Infrared Fourier-Transform Raman Spectroscopy of Flax (*Linum usitatissimum* L.) Stems. *Journal of Agricultural and Food Chemistry*, **46**, 991-998.
- [7] Ivleva NP, Wagner M, Horn H, Niessner R, Haisch C (2009) Towards a nondestructive chemical characterization of biofilm matrix by Raman spectroscopy. *Analytical and Bioanalytical Chemistry*, **393**, 197 – 206.
- [8] Jehlička J, Edwards HGM (2008) Raman spectroscopy as a tool for the non-destructive identification of organic minerals in the geological record. *Organic Geochemistry*, **39**, 371-386.
- [9] Jenkins AL, Larsen RA, Williams TB (2005) Characterization of amino acids using Raman spectroscopy. *Spectrochimica Acta Parta A*, **61**, 1585-1594.
- [10] Lopez-Diez EC, Goodacre R (2004) Characterization of Microorganisms using UV Resonance Raman Spectroscopy and chemometrics. *Analytical Chemistry*, **76**, 585-591.
- [11] Mendham AP, Potter BS, Palmer RA, Dines TJ, Mitchell JC, Withnall R, Chowdhry BZ (2009) Vibration spectra and crystal structure of the di-amino acid peptide cyclo(L-Met-L-Met): comparison of experimental data and DFT calculations. *Journal of Raman Spectroscopy*, **41**, 148-159.
- [12] Puppels GJ, Garritsen HSP, Segers-Nolten GMJ, de Mul FFM, Greve J (1991) Raman microspectroscopic approach to the study of human granulocytes. *Biophysical Journal*, **60**, 1046-1056.
- [13] Rösch P, Harz M, Schmitt M, Peschke K-D, Ronneberger O, Burkhardt H, Motzkus H-W, Lankers M, Hofer S, Thiele H, Popp J (2005) Chemotaxonomic Identification of Single Bacteria by Micro-Raman Spectroscopy: Application to Clean-Room-Relevant Biological Contaminations. *Applied Environmental Microbiology*, **71**, 1626-1637.
- [14] Rösch P, Schmitt M, Kiefer W, Popp J (2003) The identification of microorganisms by micro-Raman. *Journal of Molecular Structure*, **661-662**: 363-369.
- [15] Schmid T, Messmer A, Yeo B-S, Zhang W, Zenobi R (2008) Towards chemical analysis of nanostructures in biofilms II: tip-enhanced Raman spectroscopy of alginates. *Analytical and Bioanalytical Chemistry*, **391**, 1907 – 1916.
- [16] Schuster KC, Reese I, Urlaub E, Gapes JR, Lendl B (2000a) Multidimensional information on the chemical composition of single bacterial cells by confocal Raman Microscopy. *Analytical Chemistry*, **72**, 5529-5534.
- [17] Schuster KC, Urlaub E, Gapes JR (2000b) Single-cell analysis by Raman microscopy: spectral information on the chemical composition of cells and on the heterogeneity in a culture. *Journal of Microbiological Methods*, **42**, 29-38.
- [18] Williams AC, Edwards HGM (1994) Fourier Transform Raman Spectroscopy of Bacterial Cell Walls. *Journal of Raman Spectroscopy*, **25**, 673-677.
- [19] Zinin PV, Misra A, Kamemoto L, Yu Q, Hu N, Sharma SK (2010) Visible, near-infrared, and ultraviolet laser excited Raman Spectroscopy of the monocytes/macrophages(U937) cells. *Journal of Raman Spectroscopy*, **41**, 268-274.



6.5.5 EMP

Fig. 6.7 shows backscatter electron (CP) and cathode luminescence (AX) images and the relative intensities of Ca, Mn, Al, Si, and Fe within the fracture minerals. Complementary to the microscopic and LA-ICP-MS data, the CP and the Mn mapping clearly indicate two calcite phases, with calcite phase 1 surrounding calcite phase 2 and the latter showing a higher Mn content along with mineral growth zonation. The organic-rich amorphous layer exhibits consistently higher Al, Si and Fe concentrations than the fluorite and calcite phases, which is in good agreement with the data obtained by the LA-ICP-MS.

Fig. 6.7 EMP mappings of the fracture minerals. CP = back scatter electron image showing the different mineral phases; AX = cathode luminescence image exhibiting growth zonation within the fluorite. Note enrichment and growth zonation of Mn in calcite phase 1. Al, Si and Fe are highly enriched in the diorite, but is also accumulated along the boundary between fluorite and calcite.

6.5.6 Isotope Analysis

$\Delta^{13}\text{C}$, $\delta^{18}\text{O}$ and $^{87}\text{Sr}/^{86}\text{Sr}$ values are provided in Table 6.4. The isotope data of the individual phases are relatively homogenous. The $\delta^{13}\text{C}$ values of the calcite phases range from -8.6 to -5.3 ‰ and the $\delta^{18}\text{O}$ values from -9.3 to -8.5 ‰ (PDB). The $^{87}\text{Sr}/^{86}\text{Sr}$ ratios of the calcite phase 1 range from 0.7120 to 0.7124, whereas the calcite phase 2 and the organic-rich amorphous layer vary from 0.7133 to 0.7137. $^{87}\text{Sr}/^{86}\text{Sr}$ values in the fluorite vary significantly, from 0.7125 near calcite phase boundary to 0.7096 at the fluorite-diorite boundary. For the diorite host rock, the $^{87}\text{Sr}/^{86}\text{Sr}$ ratios of 0.7063 were obtained at about 1 cm distance from the fracture.

	$^{87}\text{Sr}/^{86}\text{Sr}$	2σ	$\delta^{13}\text{C}$	$\text{ST e } \delta^{13}\text{C}$	$\delta^{18}\text{O}$ (PDB)	$\text{ST e } \delta^{18}\text{O}$
Calcite phase 1	0.712023	0.000008	-5.268	0.005	-9.289	0.007
Calcite phase 2	0.713349	0.000015	-8.641	0.008	-8.519	0.011
Amorphous phase (P1)	0.713352	0.000029				
Amorphous phase (P1)	0.713654	0.000016				
Fluorite	0.712530	0.000024				
Diorite-fluorite border	0.709621	0.000012				
Diorite	0.706252	0.000015				

Table 6.4 Isotope data observed for the fracture minerals.

6.6 Discussion

6.6.1 Fracture mineral generations

According to the mineralogy observed, the host rock of the fracture fillings can be specified as a quartz monzodiorite (Wahlgren *et al.*, 2004, 2006).

The $\delta^{18}\text{O}$ values and the $^{87}\text{Sr}/^{86}\text{Sr}$ ratios (Tab. 4) of the calcite phases enable an assignment of the Mn-rich calcite phase 1 to fracture generation 5a (<0.7132) from Paleozoic brines of ca 80°C (Wallin *et al.*, 2007; Drake and Tullborg, 2009). The $\delta^{18}\text{O}$ values are consistent with those of previously described Mn-rich fracture calcites from the Äspö area (Tullborg *et al.*, 2008). According to Milodowski *et al.*, (2005), the uptake of high amounts of Mn(II) in the calcite lattice indicates reducing conditions during crystallization. It has also been suggested that Mn(II) incorporation in calcites is enhanced by elevated temperatures during mineral formation (Dromgoole and Walter, 1989). Both, reducing conditions and elevated temperatures, are in good agreement with a precipitation of calcite phase 1 from Paleozoic brines.

A clear assignment of calcite phase 2 and the organic-rich amorphous layer to a discrete fracture mineral generation was more difficult, as their isotopic signatures do not fit exactly into the values previously reported for different calcite generations (Drake and Tullborg, 2009). These phases exhibit slightly higher $^{87}\text{Sr}/^{86}\text{Sr}$ ratios than those reported for generation 5a, but are significantly lower than those reported for generation 5b and 6 (Drake and Tullborg, 2009). A possible explanation relates to glacially induced faulting during the Quaternary (Lund, 2006). Such

reactivation of the old fracture systems would have allowed glacial, meteoric and marine waters to deeply penetrate into the host rock. Indeed, in the Äspö Hard Rock Laboratory, traces of glacial and Littorina Sea water have been found down to depths of 840 m and 500 m, respectively (Wallin *et al.*, 2007). Partial dissolution of the pre-existing calcites (calcite phase 1) and mixing with new fluids may have caused local “blurring” of the original $^{87}\text{Sr}/^{86}\text{Sr}$ ratio during the precipitation of calcite phase 2.

Considering the sequence of the fracture minerals and the assignments of the calcite phases to the generations 5 and 6, the fluorite is most likely related to an older, Precambrian, fracture generation (1 to 4). Indeed, $^{87}\text{Sr}/^{86}\text{Sr}$ ratios at the fluorite-diorite contact zone are consistent with fracture generation 3, thereby corroborating the hypothesis that the fluorite was precipitated from Precambrian hydrothermal fluids. A somewhat higher $^{87}\text{Sr}/^{86}\text{Sr}$ ratio observed immediately at the phase boundary towards the calcite may be due to alteration of the fluorite during fracture reactivation.

6.6.2 REE and trace elements

LREE depletions and HREE enrichments, as observed in the fracture fluorite (Fig. 6.3 C), are frequent features in hydrothermal fluorite, due to different sorption and complexation properties among the REE during mineral formation (e.g. Sallet *et al.*, 2005; Schwinn and Markl, 2005). Differences between the REE patterns of the fracture fluorite and the Äspö Diorite indicate a different source rock chemistry of the hydrothermal fluid and insignificant host rock leaching (Schwinn and Markl, 2005).

The REE pattern of the calcite phases, with an enrichment of HREE over LREE (Fig. 6.3 B), is similar to that of Baltic Sea water near the Äspö area (Rönnback *et al.*, 2008). It reflects REE transport (and precipitation) mainly as carbonate complexes, which, in turn, indicates source fluids with low organic content (Tullborg *et al.*, 1999).

An enrichment of LREE over HREE, as observed in the organic-rich amorphous layer, may result from REE complexation with organic matter rather than HCO_3 (Tullborg *et al.*, 2008, and references therein; Ingri *et al.*, 2000). Increased abundances of LREE have also been described for overburden groundwaters from the Simpevarp/Äspö area, which show higher contents of Fe-rich colloids and dissolved organic matter (DOM, Rönnback *et al.*, 2008).

REE, like metal cations in general, are easily adsorbed by or form complexes with exposed negatively charged organic surfaces. Especially extracellular polymeric substances (EPS) in biofilms offer such surfaces and thus often show strong enrichments of trace elements and REE (Urrutia and Beveridge, 1993; Ngwenya *et al.*, 2009). In conclusion, the observed distinct enrichments of LREE, Mg, Al, Si, and Fe may plausibly be considered as a signature for a biofilm-derived origin of the organic-rich amorphous layer.

6.6.3 Organic matter composition

ToF-SIMS – Most of the hydrocarbon fragments observed in the organic-rich amorphous layer (Tab. 6.2a) show a relative C/H ratio between 0.4 and 0.8 which can be attributed to aliphatic hydrocarbons. Likewise $C_2H_5^+$, $C_3H_7^+$, $C_4H_9^+$ indicate saturated hydrocarbons fragments, whereas $C_3H_5^+$, $C_4H_7^+$, $C_5H_9^+$ may derive from unsaturated hydrocarbon moieties. Only few fragments, e.g. $C_9H_7^+$, have a high C/H ratio between 1 and 2, indicative for aromatic hydrocarbons (NIST database, Toporski and Steele, 2004, and references therein). $C_8H_{11}^+$, $C_8H_{13}^+$, $C_9H_{15}^+$, on the other hand, likely derive from longer saturated hydrocarbon chains, and have been reported as prominent fragments in the spectra of acyclic isoprenoids (Toporski *et al.*, 2002). Major oxygen-functionalized ions found in the organic-rich amorphous layer, namely CH_3O^+ , $C_2H_5O^+$, $C_3H_5O^+$, and $C_4H_5O^+$, are very abundant in the spectra of carbohydrates (Sjövall *et al.*, 2004). Nitrogen-containing ions such as CH_4N^+ , $C_2H_6N^+$, $C_3H_6N^+$, and $C_3H_2NO^+$ are major products of nitrogen-containing biogenic compounds such as amino acids and purines (Lu *et al.*, 2004; Spool, 2004; Lee *et al.*, 2006).

In the negative spectrum, an alkylation series ranging from m/z 255.08 to 353.20 was observed, maximizing at m/z 311.15, 325.17 and 339.19. A further parallel alkylation series ranges from m/z 239.07 to 337.18. These unidentified negative ions can tentatively be attributed to $[M-H]^-$ or $[M-OH]^-$ ions containing a major saturated hydrocarbon moiety together with (a) carboxyl or hydroxyl functional group(s). Particularly carboxylic acids produce strong $[M-H]^-$ ions rather than $[M]^+$, $[M+H]^+$ and $[M+Na]^+$ (Vickerman and Briggs, 2001). This interpretation is supported by fragments characteristic for carboxyl-bearing molecules ($C_2H_3O^-$, $C_2H_2O_2^-$; Dubey *et al.*, 2009) in the negative ToF-SIMS spectrum of the organic-rich amorphous layer.

In ToF-SIMS, it is possible to robustly assign an individual mass peak to a chemical structure only for low-mass fragments, or known analytes in pre-characterized samples (Vickerman and Briggs, 2001). The identification of unknown organic compounds, however, should ideally rely on the presence of several characteristic fragments in the spectrum, and comparison with standard data (Heim *et al.*, 2009). For negative ToF-SIMS spectral data, this is hampered by the still limited number of published reference spectra (see also Spool, 2004). Whereas no intact lipid biomarkers were identified in the organic-rich amorphous layer, the small and partly functionalized organic molecules observed may be plausibly related to EPS. EPS in biofilms are composed of polysaccharides, proteins, nucleic acids, lipids and humic substances (Nielsen *et al.*, 1997) and may constitute between 50 and 90 % of the total organic matter (Wingender *et al.*, 1999).

Raman microscopy – In the 1625 - 1568 cm^{-1} range, C=C stretching in the Raman spectra of the organic-rich amorphous layer indicate unsaturation (van de Voort *et al.*, 2001), including aromatisation (Jehlička and Edwards, 2008). Characteristic bands for amino acids (amide II),

however, are also observed in this range (Schuster *et al.*, 2000a; Ivleva *et al.*, 2009; Zinin *et al.*, 2010). Bendings of CH₂ and CH₃ groups are predominantly observed at 1481-1437 cm⁻¹ and band complexes between 1323 and 1226 cm⁻¹ further suggest the presence of amino and nucleic acids, respectively (Puppels *et al.*, 1991; Schuster *et al.*, 2000b; Zinin *et al.*, 2010). The complex band pattern between 1200 and 1000 cm⁻¹ is mainly assigned to C-O and C-C stretching. Further small bands between 968 and 881 cm⁻¹ are related to CH₂ and CH₃ rocking vibrations (Williams and Edwards, 1994; Jehlička and Edwards, 2008), whereas bands between 845-815 cm⁻¹ are related to C-C, C-O bending modes (Williams and Edwards 1994; Edwards *et al.*, 1997; Schmid *et al.*, 2008) or ring breathing modes of tyrosine (Ivleva *et al.*, 2009; Zinin *et al.*, 2010). Raman bands related to bending of NCO or tyrosine are observed at 645 cm⁻¹ (Puppels *et al.*, 1994; Williams and Edwards, 1994; Zinin *et al.*, 2010).

Considering that Raman vibrations, their variation and intensity strongly depend on the orientation and the physical conditions of the material investigated (Nasdala *et al.*, 2004), the Raman data of the organic-rich amorphous layer indicated diverse, functionalized organic molecules comprising amino acids, nucleic acids, carbohydrates, aromatic and unsaturated hydrocarbons. These results strongly support the interpretations drawn from the ToF-SIMS data, i.e., that the organic-rich amorphous layer constitutes remains of a (relatively recent) fossil biofilm.

6.7 Conclusion and potential fracture reactivation scenario

A comprehensive analytical approach enabled a reconstruction and integrated understanding of ancient environmental processes that occurred within the continental deep biosphere. The analyses were performed on minute amounts of fracture minerals, i.e. at the microscopic range (µm-scale), while leaving the integrity of the studied structures virtually intact. The Äspö Diorite contains four generations of fracture fillings. The first generation is a fluorite phase, derived from Precambrian hydrothermal fluids. The second mineral phase consists of Mn-rich calcites (calcite phase 1), precipitated from Palaeozoic brine fluids. The third mineral phase is a 20-100 µm thick, organic-rich amorphous layer that is interpreted to represent a fossilized biofilm whose formation was induced by glacial reactivation of the fracture system and subsequent water injections during the Late Pleistocene. ToF-SIMS and Raman imaging revealed fragments and bond types clearly indicative of hydrocarbon moieties as well as N- and O-containing organic heterocompounds. These organic compounds are exactly co-localized with the dark amorphous layer and may largely derive from biofilm-associated EPS. The formation and growth of a biofilm in the fracture reasonably explains the observed fractionations and accumulations of LREE, Mg, Al, Si, and Fe. The breakdown of functionalized molecules occurs rapidly when considering geological time scales, however this biofilm still shows a good preservation indicating a relatively recent formation

rather than a Palaeozoic or even Precambrian age. A change in the chemical composition (salinity and alkalinity) of the supplying water presumably lead to crystallization of the fourth fracture mineral phase (calcite mineral phase 2), thereby terminating the growth and existence of the subsurface biofilm.

Acknowledgements

.....Journal reviewers..... We are grateful to Emmeli Johansson, Magnus Kronberg, Carljohan Hardenby and Oskar Sigurdsson from SKB for technical and logistic support at the Äspö Hard Rock Laboratory. Wolfram Ibach (Witec GmbH) is acknowledged for software support. Our study received financial support from the German Research Foundation (DFG). This is publication no. XX of the DFG Research Unit FOR 571 ‘Geobiology of Organo- and Biofilms’.

References

- Abramov O, Mojzsis S (2009) Microbial habitability of the Hadean earth during late heavy bombardment. *Nature*, **459**, 419-422.
- Åhäll K-I (2001) Åldersbestämning av svårdaterade bergarter i sydöstra Sverige. Svensk Kärnbränslehantering AB, **R-01-60**, 24 p.
- Amend JP, Teske A (2005) Expanding frontiers in deep subsurface microbiology. *Palaeogeography, Palaeoclimatology, Palaeoecology*, **219**, 131– 155.
- Anbar AD (2004) Iron stable isotopes: beyond biosignatures. *Earth and Planetary Science Letters*, **217**, 223-236.
- Arouri K, Greenwood PF, Walter MR (2000) Biological affinities of Neoproterozoic acritarchs from Australia: microscopic and chemical characterisation. *Organic Geochemistry*, **31**, 75-89.
- Banerjee NR, Furnes H, Muehlenbachs K, Staudigel H, de Wit M (2006) Preservation of ~3.4-3.5 Ga microbial biomarkers in pillow lavas and hyaloclastites from the Barberton Greenstone Belt, South Africa. *Earth and Planetary Science Letters*, **241**, 707-722.
- Blumenberg M, Seifert R, Petersen S, Michaelis W (2007) Biosignatures present in a hydrothermal massive sulphide from the Mid-Atlantic Ridge. *Geobiology*, **5**, 435-450.
- Bons PD, Montenari M, Bakker RJ, Elburg M (2009) Potential evidence of fossilised Neoproterozoic deep life: SEM observations on calcite veins from Oppaminda Creek, Arkooola, South Australia. *International Journal of Earth Sciences*, **98**, 327-343.
- Brocks JJ, Pearson A (2005) Building the biomarker tree of life. *Reviews in Mineralogy and Geochemistry*, **59**, 233-258.
- Canfield DE (2001) Biogeochemistry of Sulfur Isotopes. *Reviews in Mineralogy and Geochemistry*, **43**, 607-636.

- Campos-Vallette MM, Chandía NP, Clavijo E, Leal D, Matsuhira B, Osorio-Román IO, Torres S (2009) Characterization of sodium alginates and its block fractions by surface-enhanced Raman spectroscopy. *Journal of Raman Spectroscopy*, DOI 10.1002/jrs.2517.
- Czaja AD, Kudryavtsev AB, Cody GD, Schopf JW (2009) Characterization of permineralized kerogen from an Eocene fossil fern. *Organic Geochemistry*, **40**, 353-364.
- Dideriksen K, Christiansen BC, Frandsen C, Balic-Zunic T, Mørup S, Stipp SLS (2010) Paleo-redox boundaries in fractured granite. *Geochimica et Cosmochimica Acta*, **74**, 2866-2880.
- Dobretsov NL, Kolchanov NA, Suslov VV (2006) On the early stages of the evolution of the geosphere and biosphere. *Paleontological Journal*, **40**, 407-424.
- Drake H, Tullborg E-L (2009) Paeohydrological events recorded by stable isotopes, fluid inclusions and trace elements in fracture minerals in crystalline rock, Simpevarp area, SE Sweden. *Applied Geochemistry*, **24**, 715-732.
- Drake H, Page L, Tullborg, E-L (2007) Oskarshamn site investigations. $^{40}\text{Ar}/^{39}\text{Ar}$ dating of fracture minerals. Svensk Kärnbränslehantering AB, **P-07-27**, 42 p.
- Drake H, Tullborg E-L (2006) Oskarshamn site investigation. Fracture mineralogy, Results from drill core KSH03A + B. Svensk Kärnbränslehantering AB, **P-06-03**, 56 p.
- Drake H, Tullborg E-L (2004) Oskarshamn site investigation. Fracture mineralogy and wall rock alteration. Results from drill core KSH01A+B. Svensk Kärnbränslehantering AB, **P-04-250**, 112 p.
- Dromgoole EL, Walter LM (1981) Iron and manganese incorporation into calcite: Effects of growth kinetics, temperature and solution chemistry. *Chemical Geology*, **81**, 311-336.
- Dubey M, Emoto K, Cheng F, Gamble LJ, Takahashi H, Grainger DW, Castner DG (2009) Surface analysis of photolithographic patterns using ToF-SIMS and PCA. *Surface and Interface Analysis*, **18**, 645-652.
- Edwards HGM, Farwell DW, Quye A (1997) 'Dragon's Blood' I – Characterization of an Ancient Resin Using Fourier Transform Raman Spectroscopy. *Journal of Raman Spectroscopy*, **28**, 243-249.
- Eydal, HSC, Jägevall S, Hermansson M, Pedersen K (2009) Bacteriophage lytic to *Desulfovibrio aespoensis* isolated from deep groundwater. *The ISME Journal*, **3**, 1139-1147.
- Gaus K, Rösch P, Petry R, Peschke K-D, Ronneberger O, Burkhardt H, Baumann K, Popp J (2006) Classification of Lactic Acid Bacteria with UV-Resonance Raman Spectroscopy. *Biopolymers*, **82**, 286-290.
- Heim C, Sjövall P, Lausmaa J, Leefmann T, Thiel V (2009). Spectral characterisation of eight glycerolipids and their detection in natural samples using time-of-flight secondary ion mass spectrometry. *Rapid Communications In Mass Spectrometry*, **23**, 2741-2753.
- Himmelsbach DS, Akin DE (1998) Near-Infrared Fourier-Transform Raman Spectroscopy of Flay (*Linum usitatissimum L.*) Stems. *Journal of Agricultural and Food Chemistry*, **46**, 991-998.
- Hinrichs, K.-U., Hayes, J. M., Sylva, S. P., Brewer, P. G., DeLong, E. F., 1999. Methane-consuming archaeobacteria in marine sediments. *Nature*, **398**, 802-805.
- Hofmann BA, Farmer JD, von Blanckenburg F, Fallick AE (2008) Subsurface filamentous fabrics: An evaluation of origins based on morphological and geochemical criteria, with implications for exopaleontology. *Astrobiology*, **8**, 87-117.

- Horsfield B, Schenk HJ, Zink K, Ondrak R, Diekmann V, Kallmeyer J, Mangelsdorf K, di Primo R, Wilkes H, Parkes RJ, Fry J, Cragg B (2006) Living microbial ecosystems within the active zone of catagenesis: Implications for feeding the deep biosphere. *Earth and Planetary Science Letters*, **246**, 55-69.
- Ingri J, Widerlund A, Land M, Gustafsson Ö, Andersson P, Öhlander B (2000) Temporal variations in the fractionation of the rare earth elements in a boreal river; the role of colloidal particles. *Chemical Geology*, **166**, 23-45.
- Ivarsson M, Lausmaa J, Lindblom S, Broman C, Holm NG (2008) Fossilized microorganisms from the Emperor Seamounts: implications for the search for a subsurface fossil record on Earth and Mars. *Astrobiology*, **8**, 1139-1157.
- Ivleva NP, Wagner M, Horn H, Niessner R, Haisch C (2009) Towards a nondestructive chemical characterization of biofilm matrix by Raman spectroscopy. *Analytical and Bioanalytical Chemistry*, **393**, 197-206.
- Jehlička J, Edwards HGM (2008) Raman spectroscopy as a tool for the non-destructive identification of organic minerals in the geological record. *Organic Geochemistry*, **39**, 371-386.
- Jenkins AL, Larsen RA, Williams TB (2005) Characterization of amino acids using Raman spectroscopy. *Spectromchimica Acta Part A*, **61**, 1585-1594.
- Joachimski MM, Ostertag-Henning C, Pancost RD, Strauss H, Freeman KH, Littke R, Sinninghe Damsté JS, Racki G (2001) Water column anoxia, enhanced productivity and concomitant changes in $\delta^{13}\text{C}$ and $\delta^{34}\text{S}$ across the Frasnian-Famennian boundary (Kowala – Holy Cross Mountains /Poland). *Chemical Geology*, **175**, 109-131.
- Jochum KP, Nohl U, Herwig K, Lammel E, Stoll B, Hofmann AW (2005) GeoReM: a new geochemical database for reference materials and isotopic standards, *Geostandards and Geoanalytical Research*, **29**, 333-8.
- Kornfält KA, Persson PO, Wikman H (1997) Granitoids from the Äspo area, southeastern Sweden; geochemical and geochronological data. *Geologiska Föreningens i Stockholm Förhandlingar*, **119**, 109-114.
- Kotelnikova S (2002) Microbial production and oxidation of methane in deep subsurface. *Earth-Science Reviews*, **58**, 367-395.
- Kotelnikova S, Pedersen K (1998) Distribution and activity of methanogenes and homoacetogenes on deep granitic aquifers at Äspö Hard Rock Laboratory, Sweden. *FEMS Microbiology Ecology*, **26**, 121-134.
- Kyle JE, Eydal HSC, Ferris FG, Pedersen K (2008) Viruses in granitic groundwater from 69 to 450 m depth of the Äspö Hard Rock Laboratory, Sweden. *The ISME Journal*, **2**, 571-574.
- Laaksoharju M, Smellie J, Gimeno M, Auqué L, Gómez J, Tullborg E-L, Gurban I (2004) Hydrogeochemical evaluation of the Simpevarp area, model version 1.1. Svensk Kärnbränslehantering AB, **R-04-16**, 398 p.
- Lee TG, Shon HK, Kim MS, Le HB, Moon DW (2006) ToF-SIMS imaging of gradient polyethylene and its amine-functionalized surfaces. *Applied Surface Sciences*, **252**, 6754-6756.

- Li J-X, Gardella JA Jr, McKeown PJ (1995) A quantitative time-of-flight secondary ion mass spectrometry study of ion formation mechanisms using acid-base alternating Langmuir-Blodgett films. *Applied Surface Science*, **90**, 205-215.
- Lopez-Diez EC, Goodacre R (2004) Characterization of Microorganisms using UV Resonance Raman Spectroscopy and chemometrics. *Analytical Chemistry*, **76**, 585-591.
- Lu D, Mo Z-Q, Xing Z-X, Gui D (2004) Analysis of amine contamination on silsicon oxide surfaces using ToF-SIMS. *Applied Surface Sciences*, **233**, 352-359.
- Lund B (2006) Stress variations during a glacial cycle at 500 m depth in Forsmark and Oskarshman: Earth model effects. Svensk Kärnbränslehantering AB, **R-06-95**, 32 p.
- Mendham AP, Potter BS, Palmer RA, Dines TJ, Mitchell JC, Withnall R, Chowdhry BZ (2009) Vibration spectra and crystal structure of the di-amino acid peptide cyclo(L-Met-L-Met): comparison of experimental data and DFT calculations. *Journal of Raman Spectroscopy*, **41**, 148-159.
- Milodowski AE, Tullborg E-L, Buil B, Gómez P, Turrero M-J, Haszeldine S, England G, Gillespie MR, Torres T, Ortiz JE, Zacharias J, Silar J, Chvátal M, Strnad L, Šebek O, Bouch JE, Chenery SR, Chenery C, Shepherd TJ, McKervey JA (2005) Application of mineralogical petrological and geochemical tools for evaluating the palaeohydrogeological evolution of the PADAMOT Study sites. PADAMOT PROJECT - EU FP5 Contract No. FIKW-CT2001-20129, Technical Report **WP2**, 228 p.
- Nasdala L, Smith DC, Kaindl R, Ziemann MA (2004) Raman spectroscopy: Analytical perspectives in mineralogical research. In *Spectroscopic Methods in Mineralogy*. Beran A., Libowitzky E., (eds) *Emu Notes in Mineralogy*, Vol. 6, 281-343.
- Ngwenya BT, Mosselmans JFW, Magennis M, Atkinson KD, Tournay J, Olive V, Ellam RM (2009) Macroscopic and spectroscopic analysis of lanthanide adsorption to bacterial cells. *Geochimica and Cosmochimica Acta*, **73**, 3134-3147.
- Nielsen PH, Jahn A, Palmgren R (1997) Conceptual model for production and composition of exopolymers in biofilms. *Water Science and Technology*, **36**, 11-19.
- NIST. EI Mass Spectrum database. <http://www.nist.gov/data/nist1a.htm>.
- Peckmann J, Thiel V (2004) Carbon cycling at ancient methane-seeps. *Chemical Geology* **204**, 443-467.
- Pedersen K (2000) Exploration of deep intraterrestrial microbial life: current perspectives. *FEMS, Microbiology Letters*, **185**, 9-16.
- Perkins MC, Roberts CJ, Briggs D, Davies MC, Friedmann A, Hart CA, Bell GA (2005) Surface morphology and chemistry of *Prunus laurocerases* L. leaves: a study using X-ray photoelectron spectroscopy, time-of-flight secondary-ion mass spectrometry, atomic-force microscopy and scanning electron microscopy. *Planta*, **221**, 123-134.
- Peters KE, Walters CC, Moldowan JM (2004) *The Biomarker Guide: Volume 1: Biomarkers and Isotopes in the Environments and Human History*. Cambridge University Press, Cambridge, 490 p.
- Puppels GJ, Garritsen HSP, Segers-Nolten GMJ, de Mul FFM, Greve J (1991) Raman microspectroscopic approach to the study of human granulocytes. *Biophysical Journal*, **60**, 1046-1056.
- Reitner J, Schumann GA, Pedersen K (2005) Fungi in subterranean environments. In Gadd GJ (ed), *Fungi in biogeochemical cycles*. Cambridge University Press, Cambridge, 378-403.

- Roberts D (2003) The Scandinavian Caledonides; event chronology, palaeogeographic settings and likely modern analogues. *Tectonophysics*, **365**, 283-299.
- Rönback P, Åström M, Gustafsson J-P (2008) Comparison of the behaviour of rare earth elements in surface waters, overburden groundwaters and bedrock groundwaters in two granitoidic settings, Eastern Sweden. *Applied Geochemistry*, **23**, 1862-1880.
- Rösch P, Harz M, Schmitt M, Peschke K-D, Ronneberger O, Burkhardt H., Motzkus H-W, Lankers M, Hofer S, Thiele H, Popp J (2005) Chemotaxonomic Identification of Single Bacteria by Micro-Raman Spectroscopy: Application to Clean-Room-Relevant Biological Contaminations. *Applied Environmental Microbiology*, **71**, 1626-1637.
- Rösch P, Schmitt M, Kiefer W, Popp J (2003) The identification of microorganisms by micro-Raman. *Journal of Molecular Structure*, **661-662**, 363-369.
- Sahl JW, Schmidt R, Swanner ED, Mandernack KW, Templeton AS, Kieft TL, Smith RL, Sandford WE, Callaghan RL, Mitton JB, Spear JR (2008) Subsurface Microbial Diversity in Deep-Granitic Fracture Water in Colorado. *Applied and Environmental Microbiology*, **74**, 143-152.
- Sallet R, Moritz R, Fontignie D (2005) The use of vein fluorite as probe for paleofluid REE and Sr-Nd isotope geochemistry: The Santa Catarina Fluorite District, Southern Brazil. *Chemical Geology*, **223**, 227-248.
- Sandström B, Tullborg E-L (2009) Episodic fluid migration in the Fennoscandian Shield recorded by stable isotopes, rare earth elements and fluid inclusions in fracture minerals at Forsmark, Sweden. *Chemical Geology*, **266**, 126-142.
- Schmid T, Messmer A, Yeo B-S, Zhang W, Zenobi R (2008) Towards chemical analysis of nanostructures in biofilms II: tip-enhanced Raman spectroscopy of alginates. *Analytical and Bioanalytical Chemistry*, **391**, 1907-1916.
- Schuster KC, Reese I, Urlaub E, Gapes JR, Lendl B (2000a) Multidimensional information on the chemical composition of single bacterial cells by confocal Raman Microscopy. *Analytical Chemistry*, **72**, 5529-5534.
- Schuster KC, Urlaub E, Gapes JR (2000b) Single-cell analysis by Raman microscopy: spectral information on the chemical composition of cells and on the heterogeneity in a culture. *Journal of Microbiological Methods*, **42**, 29-38.
- Schwinn G, Markl G (2005) REE systematics in hydrothermal fluorite. *Chemical Geology* **216**, 225-248.
- Sjövall, P., Lausmaa, J., Johansson, B.-L., Andersson, M., 2004. Surface chemical analysis of carbohydrate materials used for chromatography media by Time-of-Flight Secondary Ion Mass Spectrometry. *Analytical Chemistry*, **76**, 1857-1864.
- Spool AM (2004) Interpretation of static secondary ion spectra. *Surface and Interface Analysis*, **36**, 264-274.
- Staudigel H, Furnes H, McLoughlin N, Banerjee NR, Connell LB, Templeton A (2008) 3.5 billion years of glass bioalteration: volcanic rocks as a basis for microbial life? *Earth-Science Reviews*, **89**, 156-176.
- Steele A, Toporski JKW, Avci R, Guidry S, McKay DS (2001) Time of flight secondary ion mass spectrometry (ToFSIMS) of a number of hopanoids. *Organic Geochemistry*, **32**, 905-911.
- Szewzyk U, Szewzyk R, Stenström T-A (1994) Thermophilic, anaerobic bacteria isolated from a deep borehole in granite, Sweden. *Proceedings of the National Academy of Sciences, USA*, **91**, 1810-1813.

- Taylor SR, McLennan SM (1985) *The continental crust: its composition and evolution*. Blackwell, Oxford, 312p.
- Thiel V, Toporski J, Schumann G, Sjövall P, Lausmaa J (2007) Analysis of archaeal core ether lipids using Time of Flight - Secondary Ion Mass Spectrometry (ToF-SIMS): Exploring a new prospect for the study of biomarkers in geobiology. *Geobiology*, **5**, 75-83.
- Thiel V, Heim C, Arp G, Hahmann U, Sjövall P, Lausmaa J (2007) Biomarkers at the microscopic range: ToF-SIMS molecular imaging of Archaea-derived lipids in a microbial mat. *Geobiology*, **5**, 413-421.
- Toporski J, Steele A (2004) Characterization of purified biomarker compounds using time of flight-secondary ion mass spectrometry (ToF-SIMS). *Organic Geochemistry*, **35**, 793-811.
- Toporski J, Steele A, Westall F, Avci R, Martill M, McKay DS (2002) Morphological and spectral investigation of exceptionally well preserved bacterial biofilms from the Oligocene Enspel formation, Germany. *Geochimica et Cosmochimica Acta*, **66**, 1773-1791.
- Tullborg E-L, Drake H, Sandström B, (2008) Palaeohydrogeology: A method based on fracture mineral studies. *Applied Geochimistry*, **23**, 1881-1897.
- Van de Voort FR, Sedman J, Russin T (2001) Lipid analysis by vibrational spectroscopy. *European Journal of Lipid Science and Technology*, **103**, 815-825.
- Ventura GT, Kenig F, Reddy CM, Schieber J, Frysjinger GS, Nelson RK, Dinel E, Gaine, RB, Schaeffer P (2007) Molecular evidence of late Archaean archaea and the presence of a subsurface hydrothermal biosphere. *PNAS*, **104**, 14260-14625.
- Vickerman, JC, Briggs D (2001) *ToF-SIMS: Surface analysis by mass spectrometry*. IM Publications and Surface Spectra Limited. Charlton, Chichester, West Sussex, UK, 789 p.
- Wahlgren C-H, Ahl M, Sandahl K-A, Berglund J, Petersson J, Ekström M, Persson PO (2004) Bedrock mapping 2003 - Simpevarp subarea. Outcrop data, fracture data, modal and geochemical classification of rock types, bedrock map, radiometric dating. Oskarshamn site investigation. Svensk Kärnbänslehantering AB, **P-04-102**, 52 p.
- Wahlgren C-H, Hermanson J, Forssberg O, Curtis P, Triumf C-A, Drake H, Tullborg E-L (2006) Geological description of rock domains and deformation zones in the Simpevarp and Laxemar subareas. Preliminary site description Laxemar subarea - version 1.2. Svensk Kärnbänslehantering AB. **R-05-69**, 265 p.
- Wallin B, Laaksoharju M, Tullborg E-L (2007) Description of the different end-members identified from interpretations of groundwater chemistry and mixing models; results from Äspö and Laxemar area. In: Svensson U., (ed). *Towards a new generation of flow and transport models for the Äspö Hard Rock Laboratory*. Svensk Kärnbänslehantering AB, **R-08-74**, 61-80.
- Westall F, Folk RL (2003) Exogenous carbonaceous microstructures in early Archaean cherts and BIFs from the Isua Greenstone Belt: implications for the search for life in ancient rocks. *Precambrian Research*, **126**, 313-330.
- Williams AC, Edwards HGM (1994) Fourier Transform Raman Spectroscopy of Bacterial Cell Walls. *Journal of Raman Spectroscopy*, **25**, 673-677.

- Wingender J, Neu TR, Flemming H-C (1999) What are bacterial extracellular polymeric substances? In: Wingender J, Neu TR, Flemming H-C, (Eds) *Microbial Extracellular Polymeric Substances*. Springer, Berlin, 1-15.
- Zinin PV, Misra A, Kamemoto L, Yu Q, Hu N, Sharma SK (2010) Visible, near-infrared, and ultraviolet lased excited Raman Spectroscopy of the monocytes/macrophages (U937) cells. *Journal of Raman Spectroscopy*, **41**, 268-274.

7

Summary and Conclusions

In this thesis project, biomarkers, biomineralization processes and TREE (trace and rare earth elements) patterns in mineralizing microbial mats were established and tested as biosignatures in recent and fossil environments. To overcome limitations of conventional biomarker analysis, a comprehensive analytical approach was developed that accomplished the detection and the laterally resolved visualization of biomarkers on the same sample, and with minimal sample disruption.

In a pilot experiment, the application of ToF-SIMS (time-of-flight secondary ion mass spectrometry) enabled the simultaneous analysis of major archaeal biomarker classes in calcifying microbial mats from the Black Sea. Individual biomarker provenances on a μm -scale were identified and assigned to colonies of methanotrophic archaeal communities, namely ANME-1 vs. ANME-2 (anaerobic methane oxidizers). Previously equivocal lipid biomarkers could thus be linked to distinctive source biota without the need to isolate and culture these microbes in the laboratory. Subsequent microscopic investigations *on the same sample* provided further morphological and mineralogical evidence that corroborated the assignments made.

ToF-SIMS has a strong potential for molecule detection, identification and visualization at the microscopic range. However, because the method is still in its infancy with respect to the analysis of organic biomarkers, further evaluations of capabilities and limitations are required. In that respect, preparation protocols for geobiological samples have to be improved, and compound specific matrix effects have to be examined. Even more important, more biomarker reference standards have to be characterized and their fragmentation patterns determined to enhance the understanding and interpretation of ToF-SIMS data. To further expand the range of biomarker reference standards, ToF-SIMS spectra of selected glycerolipids were obtained, and the formation of molecular ions and specific fragments was studied in detail. These data are most useful as a basis for the identification of these and related biomarkers in environmental samples. Based on the reference data, it was possible to identify lipids (diglycerides and phosphatidylglycerol) in microscopic sections of mineralizing microbial mats from Black Sea methane seeps, and from *Gallionella ferruginea*-dominated iron-oxidizing microbial mats from the Äspö Hard Rock Laboratory (HRL).

G. ferruginea mats were also investigated to study biomineralization processes and corresponding TREE fractionations as potential biosignatures for microbially induced formation of iron oxyhydroxides. For that purpose, a long-term flow reactor experiment was established in the Äspö HRL. Biomineralization processes and concomitant TREE accumulation within these microbial mats revealed different forms of biomineral formation during growth and aging of *G. ferruginea*

and massive, up to 10^6 fold accumulations of individual metals. Further, the REE+Y fractionation patterns within the microbial iron oxyhydroxides differ significantly from chemically precipitated iron oxyhydroxides, but show a strong similarity to REE+Y patterns reported for Precambrian BIF. The findings support the idea that iron oxidizing microorganisms such as *G. ferruginea* may have significantly contributed to the formation of BIF.

In a third experiment, a comprehensive analytical approach to biosignatures within fracture minerals in the ~1.8 Ga old Äspö Diorite enabled the reconstruction and integrated understanding of ancient environmental processes that occurred within the deep continental biosphere. ToF-SIMS, CRM (Confocal Raman Microscopy) and LA-ICP-MS (laser ablation-inductively coupled mass spectrometry) and respectively electron microprobe and isotope sampling analyses were performed on two, 5 mm thick opposing rock sections, i.e. on a minute amount of fracture minerals, which enabled to retrace four different fracture mineral generations. One of them, an organic-rich amorphous layer, exhibited numerous functionalized organic molecules and accumulations and fractionations of distinct TREE and was interpreted as a fossilized biofilm. Biofilm formation was most probably induced by glacially induced fracture reactivation and water injections down to 450 m depth. Further fracture mineral formation terminated and entrapped the microbial activity that once occurred at depth.

The integrated approach used in this study led to the successful establishment of source specific biosignatures, and offers a strong tool kit for the study of mineralizing microbial mats and their interaction with the environment. The techniques employed in this study may further help to link biosignatures in recent systems to their fossil analogues and ultimately, to early complex forms of life. It can be foreseen that high resolution techniques such as ToF-SIMS and CRM will grow in importance not only in geobiology, but in all fields of natural sciences, wherever the detection and precise localization of organic compounds in environmental materials is required.

A

TERRESTRIAL DEEP BIOSPHERE

Christine Heim

Encyclopedia of Geobiology, Springer, 2011, in press

Synonyms

Continental deep biosphere, subterranean biosphere

Definition

The terrestrial deep biosphere comprises ecosystems in the marine (e.g. shelf-sediments) and continental subsurface, beneath the rhizosphere or bioturbated zone. The habitable depth is limited by space (rock porosity), the availability of water and in particular the maximum viable temperature depending on the local geothermal gradient (Gold, 1992; Pedersen, 1993, 2000, 2001, 2002; Stevens, 2002).

Introduction

Microbial life exists in, and seems to be adapted to all kinds of ecological niches on earth. From the early 30ies, increasing numbers of publications report on the occurrence of microorganisms in deep terrestrial settings, such coal mines (Lipman, 1931, 1937; Liske, 1932) and deep formation waters from oil drilling, as deep as 2000m (Ginsburg-Karagitscheva, 1933; Issatchenko, 1940). During the following decades the scientific interest in subsurface microbiology focussed on the effects of microorganisms on oil and gas exploration, such as corrosion of drilling devices, oil transformation, but also the role of microorganisms in the biological origin of natural gas resources (Zobell, 1945; Bailey *et al.*,1973; Belyaev *et al.*,1983; Colwell *et al.*,2004; Lollar *et al.*,2006). Deep subsurface microorganisms have a potential impact not only on oil and gas exploration, but also on groundwater (Chapelle, 2000), long-term storage of nuclear waste (Pedersen, 1993, 1997; Boivin-Jahns *et al.*,1996; Christofi and Philip, 1997; Hersman, 1997; Pedersen *et al.*,2008), and finally, implications for the origin of life and the search for extraterrestrial life (Stevens, 1997a; Faison, 2003; Cockell, 2004).

Scientific continental drilling (ICDP), and also site investigations for the storage of nuclear waste for a better understanding of geological, hydrological and biogeochemical processes in the deep continental crust, supported the development of contamination minimizing, drilling, sampling and

analytical techniques (Pedersen, 1993 (and references therein); Griffin *et al.*, 1997; Russel, 1997; Abyzov *et al.*, 2001; Pedersen *et al.*, 2008). Using enhanced drilling and sampling techniques, a broad diversity of microorganisms living under extreme conditions (extremophiles), i.e. under elevated temperatures and high pressure conditions, was observed (Gold, 1992; Szewzyk *et al.*, 1994; Boone *et al.*, 1995; Kotelnikova *et al.*, 1998; Bonch-Osmolovskaya *et al.*, 2003; Lin *et al.*, 2006; Sahl *et al.*, 2008). Whether the organisms observed in the deep terrestrial subsurface are indigenous or derive from surface contamination has been a major issue since the first decades of exploration and is still (even though more advanced sampling techniques are now available), an important question to be considered (Farrell and Turner, 1932; Lieske, 1932; Lipman, 1937; Phelps *et al.*, 1989; Pedersen, 1993; Griffin *et al.*, 1997; Haldemann, 1997; Russel, 1997; Stevens, 2002). Furthermore comprehensive sampling (contamination controlled sampling) and careful data interpretation is matter of major importance (Lehman *et al.*, 1995; Zhang *et al.*, 2006; Hallbeck and Pedersen 2008).

Terrestrial deep biosphere

Numerous reports about diverse, well adapted, active microorganisms, being most likely indigenous and occurring down to a depth of several km, rise the questions of (i) how the organisms got down there, (ii) how are they able to maintain, i.e. life and growth, (iii) what are the limiting factors for life in the deep biosphere.

There are different theories about microbial migration or transport into the deep subsurface can happen. One possibility is the transport of microorganism within groundwater aquifers as underground rivers (Karst systems) or percolating through the sediment or fracture systems. Groundwater may reach depths of several hundreds of meters and may have intervals from hundreds to thousands of years (Moser *et al.*, 1988; Simpkins and Bradbury, 1992; Seiler and Lindner, 1995). Further, it is assumed that living microbial matter is buried with the sediments, thus migrating vertically as a part of the rock cycle. As a consequence, some microorganisms must be capable to survive for millions of years. Reports on the detection and isolation of bacteria from the Taylorsville Triassic Basin from 2.7 km depth (Boone *et al.*, 1995), and from the Piceance Basin of western Colorado from 858 m depth (Colwell *et al.*, 1997) support this scenario.

General requirements for life are the availability of water, space, nutrients (O, C, H, N, Ca, P, S) and trace elements (Fe, Ni, Mn, W, Mo, V, Zn, Cu, Co, Se, Cr). Being independent from photosynthesis, subterranean organisms have to adapt their metabolism to local resources or form dormant stages, in order to survive at great depth (Pedersen, 1993; Amy, 1997; Kieft and Phelps, 1997; Stevens, 2002; Dobretsov *et al.*, 2006). Since the discovery of the first subsurface microorganisms, and the subsequent identification of a broad variety of aerobic, anaerobic, autotrophic and heterotrophic microbes, the potential carbon and energy sources available ad depth,

were intensively debated and approved. One major theory is the deep hydrogen-driven biosphere hypothesis (Pedersen, 1997), where acetogenic bacteria, acetoclastic methanogens and autotrophic methanogens consume abiotic, deep crustal H₂ as an energy source and CO₂ as carbon source. These organisms could be considered as the primary producers in the deep terrestrial biosphere. Experimental studies, calculating the production rates of radiolytic H₂, support the potential microbial consumption of H₂ (Lin *et al.*, 2005). Beside H₂ as electron donor, chemotrophic organisms can use for example, methane (CH₄), elemental sulfur (S⁰), sulfite (SO₃²⁻), thiosulfate (S₂O₃²⁻) with water H₂O, nitrate (NO₃⁻), sulfate (SO₄²⁻) or iron (Fe (III)), thereby forming nitrogen gas, hydrogen sulphide (H₂S) and ferrous iron, respectively (Kieft & Phelps, 1997; Stevens, 2002; Amend and Teske, 2005 and references therein).

Numerous of the microorganisms observed in the deep subsurface are not only metabolically well adapted, they also manage to survive and reproduce under extreme conditions, such as hot or freezing temperatures, high pressure, alkaline or acidic conditions and high salinity. Examples of these extremophiles and references are listed below in the section of the respective deep terrestrial environment. Moreover, some microorganisms are able to get into a dormancy stage by forming spores, cysts or other types of resting cells and survive starvation, desiccation periods, exposure to extreme temperatures, and elevated background radiation (Burke and Wiley, 1937; Amy, 1997; Suzina *et al.*, 2004; Ponder *et al.*, 2005; Johnson *et al.*, 2007).

Regarding these adaptation mechanisms and considering the ongoing discovery of unknown microorganisms, new metabolic pathways and adaptation mechanisms, it is difficult to define the limits of life in the terrestrial deep biosphere. These actual limits may be due to a combination of several factors: with increasing depth, the growing load of the overlying rocks or ice masses progressively decreases the pore space available, temperature rises due to the geothermal gradients and the water activity changes with increasing temperatures and pressures (Gold, 1992; Pedersen, 1993, 2000; Stevens, 2002).

Terrestrial deep biosphere environments

Pedersen (2000) divided the terrestrial deep biosphere into continental sedimentary rocks, ancient salt deposits, aquifers in igneous rocks and caves, whereas Stevens (2002) subdivided the deep biosphere of the continental crust into sedimentary environments, permafrost, ice sheets and glaciers, and bedrock environments. Salt deposits and permafrost soils are sediments by definition, and therefore, in this entry, they are discussed in the section of sedimentary environments. Caves exhibit a great variety of different ecosystems that might serve as models for the formation of special adaptations or symbioses and may therefore represent a link between surface and subsurface environments (Pedersen, 2000; Dattagupta *et al.*, 2009).

Sedimentary environments

Since the beginning of the last century, microorganisms in deep sedimentary environments have been frequently found and described from exploration sites, for example in coal (Liske, 1932; Lipman, 1931, 1937; Burke and Wiley, 1937). Later when advanced drilling techniques and modern sequencing methods became available, a more precise characterization of these microorganisms is possible. A strict anaerobe, *Bacillus* species (*Bacillus infernus*) was isolated from drill core samples obtained from 2700 m depth, from the Triassic Taylorsville basin (Boone *et al.*, 1995). Several sediment core samples from 856 to 2096m from the Piaceance Basin of Colorado contained Fe(III)- reducing and fermenting bacteria (Colwell *et al.*, 1997). Krumholz (2000) reported microbial communities within cretaceous rocks in New Mexico, where living sulphate reducing bacteria (SRB) and acetogens were found at the interface of porous sandstone and dense organic-rich shale. Later studies of the same site revealed high numbers of Fe(III) and S⁰-reducing bacteria (Kovacik Jr. *et al.*, 2006). Sass and Cypionka (2004) isolated moderately thermophilic SRB in porous sandstones from 600 to 1060m depth. In coal seam groundwater within 843 to 907m depth microbial communities of methanogenic archaea, denitrifying, acetogenic, and SRB were detected (Shimizu *et al.*, 2007). Thermophilic archaea and bacteria, including SRB, are common in oil reservoirs and geothermal fluids (Zobell, 1945; Bonch-Osmolovskaya *et al.*, 2003; Kimura *et al.*, 2007; Zavarzina *et al.*, 2007). Culturing experiments and biomarker studies of 170 million years old claystone indicate the presence of active SRB within the rock (Mauclaire *et al.*, 2007).

A special form of sedimentary environments are salt deposits: massive salt deposits have formed mainly due to marine transgression and regression cycles within epicontinental seas. Halophilic bacteria were described by Vreeland *et al.* (1998) from salt deposits in New Mexico and Gruber *et al.* (2004) isolated halophilic archaea in alpine salt deposits. Whether the halophilic microorganisms are indigenous and survived for millions of years in the salt, is still unclear (McGenity *et al.*, 2000). However, the isolation of viable *Halobacterium salinarium* from brine inclusion within 9600 years old halite crystals (Mormile *et al.*, 2003) indicates long term survival of the microorganisms enclosed in salt deposits.

Permafrost soils are composed of silt, loam, peat, organic material from plants, top soil and ice. Although temperatures in permafrost regions range between -10 to -30°C viable microorganisms have been detected in frozen sediment samples from Siberia, Alaska, Canada and Antarctica (Vorobyova *et al.*, 1997). Methanogenic archaea are presumably responsible for the production of high amounts of methane in permafrost soils (Rivkina *et al.*, 2000 and 2004). Gilichinsky *et al.* (1992) observed not only prokaryotes in Pliocene and Pleistocene sediments, even eukaryotic organisms were found in Holocene sediments.

Bedrock environments

Igneous and metamorphic rocks contain considerably less organic matter and pore space compared to sediments. Sampling of microorganisms is a problematic issue, as drilled rock material is often contaminated by drilling fluids (Pedersen 2000; Hallbeck and Pedersen 2008). However, investigations of a deep biosphere in igneous rocks were performed using the fracture and well water, drilling fluids and groundwater aquifers. In deep granitic aquifers of the Fennoscandian shield, anaerobic thermophilic fermenting bacteria and SRB (Szewzyk *et al.*, 1994), methanogens, homoacetogens (Kotelnikova & Pedersen, 1998; Pedersen, 2000; Kotelnikova, 2002), yeasts (Ekendahl *et al.*, 2003), viruses (Kyle *et al.*, 2008) and bacteriophages (Eydahl *et al.*, 2009) were observed. The detection of fungi in deep biosphere environments was also reported by Reitner *et al.* (2005), describing hyphae from unknown fungal mycelia in the Triberg Granite (Germany). In deep granitic fracture water and rock cores from the Henderson mine (Colorado), iron oxidizing bacteria and the “Henderson candidate division” were detected (Sahl *et al.*, 2008). In deep anaerobic and alkaline aquifers within the Columbia River Basalt Group, SRB and metal reducing bacteria were described by Fry *et al.* (1997). Drilling fluids from boreholes at 2290 to 3350m depth, from the Chinese Continental Drilling Program, exhibited a huge diversity of extreme thermophilic, anaerobic chemoorganotrophs, anaerobic Fe (III) reducers, halotolerant, alkaliphilic microorganisms (Zhang *et al.*, 2006). Lin *et al.*, (2006) report about thermophilic SRB in deep alkaline saline groundwaters in Archaean metabasalt. A remarkable finding was a star shaped bacterial morphotype at 1700m depth in a South African platinum mine, observed by Wanger *et al.* (2008).

Ice sheets & glaciers

Microbiological investigations of ice cores obtained above the subglacial lake Vostok, Antarctica, exhibited various microorganisms from moraine material, from shallow regions of the glacier, but also presumably from the lake water (Abyzov *et al.*, 2001). Poglazova *et al.* (2001) described Cyanobacteria and microalgae occurring in accreted ice of the subglacial lake Vostok. Highly diverse microbial communities in 120,000 years old deep glacier ice cores from Greenland were described and isolated by Miteva *et al.* (2004 and 2005).

General remarks

Fossil deep biosphere, evolutionary aspects and implications for extraterrestrial life.

As research on the deep biosphere continues, novel organisms, metabolic pathways and adaptation mechanisms will certainly be discovered. A look at the different subsurface environments shows,

that a generalisation of the microbial diversity and adaptation mechanisms is rather impossible, as they all host their own specialized ecosystems.

Learning more about life in deep subterranean environments, may help to understand how life might have evolved and survived during meteoric impacts, increased rates of volcanic activity or a potential global glaciation (Snowball earth). In fact, geothermal waters, H₂ and CH₄ degassing volcanic or plutonic rocks may have served as local nutrient and energy sources for chemotrophic ecosystems (Dobretsov *et al.*, 2006). Models about the habitability of the Hadean earth indicate, that even the late heavy meteoric bombardment, around 3.9 Ga would not have been able to sterilize the primeval biosphere of the earth crust, considering the existence of a near and subsurface biosphere (Abramov and Mojzsis, 2009).

Traces of a fossil subterraneous biosphere were observed in metasedimentary rocks from Timmins (Canada) from the late Archaean (Ventura *et al.*, 2007) and Bons *et al.*,(2009) report about fossilized microbes within 585 Ma old calcite veins from Oppaminda Creek (Australia).

Increased interest for research in deep terrestrial, means also extreme environments, is its implication for extraterrestrial life. A better understanding of the earth's deep biosphere allows the development of models to understand general biogeochemical processes not only for our earth but maybe for biogeochemical processes on other planets. For example, permafrost soils on Mars may comprise recent or ancient life (Gilichinsky *et al.*,1992; Rivkina *et al.*, 2000 and 2004) or Jupiter's satellites may have ice-covered lakes similar to lake Vostok (Abyzov *et al.*,2001) serving as a potential deep biosphere environments.

References

- Abramov O, Mojzsis S (2009) Microbial habitability of the Hadean earth during late heavy bombardment. *Nature*, **459**, 419-422.
- Abyzov SS, Mitskevich I N, Poglazova MN, Barkov NI, Lipenkov VY, Bobin NE, Koudryashov BB, Pashkevich VM, Ivanov MV (2001) Microflora in the basal strata at an antarctic ice core above the vostok lake. *Advances in Space Research*, **28**, 701-706.
- Amend JP, Teske A (2005) Expanding frontiers in deep subsurface microbiology. *Palaeogeography, Palaeoclimatology, Palaeoecology*, **219**, 131-155.
- Amy PS (1997) Microbial dormancy and survival in the subsurface. In Amy P, Haldeman D, (eds) *The microbiology of the terrestrial subsurface*. CRC Press, 185-203.
- Bailey NJL, Jobson AM, Rogers MA (1973) Bacterial degradation of crude oil: Comparison of field and experimental data. *Chemical Geology*, **11**, 203-221.
- Belyaev SS, Wolkin R, Kenealy M, DeNiro MJ, Epstein S, Zeikus JG (1983) Methanogenic bacteria from the bondyushskoe oil field: General characterization and analysis of stable-carbon isotopic fractionation. *Applied environmental microbiology*, **45**, 691-697.
- Boivin-Jahns V, Ruimy R, Bianchi A, Dumas S, Christen R (1996) Bacterial diversity in a deep-subsurface clay environment. *Applied and Environmental Microbiology*, **62**, 3405-3412.
- Bonch-Osmolovskaya EA, Miroshnichenko ML, Lebedinsky AV, Chernyh NA, Nazina TN, Ivoilov VS, Belyaev SS (2003) Radioisotopic, culture-based, and oligonucleotide microchip analyses of thermophilic microbial communities in a continental high-temperature petroleum reservoir. *Applied and Environmental Microbiology*, **69**, 6143-6151.
- Bons PD, Montenari M, Bakker RJ, Elburg M (2009) Potential evidence of fossilised Neoproterozoic deep life: SEM observations on calcite veins from Oppaminda Creek, Arkoola, South Australia. *International Journal of Earth Sciences*, **98**, 327-343.
- Boone DR, Liu Y, Zhao Z-J, Balkwill DL, Drake GR, Stevens TO, Aldrich HC (1995) *Bacillus infernus* sp. nov., an Fe(III)- and Mn(IV)-reducing anaerobe from the deep terrestrial subsurface. *International Journal of Systematic Bacteriology*, **45**, 441-448.
- Burke V, Wiley AJ (1937) Bacteria in Coal. *Journal of Bacteriology*, **34**, 475-481.
- Chapelle, F. H., 2000. *Ground-water Microbiology and Geochemistry*. Wiley-VCH, 496 pages.
- Christofi N, Philip JC (1997) European Microbiology related to the subsurface disposal of nuclear waste. In: Amy P, Haldeman D (eds) *The microbiology of the terrestrial subsurface*. CRC Press, 267-297.
- Cockell CS (2004) Impact-shocked rocks – insights into archaean and extraterrestrial habitats (and sites for prebiotic chemistry?). *Advances in Space Research*, **33**, 1231-1235.
- Colwell F, Matsumoto R, Reed D (2004) A review of the gas hydrates, geology, and biology of the Nankai Trough. *Chemical Geology*, **205**, 391-404.
- Colwell FS, Onstott TC, Delwiche ME, Chandler D, Fredrickson JK, Yao Q-J, McKinley JP, Boone DR, Griffiths R, Phelps TJ, Ringelberg D, White DC, LaFreniere L, Balkwill D, Lehman RM, Konisky J, Long PE (1997) Microorganisms from deep high temperature sand stones: constraints on microbial colonization. *FEMS Microbiology Reviews*, **20**, 425-435.

- Dattagubta S, Schaperdoth I, Monanary A, Mariani S, Kita N, Valley JW, Macalady JL (2009) A novel symbiosis between chemoautotrophic bacteria and a freshwater cave amphipod. *The ISME Journal*, **3**, 935-943.
- Dobretsov NL, Kolchanov NA, Suslov VV (2006) On the early stages of the evolution of the geosphere and biosphere. *Paleontological Journal*, **40**, 407-424.
- Ekendahl S, O'Neill AH, Thomson E, Pedersen K (2003) Characterisation of yeasts isolated from deep igneous rock aquifers of the Fennoscandian shield. *Microbial Ecology*, **46**, 416-428.
- Eydal HSC, Jägevall S, Hermansson M, Pedersen K (2009) Bacteriophage lytic to *Desulfovibrio aespoensis* isolated from deep groundwater. *The ISME Journal*, **3**, 1139-1147.
- Faison BD (2003) Microbial contributions to the Search for extraterrestrial life. *Advances in Applied Microbiology*, **52**, 397-432
- Farrell MA, Turner H G (1932) Bacteria in anthracite coal. *Journal of Bacteriology*, **23**, 155-162.
- Fry NK, Fredrickson JK, Fishbain S, Wagner M, Stahl D (1997) Population structure of microbial communities associated with two deep, anaerobic, alkaline aquifers. *Applied and Environmental Microbiology*, **63**, 1498-1504.
- Gilichinsky DA, Vorobyova EA, Erokhina LG, Fyodorov-Dayvdov DG, Chaikovykaya NR (1992) Long-term preservation of microbial ecosystems in permafrost. *Advances in Space Research*, **12**, 4255-4263.
- Ginsburg-Karagitscheva TL (1933) Microflora of Oil Waters and Oil-Bearing Formations and Biochemical Processes Caused by It. *Bulletin of the American Association of Petroleum Geologists*, **17**, 52-65.
- Griffin WT, Phelps TJ, Colwell FS, Fredrickson JK (1997) Methods for obtaining deep subsurface microbiological samples. In Amy P, Haldeman D (eds) *The microbiology of the terrestrial subsurface*. CRC Press, 23-44.
- Gruber C, Legat A, Pfaffenhuemer M, Radax C, Weidler G, Busse H-J, Stan-Lotter H (2004) *Halobacterium noricense* sp. nov., an archaeal isolate from a bore core of an alpine Permian salt deposit, classification of *Halobacterium* sp. NRC-1 as a strain of *H. salinarium* and emended description of *H. salinarium*. *Extremophiles*, **8**, 431-439.
- Gold T (1992) The deep hot biosphere. *Proceedings of the National academy of Sciences, USA*; **89**, 6045-6049
- Haldemann DL (1997) The storage related phenomenon: Implications for handling and analysis of subsurface samples by drilling. In Amy P, Haldeman D (eds) *The microbiology of the terrestrial subsurface*. CRC Press, 61-74.
- Hallbeck L, Pedersen K (2008) Characterization of microbial processes in deep aquifers of the Fennoscandian Shield. *Applied Geochemistry*, **23**, 1796-1819.
- Hersman LE (1997) Subsurface Microbiology: Effects on the transport of radioactive waste in the Vadose Zone. In Amy P, Haldeman D (eds) *The microbiology of the terrestrial subsurface*. CRC Press, 299-323.
- Issatchenko V (1940) On the microorganisms of the lower limits of the biosphere. *Journal of Bacteriology*, **40**, 379-381.

- Johnson SS, Hebsgaard MB, Christensen TR, Mastepanov M, Nielsen R, Munch K, Brand T, Gilbert P, Zuber MT, Bunce M, Rønn R, Gilichinsky D, Froese D, Willerslev E (2007) *PNAS*, **104**, 14401-14405.
- Kieft TL, Phelps TJ (1997) Life in the slow lane: activities of microorganisms in the subsurface. In Amy P, Haldeman D (eds) *The microbiology of the terrestrial subsurface*. CRC Press, 137-163.
- Kimura H, Ishibashi J-I, Masuda H, Kato K, Hanada S (2007) Selective phylogenetic analysis targeting 16S rRNA genes of hyperthermophilic archaea in the deep-subsurface hot biosphere. *Applied and Environmental Microbiology*, **73**, 2110-2117.
- Kotelnikova S (2002) Microbial production and oxidation of methane in deep subsurface. *Earth-Science Reviews*, **58**, 367-395.
- Kotelnikova S, Macario AJL, Pedersen K (1998) *Methanobacterium subterraneum* sp. nov., a new alkaliphilic, eurythermic and halotolerant methanogen isolated from deep granitic groundwater. *International Journal of Systematic Bacteriology*, **48**, 357-367.
- Kotelnikova S, Pedersen K (1998) Distribution and activity of methanogenes and homacetogenes on deep granitic aquifers at Äspö Hard Rock Laboratory, Sweden. *FEMS Microbiology Ecology*, **26**, 121-134.
- Kovacik Jr WP, Takai K, Mormile MR, McKinley JP, Brockman FJ, Fredrickson JK, Holben W (2006) Loewuar analysis of deep subsurface Cretaceous rock indicates abundant Fe(III)- and S⁰-reducing bacteria in a sulfate-rich environment. *Environmental Microbiology*, **8**, 141-155.
- Krumholz LR (2000) Microbial communities in the deep subsurface. *Hydrogeology Journal*, **8**, 4-10.
- Kyle JE, Eydal HSC, Ferris FG, Pedersen K (2008) Viruses in granitic groundwater from 69 to 450 m depth of the Äspö Hard Rock Laboratory, Sweden. *The ISME Journal*, **2**, 571-574.
- Lehman RM, Colwell FS, Ringelberg DB, White DC (1995) Combined microbial community-level analysis for quality assurance of terrestrial subsurface cores. *Journal of Microbiological Methods*, **22**, 263-281.
- Lieske R (1932) Über das Vorkommen von Bakterien in Kohlenflözen. *Biochemische Zeitschrift*, **250**, 339-351.
- Lin L-H, Wang P-L, Rumble D, Lippmann-Pipke J, Boice E, Pratt LM, Lollar BS, Brodie EL, Hazen TC, Andersen GL, DeSantis T Z, Moser DP, Kershaw D, Onstott TC (2006) Long-Term sustainability of a high-energy, low-diversity crustal biome. *Science*, **314**, 479-482.
- Lin L-H, Slater GF, Lollar BS, Lacrampe-Couloume G, Onstott TC (2005) The yield and isotopic composition of radiolytic H₂, a potential energy source for the deep subsurface biosphere. *Geochimica et Cosmochimica Acta*, **69**, 893-903.
- Lipman CB (1931) Living microorganisms in ancient rocks. *Journal of Bacteriology*, **22**, 183-198.
- Lipman CB (1937) Bacteria in Coal. *Journal of Bacteriology*, **34**, 483-488.
- Lollar BS, Lacrampe-Couloume G, Slater GF, Ward J, Moser DP, Gihring TM, Lin L-H, Onstott TC (2006) Unravelling abiogenic and biogenic sources of methane in the earth's deep subsurface. *Chemical Geology*, **226**, 328-339.

- Mauclaire L, McKenzie JA, Schwyn B, Bossart P (2007) Detection and cultivation of indigenous microorganisms in Mesozoic claystone core sample from the Opalinus Clay Formation (Mont Terri Rock Laboratory). *Physics and Chemistry of the Earth*, **32**, 232-240.
- McGenity TJ, Gemmill RT, Grant WD, Stan-Lotter H (2000) Origins of halophilic microorganisms in ancient salt deposits. *Environmental Microbiology*, **2**, 243-250.
- Miteva VI, Brenchley JE (2005) Detection and isolation of ultra small microorganisms from a 120,000 year-old Greenland glacier ice core. *Applied and Environmental Microbiology*, **71**, 7806-7818.
- Miteva VI, Sheridan PP, Brenchley JE (2004) Phylogenetic and physiological diversity of microorganism from a deep Greenland glacier ice core. *Applied and Environmental Microbiology*, **70**, 202-213.
- Mormile MR, Biesen MA, Gutierrez MC, Ventosa A, Pavlovich JB, Onstott TC, Fredrickson JK (2003) Isolation of *Halobacterium salinarium* retrieved directly from halite brine inclusions. *Environmental Microbiology*, **5**, 1094-1102.
- Moser H, Wolf M, Fritz P, Fontes J-C, Florkowski T, Payne BR (1988) Deuterium, oxygen-18, and tritium in Stripa groundwater. *Geochimica et Cosmochimica Acta*, **53**, 1757-1763.
- Pedersen K, Arlinger J, Hallbeck A, Hallbeck L, Eriksson S, Johansson J (2008) Numbers, biomass and cultivable diversity of microbial populations relate to depth and borehole-specific conditions in groundwater from depths of 4 to 450 m in Olkiluoto, Finland. *The ISME Journal*, **2**, 760-775.
- Pedersen K (2002) Microbial processes in the disposal of high level radioactive waste 500 m underground in Fennoscandian shield rocks. In Keith-Roach MJ, Livens FR (eds). *Interactions of microorganisms with radionuclides*. Elsevier, Amsterdam, 279-311.
- Pedersen K (2001) Diversity and activity of microorganisms in deep igneous rock aquifers of the Fennoscandian Shield. In Fredrickson JK, Fletcher M (eds), *Subsurface microbiology and biogeochemistry*. Wiley-Liss Inc., New York: 97-139.
- Pedersen K (2000) Exploration of deep intraterrestrial microbial life: current perspectives. *FEMS, Microbiology Letters*, **185**, 9-16.
- Pedersen K (1997) Microbial life in deep granitic rock. *FEMS Microbiology Reviews*, **20**, 399-414..
- Pedersen K (1993) The deep subterranean biosphere. *Earth-Science Reviews*, **34**, 243-260
- Phelps TJ, Fliermans CB, Garland TR, Pfiffner SM, White DC (1989). Methods for recovery of deep terrestrial subsurface sediments for microbiological studies. *Journal of Microbiological Methods*, **9**, 267-279.
- Poglazova MN, Mitskevich IN, Abyzov SS, Ivanov MV (2001) Microbiological characterization of the accreted ice of subglacial Lake Vostok, Antarctica. *Microbiology*, **70**, 723-730.
- Ponder MA, Gilour SJ, Bergholz PW, Mindock CA, Hollongsworth R, Thomashow MF, Tiedje JM (2005) Characterization of potential stress responses in ancient Siberian permafrost psychroactive bacteria. *FEMS Microbiology Ecology*, **53**, 103-115.
- Reitner J, Schumann GA, Pedersen K (2005) Fungi in subterranean environments. In, Gadd GJ (ed), *Fungi in biogeochemical cycles*. Cambridge University Press, Cambridge: 788-1002.
- Rivkina EM, Friedmann, EI, McKay CP, Gilichinsky DA (2000) Metabolic activity of permafrost bacteria below the freezing point. *Applied and Environmental Microbiology*, **66**, 3230-3233.

- Rivkina E, Laurinavichius K, McGrath J, Tiedje J, Shcherbakova V, Gilichinsky D (2004) Microbial life in permafrost. *Advances in Space Research*, **33**, 1215-1221.
- Russel CE (1997) The collection of subsurface samples by mining. In Amy P, Haldeman D (eds), *The microbiology of the terrestrial subsurface*. CRC Press, 45-60.
- Sahl JW, Schmidt R, Swanner ED, Mandernack KW, Templeton AS, Kieft TL, Smith RL, Sandford WE, Callaghan RL, Mitton JB, Spear JR (2008) Subsurface Microbial Diversity in Deep-Granitic Fracture Water in Colorado. *Applied and Environmental Microbiology*, **74**, 143-152.
- Sass H, Cypionka H (2004) Isolation of sulfate-reducing bacteria from the terrestrial deep subsurface and description of *Desulfovibrio cavernae* sp. nov. *Systematic and Applied Microbiology*, **27**, 541-548.
- Seiler K-P, Lindner W (1995) Near-surface and deep groundwaters. *Journal of Hydrology*, **165**, 33-44.
- Shimizu S, Akiyama M, Naganuma T, Fujioka M, Nako M, Ishijima Y (2007) Molecular characterization of microbial communities in deep coal seam groundwater of northern Japan. *Geobiology*, **5**, 423-433.
- Simpkins WW, Bradbury KR (1992) Groundwater flow, velocity, and age in a thick, fine-grained till unit in southeastern Wisconsin. *Journal of Hydrogeology*, **132**, 283-319.
- Szewzyk U, Szewzyk R, Stenström T-A (1994) Thermophilic, anaerobic bacteria isolated from a deep borehole in granite, Sweden. *Proceedings of the National Academy of Sciences, USA*, **91**, 1810-1813.
- Stevens TO (2002) The deep subsurface biosphere. In Staley JT, Reysenbach A-L (eds), *Biodiversity of microbial life. Foundation of the earth's biosphere*. Wiley-Liss, 552 pages.
- Stevens TO (1997a) Subsurface microbiology and the evolution of the biosphere. In Amy P, Haldeman, D (eds), *The microbiology of the terrestrial subsurface*. CRC Press, 203-221.
- Stevens TO (1997b) Lithoautotrophy in the subsurface. *FEMS Microbiology reviews*, **20**, 327-337.
- Suzina NE, Mulyukin AL, Kozlova AN, Shorokova AP, Dmitriev VV, Barinova ES, Mokhova ON, El'-Registan GI, Duda VI (2004) Ultrastructure of resting cells of some non-spore-forming bacteria. *Microbiology*, **73**, 516-529.
- Ventura GT, Kenig F, Reddy CM, Schieber J, Frysinger G.S, Nelson RK, Dinel E, Gaines RB, Schaeffer P (2007) Molecular evidence of late Archaean archaea and the presence of a subsurface hydrothermal biosphere. *PNAS*, **104**, 14260-14265.
- Vorobyova E, Soina V, Gorlenko M, Minkovskaya N, Zalinova N, Mamukelashvili A, Gilichinsky D, Rivkina E, Vishnivetskaya T (1997) The deep cold biosphere: facts and hypothesis. *FEMS Microbiology Reviews*, **20**, 277-290.
- Vreeland RH, Piselli Jr AF, McDonnough S, Meyers SS (1998) Distribution and diversity of halophilic bacteria in a subsurface salt formation. *Extremophiles*, **2**, 321-331.
- Wanger G, Onstott TC, Southam G (2008) Stars of the terrestrial deep subsurface: A novel 'star-shaped' bacterial morphotype from a South African platinum mine. *Geobiology*, **6**, 325-330.
- Zavarzina D, Sokolova TG, Tourova TP, Chernyh NA, Kostrikina NA, Bonch-Osmolovskaya EA (2007) *Thermincola ferriacetica* sp. Nov., a new anaerobic, thermophilic facultatively chemolithoautotrophic bacterium capable of dissimilatory Fe(III) reduction. *Extremophiles*, **11**, 1-7.
- Zhang G, Dong H, Jiang H, Xu Z, Eberl DD (2006) Unique Microbial Community in Drilling Fluids from Chinese Continental Scientific Drilling. *Geomicrobiology Journal*, **23**, 499-514.

Zobell CE (1945) The role of bacteria in the formation and transformation of petroleum hydrocarbons.
Science, **102**, 364-369.

B

MICROBIAL BIOMINERALIZATION

Christine Heim

Encyclopedia of Geobiology, Springer, 2011, in press

Synonyms

Microbial biomineral formation

Definition

Microbial biomineralization describes the formation and deposition of minerals directly mediated or indirectly influenced by microorganisms (Mann, 2001; Weiner and Dove, 2003, Ehrlich, 1999). A huge variety of minerals result from individual biomineralization pathways linked to the genetic and metabolic activity of the microorganisms involved (Minsky, *et al.*,2002; Weiner and Dove 2003). Moreover, microbial biominerals may differ distinctly from their inorganically formed equivalents in shape, size, crystallinity, isotopic and trace element composition (Weiner and Dove, 2003; Bazylinski *et al.*,2007; Haferburg and Kothe, 2007; Takahashi *et al.*,2007). A compilation of microbial biominerals and their source organisms is given in Table 1.

Two principal modes of microbial biomineralization processes occur, namely biologically induced mineralization (BIM) and biologically controlled mineralization (BCM, Lowenstam, 1981; Lowenstam and Weiner, 1989). These modes are introduced in the following.

Biologically induced mineralization (BIM):

In BIM, the nucleation and growth of biominerals are extracellular processes triggered by the metabolic activity of the microorganism. Biomineralization takes place due to changes in the chemical equilibrium of the surrounding environment and may also be linked to particular metabolic products. The resulting biominerals typically show a poor crystallinity, are chemically heterogeneous, and often closely associated with the cell wall (Frankel and Bazylinsky, 2003). An active and a passive mineralization process can be distinguished (Fortin and Beveridge, 2000; Southam, 2000). Active mineralization refers to mineralization by (i) direct redox conversion of specific metal ions bound to the bacterial surface, or (ii) by the excretion of metabolically produced ions and thereby forming minerals. The term passive mineralization is used, when *nonspecific*

binding of cations and the involvement of surrounding anions causes nucleation and growth of minerals. Passive mineralization can even be mediated by dead cells, due to the exposure of negatively charged surfaces acting as nucleation sites for metal cations (Urrutia and Beveridge, 1993). Especially in BIM, extracellular polymeric substances (EPS, see entry) are involved in the mineralization process (Ercole *et al.*, 2007; Chan *et al.*, 2009). As an example of BIM, the precipitation of iron oxyhydroxides by the iron oxidizing bacterium *Gallionella ferruginea* is displayed in figure B.1.

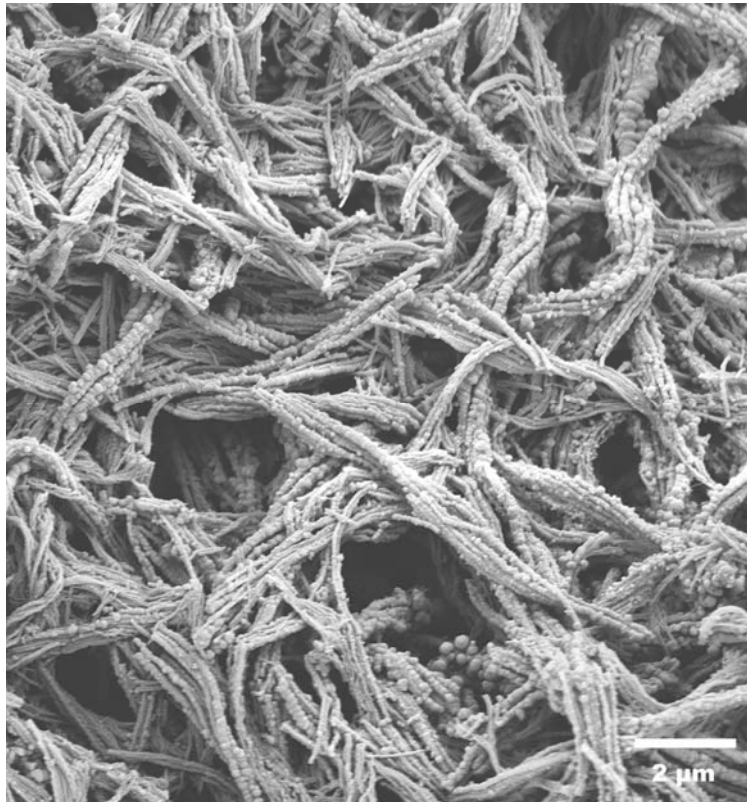


Fig. B.1 Stalk-shaped extracellular polymeric substances (EPS) produced by the iron oxidizing bacterium *Gallionella ferruginea* are heavily encrusted with iron oxyhydroxide minerals formed by BIM.

Biologically controlled mineralization (BCM):

BCM implies that the organism actively controls the nucleation site, growth, morphology and final location of the mineral (Banfield and Nealson 1997, Bazylinski and Frankel, 2003). Although the modes of exerting crystallochemical control over the mineralization process may greatly vary across species, the common characteristic of BCM is that mineral formation takes place in a closed, isolated environment. Whereas Weiner and Dove (2003) categorized BCM in *extra-*, *inter-* or *intracellular* mineralization, Mann (2001) differentiated between two key modes of BCM, namely *matrix-mediated* mineralization and *boundary-organized* mineralization. Generally speaking,

extracellular mineralization corresponds to matrix-mediated mineralization, whereas inter- and intracellular mineral formation are equivalent to boundary-organized mineralization.

Extracellular BCM implies the production of a macromolecular matrix outside the cell. This matrix is typically composed of proteins, polysaccharides or glycoproteins forming a three dimensional framework, and the cell actively supplies cations to the matrix for an ‘on-site’ nucleation and growth of the biomineral (Weiner and Dove, 2003).

Intercellular BCM occurs mostly in single-celled organisms, existing in a community. This type of mineral formation is not common in bacteria, but is commonly found in calcareous algae, e.g. *Halimeda* (Borowitzka *et al.*, 1982; de Vrind-de Jong and de Vrind, 1997).

Intracellular BCM takes place inside specific compartments within the cell, for instance vesicles or vacuoles. Thus the organism is able to exactly regulate the chemical composition, morphological structure and particle size of the mineral. The only bacteria known to perform intracellular BCM are magnetotactic bacteria, which use a vacuole based system for the crystallization of magnetic biominerals (Table B.1). Similar systems of intracellular BCM are only known from higher eukaryotic organisms, controlling e.g. the bone and teeth formation in mammals (Kirschvink and Hagadorn, 2000). An example of microbial biominerals formed by intracellular BCM, is shown in figure B.2.

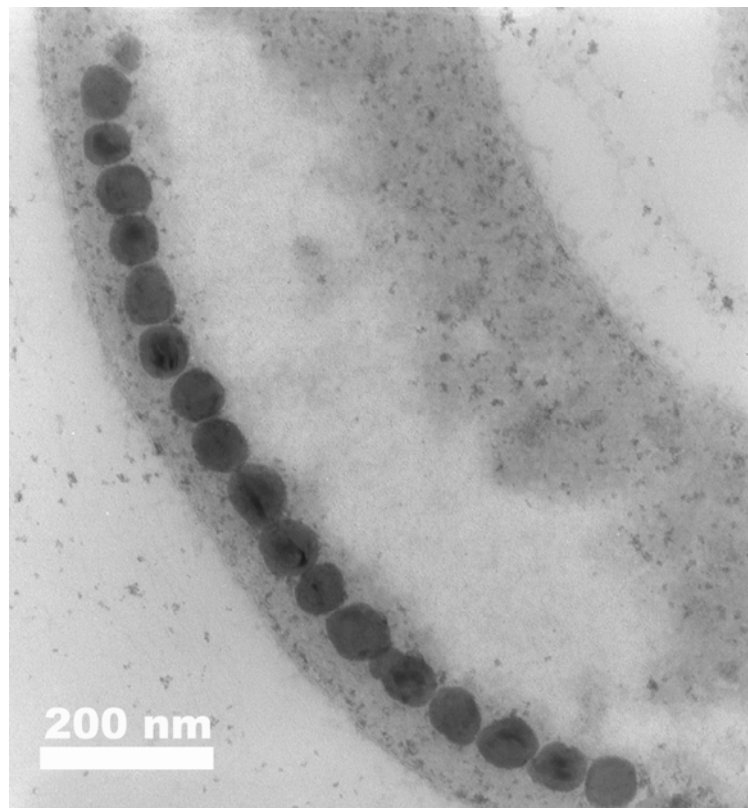


Fig. B.2 Intracellular iron sulfide (greigite, Fe₃S₄) crystals formed by BCM within a magnetotactic bacterium. Image courtesy of Joachim Reitner.

Table B.1. Overview of minerals formed by microbial biomineralization and the organism(s) involved. For comprehensive reading, the following books are recommended: Sigel et al. (2008), Baeuerlein (2000); Banfield and Nealson (1997); Dove et al. (2003); Driessens and Verbeek (1990); Lovely (2000); Lowenstam and Weiner (1989).

Chemical Formula	Mineral Name	Involved microorganism	References
Fe(OH) ₃ (approx)	Ferric / Iron oxyhydroxide	Fe-oxidizing bacteria	Chan <i>et al.</i> ,2009; Yoshida <i>et al.</i> ,2008
2Fe(OH) ₃ • Fe(OH) ₂ (approx)	Green rust	<i>Shewanella putrefaciens</i>	Kukkadapu <i>et al.</i> ,2004; O'Loughlin, 2008
α- FeO(OH)	Goethite	<i>Gallionella ferruginea</i>	Hallberg and Ferris, 2004
γ- FeO(OH)	Lepidocrocite	marine bacteriophage, <i>Bacillus subtilis</i>	Daughney <i>et al.</i> ,2004 ; Châtellier <i>et al.</i> ,2001
5Fe ₂ O ₃ • 9 H ₂ O	Ferrihydrite	<i>Gallionella ferruginea</i> , <i>Leptothrix ochracea</i> , <i>Bacillus subtilis</i>	Hallberg and Ferris, 2004; Kennedy <i>et al.</i> ,2004
Fe ₂ O ₃	Hematite	<i>Gallionella ferruginea</i>	Hallberg and Ferris 2004
Fe ₃ O ₄	Magnetite	<i>Shewanella putrefaciens</i> , (Fe(III)-reducing bacteria), Magnetotactic bacteria (e.g. <i>Magnetospirillum magnetotacticum</i>), SRB (e.g. <i>Desulfovibrio magneticus</i>), thermophilic iron-reducing bacteria	Frankel <i>et al.</i> ,1983; Lovley <i>et al.</i> ,1987; Lovley, 1991; Bazylinski <i>et al.</i> ,1993; Zhang <i>et al.</i> ,1997; Zhang <i>et al.</i> ,1998; Kukkadapu <i>et al.</i> ,2004; Bazylinski <i>et al.</i> ,2007; Faivre and Schüler, 2008
γ-Fe ₂ O ₃	Maghemite	<i>Actinobacter sp.</i> , thermophilic iron-reducing bacteria	Zhang <i>et al.</i> ,1997; Bharde <i>et al.</i> ,2008
FeCO ₃	Siderite	<i>Shewanella alga</i> , thermophilic iron-reducing bacteria	Zhang <i>et al.</i> ,1997; Parmer <i>et al.</i> ,2000
FePO ₄ • nH ₂ O	Hydrous ferric Phosphate	<i>Acidovorax sp</i>	Miot <i>et al.</i> ,2009
Fe ₃ (PO ₄) ₂ • 2H ₂ O	Vivianite	<i>Shewanella putrefaciens</i> , <i>Desulfovibrio alaskensis</i> (SRB), <i>Alkaliphilus metalliredigens</i>	Kukkadapu <i>et al.</i> ,2004; Zegeye <i>et al.</i> ,2007; Roh <i>et al.</i> ,2007
FeS	Cubic FeS (Sphalerite-type)	Magnetotactic bacteria	Pósfai <i>et al.</i> ,1998a; Pósfai <i>et al.</i> ,1998b,
FeS	Mackinawite (tetragonal FeS)	Magnetotactic bacteria, <i>Desulfovibrio desulfuricans</i>	Pósfai <i>et al.</i> ,1998a; Pósfai <i>et al.</i> ,1998b; Ivarson and Hallberg, 1976
Fe ₃ S ₄	Greigite	Magnetotactic bacteria, <i>Actinobacter sp.</i> , SRB	Bharde <i>et al.</i> ,2008; Farina <i>et al.</i> ,1990; Mann <i>et al.</i> ,1990; Heywood <i>et al.</i> ,1990; Reitner <i>et al.</i> ,2005; Faivre and Schüler , 2008
Fe _{1-x} S	Pyrrhotite	Magnetotactic bacteria	Farina <i>et al.</i> ,1990
FeS ₂	Pyrite	Magnetotactic bacteria, SRB	Mann <i>et al.</i> ,1990; Bazylinski, 1996; Folk, 2005; Wilkin and Barnes, 1997; Donald and Southam, 1999
KFe ₃ (SO ₄) ₂ (OH) ₆	Jarosite	<i>Sulfobacillus thermosulfidooxidans</i> , <i>Acidithiobacillus ferrooxidans</i> , <i>Thiobacillus ferrooxidans</i>	Ding <i>et al.</i> ,2007; Daoud and Karamanev, 2006; Ivarson and Hallberg, 1976
Fe ₈ O ₈ SO ₄ (OH) ₆	Schwertmanite	<i>Acidithiobacillus ferrooxidans</i>	Egal <i>et al.</i> ,2009
MnCO ₃	Rhodochrosite	<i>Leptothrix discophora</i>	Zhang <i>et al.</i> ,2002
MnO ₂	Manganese Oxides	<i>Pseudomonas putida</i> , <i>Leptothrix discophora</i> , <i>Bacillus sp.</i>	Tebo <i>et al.</i> ,2004; Villalobos <i>et al.</i> ,2003; Brouwers <i>et al.</i> ,2000
Na ₄ Mn ₁₄ O ₂₇ • 9H ₂ O	Birnessite	<i>Pseudomonas putida</i>	Villalobos <i>et al.</i> ,2003
S ⁰	Elemental Sulfur	<i>Chromatiaceae</i> , <i>Beggiatoa spp.</i> , <i>Thiothrix</i> , <i>Thiovulum</i> , <i>Thioploca</i>	Brune, 1989; Brune, 1995; Smith and Strohl, 1991; Strohl <i>et al.</i> ,1981; Pasteris <i>et al.</i> ,2001
Au ⁰	Elemental Gold	<i>Bacillus sp.</i> , <i>Rhodopseudomonas capsulate</i> , <i>Shewanella algae</i> , SRB	Reith <i>et al.</i> ,2009; He <i>et al.</i> ,2007, Konishi <i>et al.</i> ,2007; Konishi <i>et al.</i> ,2006; Lengke and Southam, 2006
CaCO ₃	Calcite	Communities of SRB and archaea, Cyanobacteria, Soil bacteria (<i>Bacillus megaterium</i>), Algae (e.g. <i>Halimeda</i> , <i>Emiliana huxleyi</i>)	Boetius <i>et al.</i> ,2000; Reitner <i>et al.</i> ,2005; Thompson and Ferris, 1990, Lian <i>et al.</i> ,2006; de Vrind-de Jong and de Vrind, 1997

	Aragonite	Cyanobacteria (<i>Synechococcus leopoliensis</i>), <i>Nesterenkonia halobia</i> , <i>Halomonas eurihalina</i>	Obst <i>et al.</i> ,2009; Rivadeneyra <i>et al.</i> ,2000; Rivadeneyra <i>et al.</i> ,1998
	Vaterite	<i>Kocuria</i> , <i>Myxococcus Xanthus</i> , <i>Bacillus sphaericus</i>	Zamarreño <i>et al.</i> ,2009; Rodriguez-Navarro <i>et al.</i> ,2007
CaMg(CO ₃) ₂	Dolomite	<i>Nesterenkonia halobia</i>	Rivadeneyra <i>et al.</i> ,2000
SiO ₂ • nH ₂ O	Amorphous Silica	<i>Calothrix</i> , <i>Fischerella sp.</i> , <i>Shewanella oneidensis</i>	Benning <i>et al.</i> ,2004; Konhauser <i>et al.</i> ,2001; Furukawa and O'Reilly, 2007
SiO ₂	Silica	Diatoms, radiolarians, <i>Thiobacillus</i> , <i>Bacillus Subtilis</i>	de Vrind-de Jong and de Vrind, 1997; Fortin and Beveridge, 1997; Urrutia and Beveridge, 1993
Ca ₅ (PO ₄) ₃ (OH)	Hydroxyapatite/ Calcium phosphat	<i>Ramlibacter tataouinensis</i> , <i>Corynebacterium matruchotii</i> , <i>Streptococcus mutans</i> , <i>Streptococcus sanguis</i>	Benzerara <i>et al.</i> ,2004; Van Dijk <i>et al.</i> ,1998; Streckfuss <i>et al.</i> ,1974
H ₄ PO ₄ • 6H ₂ O	Struvite	<i>Myxococcus xanthus</i> , <i>Pseudomonas</i> , <i>Flavobacterium</i> , <i>Acinetobacter</i> , <i>Yersinia</i> , <i>Corynebacterium</i> , <i>Azotobacter</i>	Da Silva <i>et al.</i> ,2000; Rivadeneyra <i>et al.</i> ,1983

References

- Bauerlein E (2000) *Biomineralization. From Biology to Biotechnology and Medical application*. Weinheim, Wiley –VCH Verlag GmbH 316 p.
- Banfield JF, Nealson KH (eds) (1997) *Geomicrobiology: Interactions between microbes and minerals. Reviews in Mineralogy*, Ribbe PH (series ed.) Washington, DC: Mineralogical Society of America. Vol. 35, 448 p.
- Bazylinski DA, Frankel RB, Konhauser KO (2007) Modes of biomineralization of magnetite by microbes. *Geomicrobiology Journal*, **24**, 465-475.
- Bazylinski DA, Frankel RB (2003) Biologically controlled mineralization in procaryotes. In Dove PM, De Yoreo JJ, Weiner S (eds), Rosso JJ (series ed.), *Biomineralization. Reviews in Mineralogy and Geochemistry*. Washington, DC: Mineralogical Society of America and Geochemical Society, Vol. 54, 217-247.
- Bazylinski DA (1996) Controlled biomineralization of magnetic minerals by Magnetotactic bacteria. *Chemical Geology*, **132**, 191-198.
- Bazylinski DA, Heywood BR, Mann S, Frankel RB (1993) Fe₃O₄ and Fe₃S₄ in a bacterium. *Nature*, **366**, 218.
- Benning LG, Phoenix VR, Yee N, Tobin MJ (2004) Molecular characterization of cyanobacterial silification using synchrotron infrared micro-spectroscopy. *Geochimica et Cosmochimica Acta*, **68**, 729-741.
- Benzerara K, Menguy N, Guyot F, Skouri F, de Luca G, Barakat M, Heulin T (2004) Biologically controlled precipitation of calcium phosphate by *Ramlibacter tataouinensis*. *Earth and Planetary Science Letters*, **228**, 439-449
- Bharde AA, Parikh RY, Baidakova M, Jouen S, Hannover B, Enoki T, Prasad BLV, Shouche YS, Ogale S, Sastry M (2008) Bacteria-Mediated Precursor-Dependent Biosynthesis of Superparamagnetic Iron Oxide and Iron Sulfide Nanoparticles. *Langmuir*, **24**, 5787-5794.

- Boetius A, Ravensschlag K, Schubert CJ, Rickert D, Widdel F, Gieseke A, Amann R, Jørgensen BB, Witte U, Pfannkuche O (2000) A marine microbial consortium apparently mediating anaerobic oxidation of methane. *Nature*, **407**, 623-626.
- Borowitzka MA (1982) Morphological and cytological aspects of algal calcification. *International review of Cytology*, **74**, 127-162.
- Brouwers GJ, Vijgenboom E, Corstjens PLAM, De Vrind JPM, De Vrind-De Jong EW (2000) Bacterial Mn²⁺ oxidizing systems and multicopper oxidases: An Overview of mechanisms and functions. *Geomicrobiology Journal*, **17**, 1-24.
- Brune DC (1995) Isolation and characterization of sulfur globule proteins from *Chromatium vinosum* and *Thiocapsa roseopersicina*. *Archives of Microbiology*, **163**, 391-399.
- Brune DC (1989) Sulfur oxidation by phototrophic bacteria. *Biochimica et Biophysica Acta*, **975**, 189-221.
- Chan CS, Fakra SC, Edwards DC, Emerson D, Banfield JF (2009) Iron oxyhydroxide mineralization of microbial extracellular polysaccharides. *Geochimica et Cosmochimica Acta*, **73**, 3807-3818.
- Châtellier X, Fortin D, West MM, Leppard GG, Ferris FG (2001) Effect of the presence of bacterial surfaces during the synthesis of Fe oxides by oxidation of ferrous ions. *European Journal of Mineralogy*, **13**, 705-714.
- Da Silva S, Bernet N, Delgenès JP, Moletta R (2000) Effect of culture conditions on the formation of struvite by *Myxococcus Xanthus*. *Chemosphere*, **40**, 1289-1296.
- Daoud J, Karamanev D (2006) Formation of jarosite during Fe²⁺ oxidation by *Acidithiobacillus ferrooxidans*. *Minerals Engineering*, **19**, 960-967.
- Daughney CD, Châtellier X, Chan A, Kenward P, Fortin D, Suttle CA, Fowl D (2004) Adsorption and precipitation of iron from seawater by a marine bacteriophage (PWH3a-P1). *Marine Chemistry*, **91**, 101-115.
- De Vrind-de Jong EW, de Vrind JPM (1997) Algal deposition of carbonates and silicates. In Banfield JF, Nealson KH (eds.), *Geomicrobiology: interactions between microbes and minerals. Reviews in Mineralogy*. Washington, DC. Mineralogical Society of America, Vol. 35, 267-307.
- Ding J-N, Gao J, Wu X-l, Zhang C-G, Qiu G-Z (2007) Jarosite -type precipitates mediated by YN22, *Sulfobacillus thermosulfidooxidans*, and their influences on strain. *Transactions of nonferrous metals. Society of China*, **17**, 1038-1044.
- Donald R, Southam G (1999) Low temperature anaerobic bacterial diagenesis of ferrous monosulfide to pyrite. *Geochimica et Cosmochimica Acta*, **63**, 2019-2023.
- Dove PM, De Yoreo JJ, Weiner S (eds) (2003) *Biomineralization. Reviews in Mineralogy and Geochemistry*, Rosso J J (series ed) Washington DC: Mineralogical Society of America and Geochemical Society, Vol. 54, 381 p.
- Driessens FCM, Verbeeck RK (1990) *Biominerals*. Boca Raton, Florida: CRC Press Inc, 440.
- Egal M, Casiot C, Morin G, Parmentier M, Bruneel O, Lebrun S, Elbaz-Poulichet F (2009) Kinetic control on the formation of tooeleite, schwertmannite and jarosite by *Acidithiobacillus ferrooxidans* strains in an As(III)-rich acid mine water. *Chemical Geology*, **265**, 432-441.
- Ehrlich HL (1999) Microbes as Geologic Agents: Their Role in Mineral Formation. *Geomicrobiology Journal*, **16**, 135-153.

- Ercole C, Cacchio P, Botta AL, Centi V, Lepidi A (2007) Bacterially induced mineralization of calcium carbonate: The role of exopolysaccharides and capsular polysaccharides. *Microscopy and Microanalysis*, **13**, 42-50.
- Faivre D, Schüler D (2008) Magnetotactic bacteria and magnetosomes. *Chemical Reviews*, **108**, 4875-4898.
- Farina M, Esquivel DMS, Lins de Barros HGP (1990) Magnetic iron-sulphur crystals from magnetotactic microorganism. *Nature*, **343**, 256-258.
- Folk RL (2005) Nannobacteria and the formation of framboidal pyrite: Textural evidence. *Journal of earth System Science*, **114**, 369-374.
- Fortin D, Beveridge TJ (1997) Role of the bacterium *Thiobacillus* in the formation of silicates in acidic mine tailings. *Chemical Geology*, **141**, 235-250.
- Fortin D, Beveridge TJ (2000) Mechanistic routes to biomineral surface development. In Bäuerlein E (ed), *Biomineralization: From Biology to Biotechnology and Medical Application*. Weinheim, Wiley-VCH GmbH, 7-24.
- Frankel RB, Bazylinski DA (2003) Biologically induced mineralization by bacteria. In Dove PM, De Yoreo JJ, Weiner S (eds), Rosso JJ (series ed.), *Biomineralization. Reviews in Mineralogy and Geochemistry*. Washington, DC: Mineralogical Society of America and Geochemical Society, Vol. 54, 95-114.
- Frankel RB, Papaefthymiou GC, Blakemore RP, O' Brien W (1983) Fe₃O₄ precipitation in Magnetotactic bacteria. *Biochimica et Biophysica Acta*, **763**, 147-159.
- Furukawa Y, O'Reilly SE (2007) Rapid precipitation of amorphous silica in experimental systems with nontronite (Nau-1) and *Shewanella oneidensis* MR-1. *Geochimica et Cosmochimica Acta*, **71**, 363-377.
- Haferburg G, Kothe E (2007) Microbes and metals: interactions in the environment. *Journal of Basic Microbiology*, **47**, 453-467.
- Hallberg R, Ferris FG (2004) Biomineralization by Gallionella. *Geomicrobiology Journal*, **21**, 325-330.
- He S, Gui Z, Zhang Y, Zhang S, Wang J, Gu N (2007) Biosynthesis of gold nanoparticles using the bacteria *Rhodospseudomonas capsulata*. *Material Letters*, **61**, 3984-3987.
- Heywood BR, Bazylinski DA, Garratt-Reed A, Mann S, Frankel RB (1990) controlled biosynthesis of greigite (Fe₃S₄) in magnetotactic bacteria. *Naturwissenschaften*, **77**, 536-538.
- Ivarson KC, Hallberg RO (1976) Formation of mackinawite by the microbial reduction of jarosite and its application to tidal sediments. *Geoderma*, **16**, 1-7.
- Kennedy CB, Scott SD, Ferris FG (2004) Hydrothermal phase stabilization of 2-line ferrihydrite by bacteria. *Chemical Geology*, **212**, 269-277.
- Kirschvink JL, Hagadorn JW (2000) 10 a Grand unified theory of Biomineralization. In Bäuerlein (ed), *The Biomineralisation of Nano- and Microstructures*. Weinheim: Wiley-VCH GmbH, 139-150.
- Konhauser KO, Phoenix VR, Bottrell SH, Adams DG, Head IM (2001) Microbial-silica interactions in Icelandic hot spring sinter: possible analogues for some Precambrian siliceous stromatolites. *Sedimentology*, **48**, 415-433.
- Konishi Y, Tsukiyama T, Tachimi T, Saitoh N, Nomura T, Nagamine S (2007) Microbial deposition of gold nanoparticles by the metal-reducing bacterium *Shewanella* algae. *Electrochimica Acta*, **53**, 186-192.

- Konishi Y, Tsukiyama T, Ohno K, Saitoh N, Nomura T, Nagamine S (2006) Intracellular recovery of gold by microbial reduction of AuCl_4^- ions using the anaerobic bacterium *Shewanella algae*. *Hydrometallurgy*, **81**, 24-29.
- Kukkadapu RK, Zachara JM, Fredrickson JK, Kennedy DW (2004) Biotransformation of two-line silica-ferrihydrite by dissimilatory Fe(III)-reducing bacterium: Formation of carbonate green rust in the presence of phosphate. *Geochimica et Cosmochimica Acta*, **68**, 2799-2814.
- Lengke M, Southam G (2006) Bioaccumulation of gold by sulfate-reducing bacteria cultured in the presence of gold(I)-thiosulfate complex. *Geochimica et Cosmochimica Acta*, **70**, 3646-3661.
- Lian B, Hu Q, Chen J, Ji J, Teng HH (2006) Carbonate biomineralization induced by soil bacterium *Bacillus megaterium*. *Geochimica et Cosmochimica Acta*, **70**, 5522-5535.
- Lovley D (ed) 2000. *Environmental microbe-metal interactions*. ASM Press, Washington, DC, 395p.
- Lovley DR (1991) Dissimilatory Fe(III) and Mn(IV) reduction. *Microbiology Reviews*, **55**, 259-287.
- Lovley DR, Stolz JF, Nord Jr GL, Phillips EJP (1987) Anaerobic production of magnetite by a dissimilatory iron-reducing microorganism. *Nature*, **330**, 252-254.
- Lowenstam HA (1981) Minerals formed by organisms. *Science*, **211**, 1126-1131.
- Lowenstam HA, Weiner S (1989) *On Biomineralization*. New York: Oxford University Press, 324 p.
- Mann S (2001) *Biomineralization: Principles and concepts in bioinorganic materials chemistry*. In Compton, RG, Davies SG, Evans J (eds), *Oxford Chemistry Masters Vol. 5*. Oxford University Press, New York, 216 p.
- Mann S, Sparks NHC, Frankel RB, Bazylinski DA, Jannasch HW (1990) Biomineralization of ferromagnetic greigite (Fe_3S_4) and iron pyrite (FeS_2) in a Magnetotactic bacterium. *Nature*, **343**, 258-261.
- Minsky A, Shimoni E, Frenkel-Krispin D (2002) Stress, order and survival. *Nature Reviews Molecular Cell Biology*, **3**, 50-60.
- Miot J, Benzerara K, Morin G, Kappler A, Bernard S, Obst M, Férard C, Skouri-Panet F, Guigner J-M, Posth N, Galvez M, Brown Jr GE, Guyot F (2009) Iron biomineralization by anaerobic neutrophilic iron-oxidizing bacteria. *Geochimica et Cosmochimica Acta*, **73**, 696-711.
- Obst M, Dynes JJ, Lawrence JR, Swerhone GDW, Benzerara K, Kaznatcheev K, Tyliszczak T, Hitchcock A P (2009) Precipitation of amorphous CaCO_3 (aragonite-like) by cyanobacteria: A STXM study of the influence of EPS on the nucleation process. *Geochimica et Cosmochimica Acta*, **73**, 4180-4198.
- O'Loughlin EJ (2008) Effects of electron transfer mediators on the bioreduction of Lepidocrocite ($\gamma\text{-FeOOH}$) by *Shewanella putrefaciens* CN32. *Environmental Science and Technology*, **42**, 6876-6882.
- Parmar N, Warren LA, Roden EE, Ferris FG (2000) Sild phase capture of strontium by the iron reducing bacteria *Shewanella alga* strain BRY. *Chemical Geology*, **169**, 281-288
- Pasteris JD, Freeman JJ, Goffredi SK, Buck KR (2001) *Chemical Geology*, **180**, 3-18.
- Pósfai M, Buseck PR, Bazylinski DA, Frankel RB (1998a) Reaction sequence of iron sulfide minerals in bacteria and their use as biomarkers. *Science*, **280**, 880-883.
- Pósfai M, Buseck PR, Bazylinski DA, Frankel RB (1998b) Iron sulfides from magnetotactic bacteria: Structure, compositions, and phase transitions. *American Mineralogist*, **83**, 1469-1481.

- Reith F, Wakelin SA, Gregg A L, Schmidt-Mumm A (2009) A microbial pathway for the formation of gold-anomalous calcrite. *Chemical Geology*, **258**, 315-326.
- Reitner J, Peckmann J, Blumenberg M, Michaelis W, Reimer A, Thiel V (2005) Concretionary methane-seep carbonates and associated microbial communities in Black Sea sediments. *Palaeogeography, Palaeoclimatology, Palaeoecology*, **227**, 18-30.
- Rivadeneira MA, Delgado G, Soriano M, Ramos-Cormenzana A, Delgado R (2000) Precipitation of carbonates by *Nesterenkonia halobia* in liquid media. *Chemosphere*, **41**, 617-624.
- Rivadeneira MA, Delgado G, Ramos-Cormenzana A, Delgado R (1998) Biomineralization of carbonates by *Halomonas eurihalina* in solid and liquid media with different salinities: crystal formation sequence. *Research in Microbiology*, **149**, 277-287.
- Rivadeneira MA, Ramos-Cormenzana A, García-Cervigon A, (1983) Bacterial formation of struvite. *Geomicrobiology Journal*, **3**, 151-163.
- Rodríguez-Navarro C, Jiménez-López C, Rodríguez-Navarro A, González-Muñoz M T, Rodríguez-Gallego M (2007) Bacterially mediated mineralization of vaterite. *Geochimica et Cosmochimica Acta*, **71**, 1197-1213.
- Roh Y, Chon C-M, Moon J-W (2007) Metal reduction and biomineralization by alkaliphilic metal reducing bacterium, *Alkaliphilus metalliredigens* (QYMF). *Geosciences Journal*, **11**, 415-423.
- Sigel A, Sigel H, Sigel RO (eds) (2008) *Biomineralization: from Nature to Application. Metal Ions in life sciences*. Wiley and Sons, West Sussex, 4 Vols, 700 p.
- Smith DW, Strohl WR (1991) Sulfur oxidizing bacteria. In Shively J. M., Barton L. L., (eds.), *Variations in autotrophic life*. Academic Press, London, 121-146.
- Southam G (2000) Bacterial surface-mediated mineral formation. In Lovley, D. R. (ed.), *Environmental microbe-metal interactions*. ASM Press, Washington DC, 257-276.
- Streckfuss JL, Smith WN, Brown LR, Campbell MM (1974) Calcification of Selected Strains of *Streptococcus mutans* and *Streptococcus sanguis*. *Journal of Bacteriology*, **120**, 502-506.
- Strohl WR, Geffers I, Larkin JM (1981) Structure of the sulfur inclusions envelopes from four beggiatoas. *Current Microbiology*, **6**, 75-79.
- Takahashi Y, Hirata T, Shimizu H, Ozaki T, Fortin D (2007) A rare earth element signature of bacteria in natural waters. *Chemical Geology*, **244**, 569-583.
- Tebo BM, Bargar JR, Clement BG, Dick GJ, Murray KJ, Parker D, Verity R, Webb SM (2004) Biogenic Manganese Oxides: Properties and mechanisms of formation. *Annual Review of Earth and Planetary Sciences*, **32**, 287-328.
- Thompson JB, Ferris FG (1990) Cyanobacterial precipitation of gypsum, calcite, and magnesite from natural alkaline lake water. *Geology*, **18**, 995-998.
- Urrutia MM, Beveridge TJ (1993) Mechanism of silicate binding to the bacteria cell wall in *Bacillus subtilis*. *Journal of Bacteriology*, **175**, 1936-1945.
- Van Dijk S, Dean DD, Zhao Y, Cirgwin JM, Schwartz Z, Boyan BD (1998) Purification, amino acid sequence, and cDNA sequence of novel calcium-precipitating proteolipids involved in calcification of *Corynebacterium matruchotii*. *Calcified Tissue International*, **62**, 350-358.

- Villalobos M, Toner B, Bargar J, Sposito G (2003) Characterization of manganese oxide produced by *Pseudomonas putida*. *Geochimica et Cosmochimica Acta*, **67**, 2649-2662.
- Weiner S, Dove PM (2003) An overview of biomineralization processes and the problem of the vital effect. In Dove PM, De Yoreo JJ, Weiner S (eds.), *Biomineralization. Reviews in Mineralogy and Geochemistry*. Mineralogical Society of America and Geochemical Society, Washington DC, Vol 54, 1-29.
- Wilkin RT, Barnes HK (1997) Formation processes of framboidal pyrite. *Geochimica et Cosmochimica Acta*, **61**, 323-339.
- Yoshida H, Yamamoto K, Murakami Y, Katsuta N, Hayashi T, Naganuma T (2008) The development of Fe-nodules surrounding biological material mediated by microorganisms. *Environmental Geology*, **55**, 1363-1374.
- Zamarreño DV, Inkpen R, May E (2009) Studies on carbonate crystals precipitated by freshwater bacteria and their use as a limestone consolidant. *Applied and Environmental Microbiology*, **75**, 5981-5990.
- Zegeye A, Huhuet L, Abdelmoula M, Carteret C, Mullet M, Jorand F (2007) Biogenic hydroxysulfate green rust, a potential electron acceptor for SRB activity. *Geochimica et Cosmochimica Acta*, **71**, 5450-5462.
- Zhang C, Liu S, Phelps TJ, Cole DR, Horita J, Fortier SM, Elless M, Valley J (1997) Phytochemical, mineralogical, and isotopic characterization of magnetite-rich iron oxides formed by thermophilic iron-reducing bacteria. *Geochimica et Cosmochimica Acta*, **61**, 4621-4632.
- Zhang C, Vali H, Romanek CS, Phelps TJ, Liu SV (1998) Formation of single-domain magnetite by a thermophilic bacterium. *American Mineralogist*, **83**, 1409-1418.
- Zhang J, Lion LW, Nelson YM, Shuler ML, Ghiorse WC (2002) Kinetics of Mn (II) oxidation by *Leptothrix discophora* SS1. *Geochimica et Cosmochimica Acta*, **65**, 773-781.

C

Frutexites

Marta Rodriguez-Martinez, Christine Heim, Nadia-Valérie Quéric, Joachim Reitner

Encyclopedia of Geobiology, Springer, 2011, in press

Synonyms

Colloform limonitic crusts; *Frutexites* crusts; *Frutexites* like forms; *Frutexites* microstromatolite; *Frutexites* tuffs; Haematitic/ferruginous/iron microstromatolites; Iron dendritic aggregates; Iron shrubs; Pillar-shaped microstromatolites.

Definition

Frutexites is a problematic microfossil rich in iron. From a taxonomic point of view only five species have been figured (*Frutexites arboriformis* Maslov, 1960; *F. microstroma* Walter and Awramik, 1979; *Frutexites* sp 1., *F. sp. 2*, *New gen. 3* Tsien, 1979), although the authors mostly use the term *Frutexites* sensu lato. The genus *Frutexites* was coined by Maslov (1960) in order to describe submillimeter-sized, iron-rich, and subordinate calcite microfossils (Figure C.1). *Frutexites* have a dendritic shape formed by diverging microcolumns. The height and width of microcolumns as well as their composition and microstructure can vary (Table C.1). The preservation of microstructure is strongly controlled by its dominant mono- or polymineral character. Microstructure is formed by convex-upward laminae which sometimes show radially arranged fibres.

Frutexites can occur as mainly monomineral as well as polymineral structures with: iron- and/or manganese-rich (hematites, iron hydroxides, iron manganese oxyhydroxides), and/or carbonate-rich (calcite, ferroan calcite, dolomite), and/or siliciclastic-rich (argillite, microquartz), and/or phosphatic-rich zones.

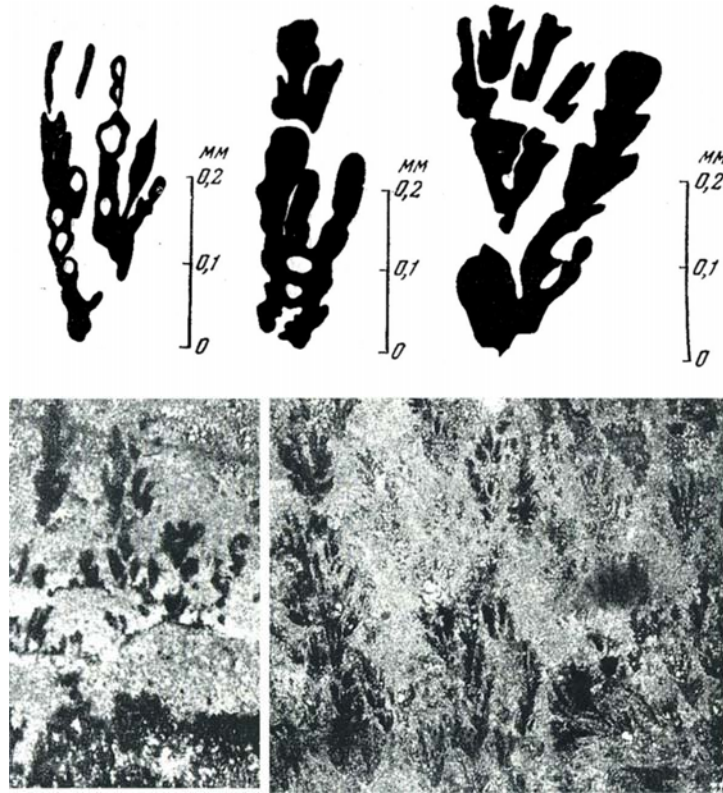


Figure C.1. Original figures describing the genus of *Frutexites* according to Maslov (1960).

Authors	Height	Width	microstructure	morphology	composition
Maslov 1960	Up to 400 μm (see Fig.1)	25-30 μm More of 50 μm	Sheets with occasionally circular spaces	Radially diverging and branched sheets	Iron hydroxide and carbonate
Horodyski 1975	20-500 μm	10-200 μm	2-10 μm convex- upward laminae	Pillar-shaped branched and not	Hematite, calcite and argillite
Walter and Awramik 1979	Up to 450 μm	5-120 μm	0.7-2.7 μm convex upward laminae and axial tube (trichome?)	Undulose layers, laminae with protruding pustules and erect branching microcolumns	Organic matter permineralised by silica
Myrow and Coniglio 1991	250 μm -4 mm most < 1mm	75-600 μm , 250 μm average	Chambers, laminae, fibres and projections	Unbranching and branching columns	Calcite, ferroan calcite, hematite and microquartz
Böhm and Brachert 1993	Up to 5 mm, average 1-2 mm		Convex laminae with radially arranged fibres		Fe-Mn oxides, calcite and phosphates
Woods and Baud 2008	Up to 800 μm	50-200 μm	Lighter- and darker coloured layers resulting chambered appearance		Hematite and/or Fe-Mn minerals and calcite

Table C.1. Sizes, morphological and compositional parameters of *Frutexites* according to different authors.

Depositional environmental occurrences

Frutexites has been described in marine environments like shallow and deep water stromatolites, microbial limestones, hardgrounds, condensed pelagic limestones as well as in cavities, sheet-cracks, veins, and Neptunian dikes. However, comparisons with continental black shrubs are common, too. *Frutexites* structures are also frequently found in veins and fractures of deep subterranean environments (Figures C.2 B,C).

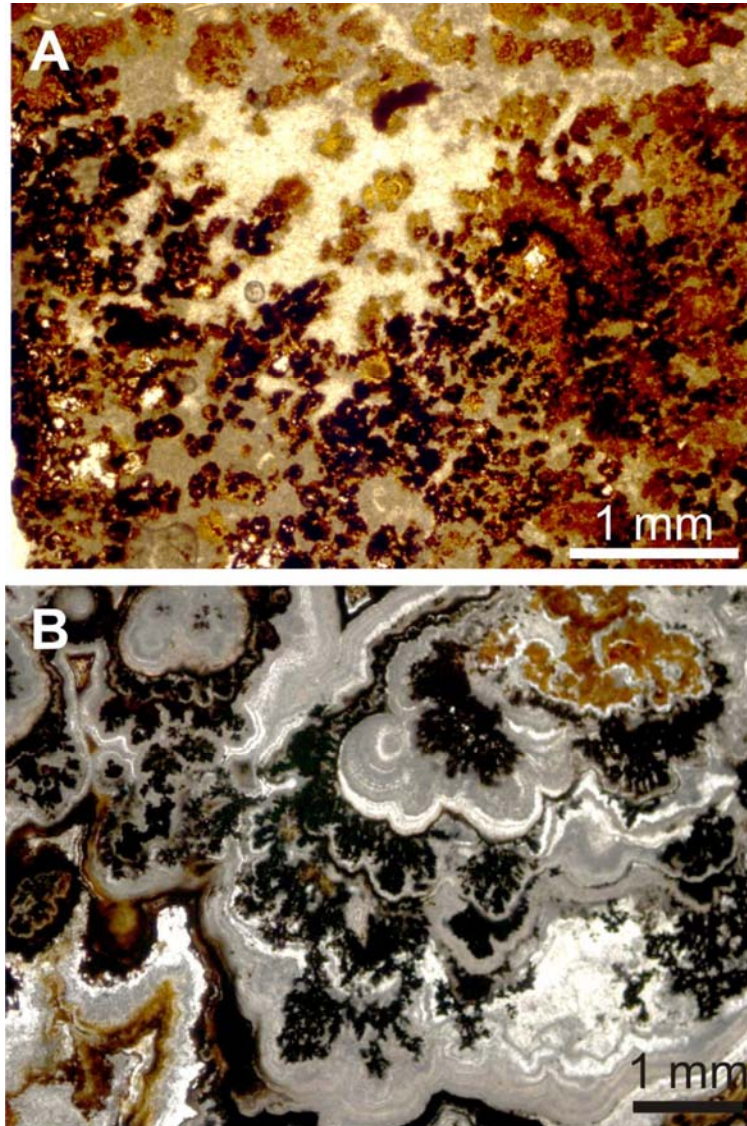


Figure C.2. (A) Marine Upper Cenomanian/Lower Turonian *Frutexites* colonies from a deepwater hardground environment (Lienres coast, Northern Spain; Reitner et al, 1995). The *Frutexites* facies is located on top of the hardground sequence and marks a fundamental change of the oceanographic conditions. (B) Deep subterranean *Frutexites* colonies growing on calcareous microstromatolites from tectonic fractures in the so-called “sole dolomite” at the base of the Naukluft Nappe Complex (NNC) in Southern Namibia. The colonies are growing upside down from the fracture ceiling. The black ones are rich in Mn oxides, the ochre parts are enriched in Fe oxides.

Stromatolites

The main record of *Frutexites* has commonly been recognized from shallow to deep calcareous stromatolites from Proterozoic to Recent examples (see Caldera lake stromatolites at Tonga, by Kazmierczak and Kempe, 2006). *Frutexites* structures grow upwards perpendicular to the stromatolite laminae, however they can sometimes cross them (Horodyski, 1975) and even destroy them. For this reason, Böhm and Brachert (1993) interpreted that stromatolite accretion was independent of *Frutexites* which would act as dweller or secondary binder in the Jurassic deep water stromatolites from Germany and Austria. Descriptions about the associated macro- and microfauna in the *Frutexites*-bearing stromatolites are not abundant. In the Canning Basin, the late Devonian *Frutexites*-bearing stromatolites show abundant metazoans in life position as crinoids and coral holdfasts encrusting the successive laminae (Playford *et al.*, 1976), which would indicate normal oxygenated water conditions (Nicoll and Playford, 1993). In Jurassic stromatolites, *Frutexites* occur with shells of *Bositra* and *Lenticulina* foraminifers.

Cavities, sheet cracks, veins, and Neptunian dikes

The second most frequent occurrence of *Frutexites* in the geologic record is related to cavity walls and fissures. On the horizontal surfaces *Frutexites* could display a dominant upward growth, but, in general, their growth is normally perpendicular to the substrate where they were nucleated. *Frutexites* occur interbedded with fibrous calcite cements as well as with internal sediment. The oldest described record is in sheet cracks within stromatolites of the upper Vendian to Lower Cambrian Chapel Island Formation, Canada (Myrow and Coniglio, 1991). *Frutexites* have been found in cavities of Devonian deep water mud mounds and grouped with *Renalcis-Epiphyton* calcimicrobes, and with deep water stromatolites assemblage (Tsien, 1979) as well as in stromatolite cavities from Viséan microbial limestones where they occur interbedded with marine isopachous crusts of fibrous and botryoidal calcite cements (Gischler, 1996). The presence of *Frutexites* in Neptunian dikes has been described only in Devonian records from the Harz Mountains in Germany (Gischler, 1996) and mud mounds of the Hamar Laghdad Ridge in Morocco (Cavalazzi *et al.*, 2007). Similar structures as *Frutexites* have also been described in voids from Toarcian Mn-rich layer at Tatra Mountains in Poland (Jach and Dudek, 2005) as well as in syndimentary karstic cavities in Pleistocene travertines in Germany (Koban and Schweigert, 1993).

Condensed pelagic limestones and hardgrounds

The last most extended occurrence of *Frutexites* is associated with condensed hemipelagic and pelagic red to grey limestones like Griotte and Hallstatt Limestone, as well as Rosso Ammonitico

facies from Devonian up to Jurassic. These facies occur during very low sedimentation rates, from deep to relatively shallow water depths, during fast transgressive and/or drowning episodes. Nektonic organisms are the dominant fauna (goniatites, nautiloids, ammonoids) and *Frutexites* occur in (i) water-sediment interfaces colonizing sessile fauna, reworked bioclasts as well as ferromanganese hardgrounds (see below) and (ii) within the micritic sediment. The first type of *Frutexites* growth in condensed pelagic limestones was described in Matagne Formation (Devonian of Belgium) by Tsien (1979) and in current-swept shallow pelagic ridge (Tafilalt Platform, Devonian of Morocco) by Wendt (1988). No less representative examples have been shown from the Triassic Hallstatt facies of Austria (Wendt, 1969; Rodríguez-Martínez *et al.*, in press) and Oman Mountains (Woods and Baud, 2008). In the Oman Mountains, the sea-floor was directly colonized by *Frutexites*-bearing microbialites and syndimentary cements. However, in the Northern Calcareous Alps, multiple ferromanganese crusts were colonized by epibenthonic sessile agglutinated foraminifers which were successively encrusted by *Frutexites* forming pillar-like structures above the seawater-sediment interface.

Similar situation has been described from deep-water hardgrounds during Mid Cretaceous times in Spain (Reitner *et al.*, 1995), (Figure C.2). In this case, a previous benthic community dominated by coralline sponges was replaced by thick limonitic stromatolites with encrusting foraminifera and colonies of *Frutexites*.

The growth of *Frutexites* within the sediment was firstly pointed out by Böhm and Brachert (1993). They described the changes in composition and shapes of *Frutexites* as a result of their growth in open spaces or in interstitial environments. Mamét and Prétat (2006) found *Frutexites* associated to other hematite microstructures in condensed Griotte facies (Coumiac Limestones, Montagne Noire, Balears Limestone Spain) and Rosso Ammonitico Limestone (Subbetic Cordillera Spain).

Continental environments

Some authors (Myrow and Coniglio, 1991; Böhm and Brachert, 1993) have compared the marine records of *Frutexites* with similar arborescent, dendritic forms found in speleothems, desert varnish, and travertines. Also continental black shrubs rich in manganese and iron have been compared with the marine *Frutexites* records (Koban and Schweigert, 1993; Chafetz *et al.*, 1998). Shapes, sizes, and polymineral character are similar in both marine and continental records.

Subterranean environments

Frutexites structures are sometimes common in light-independent, deep continental caves, fractures, and veins forming small microbial crusts and build ups often associated with calcareous stromatolitic structures. A characteristic representative was found by J. Reitner in southern Namibia (Figure C. 2B) at the base of the Naukluft Nappe Complex (NNC) which is part of the early Cambrian Damara orogeny (Miller, 2008). The deep base of the NNC is formed by the so-

called “Sole Dolomite” (Korn and Martin, 1959) which is often heavily fractured. Within these cryptic fractures *Frutexites* is very common and intergrows with calcareous stromatolitic structures. Thin-shelled freshwater type ostracodes are also abundant in this fracture system.

A modern example of *Frutexites* structures has been found in the deep tunnel of Äspö in southern Sweden (Heim *et al.*, 2007), as part of a highly oxygenated system. Wherever groundwater drops from the tunnel ceiling, a net-like, mineralized micro-system is formed on any rock surface beneath (Figure C.3). In general, the dropping system is associated to pending mineral cones which are dominated by the iron-oxidizing, chemolithotrophic bacterium *Gallionella ferruginea*.

The evolving net-like structures feature semi-solid ridges, harbouring a particular, highly diverse microbial community. The cross-section of this mineralized biofilm shows laminae with *Frutexites*-like structures (Figure C.4). These are mainly composed of iron hydroxides, iron oxides and less abundant manganese oxides. Small amounts of siderite, calcite and siliceous material occur side by side with iron and manganese oxides.

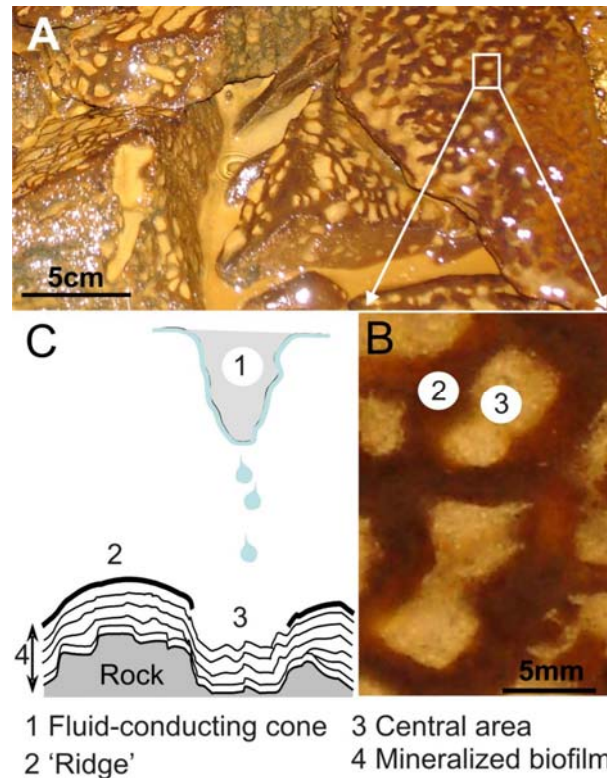


Figure C.3. (A) Net-like, mineralized microbial mat covering the surface of granitic rocks (Äspö Hard Rock Laboratory, Sweden). (B) Scheme of the dropping micro-system according to overview A., comprising a pending mineral cone as a fluid-conduit (1) and the evolving, net-like microstructure beneath, displaying a dark mineralized ridge (2) covering the laminated biofilm (3) and the central area directly exposed to the fluid dropping (4). (C) Close-up of the net-like, mineralized microbial mat, pointing to the dark mineralized ridge (2) and the bright central area (4) according to scheme B.

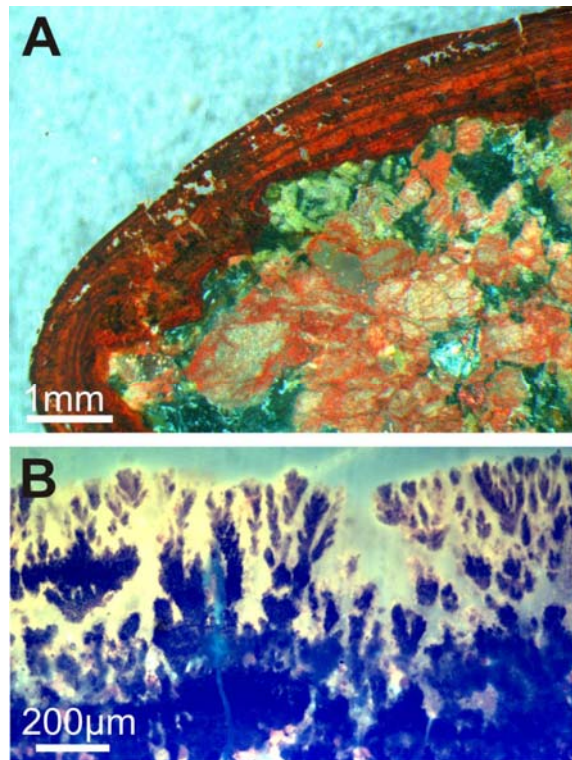


Figure C.4. (A) Thin section of the mineralized, net-like, recent biofilm from the tunnel of Äspö (Schweden) under reflected light, revealing the typical laminated structure. These laminae predominantly consist of iron oxides and hydroxides. (B) UV-Fluorescence micrograph exhibits *Frutexites*-like colonies within the laminae of the mineralized biofilm.

Interpretation

Holotypes of *Frutexites* species (*Frutexites arboriformis* Maslov, 1960; *Frutexites microstroma* Walter and Awramik, 1979) were originally described from stromatolites; thus they were genetically linked to different types of cyanobacteria (Playford *et al.*, 1976, 1984; Scytonematacea – Walter and Awramik, 1979; Rivulariaceae – Hofmann and Grotzinger, 1985; Angulocellularia – Riding, 1991). Hofmann and Grotzinger (1985) discussed the affinity of *Frutexites* to different cyanobacteria and proposed further alternatives (purely physicochemical accretion and/or iron bacteria due to the ferruginous character of stromatolites). The occurrence of *Frutexites* in cavities, fissures, and dykes was interpreted as cryptobiosis (Myrow and Coniglio, 1991). However, Tsien (1979) was the first suggesting a non-phototrophic character, sometimes linked to chemoheterotrophic cyanobacteria (Gischler, 1996) or to chemohetero- and -autotrophic bacteria (Cavalazzi *et al.*, 2007). Böhm and Brachert (1993) emphasized the cryptobiotic role, a negative phototactic downward growth as well as the cryptoendopelitic behaviour (living in interstitial habitats) of *Frutexites*. Based on these aspects the authors proposed the preference of *Frutexites* for oxygen-deficient environments (dysaerobic to anaerobic conditions). Furthermore, they suggested a bacterial precursor for the formation of *Frutexites*, but did not exclude a possible fungal and/or

physicochemical origin. According to previous publications (Maslov, 1960; Myrow and Coniglio *op cit*), Böhm and Brachert (1993) explained the ferromanganese or phosphate mineralogy of *Frutexites* as a replacement of primary carbonate mineralogy. A primary iron mineralization of *Frutexites* was postulated by Horodyski (1975), Hurley and Van der Voo (1990). Others like Hofmann and Grotzinger (1985) believed that microbiota involved in *Frutexites* could regulate the local water chemistry and iron oxyhydroxides as well as aragonite coprecipitations.

Finally, the occurrence of *Frutexites* in condensed pelagic limestones and hardgrounds has been linked to a physicochemical origin (Wendt, 1969) as well as to iron bacteria (Reitner *et al.*, 1995; Mamet and Pr  at, 2006). Reitner *et al* (1995) interpreted the *Frutexites*–foraminifera assemblage as a R-strategic community which replaced the previous K-strategic community (sponges-microbes) due to fundamental changes in oceanographic conditions (from oligotrophic to more eutrophic conditions). Mamet and Pr  at discussed the origin of red pigmentation in Phanerozoic limestones, where some condensed pelagic limestones with *Frutexites* are included. They argued that under anoxic to dysoxic conditions, ferrous iron may be available for oxidation by microaerophilic iron microbes growing at the sediment-water interface. In contrast, the recent *Frutexites*-like structures found in the deep biosphere in fact grow in air-exposed environments (under aerobic conditions). However, the presence of different mineral phases within these structures could be associated to changing redox conditions and/or to a different microbial community composition at micrometer-range.

Conclusions

The different modes of growth of *Frutexites* have been recognized within shallow to deep water stromatolites, on the seawater-sediment interface, marine micritic sediments, continental cavities, and fractures of deep subterranean environments. Such wider environmental distribution has been taken into consideration for palaeoecological interpretations. According to the occurrence of *Frutexites*, some general aspects can be summarized: i) its distribution does not show bathymetric control (although its dominant record is in deep waters); ii) it formed in environments with very low sedimentation rate (in quiet as well as in agitated waters); iii) in marine environments, *Frutexites* mainly encrusts heterozoan assemblages (crinoids, sponges, solitary corals and foraminifers); and finally, iv) there is no proof for an exclusive occurrence of *Frutexites* under anoxic and aphotic conditions.

Most of the authors considered a bacterially-induced growth *Frutexites*, but the final assessment strongly depends on which mineralogical composition they interpreted as primary (timing of iron mineralization) as well as its *loci* of growth.

References

- Böhm F, Brachert TC (1993) Deep-water stromatolites and *Frutexitis* Maslov from the Early and Middle Jurassic of S-Germany and Austria. *Facies*, **28**, 145-168.
- Cavalazzi B, Barbieri R, Ori G (2007) Chemosynthetic microbialites in the Devonian carbonate mounds of Hamar Laghdad (Anti-Atlas, Morocco). *Sedimentary Geology*, **200**, 73–88.
- Chafetz HS, Akdim B, Julia R, Reid A (1998) Mn- and Fe-rich black travertine shrubs: bacterially (and nanobacterially) induced precipitates. *Journal of Sedimentary Research*, **68**, 404-412.
- Gischler E (1996) Late Devonian-Early Carboniferous deep-water coral assemblages and sedimentation on a Devonian seamount: Iberg Reef, Harz Mts., Germany. *Palaeogeography, Palaeoclimatology, Palaeoecology*, **123**, 297-322
- Heim C, Simon K, Queric N-V, Thiel V (2007) Mineralized microbial mats with extreme lanthanum enrichments in the tunnel of Äspö, Sweden. *Geochimica et Cosmochimica Acta*, Goldschmidt Abstracts 2007, H- A390.
- Hofmann J, Grotzinger JP (1985) Shelf-facies microbiotas from the Odjick and Rocknest formations (Epworth Group; 1.89 Ga), northwestern Canada. *Canadian Journal of Earth Sciences*, **22**, 1781-1792.
- Horodyski RJ (1975) Stromatolites of the Lower Missoula Group (middle Proterozoic), Belt Supergroup, Glacier National Park, Montana. *Precambrian Research*, **2**, 215-254.
- Hurley NF, Van der Voo R (1990) Magnetostratigraphy, Late Devonian iridium anomaly, and impact hypotheses. *Geology*, **18**, 291-294.
- Jach R, Dudek T (2005) Origin of a Toarcian manganese carbonate/silicate deposit from the Kri'z'na unit, Tatra Mountains, Poland. *Chemical Geology*, **224**, 136-152.
- Kazmierczak J, Kempe S (2006) Genuine modern analogues of Precambrian stromatolites from caldera lakes of Niuafu'ou Island, Tonga. *Naturwissenschaften*, **93**, 119–126.
- Koban CG, Schweigert G (1993) Microbial origin of travertine fabrics - two examples from southern Germany (Pleistocene Stuttgart travertines and Miocene Riedoschingen travertine). *Facies*, **29**, 251–264.
- Korn H, Martin H (1959) Gravity tectonics in the Naukluft Mountains of South West Africa. *Bulletin of Geological Society of America*, **70**, 1047-1078
- Mamet B, Pr eat A (2006) Iron-bacteria mediation in Phanerozoic red limestones: State of the art. *Sedimentary Geology*, **185**, 147-157.
- Maslov VP (1960) *Stromatolites*. Trudy Instituta geologicheskikh nauk, Akademiya nauk SSR 41, 188 p.
- Miller RMcG (2008) The Geology of Namibia, Volume 2, Geological Survey of Namibia, Windhoek.
- Myrow PM, Coniglio M (1991) Origin and diagenesis of cryptobiontic *Frutexitis* in the Chapel island Formation (Vendian to Early Cambrian) of Southeast Newfoundland, Canada. *Palaios*, **6**, 572-585.
- Nicoll R S, Playford PE (1993) Upper Devonian iridium anomalies, conodont zonation and the Frasnian-Famennian boundary in the Canning Basin, Western Australia. *Palaeogeography, Palaeoclimatology, Palaeoecology*, **104**, 105-113.
- Playford PE, Cockbain AE, Druce EC, Wray JL (1976) Devonian stromatolites from the Canning Basin, Western Australia. In Walter MR (Ed.), *Stromatolites*, Elsevier, Amsterdam, 543-563.

- Playford PE, McLaren DJ, Orth CJ, Gilmore JS, Goodfellow WD (1984) Iridium anomaly in the Upper Devonian of the Canning Basin, Western Australia. *Science*, **226**, 437-439.
- Reitner J, Wilmsen M, Neuweiler F (1995) Cenomanian/Turonian Sponge Microbialite Deep-Water Hardground Community (Lienres, Northern Spain). *Facies*, **32**, 203-212.
- Riding R (1991) Calcified Cyanobacteria. In Riding R (ed.), *Calcareous Algae and Stromatolites*. Springer, Berlin, 55-87.
- Rodríguez-Martínez M, Heim C, Simon K, Reitner J, Zilla T (2010). *Tolypammina gregaria* Wendt-*Frutexites* assemblage and ferromanganese crusts: a coupled nutrient-metal interplay in the Carnian sedimentary condensed record of Hallstatt Facies (Austria). *Lecture Notes in Earth Sciences*, in press.
- Tsien H H (1979) Paleoecology of algal-bearing facies in the Devonian (Couvirtian to Frasnian) Reef Complexes of Belgium. *Palaogeography, Palaeoclimatology, Palaeoecology*, **27**, 103-127.
- Walter MR, Awramik SM (1979) *Frutexites* from stromatolites of the Gunflint iron formation of Canada, and its biological affinities. *Precambrian Research*, **9**, 23-33.
- Wendt J (1969) Foraminiferen-‘Riffe’ im karnischen Hallstätter Kalk des Feuerkogels (Steiermark, Österreich). *Paläontologische Zeitschrift*, **43**, 177-193.
- Wendt J (1988) Condensed carbonate sedimentation in the late Devonian of the eastern Anti-Atlas (Morocco). *Eclogae geologicae Helvetica*, **81**, 155-173.
- Woods AD, Baud A (2008) Anachronistic facies from a drowned Lower Triassic carbonate platform: Lower member of the Alwa Formation (Ba'id Exotic), Oman Mountains. *Sedimentary Geology*, **209**, 1-14.

D

Raman Microscopy

Jan Toporski, Thomas Dieing, Christine Heim

Encyclopedia of Geobiology, Springer, 2011, in press

Synonyms

Confocal Raman imaging (CRI)

Definition

Confocal Raman microscopy (CRM) is a non-destructive analytical technique that merges Raman spectroscopy and confocal microscopy for the visualization of molecular information over a defined sample area.

Introduction

Raman spectroscopy is well suited for studies in mineralogy and petrography, as it provides nondestructive mineral identification fast and with high specificity. In addition, Raman spectroscopy allows the characterization of complex organic materials, which makes it particularly useful in biogeoscience applications (Hild *et al.*, 2008). This technique has long been applied in geosciences, for example, for the identification and characterization of minerals, or in the observation of mineral phase transitions in high and ultra-high pressure/temperature experiments.

In most cases, measurements have been carried out in a micro-Raman set up, i.e., information was obtained from single or multiple points of interest on a sample. This way, little detail on the spatial distribution and association of components or mineral phases, or chemical variation could be observed, even though this information may contribute significantly to the understanding of a sample's complexity.

By means of CRM, such sample characteristics can be evaluated from large scale scans in the centimeter range to the finest detail with sub-micron resolution. Modern confocal Raman microscopes allow for such measurements with very high sensitivity and spatial as well as spectral resolution. CRM is a tool that not only provides complementary information to data obtained by e.g., electron microprobe (EMP), energy dispersive x-ray analysis (EDX), or secondary ion mass spectrometry (SIMS). In addition to the quantitative and semiquantitative elemental and/or isotopic data acquired by these techniques, CRM

contributes the visualization of the distribution for molecular information over a defined sample area. Furthermore, considering that most geomaterials are transparent from the UV (NUV) to VIS and NIR to some degree, this information can be obtained three dimensionally due to the confocal set-up of the microscopes. The following discussion provides background information and examples that shall serve to highlight some key analytical features of this technique for applications in geosciences. A recent and comprehensive summary on the application of CRM in geoscience can be found in Fries and Steele (2009).

Principles of confocal Raman microscopy

CRM essentially merges two techniques into one. First, Raman spectroscopy, which allows nondestructive chemical analysis; secondly, Confocal microscopy which allows the user to examine samples with diffractionlimited resolution as well as to obtain three-dimensional information from the sample. The theory behind these two techniques will be explained in the following sections, followed by an illustration of how images with chemical sensitivity can be obtained using this combination of techniques.

Raman spectroscopy

When light of a certain wavelength interacts with a molecule, most photons are elastically scattered and therefore have the same energy as the incident photons. However, a very small fraction (approximately 1 in 10^6 – 10^7 photons) is in elastically scattered, which means that the energy of the scattered photon is different (usually lower) than the energy of the incident photon.

This is called the “Raman effect”, which was discovered by Sir Chandrasekhara Raman in 1928 (Raman, 1928; Raman and Krishnan, 1928). Unlike today, he used a filtered beam of sunlight as an excitation source and his eye as a detector for the frequency shifted light. This was long before the development of the first laser by Maiman in 1960. Raman was awarded the Nobel Prize in 1930 for this discovery. The theory behind the Raman effect was derived five years earlier by Smekal (1923). The tremendous importance of the Raman effect lies in the fact that the energy shift between the exciting and the Raman scattered photon is caused by the excitation (or annihilation) of a molecular vibration. This energy shift is characteristic and therefore a fingerprint for the type and coordination of the molecules involved in the scattering process.

Theory

The following section shall provide some basic descriptions and definitions relevant to Raman spectroscopy. Readers interested in a detailed theoretical background are referred to Ibach and Lüth (2003). In quantum mechanics, the scattering process between a photon and a molecule is described as an excitation of a molecule to a virtual state lower in energy than a real electronic state and the (nearly

immediate) de-excitation. The lifetime of the virtual state is extremely short and can be calculated by the Heisenberg uncertainty relation:

$$\Delta t \cdot \Delta E \geq \frac{\hbar}{2} \quad (1)$$

With typical photon energies of 1-2eV, the lifetime of the excited state is only about 10^{-15} s. After this extremely short time, the molecule falls back either to the vibrational ground state or to an excited state (Fig. D.1). When the initial and final states are identical, the process is called Rayleigh scattering.

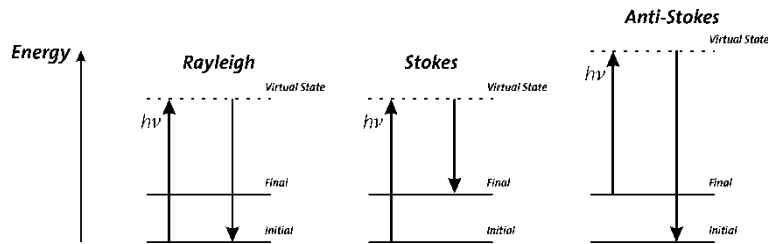


Fig. D.1 Energy level diagram for Raman scattering.

If the initial state is the ground and the final state a higher vibrational level, the process is called Stokes scattering, if the initial state is energetically higher than the final state, this is referred to as Anti-Stokes scattering. The difference in energy between the incident and the Raman scattered photon is equal to the energy of a vibration quantum of the scattering molecule. A plot of intensity of scattered light versus energy difference is called a Raman spectrum. The position of a Raman line is usually given in wavenumbers ($1/\text{cm}$), which is the energy shift relative to the excitation line:

$$\bar{\nu} = \frac{1}{\lambda_{\text{incident}}} - \frac{1}{\lambda_{\text{scattered}}} \quad (2)$$

$\lambda_{\text{incident}}$ and $\lambda_{\text{scattered}}$ are the wavelengths of the incident and Raman scattered photons, respectively.

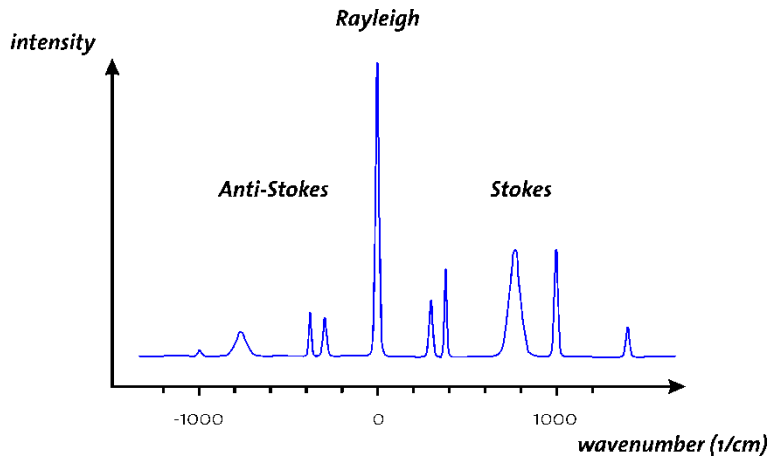


Fig. D.2: Typical Raman Spectrum

As can be seen in Fig. D.2, a typical Raman spectrum is symmetric to the Rayleigh line and the Anti-Stokes lines are smaller than the Stokes shifted lines.

From classical scattering theory, one finds that the intensity I of scattered light is proportional to the 4th power of the excitation frequency

$$I \propto \nu^4 \quad (3)$$

Exciting a sample with blue light at 400nm would therefore give a 16 times higher Raman signal than using red light at 800nm. The problem of using blue (or UV) excitation light, however, is fluorescence. Many samples show fluorescence when they are excited with blue light and Raman emissions are extremely weak compared to fluorescence. If a sample shows significant fluorescence, obtaining a Raman spectrum is usually impossible because the fluorescence background covers the Raman signal. In the red (or even IR) region of the spectrum, fluorescence is usually not a problem, but the excitation intensity must be much higher ($I \propto \nu^4$). Another problem is that Silicon detectors cannot be used above 1100nm (band gap energy of Si: 1.12eV). Other IR detectors (such as InGaAs) show much more thermal and readout noise than Silicon and photon counting detectors with low dark count rates are not available yet. In real experiments one must always find a compromise between detection efficiency and excitation power.

Confocal Microscopy

Confocal microscopy requires a point source (usually a laser), which is focused onto the sample. The reflected light (Rayleigh, Raman, fluorescence) is collected with the same objective and focused through a pinhole at the front of the detector (see Fig. D.3).

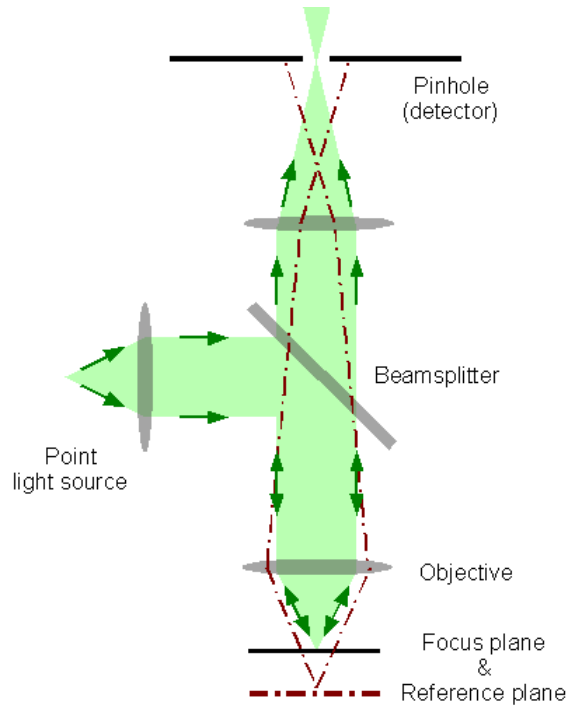


Fig. D.3: Principal setup of a Confocal microscope

This ensures that only light from the image focal plane can reach the detector, which greatly increases image contrast and with the proper selection of pinhole size, slightly increases resolution (max. gain in resolution: factor $\sqrt{2}$). As can be seen from Fig. D.3, light originating from planes other than the focal plane will be out of focus at the pinhole. Therefore its contribution to the detected signal is strongly reduced. Additionally, by changing the distance between the objective and the sample, the focal plane is moved within the sample thus allowing depth profiling or even 3D imaging (Wilson, 1990).

Pinhole size

The choice of the pinhole size is important because on one hand the signal should be as high as possible, while on the other hand the image should be as confocal as possible (highest depth resolution). To take full advantage of the lateral and depth resolution possible with confocal microscopy, the size of the pinhole should be adjusted and optimized. To obtain the highest lateral resolution, the pinhole size should be below $v_p = 0.5$. (The variable v describes the position in optical coordinates and can be derived from

$$v = \frac{2\pi}{\lambda} \sqrt{x^2 + y^2} \sin \alpha$$

. Here λ is the excitation wavelength, x and y the sample coordinates in the focal plane and α half of the aperture angle. v_p is the radius of the pinhole in optical coordinates when assuming a magnification of 1). However, at this point the transmission through the pinhole is only 5% of the scattered intensity. In practice, the pinhole size can be up to $v_p=4$ without significantly changing depth resolution and up to $v_p=2$ without significantly changing lateral resolution. It can be shown that if $v_p > 4$,

the resolution of at least a conventional microscope remains. This is due to the fact that for a large detector the resolution is always determined by the diameter of the excitation laser spot. Only the depth resolution (and therefore contrast for a thick sample) is lost in this case. In most cases a pinhole size of $v_p=2.5$ is a good compromise, since good depth resolution is maintained while $>75\%$ of the light still reaches the detector (see figure D.4).

For the experiment, the relation

$$\frac{M}{NA} \geq \frac{\pi d_0}{v_p \lambda} \quad (4)$$

should be fulfilled, where M is the magnification, d_0 the diameter of the pinhole and NA the numerical aperture of the objective. The left side of this equation is defined by the objective and the beam path and the right side by the wavelength, the pinhole size itself and v_p . If for example an objective with a magnification of 100x and a numerical aperture of 0.9 is used at a wavelength of 532nm the optimum pinhole size would be $50\mu\text{m}$ for maximum depth resolution and $10\mu\text{m}$ for maximum lateral resolution.

In actual experiments, one usually has to find a compromise between the highest resolution and collection efficiency. This is very important in confocal Raman microscopy because Raman is an extremely weak effect. If a very small pinhole is used, the collection efficiency is strongly reduced (Fig. D.4).

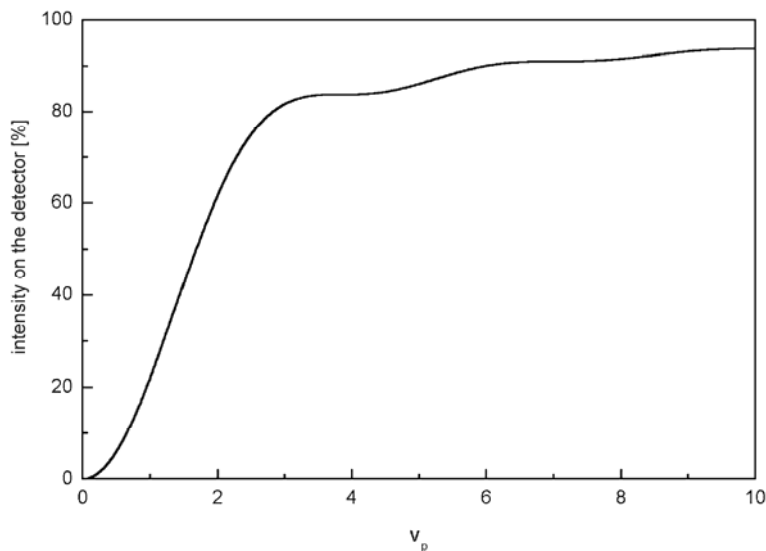


Fig. D.4: Collection efficiency as a function of the pinhole size normalized to the total power in the image plane

This graphic shows the intensity on the detector as a function of pinhole size, normalized to the total intensity in the image plane. One can see that the collection efficiency is about 75% for maximum depth resolution ($v_p=2.5$), but only 6% for maximum lateral resolution ($v_p=0.5$).

Using the appropriate pinhole size, it is therefore always possible to obtain maximum depth resolution.

Resolution

For sample scanning systems, the magnification printed on the objective used is of minor importance. The maximum scan range achievable by the sample scanner determines the maximum image size, independent of the magnification of the objective. The more important property of the objective is the numerical aperture, which together with the excitation wavelength determines the lateral resolution of the objective. The magnification is only important for the choice of the pinhole size.

The maximum resolution of a classical microscope is given by the Rayleigh criterion

$$\Delta x = \frac{0.61\lambda}{NA} \quad (5)$$

where Δx is the smallest distance between two point objects that will appear separated in the image plane, λ is the wavelength of the excitation light and NA is the numerical aperture of the microscope objective. In this case, the image of two point objects will appear (Fig. D.5).

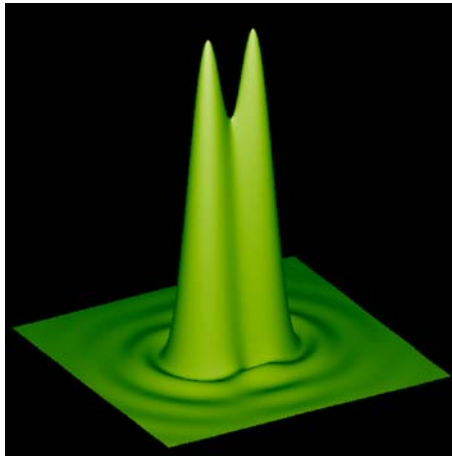


Fig. D.5: The intensity distribution of two point sources which are separated by the Rayleigh criterion.

Confocal Raman Microscopy

Instrumentation considerations

When combining Confocal microscopy and Raman spectroscopy the main challenge is the low signal intensity. As mentioned earlier, only 1 in about 10^6 to 10^7 photons is frequency shifted by the Raman effect. Thus the number of photons reaching the detector is far less than is the case for Confocal or fluorescence microscopy. The two obvious changes would be to increase the laser power and to increase the integration time. However, there are limitations to these possibilities as shown below:

a) Laser Power

If a power of only 1mW from a 532nm laser is focused diffraction limited using a 100x air objective with a NA of 0.9, the power density in the illuminated spot is approximately $10^6\text{W}/\text{cm}^2$. These levels are only possible because a single point is illuminated and the heat effectively dissipates in three dimensions. The maximum laser power on the sample is therefore typically in the range of 1-20mW.

b) Integration time

Increasing the integration time will increase the signal to noise ratio significantly. However, when Confocal Raman imaging or mapping is applied, in which an image is produced by recording a spectrum at every image pixel, the integration time per spectrum needs to be kept to a minimum. An integration time of only 1s per spectrum will, when recording an image of 128x128 pixels, result in a total acquisition time of about 4.5h, which are inconvenient time-spans for routine application.

Therefore, a system for Confocal Raman imaging must be capable of obtaining the Raman spectra in less than 50-100ms. There are several parts of a Confocal Raman microscope which should be optimized in order to allow such rapid data acquisition. These will be discussed in the following:

Laser power

As described above, the maximum laser power is limited and will heavily depend on the sample used.

Collection efficiency of the objective

Using objectives with high numerical apertures maximizes the collection efficiency.

Throughput of the microscope

In order to enhance the throughput of the microscope, the components used within the beam path should be optimized and if possible minimized.

Efficiency of the grating

Highly efficient gratings with the correct blazing angle for the excitation wavelength should be used. As an example: A grating blazed at 500nm will have an absolute efficiency of >60% up to 3000 rel.1/cm when using a 532nm laser. Using the same grating with a 785nm laser will cause the efficiency to drop to about 30% at 3000 rel.1/cm. The correct grating blazed at 750nm, however, shows an efficiency >60% up to 3000 rel.1/cm when used with the 785nm laser.

Efficiency of the spectrometer

There are a variety of spectrometers available on the market. While mirror based spectrometers can generally be used over a wide spectral range, lens-based spectrometers often show a higher throughput in the spectral range they are designed for. Lens-based spectrometers shows a transmission at 532nm of >65% (e.g. UHTS300 from WITec). Commercially available mirror-based Czerny-Turner spectrometers only have a transmission of about 30% at this wavelength.

Efficiency of the detector (CCD)

Back-illuminated CCD cameras show a quantum efficiency (QE) of >90% over the entire spectral range of interest for 532nm excitation. Deep depletion back-illuminated CCD cameras, on the other hand, show a QE of >70% for 785nm excitation. As a comparison, front illuminated CCD cameras do not exceed 55% quantum efficiency at any wavelength.

Additionally, the dark current of the cameras needs to be minimized, which is achieved through efficient Peltier cooling.

The readout noise is another limiting factor for small signals. As the analog to digital (A/D) converter of all cameras will add at least 5-10 electrons read-out noise to the signal, any signal below approximately 5 electrons will be lost in the noise. Additionally, the faster the A/D converter is operating, the higher the read-out noise will be. Electron-multiplying CCD (EM-CCD) cameras can be used to overcome this problem. With these cameras, the signal is amplified before the A/D conversion, allowing the detection of even single photons and reducing the necessary integration time down to milliseconds.

Principle of operation

Confocal Raman microscopes generally provide a variety of modes of operations. The most common are listed below:

Collection of Raman spectra at selected sample areas (Single Spectrum)

Single Raman spectra can be collected at user-selectable sample areas with integration times ranging from ms to hours. The position of the collected spectrum can normally be fully controlled in 3D. A stable and precise positioning system must be included in the instrument to ensure that the point of interest will remain fixed under the excitation focus. This is very important when spectra with longer integration times for the best quality and signal to noise ratio are to be obtained from extremely small sample volumes. For example, using an oil immersion objective (NA 1.4) with a 532nm laser and the proper pinhole size allows the sample volume to be as small as $\approx 230 \times 230 \times 550$ nm.

Collection of time series of Raman spectra at selected sample areas (Time Spectrum)

With this mode, time series of Raman spectra can be obtained to analyze dynamic sample properties. Thousands of spectra can be obtained over time and analyzed with integration times ranging from ms to tens of seconds.

Raman spectral imaging

In the Raman spectral imaging mode, the sample is moved in X and Y and a full Raman spectrum is obtained at every pixel measured. From these data sets images of e.g. the integrated intensity of various bands can be generated. This is illustrated in the following example.

A sample from the Äspö Hard Rock Laboratory, Sweden, was studied using the large area scan mode of an alpha500 R, aiming to characterize secondary cleavage fillings in a 1.8 to 1.4 Billion years old diorite.

A section was obtained from a drill core from the SKB (Swedish nuclear fuel and waste management company) core library and drilled from a tunnel at ~450 m below the surface. This sample was examined by confocal Raman imaging (WITec alpha500R confocal Raman microscope) with a 532nm laser and a 50x air objective (NA 0.55). The scan range was 8000 μ m in X and 2000 μ m in Y with 800x200 points resolution. Each spectrum was integrated for 36ms. Fig. 6 shows the characteristic spectra of Calcite, Fluorite and Quartz found in the sample. Integrating over, for example, the area marked in green in Fig. D.6d results in a single value for each of the 160000 spectra and this can then be displayed as an image as shown in Fig. D.6a for Quartz. Here brighter values indicate a higher integrated intensity of the Quartz peak. The distribution of Quartz can thus be seen from this image. Other spectra of the same scan show the characteristic features of Calcite or Fluorite (Fig. D.6d). Using these, the Calcite (Fig. D.6b) and Fluorite (Fig. D.6c) images can easily be generated by using additional integral filters for the marked regions. Other features of the spectra such as the width of peaks or their position can also easily be evaluated by applying the corresponding filters.

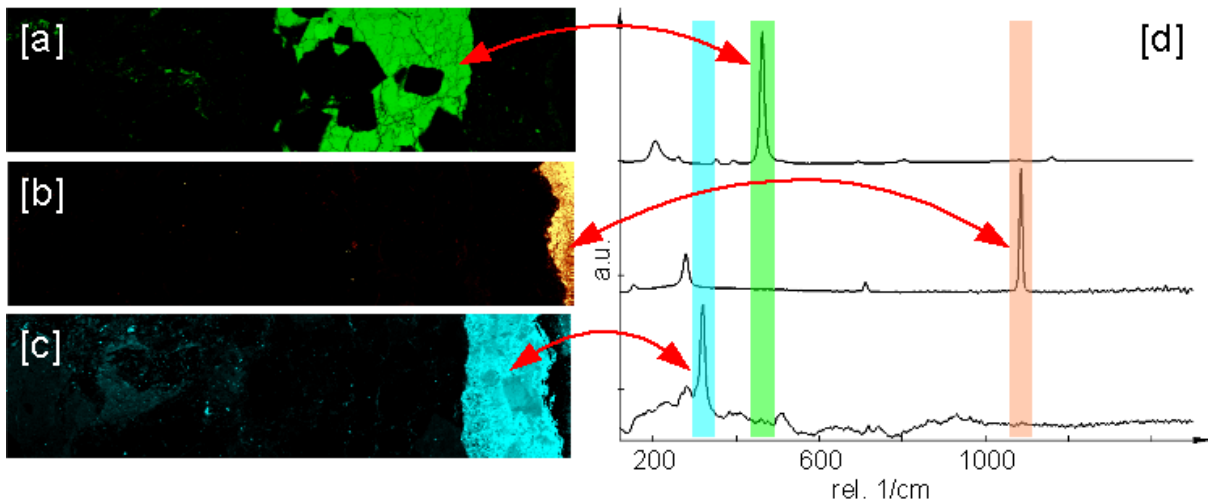


Fig D.6: Spectra (d) and spectral images of Quartz (a), Calcite (b) and Fluorite (c) recorded from the diorite (a) and the fracture fillings (b and c).

Further evaluation of the data allows the averaging of similar spectra (for which a cluster analysis is often used) and the subtraction of, for example, pure spectra from mixed spectra to extract the spectra of the various components. These spectra can then be used with the basis analysis, where each of the spectra recorded are fitted with a linear combination of the basis spectra. The result of such an analysis is one image for each basis spectra and these images can then be combined to generate a false color image showing the distribution of all components in one image (Fig. D.7). Mixed areas are shown as the corresponding mixed color and the spectra are color coded in the same way as the image.

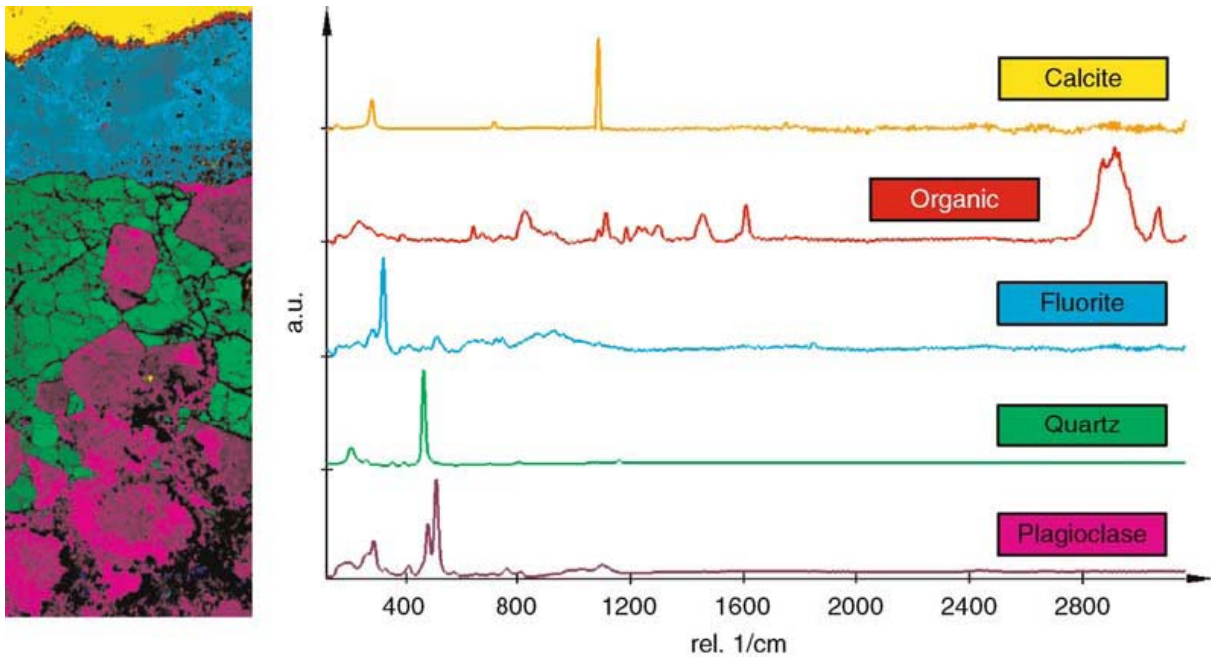


Fig D.7: Averaged and subtracted spectra of the various components in the diorite and the adjacent fracture minerals with the combined image on the left.

The color-coded Raman image and corresponding spectra in Fig. D.7 allow for the general assignment of mineral phases and their gross distribution over the scanned area. In addition to the mineralogical context information, organic components were identified, spectrally characterized and located, trapped between two generations of fracture fillings, (the hydrothermal Fluorite and low temperature Calcite, *Tullborg et al.*, 2008; Wallin and Petermann, 1999), indicating at which point in time a “deep biosphere” was active within these rocks.

Cluster analysis of the data set revealed discrete areas of variation in the mineral phases (Fig. D.8). This is exemplified by the Quartz phase four distinct regions were identified based on variations in relative peak intensity. Plotting regions of equal intensities of the Quartz line at ca. 200 cm^{-1} shows discrete regions in the sample corresponding to each of the identified spectra.

Quartz was selected as an example to highlight the feasibility of color-coded Raman imaging to locate changes of different mineral phases. These changes can likely be attributed to different levels of crystallinity and crystal orientation. It is noteworthy that the discrete phase colored green only occurs at the interface with the Plagioclase minerals, which can be attributed to a secondary phase due to the alteration and phase changes of the Plagioclases. Since SiO_2 -phases play an important role in biomineralisation, this example highlights the potential benefits confocal Raman imaging may provide in understanding the processes and dynamics involved in these processes.

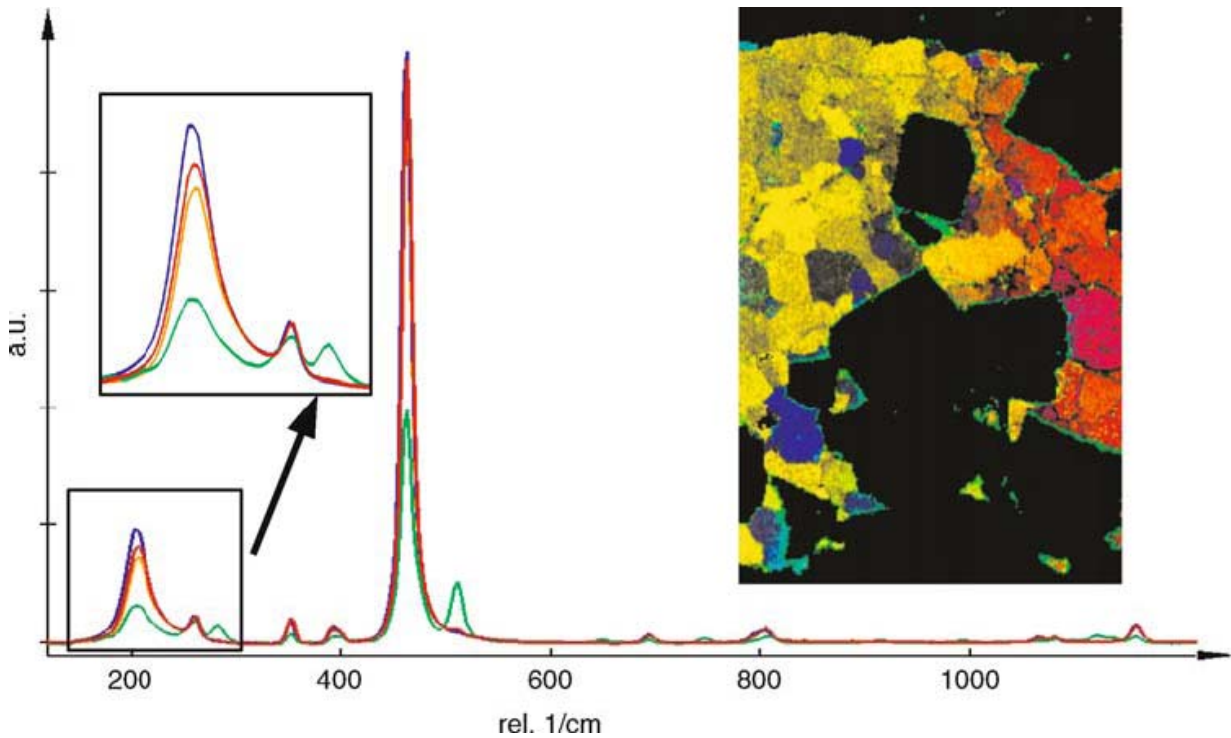


Fig D.8. Variations in the Quartz phases, due to changes in the crystallographic orientation, the crystallinity and the minerals.

Summary

CRM is a nondestructive analytical technique that merges Raman spectroscopy and confocal microscopy for the visualization of molecular information over a defined sample area. The technique makes use of the Raman effect (Raman, 1928), i.e., the energy shift between exciting and scattered photons which is caused by the excitation (or annihilation) of a molecular vibration. This energy shift is characteristic and therefore a fingerprint for the type and coordination of the molecules involved. By means of CRM, the spatial distribution and association of components in the sample, including organics as well as minerals, can be evaluated from large scale scans in the centimeter range to the finest detail with submicron resolution. This way, CRM may contribute significantly to the understanding of a sample's chemical composition, and complexity, in geological and geobiological studies.

References

- Fries M, Steele A (2009) Raman spectroscopy and confocal Raman imaging in mineralogy and petrography. In Dieing T, Hollricher O, Toporski J (eds.), *Confocal Raman Microscopy*. Springer, Heidelberg, 320p.
- Hild S, Marti O, and Ziegler A, (2008) Spatial distribution of calcite and amorphous calcium carbonate in the cuticle of the terrestrial crustaceans *Porcellio scaber* and *Armadillidium vulgare*. *Journal of Structural Biology*, **142**, 100–108.
- Ibach H, Lüth H (2003) *Solid State Physics. An Introduction to Principles of Materials Science*. Springer, Berlin, 501p.
- Raman C (1928) A new radiation. *Indian Journal of Physics*, **2**, 387.
- Raman C, Krishnan K (1928) A new type of secondary radiation. *Nature*, **121**, 501.
- Smekal A G (1923) Zur Quantentheorie der Dispersion. *Naturwissenschaften*, **11**, 873–875.
- Tullborg E-L, Drake H, Sandström B (2008) Palaeohydrogeology: A method based on fracture mineral studies. *Applied Geochemistry*, **23**, 1881-1897.
- Wallin B, Peterman Z (1999) Calcite fracture fillings as indicators of palaeohydrology at Laxemar at the Äspö Hard Rock Laboratory, southern Sweden. *Applied Chemistry*, **14**, 953–962.
- Wilson T (1990) *Confocal Microscopy*. Academic Press, London, 448p.

CURRICULUM VITAE

Christine Nora Heim

Geburtstag und Geburtsort: 24.04.1979 Hannover, Deutschland

Nationalität: Deutsch

Promotionsstudium

2005 Seit 01.08.2005 Doktorandin und wissenschaftliche Mitarbeiterin in der Abteilung
Geobiologie des Geowissenschaftlichen Zentrums der Georg-August-Universität
Göttingen

Grund- und Hauptstudium

2005 Diplom in Geologie - Diplomarbeit in Zusammenarbeit der Universität Frankfurt mit
der Abteilung Marine Geochemie des Alfred-Wegener-Institutes für Polar- and
Meeresforschung. Titel der Arbeit: Die geochemische Zusammensetzung der
Sedimente im Aralsee und Sedimentationsprozesse während der letzten 100 Jahre.

2002 Vordiplom in Geologie

1999 – 2005 Studium der Geologie an der Johann-Wolfgang-Goethe-Universität Frankfurt/Main

1998 – 1999 Freiwilliges Soziales Jahr beim Rettungsdienst des Deutschen Roten Kreuzes in Fulda

Schulzeit

1989 – 1998 Gymnasium: Winfriedschule Fulda, Abschluss: Abitur

1985 – 1989 Grundschule in Fulda- Niesig